

# Modelling of microwave induced plasmas : the interplay between electromagnetism, plasma chemistry and transport

**Citation for published version (APA):**

Jimenez-Diaz, M. (2011). *Modelling of microwave induced plasmas : the interplay between electromagnetism, plasma chemistry and transport*. [Phd Thesis 1 (Research TU/e / Graduation TU/e), Applied Physics and Science Education]. Technische Universiteit Eindhoven. <https://doi.org/10.6100/IR712628>

**DOI:**

[10.6100/IR712628](https://doi.org/10.6100/IR712628)

**Document status and date:**

Published: 01/01/2011

**Document Version:**

Publisher's PDF, also known as Version of Record (includes final page, issue and volume numbers)

**Please check the document version of this publication:**

- A submitted manuscript is the version of the article upon submission and before peer-review. There can be important differences between the submitted version and the official published version of record. People interested in the research are advised to contact the author for the final version of the publication, or visit the DOI to the publisher's website.
- The final author version and the galley proof are versions of the publication after peer review.
- The final published version features the final layout of the paper including the volume, issue and page numbers.

[Link to publication](#)

**General rights**

Copyright and moral rights for the publications made accessible in the public portal are retained by the authors and/or other copyright owners and it is a condition of accessing publications that users recognise and abide by the legal requirements associated with these rights.

- Users may download and print one copy of any publication from the public portal for the purpose of private study or research.
- You may not further distribute the material or use it for any profit-making activity or commercial gain
- You may freely distribute the URL identifying the publication in the public portal.

If the publication is distributed under the terms of Article 25fa of the Dutch Copyright Act, indicated by the "Taverne" license above, please follow below link for the End User Agreement:

[www.tue.nl/taverne](http://www.tue.nl/taverne)

**Take down policy**

If you believe that this document breaches copyright please contact us at:

[openaccess@tue.nl](mailto:openaccess@tue.nl)

providing details and we will investigate your claim.

# **Modelling of Microwave Induced Plasmas**

The interplay between electromagnetism, plasma chemistry and transport

## PROEFSCHRIFT

ter verkrijging van de graad van doctor aan de Technische Universiteit Eindhoven, op gezag van de rector magnificus, prof.dr.ir. C.J. van Duijn, voor een commissie aangewezen door het College voor Promoties in het openbaar te verdedigen op maandag 6 juni 2011 om 16.00 uur

door

Manuel Jimenez Diaz

geboren te Córdoba, Spanje

Dit proefschrift is goedgekeurd door de promotoren:

prof.dr. J.J.A.M. van der Mullen  
en  
prof.dr.ir. G.M.W. Kroesen

Copromotor:  
dr.ir. J. van Dijk

This research is sponsored by the Technology Foundation STW, The Netherlands, and the company Draka Comteq Fibre

CIP-DATA TECHNISCHE UNIVERSITEIT EINDHOVEN

Jimenez Diaz, Manuel

Modelling of Microwave Induced Plasmas: The interplay between electromagnetism, plasma chemistry and transport / by Manuel Jimenez Diaz. -  
Eindhoven : Technische Universiteit Eindhoven 2011. - Proefschrift.

A catalogue record is available from the Eindhoven University of Technology Library.

ISBN 978-90-386-2492-1

NUR 925

Subject headings : plasma modelling / non-equilibrium plasmas / microwave induced plasmas / plasma chemical vapor deposition / Maxwell equations / computational fluid dynamics

Copyright © 2011 Manuel Jimenez Diaz

All rights reserved. No part of this book may be reproduced, stored in a database or retrieval system, or published, in any form or in any way, electronically, mechanically, by print, photo-print, microfilm or any other means without prior written permission of the author.

Printed by: Ipskamp Drukkers B.V.

Cover design: Patricia Jimenez Diaz

*para mi familia*



---

# Summary

---

## **Modelling Microwave Induced Plasmas**

*The interplay between electromagnetism, plasma chemistry and transport*

In this thesis we report on a theoretical/numerical study that is concerned with *Microwave Induced Plasmas* (MIPs) in general, and the application of a MIP to the Plasma-activated Chemical Vapour Deposition (PCVD) process that is used at Draka Comteq for the production of optical fibres in particular. This was performed in the framework of the STW project (ETF.6265) titled:

*Exploring the compositional freedom in space and chemistry of Microwave Induced Plasmas: An object oriented approach.*

The primary purpose of the project was *to design an experimentally validated grand model for the microwave deposition plasma.*

Furthermore, in order to improve the deposition process, we studied *how the different microwave components shape the electromagnetic field and thus the plasma.*

To deal with these objectives, two types of models have been used:

### *1. Models describing particular aspects*

The Electromagnetic Model (chapter 3) is based on the finite difference frequency domain method and makes use of a two-dimensional orthocurvilinear grid. It is a full-vectorial approach for 3-field components that can be used as a design tool for symmetrical electromagnetic structures (chapter 6) and as a crucial part of Grand Models. The Electromagnetic Model was validated by means of a comparison of its results with those of known waveguide solutions.

The Chemistry Model (chapter 5) is a zero space-dimensional version of a Grand Model giving a time-dependent description of the chemical plasma composition. The transport mechanisms, in reality originating from two or three-dimensional structures, are described in the framework of the Chemistry model as effective source terms

---

making use of convection and diffusion frequencies. In this thesis we deal with a Chemistry Model for pulsed plasmas.

The Deposition Model (chapter 11) has been developed as a tool for obtaining insight into the role of the plasmas used for optical fibre production. The model shows how plasma mechanisms such as diffusion and convection manifest themselves in the *local* deposition profile. The *global* deposition profile is the result of the convolution of various local profiles. This convolution is realized by the movement of the plasma-creating cavity along the tube in which the deposition takes place. Results of the global profile are compared with those of experimental measurements.

## *2. Models describing multiple aspects in a self-consistent manner*

Using the insights of the electromagnetic, chemical and deposition aspects, a more complete plasma model is created. This so-called Grand Model (chapter 7) consists of a macroscopic description of plasmas based on balance equations (chapter 4) that compute the chemical composition in a self-consistent relation with the flow and the electromagnetic aspects. The boundary conditions are formed by the configuration of the plasma, the absorbed power, the overall pressure difference and the fill-chemistry. Two-dimensional Grand Models are created using the PLASIMO platform (described in chapter 2). A central role is played by the Electromagnetic Model described above, which is needed to describe the power absorbed by the plasma.

The Grand Model has been validated by comparing it with experimental results of surface wave discharges (chapters 8 and 9) thus fulfilling the first objective of this study. Furthermore in chapter 10, it is used to investigate the confinement of the plasma inside the Draka reactor.

---

# Contents

---

<b>1</b>	<b>General Introduction</b>	<b>13</b>
1.1	Introduction . . . . .	14
1.2	Microwave Induced Plasmas . . . . .	14
1.3	The PCVD Process at Draka Comteq . . . . .	16
1.4	Modelling and Simulation . . . . .	18
1.4.1	A Short Review of SWD modelling . . . . .	19
1.4.2	A Short Review of SWD modelling in Our Group . . . . .	21
1.5	Outline of this Thesis . . . . .	22
<b>I</b>	<b>Physical Models</b>	<b>25</b>
<b>2</b>	<b>PLASIMO Structure</b>	<b>27</b>
2.1	Introduction . . . . .	28
2.2	The History of PLASIMO . . . . .	28
2.3	PLASIMO Overview . . . . .	31
2.4	Governing Equations in PLASIMO . . . . .	35
2.5	Boundary Conditions . . . . .	36
2.6	The Coordinate System . . . . .	37
2.6.1	Tensor Calculus in OCL Coordinate Systems . . . . .	39
2.7	The Numerical Mesh . . . . .	40



2.8	Discretisation — LinSys . . . . .	41
<b>3</b>	<b>Electromagnetic Model</b>	<b>45</b>
3.1	Introduction . . . . .	46
3.2	Physical Model: the Maxwell Equations . . . . .	46
3.3	Numerical Model . . . . .	48
3.3.1	Geometry and Grid Generation . . . . .	49
3.3.2	Discretisation . . . . .	51
3.3.3	Solution Procedure for the Resulting Matrix Problem . . . . .	51
3.4	Boundary Conditions . . . . .	52
3.5	Analytical Solutions and Model Validation . . . . .	54
3.5.1	The Vector Helmholtz Equation for $\mathbf{H}$ . . . . .	54
3.5.2	Validation Case: Short-circuited Coaxial Waveguide . . . . .	55
3.5.3	Numerical Dispersion . . . . .	58
3.6	Conclusion . . . . .	60
<b>4</b>	<b>Transport</b>	<b>63</b>
4.1	Introduction . . . . .	64
4.2	From Kinetic to a Fluid Description . . . . .	65
4.3	Multi-Fluid Description in PLASIMO . . . . .	66
4.3.1	The Specific Density Balances . . . . .	67
4.3.2	The Specific Momentum Balances . . . . .	68
4.3.3	Fick Diffusion . . . . .	68
4.3.4	Self-Consistent Multicomponent Diffusion . . . . .	69
4.3.5	Ohm’s Law: the DC Current Density and Conductivity . . . . .	70
4.3.6	Ohm’s Law: the Complex Current Density and Conductivity . . . . .	71
4.3.7	The Specific Energy Balances . . . . .	72
4.4	The Balance Equations for the Plasma Bulk . . . . .	73
4.5	Overview . . . . .	76

4.6	Local Thermal Equilibrium . . . . .	76
4.7	The Canonical Transport Equation: The $\phi$ -equation . . . . .	78
4.7.1	Discretisation . . . . .	79
4.7.2	Transport Coefficients . . . . .	80
4.8	Particle Interactions: Cross sections and Relations . . . . .	81
4.8.1	Elastic Interactions . . . . .	81
4.8.2	Inelastic Interactions . . . . .	83
4.9	Assumptions . . . . .	83
4.10	Summary . . . . .	85
<b>5</b>	<b>Chemistry</b>	<b>87</b>
5.1	Introduction . . . . .	89
5.2	Chemistry versus Transport and Configuration . . . . .	92
5.3	Coupled Species Equations; two Methods . . . . .	94
5.4	Transport and Wall Reactions . . . . .	96
5.5	The Electron Balances . . . . .	97
5.6	Global Plasma Models and Plasma Classification . . . . .	99
5.7	The new Model RateLab . . . . .	100
5.8	The User Interface . . . . .	101
5.9	A pulsed argon plasma as case-study . . . . .	105
5.10	Summary . . . . .	108
<b>II</b>	<b>Applications</b>	<b>109</b>
<b>6</b>	<b>The effect of the remote field electromagnetic boundary conditions on microwave induced plasma torches</b>	<b>111</b>
6.1	Introduction . . . . .	113
6.2	Configuration, Plasma and Geometry . . . . .	115
6.2.1	Geometry . . . . .	117

6.3	Model . . . . .	117
6.3.1	Maxwell Equations . . . . .	119
6.3.2	Grid . . . . .	122
6.3.3	Boundary Conditions . . . . .	123
6.3.4	Numerics . . . . .	125
6.4	Results and Discussion . . . . .	127
6.4.1	Effect of the Remote Field Boundary Conditions . . . . .	127
6.4.2	Effect of the Electron Density Value . . . . .	133
6.4.3	Effect of the Shape of the Transition Region (the 'gap') . . . . .	135
6.5	Conclusions . . . . .	138
<b>7</b>	<b>Surface Wave Discharges: Introduction, Characteristics, and Simulations</b>	<b>141</b>
7.1	Introduction . . . . .	142
7.2	Surface Wave Discharge Modelling . . . . .	143
7.3	Simulations . . . . .	146
7.3.1	Configuration: Geometry . . . . .	148
7.3.2	Configuration: Boundary conditions and Control Parameters . . . . .	149
7.3.3	Chemistry . . . . .	150
7.3.4	The Iterative Scheme . . . . .	153
7.4	Summary . . . . .	153
<b>8</b>	<b>Surfaguide Argon Plasma Model at High Pressure</b>	<b>155</b>
8.1	Introduction . . . . .	156
8.2	Model . . . . .	156
8.2.1	Geometry . . . . .	156
8.2.2	Boundary Conditions . . . . .	157
8.3	Results and Discussion . . . . .	159
8.3.1	Effect of the Absorbed Power on the Plasma Column Length . . . . .	160
8.3.2	Influence of the Wall Temperature on Contraction . . . . .	161
8.4	Conclusions . . . . .	162

<b>9</b>	<b>Surfatron Argon Plasma at Intermediate Pressures</b>	<b>165</b>
9.1	Introduction . . . . .	166
9.2	Physical Model . . . . .	167
9.2.1	Configuration: Geometry . . . . .	167
9.2.2	Configuration: Boundary Conditions . . . . .	169
9.3	Numerical Model . . . . .	171
9.4	Results and Discussion . . . . .	171
9.4.1	Plasma Region Inside the Launcher . . . . .	171
9.4.2	The Plasma Outside the Launcher . . . . .	178
9.4.3	Comparison with Experimental Results . . . . .	179
9.5	Conclusions . . . . .	185
<b>10</b>	<b>Deposition Reactor Argon Plasma at Intermediate Pressure</b>	<b>187</b>
10.1	Introduction . . . . .	188
10.2	Model . . . . .	191
10.2.1	Configuration: Geometry . . . . .	191
10.2.2	Configuration: Boundary Conditions . . . . .	192
10.3	Results . . . . .	195
10.3.1	Effect of the Choke Depth on Transmission . . . . .	199
10.4	Conclusions . . . . .	202
<b>11</b>	<b>Static and dynamic plasma deposition model: analytical and semi-empirical determination of local profiles and optimization of dynamic profiles</b>	<b>203</b>
11.1	Introduction . . . . .	204
11.2	Local Deposition Profile . . . . .	204
11.3	Deposition Profile for a Static Reactor . . . . .	210
11.4	Global Deposition Profile: Moving Deposition Reactor . . . . .	211
11.4.1	A Constant Reactor Velocity Profile . . . . .	213
11.4.2	An Arbitrary Reactor Velocity Profile (Multiple Ramps) . . . . .	213

## Contents

---

11.5 Numerical Integration . . . . .	219
11.6 Conclusions . . . . .	222
<b>12 General Conclusions</b>	<b>223</b>
12.1 Introduction . . . . .	224
12.2 Design of new models and modules . . . . .	224
12.3 Scientific Insight Obtained . . . . .	227
12.4 Recommendations for Future Work . . . . .	229
<b>Appendices</b>	<b>231</b>
<b>A Study on Model Resonances Using Equivalent Circuit Theory</b>	<b>231</b>

---

1

General Introduction

---

## 1.1 Introduction

Nowadays, plasma technology is used in a variety of applications, such as materials processing [1–3], gas volume cleaning [4], the construction of sources of ions [5] and radicals [6], and in plasma lighting [7–9]. The success of plasma technology can be attributed to the fact that plasma *sources* can create high densities and flux densities of photons and radicals, the plasma *products*.

In this thesis we report on a theoretical/numerical study that is concerned with *Microwave Induced Plasmas* (MIPs) in general, and the application of a MIP to the plasma-activated Chemical Vapour Deposition (PCVD) process that is used at Draka Comteq for the production of optical fibres in particular. This was performed in the framework of the STW project (ETF.6265) with title:

*Exploring the composition freedom in space and chemistry of Microwave Induced Plasmas; An object oriented approach.*

The primary purpose of the project was *to design an experimentally validated Grand model for the microwave deposition plasma.*

This thesis can be seen as an extension of the research line started by Ger Janssen [10] and Michiel van den Donker [11]. The model has been validated by comparing it with experimental results of surface wave discharges (see chapter 8 and 9) thus fulfilling the primary objective of this study.

Furthermore, in order to improve the deposition process, it is important to study *how the different microwave components shape the electromagnetic fields and thus the plasma.* This is the purpose of chapter 10, where we have investigated the confinement of the plasma inside the Draka reactor.

This chapter continues with an introduction to MIPs (section 1.2) and to the PCVD process (section 1.3). In section 1.4 we will discuss the role of modelling and numerical simulation in plasma science and technology. The chapter concludes with an outline of the thesis (section 1.5).

## 1.2 Microwave Induced Plasmas

In Microwave Induced Plasmas, the plasma gets its sustaining energy from electromagnetic microwaves. The frequency of the waves are in the range 300 MHz-300 GHz. One advantage of MIPs is that they can be created without the presence of electrodes which prevents the plasma contamination by electrode material.

The microwave systems that are used to sustain MIPs are comparable to those that

are found in domestic microwave ovens, like the one depicted in figure 1.1. Here we can recognise a power supply and a magnetron that generates the electromagnetic waves. The wave generated by the magnetron travels to a coupler system, in this case a stirred fan, that drives the wave into a cavity where the heated target is placed. It is common to have some shielding in order to protect the user from the microwave radiation and as a mean to shape the fields. A microwave induced plasma can be created if the heated target (i.e. the chicken) is substituted by a dielectric container filled with a gas (e.g. argon). Of course in the case of food the water molecules are responsible for the energy coupling, whereas in the plasma the charged particles play this role.

An important characteristic of microwave heating and MIPs is that they can be operated remotely with the heated target surrounded by dielectric material (e.g. a plastic box for food, a quartz container for the plasma). Moreover, due to the absence of electrodes, corrosive plasma-electrode interactions can be avoided so that there are much less limitations in selecting the chemical composition. This implies that there are many different ways to create and operate MIPs. Apart from changing control parameters as power and pressure, one can manipulate the size and shape of the plasma by choosing the chemical composition, with almost limitless freedom.

In the wave-plasma energy transfer a dominant role is played by the electrons. They oscillate with the frequency of the EM fields and when a collision between an electron and heavy particle takes place both particles gain energy.

The energy gained from the EM wave is used to maintain the discharge. Herein different processes take place such as sustaining the losses of energy associated with the efflux of electron-ion pairs, creation of excited states, radiation losses, etc. Note that not all the electrons contribute to maintain the discharge in the same way; the electrons with higher energies are responsible for maintaining the discharge by means of ionisation processes. This can be reflected in the shape of the electron energy distribution function (EEDF), particularly on the tail (electrons with energies higher than the first excitation energy).

### **Classification of MIPs based on application of EM fields**

With respect to the way in which the electromagnetic fields are applied to the plasma and how the plasma dimensions compare with the EM wavelength, we can classify the MIPs as [12, 13]:

*Localised active zone MIPs.* The plasma is contained in a *waveguide circuit* and the plasma dimensions are in the order of or smaller than the electromagnetic wavelength. This is the case of the Beenakker cavity [14] and the microwave plasma torches [15, 16] (see chapter 6).



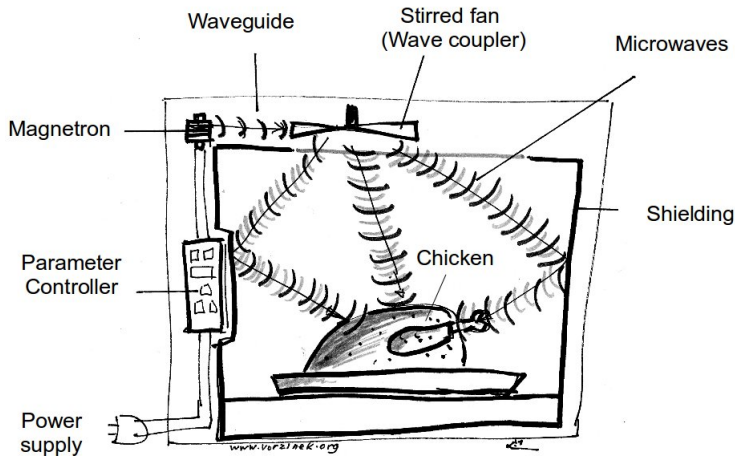


Figure 1.1: Schematic view of a microwave oven. A magnetron fed by a power supply generates electromagnetic waves. They travel through a waveguide until a stirred fan guide them to the domain where the heated target is placed (a chicken in this case). Shielding is provided to protect the user. A parameter controller allows to set the power delivered. A microwave induced *plasma* can be created if the chicken is substituted by a dielectric container filled with a gas (e.g. argon). Reference: F. Cecconi (vorzinek.org), *microwave oven*, Creative Commons Attribution-ShareAlike 3.0 Unported License.

*Travelling wave MIPs.* The plasma dimensions are larger than the electromagnetic wavelength. This is the case of plasmas contained inside a waveguide structure [17] or plasmas sustained by a leaking slotted waveguide [18]. A particular class of travelling wave discharges are surface wave discharges (SWDs). The specific feature of this class is that an electromagnetic wave propagates along the plasma column creating the plasma that, at the same time, serves as a propagation medium bringing the energetic wave to regions located further away from the *field applicator*. This device that transfers the energy from the microwave power supply to the SWD is also known as the *launcher* (see chapter 7).

### 1.3 The PCVD Process at Draka Comteq

A well-known application of MIPs is Plasma-activated Chemical Vapour Deposition (PCVD) used among others for the production of optical fibres [3, 19]. The fabrication of fibre optics consists on three steps: Deposition, Collapsing and Drawing [3]. The

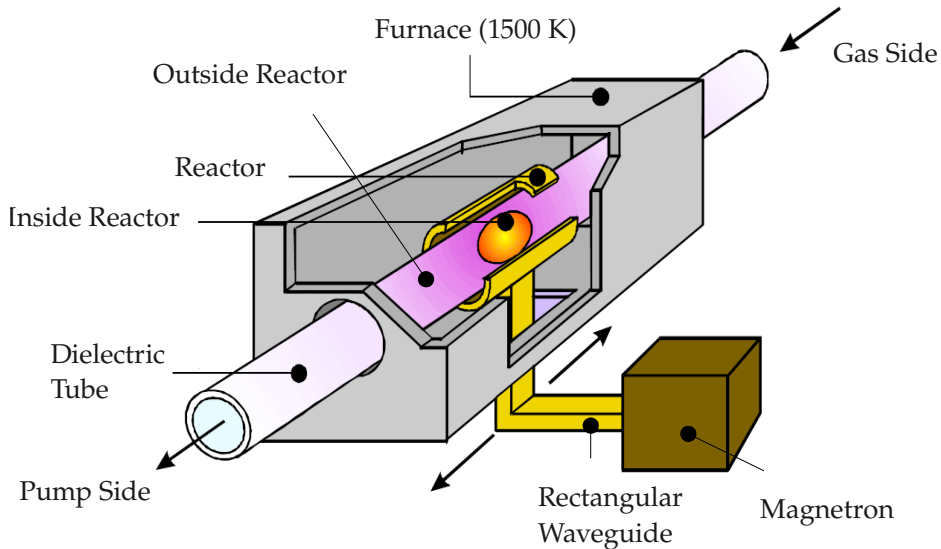


Figure 1.2: The plasma-activated chemical vapour deposition (PCVD) reactor used for the production of fibre optics.

PCVD is only essential in the first step (see chapter 10).

The set-up for the microwave deposition reactor was designed by Philips Research Laboratories in 1976 [3, 20]; it is given in figure 1.2 (see also [10, 11, 19]). A coaxial microwave cavity (reactor) surrounds the dielectric (quartz) tube. A gap in the reactor couples the EM-energy to a plasma mainly based on oxygen. The  $\text{SiCl}_4$  gas provided at the gas side reacts with the oxygen plasma producing the radicals needed to create the composition of several deposition layers at the inner wall of the tube. The forward and backward movement of the reactor allows to create deposition layers along the dielectric tube. During the deposition of each layer, it is possible to select the gas mixture by adding different dopants ( $\text{C}_2\text{F}_6$ ,  $\text{GeCl}_4$ ) and to control the refractive index. After the internal deposition process, the tube is collapsed into a *preform* from which a fibre can be drawn.

The plasma of interest is the discharge formed inside the reactor. Two chokes in the metal wall of the reactor function to confine the plasma region, their task is to minimise the power leaving this region, the *residual* power. The reason is that this emitted residual power can interact with the metal walls that shield the whole set-up,

and produce standing waves that can spoil the deposition procedure. Modelling is indispensable for the understanding of the power confinement. The model must describe the EM housekeeping as complete as possible; power absorption by the plasma in the reactor, the plasma outside the reactor and the residual waves leaving the reactor. This is studied in chapter 10.

## 1.4 Modelling and Simulation

In order to optimise a plasma application, one needs to understand the influence of the plasma design and operating parameters on the creation of the plasma products. This in turn requires insight into the plasma itself, into *internal* plasma properties such as the spatial variations of the electromagnetic fields, the velocity field and the densities and temperatures of the plasma constituents.

That insight is usually obtained via a combination of experimental and theoretical techniques. Since the work in this thesis is based on the latter, we will say a few words about the approaches in the field of computational plasma physics. It usually consists of two stages:

- *modelling*: the construction of a theoretical framework that describes the physical phenomena that are relevant for the model;
- *simulation*: the application of the model to concrete systems. Nowadays this is usually done with the help of numerical computing, in which case one speaks of *numerical simulation*.

Models can be classified according to their scope and by the degree to which the real system has been approximated. We will distinguish *specific*, *global* and *Grand* models.

A *specific model* normally deals with the relation between two or more internal plasma quantities. For instance the determination of rates of (composed) reactions assuming known values of the electron density and temperature. On the higher level we can combine various collisional and radiative processes to determine effective ionisation and/or recombination coefficients of a plasma gas (chapter 5). This is one of the tasks of a so-called collisional radiative model.

Another example of a specific model is a Boltzmann solver; it provides the electron energy distribution function (EEDF) and certain transport coefficients for a situation with given electric field strength and degree of ionisation.

Nowadays several types of so-called *global plasma models* are constructed. In these models the chemistry is reduced into main reaction paths while the transport is

replaced by transport rates, among others determined by the size of the plasma. So, in fact global plasma models are zero-dimensional models that offer (quasi analytical) relations between the control parameters like pressure, fill chemistry, dimensions and power on the one hand and internal properties like electron density and temperature on the other hand. They do *not* give insight in the spatial distribution of plasma species; for that a Grand model must be employed.

A *Grand model* simulates the plasma as a whole in conjunction with its direct environment (e.g. the input and output). The input of the model is, just as in practice, formed by the set of plasma control parameters such as the value of the power input, the mass flow, the inlet pressure, fill-gas composition and the vessel configuration. The output is the set of internal plasma properties like the distribution of the electric field strength, the electron temperature, the density of the electrons, radicals and light emitting species. From that information the plasma products can be deduced; for instance the efflux of heat, light and radicals. In a Grand model the route from input to output is guided by the laws of nature while the transport coefficients and source terms are based on well documented collision theories and experimental data. An essential task of *Grand modelling* is to give insight in the transport phenomena, how these are influenced by the configuration and the chemical composition.

In this thesis we will present one specific, two global and three Grand models. The specific model is constructed to get a tool for the study of the EM responses of a system (such as a vessel, plasma or a combination of both) to microwaves. One of the global models is designed to provide a stand-alone platform on which the influence of chemical species and reactions on plasma features can be studied. The other is a deposition model that is devoted to predict the deposition profile of a moving deposition reactor.

The three Grand models constructed and validated in this thesis are all dedicated to Surface Wave Discharges; a special class of MIPs. In the next section this effort will be placed in perspective with the history of SWD modelling.

### 1.4.1 A Short Review of SWD modelling

The first works related with modelling of microwave structures are found in the books of the MIT Radiation Laboratory Series, written during the World War II. See for instance the *Waveguide Handbook* of Nathan Marcuvitz, where different microwave components were characterised and modelled using the Equivalent Circuit Theory (ECT) [21]. ECT can be considered as the first model for microwave structures and microwave induced plasmas. In 1958, Trivelpiece studied the slow wave propagation [17] for cylindrical plasma-filled waveguides using ECT and the wave dispersion relation. He observed and explained that when the plasma partially fills the waveguide,

a surface wave mode can propagate along the plasma-dielectric interface. This mode exists only under plasma presence. Trivelpiece characterised the wave propagation using the wave dispersion relation i.e. an *analytical* expression that depends on local quantities such as the electron density. It was a collisionless approximation where the attenuation it is not included; only the (real) wavenumber was used to characterise the wave propagation. The term *slow wave propagation*, often used in this context, means that the phase velocity of the plasma surface waves is smaller than the speed of light.

In 1977 Moisan [22] shows that EM surface waves can be used for *sustaining* long plasmas columns.

The early models for surface wave discharges considered a *local power balance law* (i.e. a simplified electron energy balance equation in which the electron energy transport is neglected) coupled with the dispersion relation. This is done in the work of Glaude [23] where a differential equation for the electron density is obtained from the local power balance. To derive this relation Glaude assumed that the power lost per electron-ion pair  $\theta$  is independent of the electron density. This model was improved by Ferreira in [24] by including the dependency of  $\theta$  on the electron density and the dependency of the wave attenuation on the collision frequency for momentum transfer  $\nu$  via the dispersion relation. The work of Ferreira is based on simplifications of the continuity and momentum transport equations for electron and ions, the local power balance equation for electrons, and the equations for the wave electric field in the plasma. Furthermore, Ferreira obtained from further simplification of the above equations the so-called *similarity laws*, i.e. the dependency of  $\nu$  and  $\theta$  on gas density and the discharge radius. These similarity laws were confirmed experimentally by Sola *et al.* in [25]. Another approach to SWD modelling was suggested by Zhelyazkov in [26], being equivalent to the previous model of Glaude under certain conditions (the so called *diffusion regime*).

In the next improvement a Boltzmann solver was included. In this way the EEDF was coupled to the wave dispersion relation, the wave energy balance and the species balance for atomic ions [27] or for a set of excited states and atomic and molecular ions [28].

A radial description for SWDs was obtained by Ferreira [29] without including the EEDF. The work in [24] was an extension to the radial theory described in [29] to include the axial evolution of the radially average plasma properties. A more advanced radial description is given in [30] where the electron temperature is described taking the transport of electron energy into account. Special attention is given to the boundary condition for the electron temperature in [30].

The previous models aim to describe SWDs at low and intermediate pressures ( $pR <$

1000 Pa · mm, with  $R$  the radius of the discharge tube)<sup>a</sup>.

For higher pressures recombination becomes more important leading to radial contraction in the discharge. This was studied by Castaños in [31].

With respect to two-dimensional modelling of SWD that describes self-consistently the electromagnetic and fluid aspect, we could find only two works. The first model was developed by Hagelaar [32] at intermediate pressure (around 400 Pa). The model shows the result for the two-dimensional distribution of the radiation standing pattern in an argon surfatron plasma. This is consequence of the reflection of the EM waves at the position where the tube radius increases steeply. The model is based on [33, 34] and it is a time-dependent model. The second model was developed by Kabouzi [35] at high pressure (around  $10^5$  Pa) for an argon surfaguide plasma. The model describes the plasma contraction in dependence on molecular ions.

Other important phenomena are plasma resonances and non-collisional heating [36, 37]. This was an issue in [35] where, in order to avoid the plasma resonance, the electron density was multiplied by 2 when used for the complex plasma permittivity (see chapter 3 and appendix A).

Furthermore, it is important to distinguish between the *cold* plasma model and the *warm* plasma model [38]. The difference is that in the cold plasma model the effects due to the thermal motion of electrons and the gradient of electron pressure are neglected. In this thesis a cold plasma model is assumed for the electrons as shown in chapter 4, although the electron temperature is also calculated. For a more in detail review of warm plasma models, we refer to the work of Bowers [39].

More information about SWDs can be found in the reviews [40], [41] and [42].

### 1.4.2 A Short Review of SWD modelling in Our Group

This section provides a short introduction to previous models for MIP and SWD modelling that has been developed in the group EPG using the PLASma SIMulation MOdel platform PLASIMO. Further details about PLASIMO are given in chapter 2. In 2000, Ger Jansen developed a microwave induced plasma model for the Draka deposition reactor [10]. Here the electromagnetic model incorporates the geometry in an explicit way. From 2002 to 2008 Michiel van den Donker adapted the electromagnetic model to C++, the current language used to develop PLASIMO. The model contained only two regions: plasma and quartz regions and was not very flexible with respect to the introduction of different geometries.

---

<sup>a</sup>The correct parameter is the gas density times the radius of the discharge which is based on the similarity laws of Ferreira, see also chapter 7, particularly table 7.1.

In 2009, Jan van Dijk and Manuel Jimenez designed and implemented a new electromagnetic model for microwave modelling [43]. In this model, we facilitate the inclusion of different geometries and materials by defining a geometry layout in the input file (see chapter 4).

## **1.5 Outline of this Thesis**

The thesis is divided in two parts: in the first we will present the physical models and mathematical and numerical concepts that provide the basics for MIP simulations. The second part is devoted to applications.

### **Physical Models**

Most simulations in this thesis are performed using the PLASIMO toolkit. A brief introduction to PLASIMO will be presented in chapter 2. It also summarises the physics building blocks that are relevant for the present study, explains the basics of ortho-curvilinear coordinate systems and discusses the numerical mesh on which the relevant equations are discretised.

Chapter 3 provides an in-depth discussion of the microwave module that has been developed as part of this project. After an exposition of the relevant form of the Maxwell equations, it discusses the discretisation and solution procedure. Results will be presented for test cases that can also be handled analytically. An analysis of the numerical errors due to truncation, round-off and numerical dispersion is provided.

Chapter 4 presents the equations for the transport of mass, momentum and energy in multi-component systems. These are based on the (multi-)fluid approach.

Chapter 5 is devoted to chemistry. After giving an overview of the various methods to investigate the importance of species and reactions, we present a new Global Plasma Model named RateLab; it can be seen as a synthesis of the existing methods and models-types and it is validated by means of a case-study on a pulsed argon plasma.

### **Applications**

In chapter 6 the application of the electromagnetic model (chapter 3) to Microwave Plasma Torches (MPT's) is demonstrated. The influence of the boundary configurations on the electromagnetic field distribution and plasma operation is analysed in detail. This chapter is published [44] as:

M Jimenez-Diaz, J van Dijk, and J J A M van der Mullen. Effect of remote field electromagnetic boundary conditions on microwave-induced plasma torches. *Journal of Physics D: Applied Physics*, 44(16), pag. 165203, 2011.

Chapter 7 gives an introduction to surface wave discharges (SWDs) in argon. We discuss the main characteristics, the modelling aspects and introduce and compare various types of SWDs: the surfaguide, the surfatron and the deposition reactor.

The atmospheric surfaguide argon plasma is studied in chapter 8 and we show the dependency of plasma contraction on the wall temperature and how the plasma length scales with the power and wall temperature.

In chapter 9 we study the surfatron plasma at intermediate pressure. A comparison with experimental results, obtained with Thomson scattering, is given.

Chapter 10 is devoted to the deposition reactor that is used at Draka Comteq with special focus on the electromagnetic power confinement in the reactor.

In chapter 11 we introduce a model for studying the deposition resulting from the movement of the deposition reactor at Draka Comteq.

General conclusions and recommendations are provided in chapter 12.





## **Part I**

# **Physical Models**



---

2

PLASIMO Structure

---

## 2.1 Introduction

This chapter provides an overview of the PLASma SIMulation MOdel (PLASIMO) platform. In section 2.2 we discuss how PLASIMO has come about. Section 2.3 provides a bird's-eye view on the PLASIMO code. In the remaining sections the key physical equations will be mentioned (2.4), the usage of ortho-curvilinear (OCL) coordinate systems is motivated 2.6 and the relevant tensor operations in such coordinate systems are presented (2.6.1). Finally, PLASIMO's numerical mesh creation (2.7) and its LinSys discretisation framework (2.8) are presented.

## 2.2 The History of PLASIMO

The plasma groups at the faculty of applied physics of the TUE, have a long transition in the field of Collisional Radiative Models (CRMs). In the past these were mainly used as diagnostic tools, i.e. for the interpretation of spectroscopy. In 1990 the idea came up to construct a model for a more "complete" plasma description and to bring spectroscopy in relation with other plasma properties.

A group of students formed by Emile de Jong (master student), Dany Benoy and Frank Fey (both PhD students) started under guidance of Joost van der Mullen with the construction of a 2-dimensional plasma transport code. Using the computer language Pascal a model was constructed for studying the atmospheric Inductively Coupled Plasmas (ICP) in Ar; a well-known plasma source used in the field of spectrochemical analysis. Basic ingredients were the algorithm for the magnetic vector potential, the hydrodynamic equations and the module for the chemistry of a non-LTE argon plasma. Anticipating to geometrically pinched configurations the code was written in generalised ortho-curvilinear coordinates. When Emile de Jong finished his study it was possible to model not only the ICP but also the cascade arc; a DC driven plasma source. So, two different plasma sources could be modelled using modules of one and the same code. Modularity had always been a driving concept; it was the reason to choose Pascal instead of Fortran, a language that at that time was more familiar in the field of scientific computing.

In 1992 the code was rewritten by Dany Benoy in the language C and was called PLASIMO, an acronym for PLASma SIMulation MOdel. This version of the code was the basis of his thesis (Benoy, 1993, [45])<sup>a</sup> extended and used by Ger Jansen who got in 2000 his PhD degree on a thesis [10] based of a design concept; the design of PLASIMO. Apart from the Ar chemistry (atomic plasma) attention was paid to the modelling of

---

<sup>a</sup>The name of the author and the year of publication are sufficient to find the dissertation via [http://w3.tue.nl/en/services/library/digilib/publications\\_from\\_tue/dissertations](http://w3.tue.nl/en/services/library/digilib/publications_from_tue/dissertations).

molecular plasmas; to that end the chemistry of H<sub>2</sub> and O<sub>2</sub> plasmas was explored. Apart from the plasma created in the cascaded arc and in a plasma expansion chamber he also worked on the microwave induced plasma (MIP) system as used by POF (Plasma Optical Fibres); a company (-division) that afterwards merged into Draka Comteq, the same company that initiated the current research by supporting the STW project that made this study possible.

The plasma source studied by Jan van Dijk (thesis in 2001, [46]) was the QL lamp; an induction lamp that Philips brought on the market in 1990<sup>b</sup>. Ingredients of previous studies of Benoy and Janssen were used, such as the ortho-curvilinear grid generation module and the magnetic vector potential. A difference with previous studies was the chemistry. Like the tubular fluorescence lamp the plasma of the QL lamp burns on Hg in a buffer gas; mainly Ar. But most importantly was the change in language; C was replaced by C++. Moreover, the modularity aspects got much more attention. The programming style, based on an *object-oriented approach*, made it possible to reuse and extend existing code easily.

With the aim to make the model more user-friendly and applicable in industrial environment, a Graphical User Inter-phase GUI was developed. This new C++ based version of PLASIMO is the bases of this and several other studies. It features a graphical front-end which represents the hierarchical structure of the model, guides the simulation, controls the calculation and allows the user to monitor the behaviour of the variables involved in the plasma model. PLASIMO became much more a *model construction platform* than just one (single) model.

In constructing the current C++ version of PLASIMO, Jan van Dijk worked closely together with Harm van der Heijden, Bart Hargers and Kurt Garloff. Van der Heijden (thesis 2003,[7]) used the platform for the study of radiation transport in the sulphur lamp while Hartgers (2003, [47]) was mainly devoted to time dependent modelling of the plasmas in fluorescence lamps. The C++ version was further used by Colin Johnston (2003, Sulphur lamp, [8]), Bart Broks (2006, Plasmas for laser wakefield acceleration, [48]), Mark Beks (2008, elemental diffusion in HID lamps, [49]) and Michiel van den Donker (2008 MIPs, [11]).

Under guidance of Frits de Hoog, Gerjan Hagelaar started in 1997 in the adjacent group EPG with the modelling of micro discharges. Based on experiences with the SIGLO codes<sup>c</sup> that were written in Fortran by Lean Leanne Pitchford and Jean-Pierre Boeuf at Université Paul Sabatier in Toulouse, France, he constructed the Micro-Discharge 2-Dimensional (MD2D) code (2000, [50]). In this work [50], supported by the Philips Research laboratory, much attention was paid to plasma-electrode interactions. So, in contrast to PLASIMO, MD2D had to cope with space charge; it

---

<sup>b</sup>See [http://en.wikipedia.org/wiki/Electrodeless\\_lamp](http://en.wikipedia.org/wiki/Electrodeless_lamp)

<sup>c</sup>See <http://www.siglo-kinema.com/>

PLASIMO	MD2D
Charge neutrality	Non-Charge neutrality
Vector potential	Poisson equation
$\nabla p \neq 0$ ; Navier Stokes	$\nabla p = 0$ ; no bulk flow
Ortho-curvilinear grid generation	Rectangular grids
Plasma only	Dielectrics

Table 2.1: A comparison of the features of PLASIMO and MD2D in 2001.

therefore had a *Poisson* equation solver on board. On the other hand as the closed systems of micro discharges under study are non-flowing, MD2D was not equipped with a solver to compute pressure driven flows (a *Navier Stokes* solver [10, 45, 51]). The (initial) difference(s) between PLASIMO and MD2D are given in table 2.1.

When Joost van der Mullen moved from the group ETP (equilibrium and transport in plasmas) to EPG he took the PLASIMO platform with him. There, special features of PLASIMO were used for MD2D. It was rewritten in C++ and equipped with the PLASIMO GUI features. This was done by Jan van Dijk, who got a Post Doc position at EPG and Wouter Brok, at that time a PhD student at EPG. One of the topics of his thesis (2005) was the modelling of plasma ignition. Apart from *fluid modelling* he also constructed the basis for a Monte Carlo module. This MC module was used by Marc van der Velden (2008) to create a Particle In Cell *Monte Carlo* model to study radiation created plasmas. The C++ version of MD2D was used by Diana Mihailova for her study on sputtering hollow cathode discharges (2010).

The two codes PLASIMO and MD2D are now in a gradual process of merging together. The aim is to come to a modelling platform that can be used to construct different models for different types of plasmas; LTE and non-LTE, steady state or transient, flowing or non-flowing, with or without space charges. The transport modes can be kinetic (particle-driven like in MC), fluid or ruled by ray tracing. By means of the menu the user can compose plasmas of different fill chemistry, construct the geometrical configuration and select the nature of EM power (quasi-)DC, ICP, Microwave, Radiation). At the moment the PhD students working with and on PLASIMO are Kim Peerenboom (magnetised plasmas), Niels Lammers (turbulence), Wouter Graef (CRMs), Lei Liu (lamp ignition), Sara Rahimi, and Efe Kemaneci (both on MIPs).

To achieve the ultimate goal of constructing a versatile modelling platform for technology, science and education much has to be done still. One of the routes in the road map is completing the merging process of PLASIMO and MD2D.

This thesis on non-LTE flow-driven MIPs, can be seen as an extension of the line of Ger Janssen and Michiel van den Donker. It will not deal with MC and the solution of

Poisson equation. However, if possible and instructive we will refer to the aspects that are not directly used in this study. As such, this thesis intends to give, as a side-product, an overview of the basis and components of the PLASIMO-MD2D platform.

## 2.3 PLASIMO Overview

PLASIMO has been designed as a modular simulation *toolkit*. This means that it is shaped as a collection of *modules* that implement specific models. Examples of such sub-models are those for calculating the gas temperature, the chemical composition of an LTE mixture or the flow field. The strength of the design is that these specific models can be used not only in isolation, but can also be combined to create (self-consistent) Grand models.

The implementation of the modules uses a number of shared, re-usable facilities, that form the *numerical framework*. This provides such concepts as tensor fields, matrix solvers and an input file parser. From a developer's perspective, PLASIMO can therefore be divided in two parts:

- a numerical framework;
- its applications.

This is visualised in figure 2.1. Every layer in this picture uses and extends the facilities that are provided by the layers below. At the bottom you find the elementary building blocks of the code, at the top the applications. For a further discussion of this design we refer to [46, chapter 2].

The above division into a numerical framework and its applications is appropriate from a developer's viewpoint, but does not reflect the user's perception of the ingredients of a Grand plasma model. That is better represented by figure 2.2, which divides a plasma model in 3 main parts,

- Configuration;
- Transport;
- Chemistry.

Here *Configuration* refers to the coupling of the plasma to the *environment* whereas *Transport* is the subsequent response in the plasma. It is guided by transport coefficients and driven by sources of which the origin lays in plasma *Chemistry*.



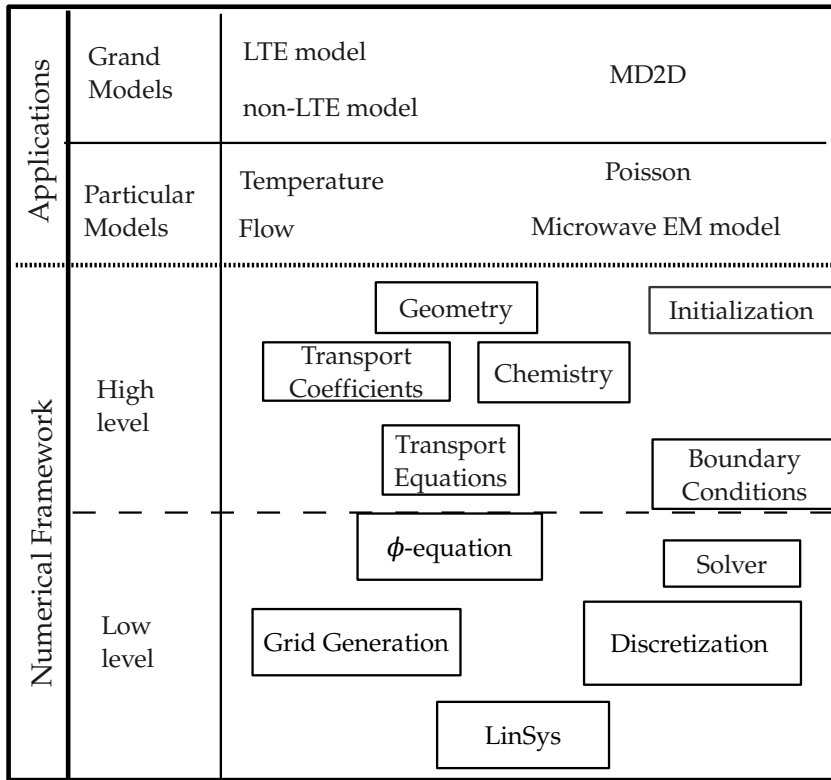


Figure 2.1: A schematic view of the PLASIMO structure divided into the numerical framework and the applications. The complexity and level of detail of the applications, models and components decreases from the top toward the bottom of the figure, e.g. the Grand model applications are at the top meanwhile the pillars of the numerical frame work such as the  $\phi$ -equation, LinSys (see [52]) and the solvers are at the bottom.

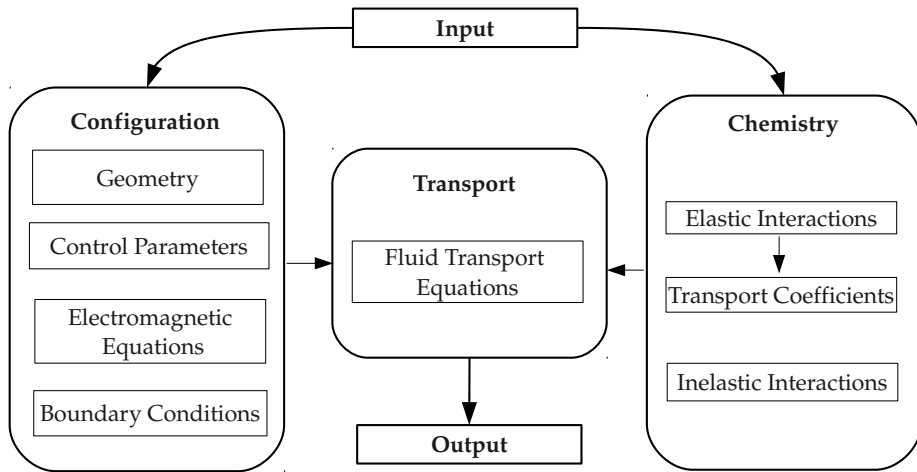


Figure 2.2: The division of the Grand plasma model implemented in PLASIMO from the perspective of a plasma (Transport) modified by environment (Configuration) and chemical composition (Chemistry) [10, 47].

This division aims to reflect how the plasma is modified by the environment, for instance by shaping the electromagnetic fields with metals, slits, chokes and other features and by the chemical composition. Moreover, this is the division that guides the structure of this thesis.

Of course other divisions are possible as the one given in figure 2.3, where the key physical equations that can be included in a PLASIMO model are solved using as input information provided from the user, a data base for the chemistry aspect and the external parameters such as power absorbed and working pressure. Note that this division is appropriate even for specific models such as a stand alone electromagnetic model or radiation transport model. Moreover, as we indicate in the figure, the plasma model is implemented with the help of low level features from the numerical framework such as the LinSys library (see section 2.8), or grid generation.

In the next section the governing equations in PLASIMO are introduced.

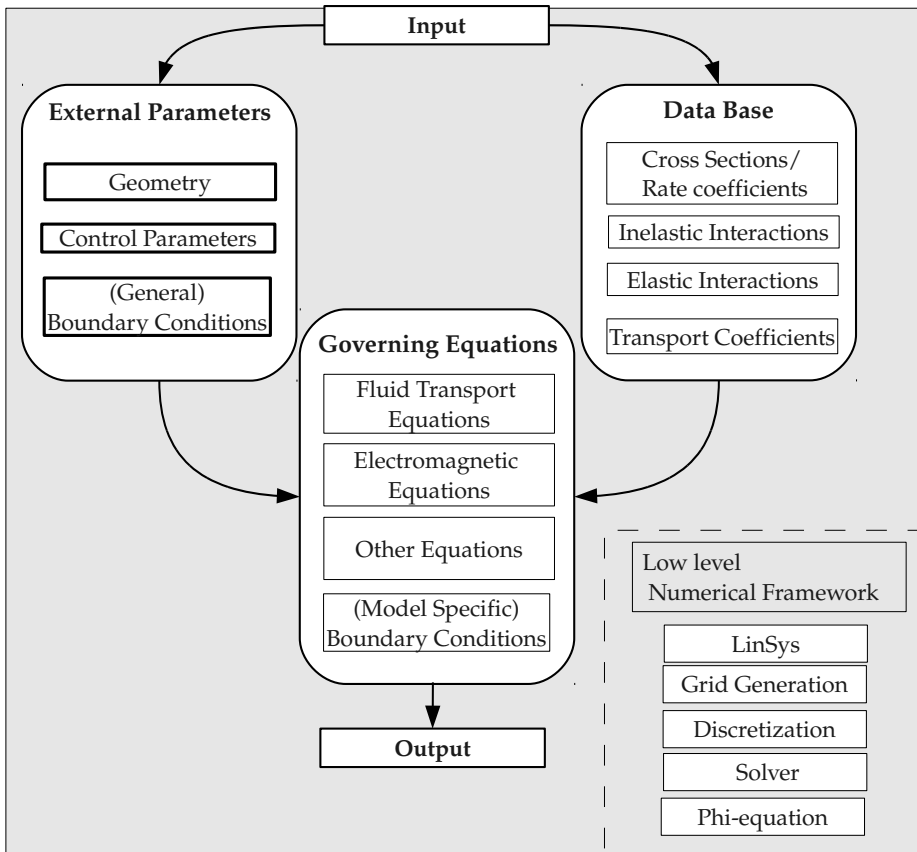


Figure 2.3: The division of a plasma model in PLASIMO and its connection with the numerical framework.

## 2.4 Governing Equations in PLASIMO

Let us now summarise the key equations that can be solved with PLASIMO. We will first present the Maxwell equations for the electromagnetic field and expose the modules that are available in PLASIMO for solving them for particular plasmas. An in-depth discussion of the new module for solving the fields in MIPs is given in chapter 3.

Next we will define the  $\phi$ -equation, the canonical form of transport (balance) equations. In chapter 4 and later we will see its applications in the modelling of mass, momentum and energy transport. For completeness, we conclude with some other PLASIMO features as *Radiation Transport* and *Monte Carlo* models, which have not been used in the present project.

### Electromagnetic equations

The electromagnetic models are based on the Maxwell equations [53]:

$$\nabla \cdot \mathcal{D} = \rho_c, \quad (2.1)$$

$$\nabla \cdot \mathcal{B} = 0, \quad (2.2)$$

$$\nabla \times \mathcal{E} = -\frac{\partial \mathcal{B}}{\partial t}, \quad (2.3)$$

$$\nabla \times \mathcal{H} = \mathcal{J} + \frac{\partial \mathcal{D}}{\partial t}, \quad (2.4)$$

PLASIMO does not provide a single module for solving the Maxwell equations. Rather, it provides dedicated EM modules for particular plasmas. Examples are those for continuous and pulsed mode Direct Current (DC) discharges [54] and for inductively coupled plasmas [46]. In chapter 3 we discuss the new microwave module that was developed as part of this project. This supersedes the microwave modules that were used in previous studies [8, 10, 11].

### Fluid Transport Equations

The  $\phi$ -equation [51] is used to describe the transport of fluid quantities. It is given by

$$\frac{\partial \phi}{\partial t} + \nabla \cdot \Gamma_\phi = S_\phi. \quad (2.5)$$

Here  $\phi$  is the quantity of interest,  $\Gamma_\phi$  its flux density and  $S_\phi$  the net volumetric production rate of the quantity  $\phi$ . The meaning of this equation is made more clear by

moving the second term over to the right-hand side and applying Gauss' divergence theorem, yielding

$$\frac{\partial}{\partial t} \int_V \phi d^3V = \int_V S_\phi d^3V - \int_A \Gamma_\phi \cdot \mathbf{n} d^2A. \quad (2.6)$$

Here  $A$  is the (closed) boundary surface of a volume  $V$ . This form of the equation can clearly be recognised as a conservation law: it states that the accumulation of  $\phi$  in the volume  $V$  is the result of the production inside that volume, corrected for the outward transport of  $\phi$  through the boundary surface  $A$ . For more details and applications of this equation, we refer to chapter 4 and, particularly, table 4.2.

### Other main physical models

*Radiation transport* [7, 49] is given by

$$\frac{dI_\nu}{ds} = j_\nu - kI_\nu \quad (2.7)$$

where  $I_\nu$  is the radiation intensity,  $k_\nu$ , the local coefficient for absorption along rays passing through the discharge, and  $j_\nu$  is the emission coefficient. The subscript  $\nu$  indicates that the quantities are defined per frequency interval. Note that all quantities in equation 2.7 are functions of  $\nu$ . These functions, depending on the various broadening mechanisms, can be very capricious.

PLASIMO provides a ray-tracing based radiation transport module that can handle spherical and cylindrical problems in one and two dimensions [7, 49]. In [55] a general treatment is given of the interplay between fluid and radiative transport phenomena in symmetric plasmas; this Ray-Trace Control Volume (RTCW) technique can be seen as a hybrid transport method.

A *Monte-Carlo* model is available in PLASIMO. This has been used in stand-alone applications and in combination with a *Particle In Cell* approach ([56]) and a drift-diffusive code in hybrid modelling. For details of this work, we refer to [57, 58].

## 2.5 Boundary Conditions

For solving the electromagnetic and transport equations, boundary conditions are required. In general three different types of boundary conditions (BC) can be defined for a scalar field or vector field component  $F$  at a surface  $\mathcal{B}$

1. Dirichlet:

$$F(\mathbf{x}) = p(\mathbf{x}),$$

2. Neumann:

$$\mathbf{n} \cdot \nabla F(\mathbf{x}) = q(\mathbf{x}),$$

3. Mixed:

$$\mathbf{n} \cdot [\nabla F(\mathbf{x}) + h(\mathbf{x})F(\mathbf{x})] = w(\mathbf{x}).$$

Here  $\mathbf{x}$  is the position vector of a point on  $\mathcal{B}$ ,  $\mathbf{n}$  the normal on  $\mathcal{B}$  while  $p(\mathbf{x})$ ,  $q(\mathbf{x})$ ,  $h(\mathbf{x})$ , and  $w(\mathbf{x})$  are explicitly known functions of  $\mathbf{x}$ . If  $p(\mathbf{x})$ ,  $q(\mathbf{x})$  or  $w(\mathbf{x}) = 0$  for all  $\mathbf{x} \in \mathcal{B}$ , the BC is named *homogeneous*, otherwise the boundary is called *inhomogeneous*.

These types of BC will be referred to in the chapters where the electromagnetic and transport equations are defined.

## 2.6 The Coordinate System

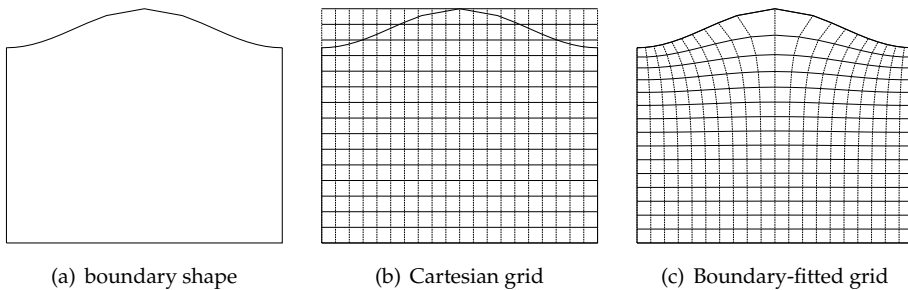


Figure 2.4: In order to describe the region of interest with the boundary shape in figure (a) one may introduce a Cartesian grid (b) or boundary-fitted OCL grid (c).

So far, the equations of interest have been written in vector form. In order to solve these equations numerically we will need to choose a *coordinate system*. In PLASIMO, ortho-curvilinear coordinate systems are used consistently [45, 52], which allows the usage of *boundary-fitted* meshes for regions of interest with curved boundaries [59].

As an example, let us consider the region with the boundary shape that is depicted in figure 2.4(a). If we were to use a rectangular coordinate system for this mesh, we would arrive at the grid that is shown in figure 2.4(b). Since the coordinate lines are not aligned to the boundary curves, imposing boundary conditions is not trivial, and prone to numerical errors [59]. The *ortho-curvilinear grid* that is shown in figure 2.4(c) obviously does not suffer from these problems. All four boundary curves coincide with a coordinate line.

PLASIMO comes with a module for generating ortho-curvilinear grids. It also supports the special cases of the usual Cartesian, cylindrical and spherical grids. In all cases, the coordinates are written as  $x_i$ , and are accompanied by base vectors  $\hat{e}_i$ . Since the grid lines intersect perpendicularly, the *metric tensor* of the coordinate system only has diagonal elements,  $\bar{g} = \text{diag}(h_i^2)$ . The numbers  $h_i$  are the *scale factors* of the coordinate system. The coordinates and scale factors of some standard OCL coordinate systems are shown in table 2.2.

System.	Coordinates	Scale Factors
OCL	$(x_1, x_2, x_3)$	$(h_1, h_2, h_3)$
Cartesian	$(x, y, z)$	$(1, 1, 1)$
Cylindrical	$(z, r, \phi)$	$(1, 1, r)$
Spherical	$(r, \theta, \phi)$	$(1, r, r \sin(\theta))$

Table 2.2: Coordinates and scale factors of common OCL coordinate systems.

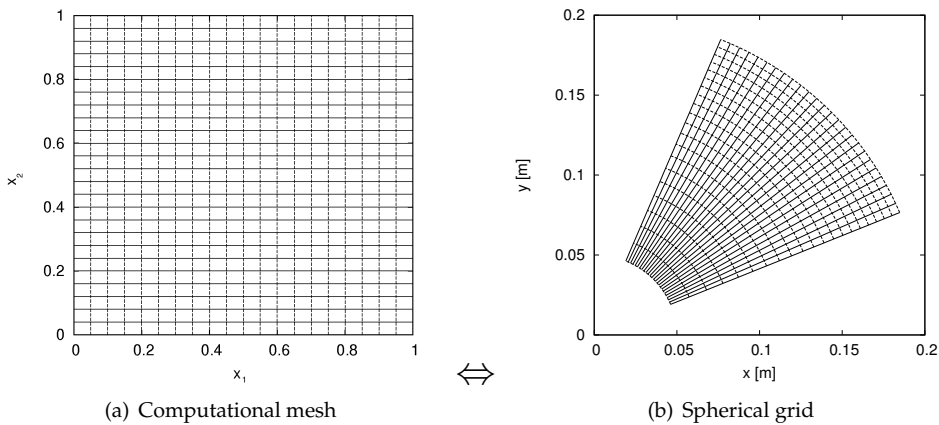


Figure 2.5: In PLASIMO, calculations take place in terms of normalised ortho-curvilinear computational coordinates ( $x_i$ ) (figure a). The grid generation code calculates the mapping between the computational points ( $x_i$ ) and the points ( $x, y$ ).

The ortho-curvilinear coordinate system that is used in PLASIMO is *equidistant* and *normalised*, such that  $x_i \in [0, 1]$ . The relation between the computational coordinates and a stretched spherical coordinate system has been illustrated in figure 2.5.

Furthermore, it is important to stress that we are now able to model *step-changes* and *obstructions* in the geometry. These are essential for the modelling of torches

(chapter 6) and surface wave discharges (chapters 7, 8, 9), including the optimisation of the Draka deposition reactor (chapter 10).

## 2.6.1 Tensor Calculus in OCL Coordinate Systems

In order to derive the expressions for the equations of interest in terms of OCL coordinate systems, we need the expressions for the usual vector operations in terms of these coordinates. Like in PLASIMO, the expressions below give and take the *physical components* of the vectors. Essentially this means that the associated base vectors are normalised and dimensionless, for details we refer to [60, p. 756].

### The curl of a vector field

The curl of a vector  $\mathbf{F} = (F_1, F_2, F_3)$  is given by<sup>d</sup>

$$\nabla \times \mathbf{F} = \frac{h_i}{\Pi_m h_m} e^{ijk} \frac{\partial h_k F_k}{\partial x^j} \hat{\mathbf{e}}_i. \quad (2.8)$$

Here  $e_{ijk}$  is the Levi-Civita permutation symbol [60, page 723] that equals 1 if  $(i, j, k)$  is an even permutation of  $(1, 2, 3)$ ,  $-1$  in case of an odd permutation, and 0 otherwise. Equation (2.8) can also be expressed as

$$\nabla \times \mathbf{F} = \frac{1}{h_1 h_2 h_3} \begin{vmatrix} h_1 \hat{\mathbf{e}}_1 & h_2 \hat{\mathbf{e}}_2 & h_3 \hat{\mathbf{e}}_3 \\ \frac{\partial}{\partial x_1} & \frac{\partial}{\partial x_2} & \frac{\partial}{\partial x_3} \\ h_1 F_1 & h_2 F_2 & h_3 F_3 \end{vmatrix}. \quad (2.9)$$

With the help of the Stokes theorem, the curl of a vector  $\mathbf{F}$  can be written in integral form,

$$\oint_C \mathbf{F} \cdot d\mathbf{l} = \iint_A \nabla \times \mathbf{F} \cdot \mathbf{n} \, d^2 A. \quad (2.10)$$

Here  $A$  is an open surface and  $C$  the contour bounding it. If we choose  $A = A_i$  to be a flat surface perpendicular to the coordinate direction  $i$ , and the curl is constant over  $A_i$ , we find that

$$(\nabla \times \mathbf{F})_i = \frac{1}{A_i} \oint_C \mathbf{F} \cdot d\mathbf{l}. \quad (2.11)$$

<sup>d</sup>We use the Einstein index summation convention: if the same index occurs as a subscript and also as a superscript, summation over that index is implied.



### The divergence of a vector field

In OCL coordinates, the expression for the divergence of a vector field is given by

$$\nabla \cdot \mathbf{F} = \frac{1}{h_1 h_2 h_3} \left[ \frac{\partial}{\partial x_1} (h_2 h_3 F_1) + \frac{\partial}{\partial x_2} (h_3 h_1 F_2) + \frac{\partial}{\partial x_3} (h_1 h_2 F_3) \right]. \quad (2.12)$$

By applying Gauss divergence theorem this can be written in integral form as

$$\int_V (\nabla \cdot \mathbf{F}) dV = \int_A \mathbf{F} \cdot \mathbf{n} d^2 A. \quad (2.13)$$

In case  $\nabla \cdot \mathbf{F}$  is constant inside a volume  $V_i$ , we find that

$$(\nabla \cdot \mathbf{F})_i = \frac{1}{V_i} \int_A \mathbf{F} \cdot \mathbf{n} d^2 A. \quad (2.14)$$

Equations (2.11) and (2.14) can be used to evaluate the curl and the divergence in a control volume setting.

## 2.7 The Numerical Mesh

In order to rewrite the equations of interest in a form that is suitable for numerical computing, these must be *discretised* on a *numerical mesh* or *grid*. In this section we summarise the process of creating numerical meshes. We will be guided by figure 2.6.

### The geometry layout

The generation of the numerical meshes starts by reading the *geometry layout*, see figure 2.6(a). This is a matrix of character values that identify material types. The geometry layout can be used to compose a region of space that consists of metals, quartz, air and a plasma region. Without refinement each cell of the geometry matrix corresponds to a rectangular cell in the *computational* coordinate system, see figure 2.5. The actual shape of this material cell is influenced by the coordinate transformation, as is clear from figure figure 2.5. In order to facilitate the specification of fine meshes, the user can specify a *refinement factor*. A refinement factor  $b$  means that every cell is replaced by  $2^{2b}$  cells of the same type, as shown below figure 2.6(a).

### Region

A region is composed of one or more material types that occur in the geometry layout. Each sub-model of the simulation is solved on a particular region. As an example,

the region in which the electromagnetic equations are solved in case of a surfatron plasma consists of the plasma and quartz ‘materials’. On the other hand, the plasma transport equations (section 4.3) are solved in the plasma region, formed by the cells of ‘material’ type plasma.

### Grid Cell

The cells that are defined by the refined geometry matrix are the natural setting for our computations. We can distinguish between two types of grid cells, *Stokes* and *Gauss* cells.

The Stokes cell type is depicted in figure 2.6(e). It is the basis of the discretisation of the electromagnetic equations (chapter 3). The location of the discrete fields components in the Yee cell ensures continuity of the electromagnetic fields at the material interfaces (see chapter 3).

A Gauss cell, depicted in figure 2.6(f), is also known as a control volume (CV). The CV’s are used to discretise and solve the balance, or  $\phi$ -equations, that are discussed in chapter 4. The field variables  $\phi$  and the source terms are defined at the centre of the CV’s, while the transport fluxes are defined at the centre of the faces of the CV’s (see figure 2.6(f)). The discrete version of the  $\phi$ -equations is obtained by integrating over a control volume. The most important feature of the CV-method is that it facilitates an integral approach which guarantees the *exact* integral conservation of mass, momentum and energy over any group of CV’s. For more information and for the definitions of the terms we refer to chapters 3 and 4.

## 2.8 Discretisation — LinSys

We conclude with a few words about the LinSys class template library [43]. LinSys provides support for such concepts as tensor values, tensor fields and systems of equations involving such fields. Since it allows its users to define custom domain classes, its usage is not restricted to within PLASIMO and indeed, it has also been successfully used by external parties [61].

LinSys also facilitates the discretisation of (coupled) field equations. As an example, in chapter 3 we transform the Maxwell equation into the harmonic form

$$\nabla \times \mathbf{E} + k_0 \tilde{\mathbf{H}} = 0, \quad (2.15)$$

$$\nabla \times \tilde{\mathbf{H}} + k_0 \hat{\epsilon}_r \mathbf{E} = 0. \quad (2.16)$$

Here  $\tilde{\mathbf{H}}$  is the normalised magnetic field in  $V/m$ ,  $k_0$  the vacuum wavenumber and  $\hat{\epsilon}_r$  the complex relative permittivity. Using the LinSys library the discretisation of equations (2.15) and (2.16) can be done with merely two lines of C++ code,

```
(yee_curl(lin(E)) + k0*lin(h) =0).foreach(h);  
(yee_curl(lin(h)) + k0*eps_r_hat*lin(E)=0).foreach(E, interior);
```

This code does not only closely resemble equations 2.15 and 2.16, it also has the advantage of being independent of the dimension and coordinate system: indeed, the code works for arbitrary ortho-curvilinear coordinate systems (section 2.6) and changing to different geometries merely requires modifying the model's input file. In the microwave module that has been developed as part of this project, this technique has been successfully put to test for the first time.

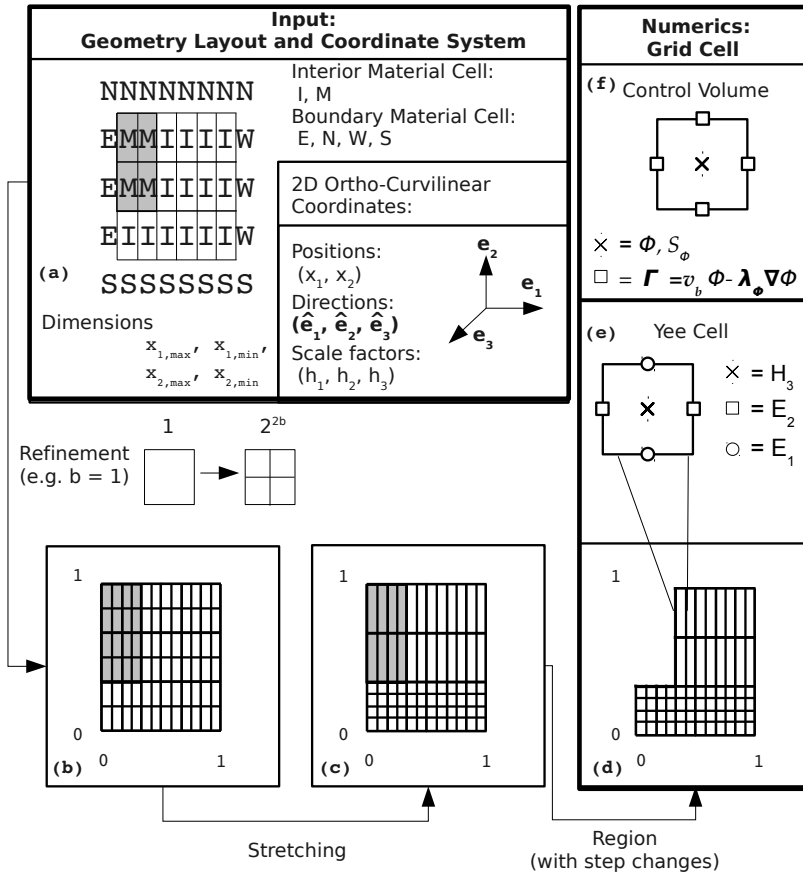


Figure 2.6: Steps in the generation of the numerical mesh. See text for details.



---

3

Electromagnetic Model

---

### 3.1 Introduction

The modelling platform PLASIMO has been extended with a new electromagnetic model. In the design and construction of this EM model we follow the philosophy of PLASIMO by creating a modular and flexible model valid for orthogonal curvilinear coordinates.

The new EM model has been applied to model different MIPs such as MIP torches (chapter 6), surface-wave discharges (chapters 8 and 9), and the Draka deposition reactor (chapter 10).

The electromagnetic model computes the response of an electromagnetic structure to an excitation source. The response consists of the electromagnetic field distributions in the domain and, in the case of a dissipative medium, also the power dissipation. The electromagnetic structure is defined by the geometry and boundary conditions. In our case the excitation is imposed via the boundary conditions, that is because the EM wave enters the domain via (one of the) boundaries.

This chapter starts with a description of the physical model in section 3.2. Section 3.3 presents the numerical model and section 3.4 explains the boundary conditions. Finally, section 3.5 shows a validation test case and a study on the numerical errors.

### 3.2 Physical Model: the Maxwell Equations

We assume a medium that is dissipative, linear and *non-magnetic*<sup>a</sup>. In this case the Maxwell equations (2.1), (2.2), (2.3) and (2.4) (see [53]) reduce to

$$\nabla \cdot (\epsilon_0 \epsilon_r \mathcal{E}) = \rho_c, \quad (3.1)$$

$$\nabla \cdot \mathcal{H} = 0, \quad (3.2)$$

$$\nabla \times \mathcal{E} = -\mu_0 \frac{\partial \mathcal{H}}{\partial t}, \quad (3.3)$$

$$\nabla \times \mathcal{H} = \mathcal{J} + \epsilon_0 \epsilon_r \frac{\partial \mathcal{E}}{\partial t}, \quad (3.4)$$

with  $\mathcal{E}$  the electric field intensity [V/m],  $\mathcal{H}$  the magnetic field intensity [A/m],  $\mathcal{J}$  the electric current density [A/m<sup>2</sup>],  $\rho_c$  the electrical charge density [C/m<sup>3</sup>],  $\mu = \mu_0$  the

---

<sup>a</sup>We follow the definition of non-magnetic as given in [62]. For most linear media, the permeability equals that of free-space,  $\mu = \mu_0$ , except *ferromagnetic* materials which are generally non-linear. Moreover in *ferromagnetic* materials high values of  $\mu$  are obtained only for radio frequency or DC magnetic fields, whereas for high frequencies  $\mu \sim \mu_0$  [62]. A medium is linear when the electric field flux  $\mathcal{D}$  and the electric current density  $\mathcal{J}$  are proportional to the electric field intensity  $\mathcal{E}$ , whereas the magnetic field flux  $\mathcal{B}$  is proportional to the magnetic field intensity  $\mathcal{H}$ . An example of non-linear material is a surface wave discharge with an axial constant magnetic field [17, 41].

### 3.2. Physical Model: the Maxwell Equations

---

permeability of free space [H/m],  $\epsilon_0$  the permittivity of free space [F/m], and  $\epsilon_r$  the relative permittivity of the medium.

For fields with a sinusoidal (i.e. harmonic) time dependency, it is convenient to use the phasor notation so that time dependency can be removed from the Maxwell equations.

A field in time domain  $\mathcal{F}$  is related to the field in phasor form  $F$  as

$$\mathcal{F} = \text{Re} \left( F e^{i\omega t} \right). \quad (3.5)$$

Note that the phasor  $F$  is a complex number.

The Maxwell equations in phasor form (or frequency domain) are

$$\nabla \cdot (\epsilon_0 \epsilon_r \mathbf{E}) = \rho_c, \quad (3.6)$$

$$\nabla \cdot \mathbf{H} = 0, \quad (3.7)$$

$$\nabla \times \mathbf{E} = -i\omega\mu_0\mathbf{H}, \quad (3.8)$$

$$\nabla \times \mathbf{H} = \mathbf{J} + i\omega\epsilon_r\epsilon_0\mathbf{E}. \quad (3.9)$$

Assuming that Ohm's law in the form  $\mathbf{J} = \hat{\sigma}\mathbf{E}$  (see equation (4.24)) is valid, we can rewrite the last equation as

$$\nabla \times \mathbf{H} = i\omega\epsilon_0 \left( \frac{\hat{\sigma}}{i\omega\epsilon_0} + \epsilon_r \right) \mathbf{E} \equiv i\omega\epsilon_0 \hat{\epsilon}_r \mathbf{E}, \quad (3.10)$$

where the *complex relative permittivity* is introduced and defined as

$$\hat{\epsilon}_r \equiv \epsilon_r - i \frac{\hat{\sigma}}{\omega\epsilon_0}. \quad (3.11)$$

Only equations (3.9) and (3.8) are included in the model (see [63]).

We introduce the *scaled magnetic field*  $\tilde{\mathbf{H}} = iZ_0\mathbf{H}$ . This quantity has the same units as the electric field and is of the same order of magnitude. Furthermore,  $Z_0 = \sqrt{\mu_0/\epsilon_0}$  (in  $\Omega$ ) is the impedance of free space. In terms of  $\tilde{\mathbf{H}}$  the equations (3.8) and (3.10) can be written as

$$\nabla \times \mathbf{E} + k_0 \tilde{\mathbf{H}} = 0, \quad (3.12)$$

$$\nabla \times \tilde{\mathbf{H}} + k_0 \hat{\epsilon}_r \mathbf{E} = 0, \quad (3.13)$$

where we have also introduced the vacuum wave number  $k_0 = \omega/c_0 = \omega\sqrt{\epsilon_0\mu_0}$ . Note that the above system of equations is homogeneous meaning that the right-hand side equals zero. For this kind of problems the solution consists of a linear



combination of base (orthogonal) solutions with undetermined amplitudes. These follow from the boundary conditions to which the fields are subjected.

We have included only  $E_z$ ,  $E_r$  and  $H_\phi$  as EM field components in the our model. This is sufficient to simulate the  $TM_{01}$  mode propagating in a waveguide along the  $z$  direction in cylindrical coordinates [62]. This mode is commonly found in surface wave discharges [12, 41, 42], particularly, those described in chapters 8, 9 and 10.

Using cylindrical coordinates equations (3.12) and (3.13) transform into

$$\frac{\partial E_z}{\partial r} - \frac{\partial E_r}{\partial z} = k_0 \tilde{H}_\phi, \quad (3.14)$$

$$\frac{\partial \tilde{H}_\phi}{\partial z} = k_0 \hat{e}_r E_r, \quad (3.15)$$

$$\frac{1}{r} \frac{\partial r \tilde{H}_\phi}{\partial r} = -k_0 \hat{e}_r E_z \quad (3.16)$$

The time-averaged power density  $Q$  in  $W/m^{-3}$  is computed as

$$Q = \frac{1}{2} \text{Re}(\mathbf{J}^* \mathbf{E}) = \frac{1}{2} \text{Re}(\hat{\sigma}) |\mathbf{E}|^2. \quad (3.17)$$

So that the total power absorbed in volume  $V$  equals

$$P_{abs} = \int_V Q dV = \frac{1}{2} \int_V \text{Re}(\hat{\sigma}) |\mathbf{E}|^2 dV. \quad (3.18)$$

The complex Poynting vector in this case reads

$$\mathbf{S} = \frac{1}{2} \mathbf{E} \times \mathbf{H}^* = \frac{1}{2} \begin{vmatrix} \hat{e}_z & \hat{e}_r & \hat{e}_\phi \\ E_z & E_r & 0 \\ 0 & 0 & H_\phi^* \end{vmatrix} = \frac{1}{2} E_r H_\phi^* \hat{e}_z - \frac{1}{2} E_z H_\phi^* \hat{e}_r, \quad (3.19)$$

and the time-averaged Poynting vector is

$$\bar{\mathbf{S}} = \text{Re}(\mathbf{S}). \quad (3.20)$$

### 3.3 Numerical Model

Three main aspects of the numerical method can be distinguished: the geometry and grid generation 3.3.1, discretisation 3.3.2, and the solution procedure 3.3.3.

### 3.3.1 Geometry and Grid Generation

As explained in chapter 2, structure domains and boundary-fitted ortho-curvilinear coordinates-systems are used to describe the geometry of electromagnetic structures. The ortho-curvilinear system includes the standard cases of *Cartesian*, *cylindrical* and *spherical* coordinates. The grid generation was explained in chapter 2. Here we only apply cylindrical coordinates.

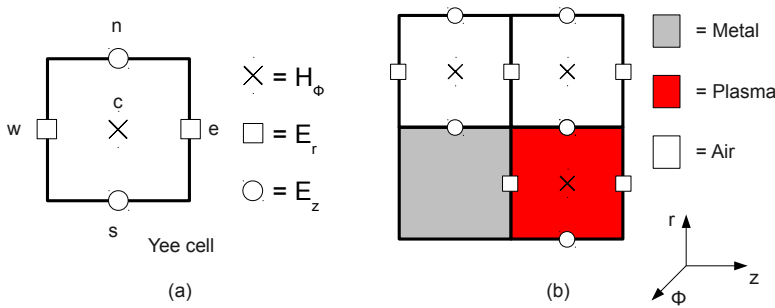


Figure 3.1: Part (a): the general structure of the standard (Yee) cell used in the numerical method. Part (b): Example of the interface between different types of material cells.

Figure 3.1 gives a sketch of a *standard* Yee cell. This is a cell that coincide with the control-volume used for the solution of the transport equations (see chapter 4). In the nodal point of the standard Yee cell, we find  $H_\phi$ . The  $E_r$  and  $E_z$  components are positioned on boundaries of this cell. It is important to mention that the standard Yee cell results from the projection of a 3D Yee cell onto 2D space. In this 3D cell the  $H_\phi$  is located at the centre, whereas the electric field components are defined at the centre of the corresponding edge. A 3D staggered Yee cell is defined with its centre located at the corner of the 3D Yee cell, such that the electric field components are perpendicular to the corresponding face of the 3D staggered Yee cell. These faces are shown in figures 3.2(b) for  $E_z$  and 3.2(b) for  $E_r$ , noted with the label '3D'. The projection onto the 2D spaces defines the corresponding grid cell for the  $E_r$  and  $E_z$  components.

The location of the discrete fields components in the Yee cell (figure 3.1(d)) ensures continuity of the tangential field components at the interfaces of different EM materials.

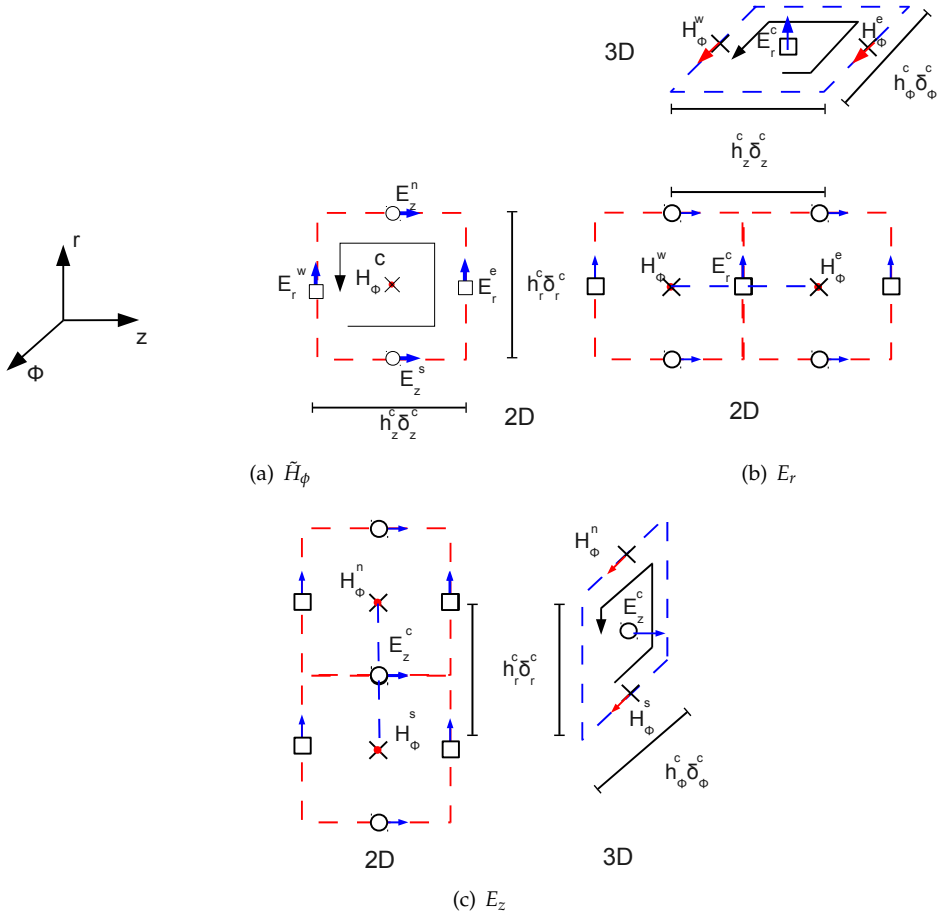


Figure 3.2: A sketch of the application of the Stokes Theorem to discretise the curl around a standard Yee cell centred around the  $H_\phi$  (a), and the staggered Yee cells which is centred around the  $E_r$  (b) or  $E_z$  (c) components. In order to see the circulation curve used to integrate the curl, we provide a three-dimensional perspective of these 'faces' denoted by the label 3D in (b) and (c). Actually, as [64] shows, the standard and staggered 2D Yee cells are projections of the standard and staggered 3D Yee cells onto the 2D plane.

Boundary conditions are applied to the tangential components of the electric field on boundary locations. Note that the field  $H_\phi$  is not represented in any boundary point.

### 3.3.2 Discretisation

The Finite Difference Frequency Domain (FDFD) method transforms the harmonic form of the Maxwell equations into a set of linear algebraic equations using finite-differences. The continuous functions (EM fields, permittivity, and others) are fitted to the standard and staggered Yee grids where function values are only known at discrete points. Intermediate values are obtained through interpolation, when needed.

In general, the complete **vector** equations (equations (3.12) and (3.13)) must be discretised and solved. In view of the cylindrical symmetry, only three scalar equations remain, in cylindrical coordinates these are given by equations (3.14), (3.15) and (3.16).

The discretisation of equation (3.14) is guided by Stokes' theorem,

$$\iint_A \nabla \times \mathbf{V} \cdot \mathbf{n} da = \oint_C \mathbf{V} \cdot d\mathbf{l}. \quad (3.21)$$

By applying this theorem to equation (3.14) and evaluating the result on the *magnetic grid cell* that is depicted in figure 3.2(a) we get

$$k_0 \tilde{H}_\phi^c \delta_z^c \delta_r^c h_z^c h_r^c + E_z^s \delta_z^s h_z^s + E_r^e \delta_r^e h_r^e - E_z^n \delta_z^n h_z^n - E_r^w \delta_r^w h_r^w = 0. \quad (3.22)$$

The equations (3.15) and (3.16) are discretised on the *electric grid cells*. With respect to the *magnetic grid cell*, these are shifted in the east-west ( $E_r$  component) or north-south ( $E_z$  component) direction (see [65]). For the field component  $E_r$ , the *electric grid cell c* is shown in figure 3.2(b) and the discretisation gives

$$k_0 \hat{\epsilon}_r^c E_r^c h_\phi^c \delta_1^c h_1^c - [\tilde{H}_\phi^w \delta_\phi^w h_\phi^w - \tilde{H}_\phi^e \delta_\phi^e h_\phi^e] = 0. \quad (3.23)$$

Similarly, for the field  $E_z$  at *electric grid cell c* depicted in figure 3.2(c), the discretisation gives

$$k_0 \hat{\epsilon}_r^c E_z^c \delta_r^c h_r^c \delta_\phi^c h_\phi^c - [\tilde{H}_\phi^n \delta_\phi^n h_\phi^n - \tilde{H}_\phi^s \delta_\phi^s h_\phi^s] = 0. \quad (3.24)$$

### 3.3.3 Solution Procedure for the Resulting Matrix Problem

After applying appropriate boundary conditions, which will be discussed in the next section, the discretisation procedure generates a system of linear equations of the form

$$\overline{\overline{A}} \mathbf{x} = \mathbf{b}. \quad (3.25)$$

Here  $\overline{\overline{A}}$  is a sparse matrix resulting from the discretised operator;  $\mathbf{x}$  represents the discrete fields components, and  $\mathbf{b}$  contains the discrete source.

The solution of the above system of equations is obtained using the SuperLU solver [66], which is optimised for sparse matrices. Different options are available with respect to the *pre-ordering* of columns of  $\overline{\overline{A}}$  before the factorisation takes place in the SuperLU solver. We found that the Multiple Minimum Degree method [67] applied to the structure  $A^T A$  [66] is the fastest option.

### 3.4 Boundary Conditions

	Homogeneous (H)	Inhomogeneous (I)
Dirichlet (1)	Perfect Electric Conductor (PEC)	Excitation ( $P_{abs}$ imposed)
Neumann (2)	Axis of symmetry	
Mixed (3)	Propagation Boundary Condition (ABC)	Excitation Coaxial Waveguide ( $P_{for}$ imposed)

Table 3.1: Example of boundary conditions for the EM fields used in this thesis

In this section we discuss the *mathematical form* of the boundary conditions. They will be applied to the two components  $E_r$  and  $E_z$  of the electric field.

For an electric field component  $F$  being  $E_z$  or  $E_r$  at a surface  $\mathcal{B}$  with normal surface vector  $\mathbf{n} = \hat{\mathbf{e}}_z$  or  $\hat{\mathbf{e}}_r$ , the following types of boundary conditions can be applied

1. Dirichlet:  $F(\mathbf{x}) = p(\mathbf{x}), \quad \mathbf{x} \in \mathcal{B}$
2. Neumann:  $\mathbf{n} \cdot \nabla F(\mathbf{x}) = q(\mathbf{x}), \quad \mathbf{x} \in \mathcal{B}$
3. Mixed:  $\mathbf{n} \cdot [\nabla + h(\mathbf{x})] F(\mathbf{x}) = w(\mathbf{x}), \quad \mathbf{x} \in \mathcal{B}$

where  $\mathbf{x} = z\hat{\mathbf{e}}_z + r\hat{\mathbf{e}}_r \equiv (z, r)$  is the position vector for a location on the boundary surface  $\mathcal{B}$  and  $p, q, h$ , and  $w$  are explicitly known functions of  $\mathbf{x}$ . If  $p(\mathbf{x}), q(\mathbf{x})$  or  $w(\mathbf{x}) = 0$  for all  $\mathbf{x} \in \mathcal{B}$ , the boundary condition is named homogeneous (H), otherwise the boundary is called inhomogeneous (I). Some examples are given in table 3.1.

Below we will mention four *physical boundary types*, together with the corresponding boundary conditions. They can be identified briefly as *metal, symmetry axis, propagation* and *excitation*.

### Metal

On metal boundaries, a homogeneous Dirichlet boundary condition is specified for the tangential field, i.e. type 1 with  $q(\mathbf{x}) = 0$ . The reason is that the metal is considered to be a Perfect Electrical Conductor (PEC), which does not support an electric field. Using the continuity of the tangential field component (see [53]) we conclude that the tangential component of the electric field is zero also on the inner side of a PEC boundary.

### Axis

Cylindrical symmetry dictates a homogeneous Neumann boundary condition (type 2) for the tangential field component  $E_z$  on the axis of symmetry.

### Propagation boundary condition (PBC)<sup>b</sup>

The propagation boundary condition is based on the assumption that locally the outgoing wave can be expressed in a known analytical form. It is inspired by the work of [68, 69], and given in the review paper [70]. It is of type 3. We also used this boundary condition in [44] (chapter 6 of this thesis).

### Excitation Boundary

The excitation boundary requires an inhomogeneous boundary condition. Currently there are two boundary conditions available:

*Power Absorbed in Domain:* This is an inhomogeneous (I) Dirichlet boundary condition i.e. of type 1. This boundary condition is applied to a boundary where an analytical solution of the EM field is known, for example at the inside of a waveguide or cavity. In this boundary condition the absolute value of the field at the excitation boundary is not important because the electromagnetic field scales with the square of the power absorbed in the domain (see equation (4.24)). When using this BC, we scale the power absorbed in the domain  $Q_{abs}$ , such that the power absorbed  $P_{abs}$  matches the power given as input,  $P_{in}$ . The scale factor is

$$s = \frac{P_{in}}{P_{abs}}. \quad (3.26)$$

The absolute value of the electromagnetic field intensity is found by multiplying the previous value of the electromagnetic field intensity with  $\sqrt{s}$ .

Note that if there is no dissipative material in the domain, we cannot use this scaling as  $P_{abs} = 0$  and the boundary condition sets the absolute value of the electromagnetic fields. This boundary condition is used in the comparison of

---

<sup>b</sup>This BC is often referred to as the absorbing BC (see [68]). However, since we use absorption in another meaning and since this BC deals with the propagation of the wave to the exterior of the domain we prefer to call this the Propagation BC.

the model results with analytical solutions in section 3.5 and in chapters 8, 9, and 10.

*Incident Power to the Domain:* This is an inhomogeneous mixed boundary condition, i.e of type 3(I). In this case we want to impose the amount of power entering the domain i.e. the forward power  $P_{for}$ .

To that end the field must be decomposed in a *forward* and *reflected* component. An inhomogeneous Dirichlet condition is imposed to the forward component such that it carries the forward power. For the reflected component a PBC is used, so that the system is free to response with the corresponding reflected power. We have implemented this boundary condition for the case of a coaxial waveguide; it is used in chapter 6 and in [44].

As the forward power plays the role of the fixed input power (a control parameter), it is not appropriate to scale the electromagnetic fields such that the absorbed power in the conductive materials matches the power input.

## 3.5 Analytical Solutions and Model Validation

In order to validate the electromagnetic model for microwave modelling, we have simulated systems for which analytical solutions exist of the *vector Helmholtz equation*. Here we report the case of a coaxial waveguide short-circuited at one end. The model results are compared to the analytical solutions.

### 3.5.1 The Vector Helmholtz Equation for $\mathbf{H}$

By taking the curl of equation (3.10) and substituting in the result equation (3.8), we get

$$\nabla \times \nabla \times \mathbf{H} - k_0^2 \hat{\epsilon}_r \mathbf{H} - \left( \frac{\nabla \hat{\epsilon}_r}{\hat{\epsilon}_r} \right) \times \nabla \times \mathbf{H} = 0; \quad (3.27)$$

The last term on the left-hand side vanishes for a medium with uniform complex permittivity; the result is the *vector Helmholtz equation* for the magnetic field,

$$\nabla \times \nabla \times \mathbf{H} = k_0^2 \hat{\epsilon}_r \mathbf{H}. \quad (3.28)$$

This can also be written as

$$\nabla \times \nabla \times \mathbf{H} = k^2 \mathbf{H}. \quad (3.29)$$

Where the wavenumber  $k$  has been defined as  $k = k_0 \sqrt{\hat{\epsilon}_r}$  with  $k_0 = \omega \sqrt{\mu_0 \epsilon_0}$  the vacuum wavenumber. Note that we can also obtain the Helmholtz equation for  $\mathbf{E}$ .

### 3.5.2 Validation Case: Short-circuited Coaxial Waveguide

In order to study the numerical error, we created a numerical model of a coaxial waveguide with a short-circuit at one end (see figure 3.3). For the inner radius we take  $a = 9$  mm and for the outer radius  $b = 54$  mm.

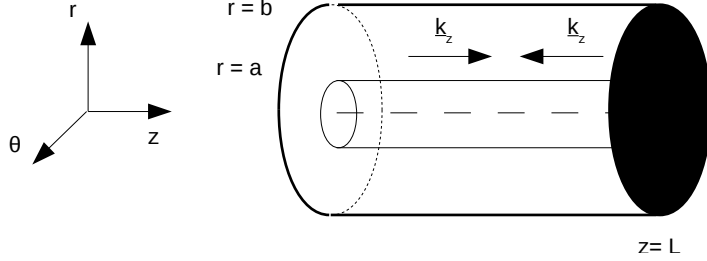


Figure 3.3: Schematic view of a coaxial waveguide, short-circuited at  $z = L$ . The inner radius is  $r = a$  and the outer radius is given by  $r = b$ .

In a coaxial waveguide the fundamental mode, i.e. the solution to equation (3.29) with minimum cut-off frequency, is the TEM mode. The corresponding distributions in vacuum are given by

$$H_\phi(z, r) = C \cdot \frac{1}{r} \exp(-ik_z z) \quad (3.30)$$

$$E_r(z, r) = \frac{C}{Z_0} \cdot \frac{1}{r} \exp(-ik_z z) \quad (3.31)$$

where  $k_z = k_0$  in vacuum and  $Z_0 = \sqrt{\mu_0/\epsilon_0}$  is the impedance of free space.

The short-circuit is a metallic wall placed perpendicular to the direction of the incident wave propagation  $\mathbf{e}_z$ . The incident wave is reflected back and the interaction of the reflected wave with the incident wave generates *standing waves*. In this case the distribution of the absolute value of the magnetic field is given by

$$|H_\phi(z, r)| = C' \cdot \frac{1}{r} |\cos[k_0(z - L)]| \quad (3.32)$$

For the scaled magnetic field we find

$$|\tilde{H}_\phi^{\text{ana}}(z, r)| = Z_0 C' \cdot \frac{1}{r} |\cos[k_0(z - L)]| \quad (3.33)$$

The numerical solution is obtained for a geometrical computational domain consisting of  $N_z = 30$  (standard Yee) grid cells in axial direction and  $N_r = 15$  grid cells in the



radial direction. The grid is not stretched, meaning that the size of the grid cell is uniform in both axial and radial directions. The excitation boundary condition sets the electric field equals to  $1V/r$  at the boundary  $z = 0$ .

We define the normalised axial numerical distribution of the scaled magnetic field at  $r = r^*$  as

$$f_{\text{num}}(z) = \frac{|\tilde{H}_{\phi}^{\text{num}}(z, r^*)|}{\max(|\tilde{H}_{\phi}^{\text{num}}(z, r^*)|)} \quad (3.34)$$

where  $\tilde{H}_{\phi}^{\text{num}}$  is the numerical solution defined at the corresponding grid cell positions.

In a similar way, the normalised axial analytical distribution of the scaled magnetic field at  $r = r^*$  is defined as

$$f_{\text{ana}}(z) = \frac{|\tilde{H}_{\phi}^{\text{ana}}(z, r^*)|}{\max(|\tilde{H}_{\phi}^{\text{ana}}(z, r^*)|)} = |\cos[k_0(z - L)]|. \quad (3.35)$$

Figure 3.4 shows an excellent agreement between the analytical  $f_{\text{ana}}(z)$  and numerical  $f_{\text{num}}(z)$  solutions for  $r^* = 24$  mm.

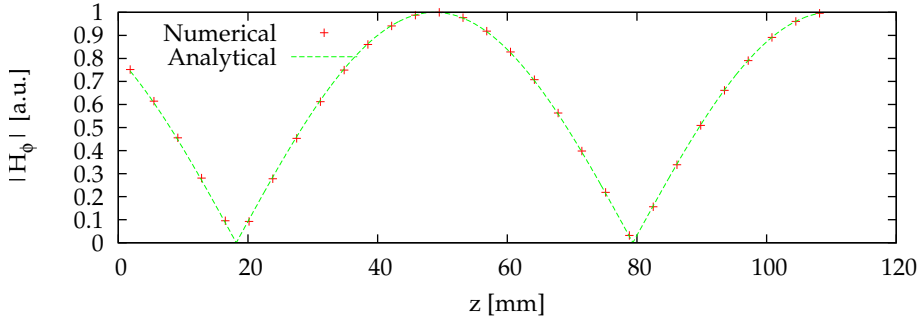


Figure 3.4: Comparison of the axial distribution of the analytical  $f_{\text{ana}}$  and numerical  $f_{\text{num}}$  solution. The geometry is that of a coaxial waveguide short circuited at  $z = 110$  mm. The number of grid points for the computational domain equals  $N_z = 30$  in axial direction and  $N_r = 15$  in the radial direction.

The normalised error has been defined as

$$\sigma = |f_{\text{ana}}(z) - f_{\text{num}}(z)| \quad (3.36)$$

Note that the absolute error is related to the normalised error via

$$\text{error} = \max(|\tilde{H}_{\phi}^{\text{num}}(z, r^*)|)\sigma. \quad (3.37)$$

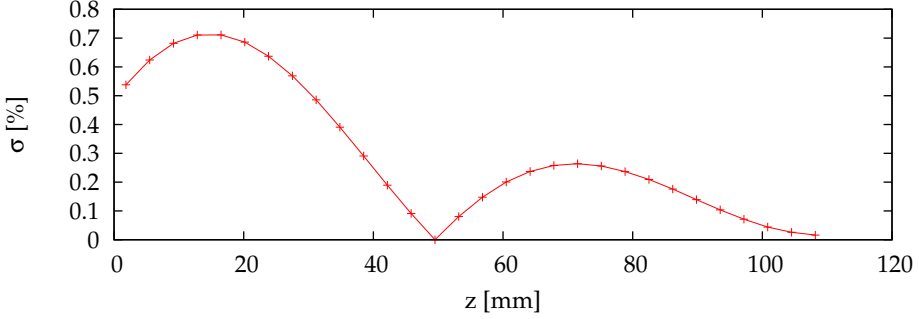


Figure 3.5: The normalised error for comparing the axial distribution of the normalised analytical  $f_{\text{ana}}$  and numerical  $f_{\text{num}}$  solution. The number of grid points in the rectangular computational domain equals  $N_z = 30$  in axial direction and  $N_r = 15$  in the radial direction.

The axial distribution of the error  $\sigma$  is shown in figure 3.5 for the same conditions as in figure 3.4. Note that the error increases from  $z = L$  toward  $z = 0$ .

To estimate the order of the discretisation error, we compared the maximum normalised error for grids with different total number of cells  $N_i$ . For a grid  $i$ ,  $N_i = N_{r,i} \times N_{z,i}$ . We also defined grid size factor per direction  $h_i = (N_i/N_0)^{1/D}$  as the ratio of total number of cells of grid  $i$  to the total number of cell of the reference grid ( $i = 0$ ) to the power of the inverse of the grid dimension  $D$  ( $D = 2$  in a two-dimensional grid as it is our case).

When the truncation error is the most important contribution, the dependency of the maximum normalised error  $\sigma^* = \max(\sigma(z))$  on  $h$  is given by [71]

$$\sigma^* = Ah^p \quad (3.38)$$

where  $A$  is a coefficient assumed to be independent of  $h$  and  $p$  is the approximated order of the discretisation method.

In figure 3.6 we plot  $\max(\sigma)$  as a function of  $h$  for 4 grids with constant refinement factor  $c = h_{i+1}/h_i = 2$ . The values of  $h$  are given in table 3.2.

The discretisation error order is estimated from the slope of equation (3.38) at each  $[h_i, h_{i+1}]$  interval as

$$p_{i,i+1} = \frac{\log(\sigma_{i+1}^*/\sigma_i^*)}{\log(c)}. \quad (3.39)$$

We obtain  $p_{1,2} = -1.94$ ,  $p_{2,3} = -1.95$  and  $p_{3,4} = -1.62$  meaning that the error in the method is apparently of second order as we change from grid  $h_1$  to  $h_2$  and from

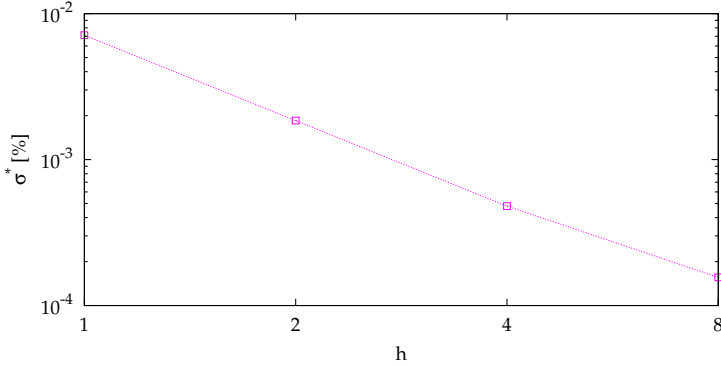


Figure 3.6: Maximum normalised error  $\sigma^*$  as a function of  $h$ .

(Grid) i	0 (reference)	1	2	3
$N_{r,i}$	15	30	60	120
$N_{z,i}$	30	60	120	240
$h_i$	1	2	4	8
$c$	2	2	2	

Table 3.2: Data for grids used in the estimation of the discretisation error order. Here  $N_{r,i}$  and  $N_{z,i}$  are the number of cells in the radial and axial direction, respectively;  $h_i = (N_i/N_0)^{1/D}$  the grid size factor per direction with  $N = N_{r,i}N_{z,i}$  and  $N_0 = N_{r,0}N_{z,0}$ ;  $c = h_{i+1}/h_i$  is the constant refinement factor.

$h_2$  to  $h_3$ . This is the behaviour expected for the truncation errors as the grid is finer. However when the grid is getting much finer as from  $h_3$  to  $h_4$  we find a lower local discretisation order, probably due to round-off errors in the computation (expected for small numbers).

Note that when the analytical solution is unknown, other techniques are needed to study the discretisation error such as the grid convergence index (GCI) [71].

### 3.5.3 Numerical Dispersion

One may find the dispersion relation for a plane wave by using the wave equation which basically relates the wavenumber and the frequency to the phase velocity of the wave. However, if one tries to find the dispersion relation for that plane wave after the discretisation of the wave equation, a relation will be found that differs from the analytical one. This dispersion is called the numerical dispersion [72], [73] and it

is another source of error in electromagnetic modelling. Because of this phenomenon there will be a phase difference between the analytical and the numerical solution leaded by the propagation of the wave. In other words, the *numerical wave* will propagate with slightly different—in general—phase velocity than the analytical wave does. In this respect, as they propagate the error term between them will increase as well. For example, the error yielded by the numerical dispersion will increase as the propagation of the electromagnetic wave increases.

A central second order discretisation of the one-dimensional version of equation (3.29) leads to

$$\frac{u_{n+1} - 2u_n + u_{n-1}}{\delta x^2} + (k^{\text{num}})^2 u_n = 0, \quad (3.40)$$

where  $u$  is a component of the magnetic field,  $\delta x$  is the grid spacing and  $n$  represents the nodal point. Assuming the solution in the form  $\exp(ikx)$  for the uniform grid spacing  $\delta x$  leads to

$$\exp(ikx) \frac{(\exp(ik\delta x) - 2 + \exp(-ik\delta x))}{\delta x^2} + (k^{\text{num}})^2 \exp(ikx) = 0. \quad (3.41)$$

Cancelling the common term and using Euler's relations it becomes

$$\frac{2 \cos(k\delta x) - 2}{\delta x^2} = -(k^{\text{num}})^2, \quad (3.42)$$

which can be rewritten as

$$\frac{\sin^2\left(k\frac{\delta x}{2}\right)}{\left(\frac{\delta x}{2}\right)^2} = (k^{\text{num}})^2. \quad (3.43)$$

If we define the ratio  $c_f$  of the numerical and real wave number,

$$c_f k = k^{\text{num}} \quad (3.44)$$

we find that

$$c_f = \frac{\sin\left(k\frac{\delta x}{2}\right)}{\left(k\frac{\delta x}{2}\right)}. \quad (3.45)$$

Equation (3.44) expresses that the numerical phase velocity  $v^{\text{num}} = \omega/k^{\text{num}}$  is not equal to the analytical phase velocity  $v = \omega/k$ . This means that the difference between the analytical and numerical solution is higher as the waves travel over a longer distance through the simulation domain. Only if the grid spacing goes to zero the relation tends to the analytical one.

In order to demonstrate the effect of numerical dispersion, we have used  $k^{\text{num}} = k/c_f$  instead of  $k$  in the analytical solutions for the coaxial waveguide, i.e we have artificially

added the numerical dispersion into the analytical solution. We will compare the relative error between the numerical results and the (numerical dispersion) corrected analytical solution.

The corrected analytical solution has a relative error with respect to the numerical solution in the order of  $10^{-5}$ , figure 3.7(a), whereas if we effectuate the comparison without correction we obtain a relative error in the order of  $10^{-3}$ , figure 3.8(a). For a higher density grid, the relative error for the comparison with numerical dispersion correction is in the same order  $10^{-5}$ , figure 3.7(b), whereas without correction we obtain a relative error that is 10 times higher, i.e. in the order of  $10^{-4}$ , figure 3.8(b).

This correction factor can be used to correct the numerical scheme for numerical dispersion, but we have not included this in the current work. We believe that this would be important for dimensions much larger than the wavelength of the wave. For more information on numerical dispersion and how to compensate it in the model, we refer to [63].

The effect of numerical dispersion is overlooked in various MIP simulation studies [11, 35, 74], although it might limit the dimensions to which an electromagnetic mode can be applied.

## 3.6 Conclusion

We have presented an electromagnetic model for microwave propagation. The model assumes harmonic fields and uses finite differences on a Yee grid. All relevant boundary conditions were discussed, special attention was paid to the *excitation boundary conditions*. From the analysis of the grid convergence we have found that the truncation error is of second order with respect to the grid size measure quantity  $h$ . However as the grid is finer i.e.  $h$  is higher, the round-off error lower the order of the error. This error also depends on the axial position due to numerical dispersion.

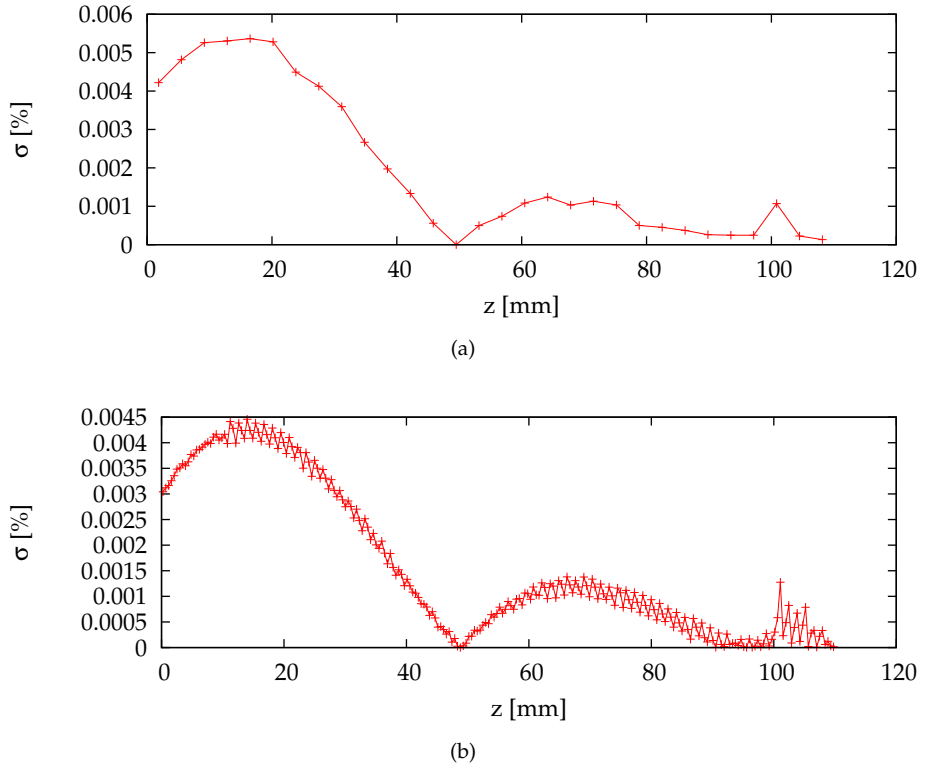
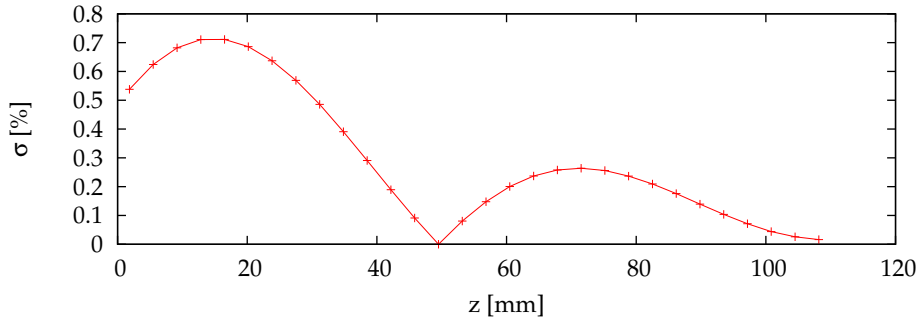
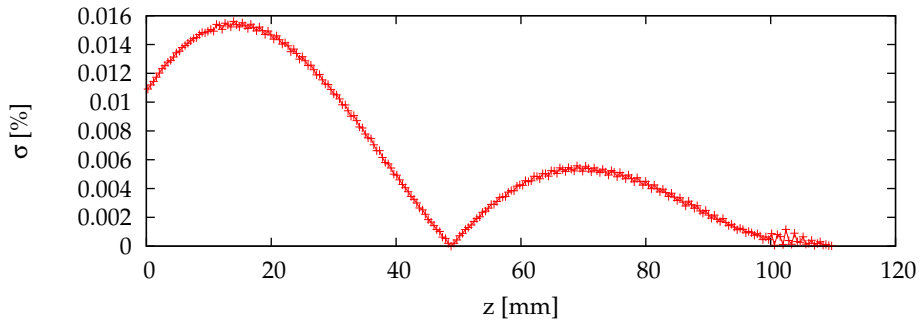


Figure 3.7: The normalised error for comparing the axial distribution of the normalised analytical  $f_{\text{ana}}$  and numerical  $f_{\text{num}}$  solution. A correction is included to reflect the numerical dispersion. In (a)  $h = 1$  with the number of grid points  $N_z = 30$  in axial direction and  $N_r = 15$  in the radial direction where as in (b)  $h = 8$  with  $N_z = 240$  and  $N_r = 120$ .



(a)



(b)

Figure 3.8: The normalised error for comparing the axial distribution of the normalised analytical  $f_{ana}$  and numerical  $f_{num}$  solution. In (a)  $h = 1$  with the number of grid points  $N_z = 30$  in axial direction and  $N_r = 15$  in the radial direction where as in (b)  $h = 8$  with  $N_z = 240$  and  $N_r = 120$ .

---

4

Transport

---



## 4.1 Introduction

In chapter 2 we divided the plasma aspects into three main blocks: *configuration*, *transport*<sup>a</sup> and *chemistry*. In this division transport plays a central role; it describes how mass, momentum and energy is distributed over the various particles and how the energetic mixture of radicals and photons is transferred to the plasma's 'application zone' (e.g. radicals toward the substrate where deposition takes place, photons via the transparent wall of a lamp to the environment).

This chapter is devoted to the transport of material-related properties. It deals with the balance equations of mass, momentum and energy on the species level but also on the level of the plasma as a whole: the bulk.

There are tight relations between plasma transport modelling (PTM) and the fields of computational fluid dynamics (CFD) and magneto-hydrodynamics (MHD). But, there are also remarkable differences. In contrast to CFD, which usually deals with the flow fields of gases with constant material properties (density, viscosity), we see that PTM has to compute how the transport phenomena is changed by the energy coupling and plasma chemistry. The difference with MHD, where the plasma is described as a single conducting fluid is that the multi-species nature of the mixture must be taken into account.

The main objective of this chapter is to give the background of the transport equations that are needed for MIP modelling for which we use the fluid description [9, 45, 46, 49, 58, 75]. However, where possible we refer to other PLASIMO transport-modes as well; for instance to those used in MD2D and to the particle (or kinetic) approach. In section 4.2 we will relate the fluid method to the kinetic approach (the techniques of Monte Carlo and Particle in Cell and the Boltzmann solver). In sections 4.3 and 4.4 we continue with the fluid approach by sketching the derivation of the balance equations for the density, momentum and energy fields. It will be shown how the common origin, the Boltzmann equation (BE), is manifest in the similarity between these balance equations. Simplifications and assumptions of the specific<sup>b</sup> balance equations for each relevant species<sup>c</sup> will be discussed; it will be shown how the

---

<sup>a</sup>With "Transport" we refer to material related transport; that is the transport as carried by particles (mass, momentum and energy); this excludes the transport of energy as carried by EM waves, this is denoted by "propagation" and as the wave is launched outside the plasma it is considered as part of the configuration; it deserves a different chapter (chapter 3).

<sup>b</sup>Here "specific" refers to "species"-related; a species is a particle-type. Particles that belong to the same species have the same internal properties; so there is no such thing as an excited species; if an atom is excited, a particle of another species is created.

<sup>c</sup>The number of species created by the plasma-action is virtually infinite; as we can not include all the species in the transport model we have to make a selection and repair the consequences of eliminating most of the species; this is discussed in chapter 5; the particle-types for which transport is here denoted by relevant species.

specific equations for the densities can be combined to form the continuity equation (CE) and how the sum of the specific momentum equations leads to the Navier-Stokes equations. These, the CE and NS equations, in conjunction, describe the bary-centric motion of the plasma. With respect to the species energy it turns out to be practical to divide the plasma species into heavy particles {h} (excited states, ions and neutrals) and electrons {e}. Thus, the energy housekeeping of the plasma has to be described by a system of two energy equations, one for {h} the other for {e}.

In section 4.7 we will write the relevant equations in the canonical form, as a  $\phi$ -equation (also see section 2.4). This abstraction is essential and it is the basis of the modular structure of PLASIMO. Section 4.8 deals with the collisions and their relation with the transport coefficients. In section 4.9 we will summarise the main assumptions for the models used in this thesis.

## 4.2 From Kinetic to a Fluid Description

Plasmas consist of an enormous amount of particles of many different types, such as electrons, ions, (excited) atoms and molecules.

The particles are subjected to (external) field forces of electromagnetic (EM) and gravitational nature but they can also interact mutually e.g. by means of collisions. In order to describe a plasma in full detail one should give the positions and velocities of all the  $N$ , say  $i$ , individual particles. This so-called microstate can be represented by a point in a  $6N$ -dimensional space. The evolution of the plasma as a result of external (and internal) forces is then given by a trajectory in that hyper-space. This can be found by tracking each particle individually. Between collisions the motion of a particle is smooth and ruled by Newton's second law. Due to collisions, the velocity will change abruptly; this can be simulated using the Monte Carlo method; a stochastic method. Using modern desktop computers, this multi-particle tracking is possible for  $N = 10^7$ . By using parallel computing the number can even be increased to  $N = 10^9$ . If  $N > 10^9$  one can introduce the concept of super-particles; computational particles that represent many real particles; e.g. thousand of electrons (or ions).

The MC method will not be used in this work but it is in function as one of the modules of the PLASIMO platform. It was initiated by Wouter Brok [58] and applied by Marc van der Velden [56], combining MC with a particle in cell (PIC) method. With the PIC method one can compute the EM field generated by the position (and velocity) of the charged particles. This EM field will subsequently modify the velocities of the individual particles. PIC-MC models are suitable for plasmas of low densities. For modelling plasmas of higher densities this kinetic approach is not practical. Instead of the behaviour of each individual particle we are more interested in averaged

quantities like the densities, averaged velocities and mean energies. For this we have to use distribution functions that describe how many particles (or couple of particles) can be found in a certain volume of space and velocity interval.

A function that is often used is the one-particle distribution function  $f_s(\mathbf{x}, \mathbf{w}, t)$  that operates on a 6-dimensional phase space spanned up by  $\mathbf{x}$ , the position vector and  $\mathbf{w}$ , the velocity vector. The function is defined such that  $f_s(\mathbf{x}, \mathbf{w}, t)d^3x d^3w$  represents the number of particles of species  $s$  in the phase space volume element  $d^3x d^3w$  at time  $t$ . The evolution of  $f_s$  is usually modelled by the Boltzmann equation,

$$\frac{\partial f_s}{\partial t} + \nabla_6 \cdot (f_s \mathbf{C}) = \left( \frac{\delta f_s}{\delta t} \right)_{CR}, \quad (4.1)$$

with  $\mathbf{C} = (d\mathbf{x}/dt, d\mathbf{w}/dt)$  the velocity and  $\nabla_6$  the divergence in phase-space. In the case that only the electric field is important we can transform the BE into

$$\frac{\partial f_s}{\partial t} + \mathbf{w} \cdot \nabla_x f_s + q \frac{\mathbf{E}}{m} \cdot \nabla_w f_s = \left( \frac{\delta f_s}{\delta t} \right)_{CR}. \quad (4.2)$$

This equation can be solved, in principle, if the electric field is known. Usually an approximate form of the BE is solved, for example based on the two-term expansion. That procedure is at the basis of the BOLSIG+ program [32], a code developed in the LAPLACE group at Université Paul Sabatier in Toulouse, France. It is often used in our group to compute the electron energy distribution energy (EEDF) an energy variant of the one-particle electron distribution function i.e.  $f_e(\mathbf{x}, \mathbf{w}, t)$ .

In our approach we assume that the EEDF attains its Maxwellian equilibrium value<sup>d</sup>. If the distribution functions are Maxwellian (or more general: if they have a known form) we can use the BE to derive conservation equations on a higher level by using the method of moments [54, 77]. For each relevant species we get a set of three balance equations, namely for the density, momentum and energy. These equations will be referred to as the ‘transport equations’.

### 4.3 Multi-Fluid Description in PLASIMO

Below we will present the balance equations for the density, momentum and energy for the species that are present in the plasma. We will then combine these equations to establish the relation of the species equations with the continuity equation (CE) and the Navier-Stokes (NS) equations for the barycentric flow quantities.

---

<sup>d</sup>In [76] and chapter 9 we find indications that this assumption is not always justified.

### 4.3.1 The Specific Density Balances

The zeroth moment of BE is obtained by integrating the BE over the velocity space. For species  $s$  the result is given by

$$\left(\frac{\partial n_s}{\partial t}\right) + \nabla \cdot \Gamma_s = S_s, \quad (4.3)$$

with  $n_s$  (in  $[\text{m}^{-3}]$ ) the species density,  $\Gamma_s$  (in  $[\text{m}^{-2}\text{s}^{-1}]$ ) the flux density and  $S_s$  (in  $[\text{m}^{-3}\text{s}^{-1}]$ ) the net production of the species in reactions.

The flux density equals  $\Gamma_s = n_s \mathbf{v}_s$ . The mean velocity  $\mathbf{v}_s$  of species  $s$  can be split up in two terms as

$$\mathbf{v}_s = \mathbf{v}_b + \mathbf{v}_{d,s}, \quad (4.4)$$

where the first term refers to the barycentric motion of the plasma (or bulk flow velocity), whereas the second refers to the diffusion velocity: that is the velocity of the species relative to the barycentric velocity. The barycentric velocity can be determined from a combination of the continuity (CE) and the Navier-Stokes (NS) equation (section 4.4).

In PLASIMO two different models are available to describe diffusion: Fick's law and the self-consistent diffusion approach. Fick's law is applicable when the species  $s$  diffuses in a dominant background gas. In the self-consistent diffusion approach  $\mathbf{v}_{d,s}$  is computed taking the mutual frictions between all the different couples of species [10, 47] into account.

Not for all species we need a transport description like that given in equation (4.3). In chapter 5 we will define *Local Chemistry* (LC) species, whose densities can be obtained on the basis of the assumption of local chemical equilibrium, see equation (5.8).

Another simplification comes in via the quasi-neutrality assumption from which the electron density can be obtained as  $n_e = e^{-1} \sum_{s \neq \{e\}} q_s n_s$ , with  $q_s$  the charge of species  $s$  and  $e$  the elementary charge. This implies that there is no need to construct a balance equation for the electron density. Furthermore, in the current work, the species density of one *dominant* species is calculated from the equation of state  $\sum_s n_s k_B T_s = p$ , instead of from equation (4.3).

Note that the PLASIMO sub-model Micro Discharge 2D (MD2D) [9, 75, 78, 79] was especially developed to handle sheath formation in front of electrodes (see table 2.1). Since these regions are in general not charge neutral, we have to solve the electron density equation and the balance equations of all the ion-species. The absence of charge neutrality then demands that the Poisson equation for the electrostatic field is solved.

### 4.3.2 The Specific Momentum Balances

To obtain the first moment of the BE, we start by multiplying the BE with  $m_s \mathbf{w}$  and integrate the result over the velocity space [38, 54]. After some algebra we get for the momentum balance for species  $s$  the equation

$$\frac{\partial m_s n_s \mathbf{v}_s}{\partial t} + \nabla \cdot (m_s n_s \mathbf{v}_s \mathbf{v}_s) = -\nabla p_s + \nabla \cdot \boldsymbol{\tau}_s + \mathbf{F}_s + \mathbf{R}_s^T + \mathbf{R}_s^F. \quad (4.5)$$

The units of the terms in equation (4.5) are in  $[\text{Nm}^{-3}]$ . From left to right we find the temporal and spatial inertial terms, the gradient of the pressure, the divergence of the viscous stress tensor, the body force, the thermophoretic (thermal diffusion) force, and the friction with other species.

For the body force we can substitute into equation (4.5)

$$\mathbf{F}_s = n_s q_s (\mathbf{E} + \mathbf{v}_s \times \mathbf{B}) + m_s n_s \mathbf{g}, \quad (4.6)$$

where we find at the right-hand-side the electro-static force, and the Lorentz and gravitation force. The friction force term [10, 47] in equation (4.5) is given by

$$\mathbf{R}_s^F = - \sum_{s'} f_{s,s'} (\mathbf{v}_s - \mathbf{v}_{s'}) = - \sum_{s'} f_{s,s'} (\mathbf{v}_{d,s} - \mathbf{v}_{d,s'}), \quad (4.7)$$

and shows that the friction force per unit volume exerted on species  $s$  due to collisions with other species  $s'$  is proportional to the difference between the mean velocities of these species. The proportionality constants are the *friction coefficients*  $f_{s,s'} = m_{s,s'} n_s \nu_{s,s'}$ , which depend on the densities  $n_s$  of the species  $s$ , the momentum transfer frequencies  $\nu_{s,s'}$  and the reduced masses of the interacting species  $m_{s,s'}$ . The friction between species plays a crucial role in the specific force balances but we will see that it is absent in the force balance for the bulk plasma in section 4.4.

Using the features of the friction term, we will discuss below Fick diffusion, self consistent diffusion, and two versions of Ohm's law.

### 4.3.3 Fick Diffusion

In many cases the combination of equation (4.5) and (4.6) can be simplified to [11, 75]

$$-\nabla (n_s k_B T_s) + q_s n_s \mathbf{E} + \mathbf{R}_s^F = 0, \quad (4.8)$$

where we have neglected time dependency, the inertia effects, viscosity, the gravity and the magnetic force.

If there is only one dominant species, i.e. the species of the buffer gas, we can transform the friction term (4.7) of all other species into

$$\mathbf{R}_s^F = -f_{s,0}(\mathbf{v}_s - \mathbf{v}_0), \quad (4.9)$$

where the properties of the buffer gas are labelled with index 0. Assuming that the temperature is uniform ( $\nabla T = 0$ ) we obtain the *drift-diffusion-convection equation* [80, 81]:

$$n_s \mathbf{v}_s = \frac{n_s q_s}{m_{s,0} v_{s,0}} \mathbf{E} - \frac{k_B T_s}{m_{s,0} v_{s,0}} \nabla n_s + n_s \mathbf{v}_0. \quad (4.10)$$

The first term at the right hand side gives the flux due to the electric field (drift), the second term due to density gradients (diffusion), while the last term is the barycentric motion (convection). This equation can be written in the more common form:

$$\mathbf{\Gamma}_s = n_s \mathbf{v}_s = n_s \mu_s \mathbf{E} - D_s \nabla n_s + n_s \mathbf{v}_0, \quad (4.11)$$

where two transport coefficients have been introduced: the mobility  $\mu_s$  and the diffusion coefficient  $D_s$ ,

$$\mu_s = \frac{q_s}{m_{s,0} v_{s,0}}, \quad D_s = \frac{k_B T_s}{m_{s,0} v_{s,0}}. \quad (4.12)$$

Equation (4.12) immediately leads to the Einstein relation

$$\frac{D_s}{\mu_s} = \frac{k_B T_s}{q_s}. \quad (4.13)$$

For neutral particles the drift term  $n_s \mu_s \mathbf{E}$  is absent so that only diffusion and convection remain. The diffusion in this version is known as Fick diffusion; it only depends on the gradient of the density of the species in question.

Equation (4.11) is one of the basic equations of MD2D. In most cases only the two first terms at the right-hand side are used and the corresponding equation is known as the *drift-diffusion* equation. The convection term cannot be calculated by MD2D. The velocity field has to be computed using a NS solver. This approach was used by [48, 81]. In PLASIMO the barycentric velocity can be computed using the SIMPLE algorithm whereas the diffusive velocities can be obtained either using the Fick's law or using the self-consistent multicomponent diffusion method [10, 47]. Although in the current work only Fick's law is used to describe the diffusion velocities, we give a global description of self-consistent multicomponent diffusion in next section.

#### 4.3.4 Self-Consistent Multicomponent Diffusion

The main element of the plasmas used for fibre fabrication is oxygen. Due to the high power density the dominant species in the centre of these plasmas is the oxygen

atom, O, whereas the wall region is ruled by the molecule O<sub>2</sub>. This is an example of a plasma for which Fick's diffusion can not be applied, since there is no species that is dominant everywhere. This situation has to be treated by self-consistent diffusion.

In the framework of the PLASIMO project several studies were devoted to self-consistent diffusion [10, 47, 82]. The set of equations can be found starting with equation (4.5) in which equation (4.7) is substituted. Neglecting time dependency, the inertia effects, viscosity, gravity and the magnetic force we find

$$0 = -\nabla p_s + n_s q_s \mathbf{E} - \sum_{s'} f_{s,s'} (\mathbf{v}_{d,s} - \mathbf{v}_{d,s'}). \quad (4.14)$$

Defining  $f_s^{eff} = \sum_{s'} f_{s,s'}$ , it is possible to transform this into

$$f_s^{eff} \mathbf{v}_s = -\nabla p_s + n_s q_s \mathbf{E} + \sum_{s' \neq s} f_{s,s'} \mathbf{v}_{d,s'}, \quad (4.15)$$

which can be written in matrix-vector form as (see [47])

$$\bar{\mathbf{F}} \cdot \mathbf{V} = \mathbf{G}. \quad (4.16)$$

Note that  $\mathbf{V}$  is a vector in species space thus with a dimension that equals the number of (transport sensitive) species.  $\bar{\mathbf{F}}$  is a matrix that contains the  $f_{s,s'}$  and  $f_s^{eff}$  terms, and  $\mathbf{G}$  is a vector containing the source terms, of which the main contributions come from  $\nabla p$  and  $\mathbf{E}$ . Such an equation can be constructed for all velocity directions independently.

The presence of a magnetic field makes the situation extra complicated. Due to the Lorentz force the direction across is coupled to that around the B field lines. This anisotropy can be addressed by using complex numbers. For this we refer to the work of Kim Peerenboom [82].

### 4.3.5 Ohm's Law: the DC Current Density and Conductivity

In PLASIMO, two versions of Ohm's law have been implemented: the steady state bulk current [10, 45, 47] and the complex impedance version [10, 11]. We will first give a sketch of the steady state bulk version without magnetic field.

Starting from equation (4.5) we can find the dependency of the flux of species  $s$  on the pressure gradient, the electric field and the friction with other particles. Multiplication with the charge  $q_s$  yields the contribution in the current density by the motion of particles  $s$

$$\mathbf{J}_s = q_s \Gamma_s (\nabla p, \mathbf{E}, \mathbf{R}^F). \quad (4.17)$$

The summation over all species gives the bulk current density

$$\mathbf{J}_b = \Sigma \mathbf{J}_s = \sigma \mathbf{E} - \sum_s \mu_s \nabla p_s + \sum_s \mu_s \sum_r f_{sr} v_r, \quad (4.18)$$

where the DC conductivity is defined as  $\sigma_{\text{DC}} = \sum n_s q_s \mu_s$  with  $\mu_s = n_s q_s / f_s^{\text{eff}}$  the mobility of (charged) species  $s$ , a quantity that depending on the charge  $q_s$  can be positive or negative.

This DC treatment of Ohm's law can be found in [47] and [10]. It will not be used in the current study which is based on the *complex* conductivity

### 4.3.6 Ohm's Law: the Complex Current Density and Conductivity

Equation (4.8) provides the velocity of particles for the case time-dependency is not important. This is in many situations a reasonable description, especially for the velocity of heavy particles. However, for electrons under the effect of a microwave field, the time dependent contribution must be considered. The reason is that due to their high mobility, electrons can follow the time dependent E-field, at least partially. In the following the time contribution of a quantity  $\mathbf{F}$  is denoted as  $\tilde{\mathbf{F}}$ .

For many conditions we can, for the electrons, combine equation (4.5) and equation (4.7) into

$$m_e n_e \frac{\partial \tilde{\mathbf{v}}_e}{\partial t} = -\nabla \tilde{p}_e - e n_e \tilde{\mathbf{E}} + \tilde{\mathbf{R}}_e^F. \quad (4.19)$$

From equation (4.7) we get for the friction on the electron motion

$$\tilde{\mathbf{R}}_e^F = -\sum_s m_{e,s} n_e \nu_{e,s} \tilde{\mathbf{v}}_e, \quad (4.20)$$

where the reduced mass can be replaced by the mass of the electron  $m_{e,s} \sim m_e$ , since  $m_s \gg m_e$ . Defining a total momentum transfer frequency as  $\nu_{eh} = \sum_s \nu_{e,s}$ , we can write

$$\tilde{\mathbf{R}}_e^F = -m_e n_e \nu_{eh} \tilde{\mathbf{v}}_e. \quad (4.21)$$

Considering the *cold plasma approximation*, in which  $\tilde{p}_e = 0$  [38], and assuming that  $\tilde{\mathbf{v}}_e$  behaves with the same harmonic time dependency as that of the imposed electric field (i.e.  $\tilde{\mathbf{v}}_e \propto \exp(i\omega t)$ ) we get (see [11, 39, 83])

$$i\omega \tilde{\mathbf{v}}_e + \nu_{eh} \tilde{\mathbf{v}}_e = -\frac{e}{m_e} \tilde{\mathbf{E}}, \quad \text{thus} \quad \tilde{\mathbf{v}}_e = \frac{-e \tilde{\mathbf{E}}}{m_e (\nu_{eh} + i\omega)}, \quad (4.22)$$



where  $\tilde{\mathbf{E}}$  and  $\tilde{\mathbf{v}}_e$  are the harmonic electric field and electron velocity (now represented in phasor notation).

For the time-dependent electron current density we have density, we have

$$\tilde{\mathbf{J}} = q_e \tilde{\Gamma}_e = -en_e \tilde{\mathbf{v}}_e, \quad (4.23)$$

which by substituting equation (4.22) gives

$$\tilde{\mathbf{J}} = \frac{e^2 n_e}{m_e (v_{eh} + i\omega)} \tilde{\mathbf{E}}. \quad (4.24)$$

This can be seen as an expression of Ohm's law  $\tilde{\mathbf{J}} = \hat{\sigma} \tilde{\mathbf{E}}$  with a complex conductivity

$$\hat{\sigma} = \frac{e^2 n_e (v_{eh} - i\omega)}{m_e (v_{eh}^2 + \omega^2)}. \quad (4.25)$$

This relation between the current density and the  $\mathbf{E}$  field was used in the treatment of the Maxwell equations in chapter 3. Note that in that chapter and the following sections, we use  $\mathbf{J}$  and  $\mathbf{E}$  instead of  $\tilde{\mathbf{J}}$  and  $\tilde{\mathbf{E}}$ ; the possible role of the time-dependency can be deduced from the context.

### 4.3.7 The Specific Energy Balances

The first step in deriving the thermal energy balance for species  $s$  is to multiply the BE with  $m_s w^2/2$  and integrate the result over velocity space. After some tedious algebraic transitions we obtain

$$\frac{\partial(n_s \varepsilon_s)}{\partial t} + \nabla \cdot (n_s \varepsilon_s \mathbf{v}_s) + p_s \nabla \cdot \mathbf{v}_s - \tau_s : \nabla \mathbf{v}_s + \nabla \cdot \mathbf{q}_s = Q_s \quad (4.26)$$

where  $\varepsilon_s$  is the thermal energy of species  $s$ ,  $\tau_s : \nabla \mathbf{v}_s$  the viscous dissipation term [45] while  $\mathbf{q}_s$  is the conductive heat flux. Assuming that Fourier's law  $\mathbf{q}_s = -\lambda_s \nabla T_s$  can be applied we can link the conductive heat flux to the temperature gradient by using the thermal conductivity  $\lambda_s$  of species  $s$ .

## 4.4 The Balance Equations for the Plasma Bulk

The specific balance equations for densities, momentum and energy will now be combined to describe the bulk features of the plasmas. In the first step we will sum up all density balances that lead to the continuity equation (CE). The summation of the specific momentum balances will give the Navier-Stokes (NS) equation, the (total) momentum balance equation for the bulk plasma. The combination of CE and NS will give a description of the barycentric plasma velocity in terms of pressure, viscosity, gravity and Lorentz force.

Energetically we will regard the plasma as being composed by electrons and heavy particles. That means that the specific energy balances of all heavy particles have to be summed up while the energy of electrons must be treated independently. For a detailed explanation we refer to [45].

- The continuity equation (for the plasma bulk)

By multiplying equation (4.3) with the mass of species  $s$  and summing for all species, we get the continuity equation for the plasma bulk [10]

$$\frac{\partial \rho_b}{\partial t} + \nabla \cdot (\rho_b \mathbf{v}_b) = 0. \quad (4.27)$$

Here  $\rho_b = \sum_s m_s n_s$  is the total mass density of the plasma bulk. The source terms vanishes in this addition procedure since the creation of one species is compensated by the destruction of another.

- The momentum balance for plasma bulk

The plasma bulk velocity  $\mathbf{v}_b$  is given by the total momentum balance for the bulk plasma [10]

$$\frac{\partial \rho_b \mathbf{v}_b}{\partial t} + \nabla \cdot (\rho_b \mathbf{v}_b \mathbf{v}_b) = -\nabla p + \nabla \cdot \boldsymbol{\tau} + \mathbf{J}_b \times \mathbf{B} + \rho_b \mathbf{g}. \quad (4.28)$$

In this addition the friction terms disappear due to Newton's third law: the friction exerted by species  $s$  on  $s'$  is minus that of  $s'$  on  $s$ . Another aspect is that due to quasi neutrality the electrostatic forces on the bulk will disappear. Thus from the external forces only the gravitation and magnetic force terms remain.

In the above equation  $p$  is the plasma pressure which is assumed to be related to the species densities and temperatures via the equation of state ( $p = \sum_s n_s k_B T_s$ ).

The components of the viscous stress tensor can, assuming a Newtonian fluid, be written as

$$\tau_{ij} = 2\mu\Gamma_{ij} + \mu_2 (\nabla \cdot \mathbf{v}_b) \delta_{ij}, \quad (4.29)$$

where the stress tensor  $\Gamma_{ij}$  is defined as (in Cartesian coordinates)

$$\Gamma_{ij} = \frac{1}{2} \left( \frac{\partial v_{b,i}}{\partial x_j} + \frac{\partial v_{b,j}}{\partial x_i} \right), \quad (4.30)$$

where  $\delta_{ij}$  is the Kronecker delta function.

The dynamic viscosity  $\mu$  is calculated using mixture rules [84] (section 4.7.2).

The second coefficient for viscosity  $\mu_2$  depends on the nature of the gas. For a mono-atomic gas  $\mu_2 = -2/3\mu$  [85].

We would like to remark that equation (4.28) has been obtained with all fluid quantities, e.g.  $p$  and  $\tau$ , defined with respect to the *bulk velocity flow* whereas in equation (4.5) these quantities are defined with respect to the *specific velocity* of the species  $s$  [10, 45]. The transformation of the quantities from one reference system to another is not trivial (cf. [47, chapter 7], [45, chapter 2]).

- The energy balance for the heavy particles

Adding the specific energy balance of the heavy particles gives [10]

$$\begin{aligned} \frac{\partial}{\partial t} \left( \sum_{s \neq e} n_s c_{v,s} T_h \right) + \nabla \cdot \left( \sum_{s \neq e} n_s c_{v,s} T_h \mathbf{v}_b \right) \\ + \sum_{s \neq e} p_s \nabla \cdot \mathbf{v}_b + \nabla \cdot \mathbf{q}_h = \tau : \nabla \mathbf{v}_b + Q_{eh}^{elas} + Q_{h^*h}^{inel}. \end{aligned} \quad (4.31)$$

Here  $T_h$  is the heavy particle temperature. The specific heat capacity  $c_{v,s}$  at constant volume for species  $s$  is defined such that  $c_{v,s} T_s = \epsilon_s$ , with  $\epsilon_s$  the mean kinetic energy of heavy particle species  $s$ .

The heavy particle heat flux is defined as  $\mathbf{q}_h = -\lambda_h \nabla T_h$  with the heavy particle thermal conductivity,  $\lambda_h$ , obtained from mixture rules [84] (section 4.7.2).  $Q_{eh}^{elas}$  denotes the energy gain or loss through elastic collisions with electrons (see section 5.5)

$$Q_{eh}^{elas} = \sum_{s \neq e} \frac{3}{2} n_e v_{es} \left( \frac{2m_e}{m_s} \right) k_B (T_e - T_h), \quad (4.32)$$

whereas  $Q_{h^*h}^{inel}$  refers to the energy gain or loss through inelastic collisions [10] in which internal energy is converted into heat.

The Newtonian viscous dissipation is given in [10] by

$$\tau : \nabla \mathbf{v}_b = 2\mu \sum_{ij} \Gamma_{ij} \Gamma_{ij} + \mu_2 (\nabla \cdot \mathbf{v}_b)^2. \quad (4.33)$$

- The energy balance for electrons reads

$$\begin{aligned} \frac{\partial}{\partial t} (n_e c_{e,v} T_e) + \nabla \cdot (n_e c_{e,v} T_e \mathbf{v}_b) \\ + p_e \nabla \cdot \mathbf{v}_b + \nabla \cdot \mathbf{q}_e = Q_{\text{Ohm}} - Q_{eh}^{\text{elas}} - Q_{eh}^{\text{inel}} - Q_{\text{rad}}. \end{aligned} \quad (4.34)$$

The conductive heat flux is defined as  $\mathbf{q}_e = -\lambda_e \nabla(T_e)$ , with the electron thermal conductivity,  $\lambda_e$ , obtained from mixture rules [84] (section 4.7.2).

The  $Q_{eh}^{\text{inel}}$  refers to the energy gain or loss through inelastic collisions which yields

$$Q_{eh}^{\text{inel}} = \sum_l R_l \Delta \varepsilon_l, \quad (4.35)$$

with  $R_l$  the rate of collision (chapter 5) and  $\Delta \varepsilon_l$  the average energy exchanged per collision  $l$ .

The energy related to the generation of radiation can be neglected for the plasmas under study in this thesis. Moreover, it can be shown that in under many conditions the terms at the left hand side of equation (4.34) are of less importance [33]. This implies that in good approximation equation (4.34) transforms into a balance between Ohmic heating as energy gain and the addition of elastic and inelastic interactions as loss term. This lead to the so-called *Local Power Balance* equation [12]

$$Q_{\text{Ohm}} = Q_{eh}^{\text{elas}} + Q_{eh}^{\text{inel}}. \quad (4.36)$$

Since all terms scale with the electron density, it is useful to introduce the quantity  $\theta = Q_{\text{Ohm}}/n_e$  the power needed to sustain an electron-ion pair. This quantity is an important parameter in microwave plasmas, especially in the surfatron [86], also see chapters 7, 8, 9, and 10 of this thesis.

Neglecting the transport terms in the energy balance is comparable to what is done with the density balance for the local chemistry species (cf. chapter 5).

In the modelling of MIPs, the time-averaged power density absorbed in the domain  $Q_{\text{Ohm}}$  ( $\text{W}/\text{m}^{-3}$ ) is computed as

$$Q_{\text{Ohm}} = \frac{1}{2} \text{Re}(\mathbf{J}^* \mathbf{E}) = \frac{1}{2} \text{Re}(\hat{\sigma}) |\mathbf{E}|^2, \quad (4.37)$$

where equation (4.24) is used to relate the current density  $\mathbf{J}$  to the harmonic electric field

$$\mathbf{J} = \hat{\sigma} \mathbf{E}. \quad (4.38)$$

## 4.5 Overview

In this section we will present an overview of the route from ‘micro’ to ‘macro’ as presented in previous sections; this will be illustrated by table 4.1.

The first column deals with the individual particle description; i.e. the domain of PIC/MC methods. The second deals with the species that are specified by the distribution function  $f_s(r, v, t)$ ; the evolution of  $f_s$  is described by the Boltzmann equation (BE). This differential equation can be solved in principle to yield the EEDF, if the EM-fields are known.

In the integral approach, the methods of moments, we multiply the BE with 1,  $m_s v$ , and  $\frac{1}{2} m_s v^2$  and integrate the results over velocity spaces. This gives the specific balances of (mass) density, momentum and energy; thus 3 balances for each species. This is only done for the *relevant* species for which the transport is of importance. For these TS-species we can, in most cases, simplify the momentum equations to the drift-diffusion-convection (DDC) equation. A special role is played by the momentum balance of the electrons  $\{e\}$  which leads to time dependent Ohm’s law and the complex conductivity. The penultimate column gives the  $2T$  Bulk structure; the addition of the specific balances of mass and momentum leads to the continuity equation (CE) (equation (4.27)) and the Navier-Stokes (NS) equation (equation (4.28)). The combined solution of CE and NS gives the velocity field.

In the energy domain we retain the specific energy equation of the electrons  $\{e\}$  while the energy balances of all the other particles the heavies  $\{h\}$  are summed up. In LTE, the last column, we have to describe *elemental* transport, to combine that with the CE and NS and total energy balance, that of  $\{e\}$  and  $\{h\}$  combined. There is only one temperature.

## 4.6 Local Thermal Equilibrium

The equations derived above give enough tools to simulate the transport in MIP plasmas: plasmas that are in non-LTE and ruled by two temperatures. Although it is beyond the topic of this thesis we will shortly sketch the equations that are needed in case of LTE (local thermal equilibrium). The corresponding equations are also present in the PLASIMO toolbox and developed in the studies of Van der Heijden [7], Hartgers [47] and Beks [49] devoted to the simulations of HID lamps.

A key quantity to describe LTE plasmas is *elemental concentration* that will be introduced here by taking the example of a water plasma. The hydrogen nucleus (in fact the protons) in such a plasma can be carried as part of the H atoms, excited hydrogen

Particles	Species		Multi fluid for TS	Bulk 2T	LTE	
PIC, MC	$f_s(r, v, t)$ BE ↘	↗ EEDF ↘	$\int BE dw$	$\sum_s \rightarrow \text{CE}$	elements CE	
			$\int BE mwdw$	$\{h\}: \sigma_{DC}$ DDC $\{e\} \hat{\sigma}$ Ohm's	$\sum_s \rightarrow \text{NS}$	NS
			$\int BE \frac{1}{2}mw^2dw$	$\{h\}, \{e\}$	$\sum \text{all } \{s\}$	

Table 4.1: Overview of the route from micro to macro as presented in this chapter. Here, PIC stands for Particle in Cell, MC for Monte Carlo, BE for Boltzmann Equation, EEDF for Electron Energy Distribution Function, TS for Transport Sensitive, DDC for Drift-Diffusion-Convection. The  $\sigma_{DC}$  is the DC conductivity defined in equation (4.18) and  $\hat{\sigma}$  is the complex permittivity (equation (4.25)).

atoms  $H^*$  or as part of  $OH/OH^-$  radicals,  $H_2O$  molecules etc. In the latter case the displacements of one  $H_2O$  molecule implies the movement of two protons. It is therefore useful to define the elemental density of hydrogen as

$$n_{\{H\}} = n_H + n_{H^*} + n_{OH} + n_{OH^-} + 2n_{H_2O} + 2n_{H_2} + 3n_{H_3} + \dots \quad (4.39)$$

Note the difference between the notation  $n_{\{H\}}$  and  $n_H$ . The former represents the elemental density of H, i.e. the presence of H nuclei per volume irrespective their state of binding or excitation whereas  $n_H$  refers to the concentration of unbound atomic H in the ground state. Equation (4.39) thus shows that the density of a particular element is given by the density of the species multiplied with the number of nuclei of the element in that species. In general, the density of an element is given by:

$$n_\alpha = \sum_i R_{i,\alpha} n_i, \quad (4.40)$$

with  $R_{i,\alpha}$  the stoichiometric coefficient that gives the number of elements  $\alpha$  in species  $i$ . The index runs over all species in the plasma. If a species  $j$  does not contain a nucleus of  $\alpha$  it is simply  $R_{j,\alpha} = 0$ . In a comparable way we define the elemental fluxes

$$\Gamma_\alpha = \sum_i R_{i,\alpha} n_i \mathbf{v}_i, \quad (4.41)$$

with  $n_i$  and  $\mathbf{v}_i$  the density and velocity of compound (species)  $i$ . Since elements are neither created nor destroyed, the continuity equation for elements is source-less and

reads:

$$\frac{\partial n_\alpha}{\partial t} + \nabla \cdot \Gamma_\alpha = 0, \quad (4.42)$$

an equation that is similar to the continuity equation (CE). This elemental conservation equation looks very simple but one should realise that due to equation 4.41 the transport of the element depends in a complicated way on that of the species. To get a complete description of LTE transport this equation has to be combined with the NS, the CE and the energy balance. The latter is in steady state given by

$$\nabla \cdot (c_p \mathbf{v}_b T) - \nabla \cdot (\lambda_c \nabla T) = P + Q_{rad}, \quad (4.43)$$

where  $P$  refers to Ohmic heating and  $Q_{rad}$  to the power density associated to net absorption. Note that there is only one temperature. The combination of CE, NS and equation (4.41) and (4.42) can be solved. Driven by the temperature-gradient, diffusion, convection and radiation we get for every element a spatial distribution. From the elemental concentration thus obtained one can determine the local densities of species using the equilibrium distribution laws like those of Boltzmann, Saha and Guldberg Waage. Concluding we may state that:

- the elements can be seen as a structure layer in between the species and the bulk,
- a conservation law holds for any element independently,
- the presence of LTE does not imply the absence of transport and
- LTE transport is not trivial at all.

## 4.7 The Canonical Transport Equation: The $\phi$ -equation

All the transport equations given above originate from the integration of a product of the BE over the velocity space. It is therefore not surprising that the main structure of the Boltzmann equation

$$\text{Accumulation} + \text{Transport} = \text{Production}. \quad (4.44)$$

is reflected in the transport equations. Indeed we can cast all transport equations in the following general form, known as the canonical transport equation [7] or  $\phi$ -equation,

$$\frac{\partial \phi}{\partial t} + \nabla \cdot \Gamma_\phi = S_\phi, \quad (4.45)$$

with the generalised flux density

$$\Gamma_\phi = f_\phi \rho \mathbf{v}_b \phi - \lambda_\phi \nabla \phi,$$

having two contributions denoted by convection and diffusion.

The role of  $\phi$  can be played by a density, momentum or energy. Hereafter, these will be denoted *transportables*. The  $f_\phi$  is an adjustment parameter whereas the factor  $\lambda_\phi$  stands for the generalised diffusion coefficient. At the right hand side of (4.45) we find the source term  $S_\phi$ .

The equations (4.3), (4.27),(4.28), (4.31) and (4.34) are modified [10] to fit the  $\phi$  – equation and the coefficients are given in table 4.2. The term  $\nabla \cdot (\mu \nabla v_{b,i})$  is required to write the momentum equation as equation (4.45) whereas  $K_i$  is a correction term related to tensor operations in ortho-curvilinear coordinates (see [10]).

$\frac{\partial \phi}{\partial t} + \nabla \cdot (f_\phi \rho \mathbf{v}_b \phi) - \nabla \cdot (\lambda_\phi \nabla \phi) = S_\phi$				
$\phi$	$f_\phi$	$\lambda_\phi$	$S_\phi$	Eq.
$n_s$	$1/\rho_b$	$D_s$	$S_s$	(4.3)
1	1	0	0	(4.27)
$v_{b,i}$	1	$\mu$	$-(\nabla p)_i + \nabla \cdot \tau - \nabla \cdot (\mu \nabla v_{b,i}) - K_i$	4.28
$T_h$	$\sum_s (c_{v,s} + 1) k_b n_s / \rho$	$\lambda_h$	$\mathbf{v}_b \cdot \nabla (\sum_x p_x) + \tau_h : \nabla \mathbf{v}_b + Q_{eh}^{elas} + Q_{h^*h}^{inel}$	(4.31)
$T_e$	$(3/2 + 1) k_b n_e / \rho$	$\lambda_e$	$\mathbf{v}_b \cdot \nabla p_e + Q_{ohm} - Q_{eh}^{elas} - Q_{eh}^{inel} - Q_{rad}$	(4.34)

Table 4.2: Expression for  $\phi$ , factors  $f_\phi$ ,  $\lambda_\phi$  and source  $S_\phi$  for equations (4.3), (4.27),(4.28), (4.31) and (4.34). The index  $s$  refers to the kind of species, and  $i$  to the direction for the velocity vector.

The corresponding transport coefficients and sources term are given in sections 4.7.2 and 4.8.

### 4.7.1 Discretisation

To solve the  $\phi$ -equations we use a Control Volume (CV) method [10, 45]. In this method, the computational domain is divided into control-volumes.

Figure 4.1 gives an example of a CV showing that the field variables  $\phi$  and the source terms  $S_\phi$  are defined at the centres of the CV's, whereas the transport fluxes  $\Gamma_\phi$  are defined at the (centres of) the CV faces. The discrete version of the  $\phi$  -equations is obtained by integrating the equations over a control volume. The most important



feature of the CV-method is that it facilitates an integral approach that guarantees the *exact* integral conservation of mass, momentum and energy over any group of CV's.

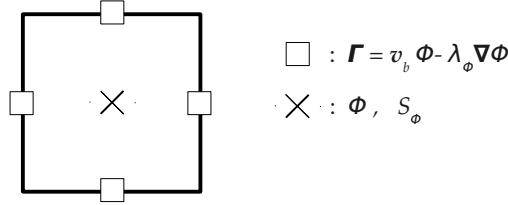


Figure 4.1: Control Volume (Grid Cell). The field variables  $\phi$  and the source terms  $S_\phi$  are defined at the centre of the CV, the transport fluxes are defined at (the centre of) the faces of the CV. This guarantees the *exact* integral conservation of mass, momentum and energy equations over any group of CV's.

## 4.7.2 Transport Coefficients

The transport coefficients (for diffusion, thermal conductivity, viscosity, etc.) include the effect of elastic particle interactions into the transport equations. They are based on the molecular theory of gases and fluids [84]. We distinguish between transport coefficients for electrons and heavy particles.

### Heavy Particles

The *effective diffusion coefficient* is obtained [10] as

$$D_i = \left( \sum_{j \neq i} (p_i / p) / D_{ij} \right)^{-1}, \quad (4.46)$$

where  $p_i = n_i k_B T_i$  is the partial pressure and  $D_{ij}$  the binary diffusion coefficient is defined in first approximation as

$$D_{ij} = \frac{3}{16} \frac{f_{ij} k_B^2 T_i T_j}{p m_{ij} \Omega_{ij}^{(1,1)}(T_{ij})}. \quad (4.47)$$

Here,  $m_{ij} = m_i m_j / (m_i + m_j)$  is the reduced mass of the  $(i, j)$  system,  $T_{ij} = (m_i T_i + m_j T_j) / (m_i + m_j)$  the corresponding effective temperature,  $f_{ij}$  a correction factor and  $\Omega_{ij}^{(1,1)}$  the first approximation of the collision integral equation (4.54) as given in [84].

The *viscosity* and the *heavy thermal conductivity* are obtained from the Chapman-Enskog-Burnett theory as explained in [84]. This involves the collision integrals  $\Omega_{ij}^{(l,s)}$  with  $l, s = 1, 2$  (see equation (4.54)).

## Electrons

The electron thermal conductivity is obtained from the Frost mixture rules [77, 87], which takes into account the electron-electron, electron-ions and electron-atoms interactions. The direct current conductivity is also computed using the Frost mixture rules. For microwave induced plasmas, the conductivity is given by equation (4.25).

## 4.8 Particle Interactions: Cross sections and Relations

The particle interactions in a plasma can be divided in *elastic* and *inelastic* collisions. In this section we give insight in how we deal with the particle interactions in PLASIMO.

### 4.8.1 Elastic Interactions

The elastic interactions are described via the cross-sections

- *Differential Cross Section*

For a beam of  $N_e$  electrons,  $N_e \sigma_{e,diff}(E, \theta)$  electrons per  $m^2$  strike a target of  $N_t$  molecules in a volume.

The number of electrons  $dN_s$  which are scattered elastically per second at angle  $\theta$  into the solid angle  $d\Omega$  is [88] defined by

$$dN_s = \sigma_{e,diff}(E, \theta) N_e N_t d\Omega, \quad (4.48)$$

where  $\sigma_{e,diff}(E, \theta)$  is the differential cross section. The energy of each electron equals  $E$ .

- *Total Elastic Scattering and Momentum Transfer Cross Section*

The total elastic scattering cross section is defined as

$$\sigma_{e,t}(E) = \int_0^{2\pi} \int_0^\pi \sigma_{e,diff}(E, \theta) \sin \theta d\theta d\phi, \quad (4.49)$$

while the momentum transfer cross section is defined as

$$\sigma_m(E) = \int_0^{2\pi} \int_0^\pi \sigma_{e,diff}(E, \theta) (1 - \cos \theta) \sin \theta d\theta d\phi. \quad (4.50)$$

The factor  $(1 - \cos \theta)$  represents the weight factor that gives more importance to large angle scattering. This is needed as the transfer of scattering with large  $\theta$  values contributes more to the momentum transfer than small  $\theta$  collisions. This becomes more clear when we write equation (4.50) as

$$\sigma_m(E) = \sigma_{e,t}(E) - \int_0^{2\pi} \int_0^\pi \sigma_{e,diff}(E, \theta) \cos \theta \sin \theta d\theta d\phi, \quad (4.51)$$

which shows that in the case for which the differential elastic cross section is  $\theta$  independent, the second term vanished so that the total elastic cross-section and the momentum transfer cross section are equal i.e.

$$\sigma_m(E) = \sigma_{e,t}(E), \text{ if } \sigma_{e,diff}(E, \theta) = \sigma_{e,diff}(E). \quad (4.52)$$

The elastic and momentum transfer cross sections are the basis for the definition of other quantities such as the *average elastic cross section* and the *collision integral* which are the basis of the definition of transport coefficients such as the collision frequency for momentum transfer, diffusion coefficients, thermal conductivities, mobilities, etc.

- *Average Elastic Cross Section*

The *average momentum transfer cross-section*,  $Q_m$ , in  $[\text{m}^2]$  is defined as

$$\sigma_m^{av}(T) = \frac{\langle \sigma_m(E)v(E) \rangle}{v^{th}}, \quad (4.53)$$

with  $\langle \sigma_m(E)v(E) \rangle$ , obtained as average values for a distribution  $f(E; T)$ . For a Maxwellian distribution the thermal velocity is given by  $v^{th} = \sqrt{8k_B T / (\pi m)}$ .

- *Elastic Collision Integrals*

The elastic collision integrals are defined as

$$\Omega_{ij}^{(l,s)}(T) = \sqrt{\frac{k_B T}{2\pi m_{ij}}} \int_0^\infty e^{-\gamma^2} \gamma^{2s+3} Q^{(l)}(g) d\gamma, \quad (4.54)$$

where  $g = v\sqrt{\mu/2kT}$  is the initial relative speed in the binary encounter,  $\gamma = \sqrt{m_{ij}/2k_B T}g$  the reduce relative speed while  $Q^l$  is defined as

$$Q^{(l)}(g) = 2\pi \int_0^\infty (1 - \cos^l \chi) b db \quad (4.55)$$

where  $b$  is the impact factor and  $\chi$  the scattering angle.

The scattering angle depends on  $b$  and the interaction potential. By default, Coulomb is used for charge-charge particle interaction, Langevin for charge-neutral interaction, whereas a hard-sphere is used for neutral-neutral interactions [8].

### 4.8.2 Inelastic Interactions

The source term  $S_h$  in equations (4.3), (4.34) and (4.31) depends on the stoichiometric coefficients, the species densities and rate coefficients as explained in chapter 5.

The rate coefficients can be provided as formulas or in the form of lookup tables, obtained from distribution function and inelastic cross-section data. An example for argon chemistry is given in chapter 7.

## 4.9 Assumptions

The assumptions used for deriving the equation for the multi-fluid description of the plasma under study are the following:

- *Quasi-neutrality*

The quasi-neutral character of a plasma is dominant for plasma length scales that are much larger than the Debye length, which is given by

$$\lambda_D = \sqrt{\frac{\epsilon_0 k_B T_e}{n_e q_e^2}}. \quad (4.56)$$

Typical values found in this thesis are  $10^{-5} - 10^{-6}$  m, whereas the plasma length scales (radius) are in the order of  $10^{-3}$  m.

Using the quasi-neutral character of the plasma it is possible to obtain the electron density as  $n_e = e^{-1} \sum_{s \neq \{e\}} q_s n_s$ , with  $q_s$  the charge of species  $s$  and  $e$  the elementary charge. This implies that there is no need to construct a balance equation for the electron density.

- *Steady State*

PLASIMO can handle both steady state and transient problems. However, this work only deals with quasi steady state, which means that we assume time scales larger than the inverse of the plasma frequency.

For a microwave induce plasma model, it is important to know if the electron energy distribution function (EEDF) behaves stationary or not. When  $\omega/\nu_e \gg 1$  with  $\nu_e = (2m_e/m_i \nu_{ih})$ , the energy transfer from electrons to heavy particles does not change much during one cycle of the field oscillation so that the EEDF remains stationary [45]. Typical values found in this thesis are  $\omega/\nu_e = 10^5 - 10^3$ .

- *Non-turbulence*

We assume that turbulence is absent in the plasmas under study. Therefore, low Reynolds number are required. The Reynolds number is defined as

$$\text{Re} = \rho_b D v_b / \mu, \quad (4.57)$$

where  $\rho_b$  is the total mass density of the plasma bulk,  $D$  the tube diameter,  $v_b$  the (maximum) flow velocity of the plasma bulk and  $\mu$  dynamic viscosity [ $\text{kg m}^{-1} \text{s}^{-1}$ ]. Typical values found for the plasmas in this thesis are  $\text{Re} = 0.004 - 10$ , whereas turbulence can be expected for Re-values above 2000.

A two equation  $k$ - $\epsilon$  turbulence model is currently under development by Niels Lammers.

- *Equation of State*

The equation of state is given by Dalton's law of partial pressures and the ideal gas law

$$p = \sum_s p_s \quad \text{with } p_s = n_s k_B T_s, \quad (4.58)$$

with  $p_s$  the partial pressure of species  $s$ . In the current work, this equation is used to compute the density of one species instead of using equation (4.3).

- *Newtonian Fluid*

In a Newtonian fluid a linear relation is found between the applied stress and the *deformation* generated by the applied stress on the fluid. The viscosity is the constant of proportionality in this linear relation (equation (4.29)).

- *Two Temperature Description*

When the electron energy distribution function (EEDF) is a Maxwellian Distribution, the electron temperature can be defined as

$$\varepsilon_e = c_{v,e} T_e = \frac{3}{2} k_B T_e, \quad (4.59)$$

where  $\varepsilon_e$  is the mean electron energy.

We assume that most of the electrons follow the Maxwellian distribution. However, the tail of the distribution can be depleted due to excitation processes in conditions of low degree of ionisation (see chapter 9).

With respect to the heavy particles, it is assumed that the exchange of kinetic energy between heavy particles is in equilibrium and that therefore a single heavy particle temperature  $T_h$  can be defined as

$$T_h = T_s, \quad (4.60)$$

for every species  $s \neq \{e\}$ .

- *Radiation*

We will deal with reactive plasmas for which the generation and transport of radiation can be neglected. For information on the PLASIMO activities related to the generation and transport of radiation we refer to the work of H. W. P. van der Heijden [7] and M. L. Beks [49].

## 4.10 Summary

This chapter gives an overview of the tools provided by PLASIMO to simulate the transport as carried by particles. Most attention is paid to the transport phenomena present in the Microwave Induced Plasmas (MIPs) under studies. With respect to transport, these MIPs belong to the group of two-temperature, quasi-neutral, non-LTE, laminar-flow driven plasmas.

In general plasma transport can be studied on five different structure-levels; the domain of individual particles, the distribution functions, the species, elements and the bulk. To explore the domain of the particles (Particle-In-Cell) Monte Carlo methods can be applied. To compute distribution functions one needs a Boltzmann solver. Both methods are present and under improvement in the PLASIMO framework but they are not used to study the transport in MIPs.

In this chapter we assume that for the plasmas under study the velocity distribution functions are Maxwellian so that there is no need to solve the Boltzmann equation (BE). By applying the method of moments to the BE the various fluid equations can be obtained. These are applied to the structure-level of the species, and the bulk. The transportables in the multi-fluid approach are the (mass) densities, momentum-components, and energies.

It is shown how the common features of these equations can be deduced from their common origin: the BE. It is also shown how these similarities lead to the canonical transport equation, the  $\phi$ -equation: one of the key-stones of the modularity of the object oriented architecture of PLASIMO.

Since transport is driven by sources and facilitated by transport-coefficients these have to be programmed as well. It is shown how they, originating on the particle level, depend on elementary interactions that can be divided into elastic and inelastic collisions. The former shapes the transport coefficients, the latter the sources.



---

5

Chemistry

---



**Abstract.** A model is constructed that aims to give insight in possible routes to simplify the Chemistry of complex chemistry plasmas. The core of the method is a time dependent model that can be employed to trace the Principal Density Reservoirs (PDR) of the chemical mixture and the Effective Conversion Coefficients (ECC) between these PDRs. The collection of PDRs with the corresponding ECCs forms the basis of a reduced chemistry description of two-dimensional simulations of complex chemistry plasmas. A case study of a pulsed argon plasma is presented to show the capabilities of the model.

## 5.1 Introduction

Plasma aspects can be divided into three main blocks: *Configuration*, *Transport* and *Chemistry*. Configuration deals with the impact of the environment on the plasma, and thus, among others, with the shape and sizes of the plasma (vessel), the boundary conditions and the energy coupling. Transport describes the transport of species, momentum and energy *within* the plasmas. It is driven by sources and facilitated by transport coefficients. Chemistry, the topic of this chapter, primarily deals with the creation and destruction of plasma species. However, chemistry also has an important impact on the sources and coefficients that drive and facilitate transport. Moreover, by controlling the composition and thus the electrical conductivity, Chemistry will also play a crucial role in the energy coupling mechanism.

Due to the plasma action, a myriad of species is created, and an important issue is how this wide variety has to be tackled. The central question is how many active species have to be taken into account to get a proper description of the plasma chemistry and the plasma features determined by plasma chemistry.

In chapters 8, 9 and 10, we will construct Grand models based on a simplified argon chemistry. Five species namely Ar (in the ground state), Ar(4s), Ar(4p), Ar<sub>2</sub><sup>+</sup> and Ar<sup>+</sup> will be considered. The sum of the species densities is very close to the elemental (i.e. the total) density of Argon. Thus, describing the transport of these five Ar species gives a very good description of the transport of mass. Since the convergence of the Grand models takes much time, it is tempting to reduce the chemistry further by dropping the species Ar(4s) and Ar(4p); this seems to be justified since their contribution to the mass density is negligible; the Principal Density Reservoirs (PDR) of the chemical composition are the atoms and ions in the ground level.

However, the excited species play an essential role in the conversion from Ar to Ar<sup>+</sup> (ionisation) and vice versa (recombination). Thus, if Ar(4s) and Ar(4p) are removed this will drastically change the plasma with respect to the ionisation degree, charge distribution and thus EM properties. Removing excited species is only allowed if we restore the effective conversion coefficients (ECC) between principal density reservoirs (PDRs) in some way or another.

Important questions in the use of plasma chemistry in Grand modelling are:

- (a) what is the minimum set of relevant species that has to be taken into account in order to get a good description of the distribution of the mass over the species?
- (b) can simple expressions be found for the effective conversions between these selected relevant species so that minority species can be removed without affecting the electromagnetic features of plasmas?

- (c) can we construct models that describe the essential chemistry-induced features of the plasma; models that are flexible and zero-dimensional in which chemistry is isolated from the other main plasma aspects configuration and transport.

To deal with these questions, various types of models are described in literature. Here they are classified into three types denoted by Collision Radiative Models (CRM), Reaction Exploration Models (REM) and Global Plasma Models (GPM). The PLASIMO team has experience with all these types of models.

*Collisional Radiative Models (CRM):*

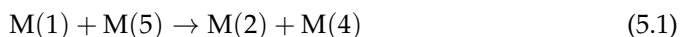
These models, initiated by the classical paper of Bates *et al.* [89], find their origin in *astrophysics and plasma spectroscopy*. They are (mostly) based on a linear decomposition of the atomic state distribution function (ASDF) in two components; one attached to the ground state of the atom the other to that of the ion cf. [90–94].

The two ground states are the PDRs. By means of electron collisions and radiative transitions, the densities of these two PDRs are distributed over the excited levels. Electrons and photons can be seen as *external* agents that rule the (de)excitation and ionisation/recombination. Working with external agents makes these CRMs *linear*. It is possible to divide an atomic system in more than two PDRs. This was done by Jan van Dijk *et al.* in [94] in order to treat the generation and transport of resonance radiation in low pressure Hg lamps.

*Reaction Exploration Models (REM):*

These model-types, developed in the field of *plasma chemistry*, are mainly based on the interest in (plasma) reaction kinetics especially for molecular plasmas. Several of these models are available now; for instance we refer to ZDPlaskin [95] and the commercial software Quantemol-P [96].

The population of species in molecular plasmas is not only ruled by electrons and photons but also by heavy particle collisions. As an example we take the collision



between two molecules in vibrational state  $v = 1$  and  $v = 5$  creating the couples in  $v = 2$  and  $v = 4$ . The densities of none of these species can be neglected. This means that the model has to deal with several species “on an equal footing”. In contrast with atomic CRMs, these molecular methods are non-linear and deal with many species of comparable importance.

The PLASIMO team also has expertise in this field. In [11], a model named Pyrate was presented, which aims to give insight into the oxygen chemistry for plasmas with a given elemental oxygen concentration, electron density and electron temperature. The underlying method was based on the tele-projective numerical technique to integrate

a stiff set of equations *in time*. From the time behaviour of the density, a hierarchy between the species can be established; the PDRs can be spotted. By analysing the various reaction paths, it is in principle possible to get the effective conversion routes between PDRs.

In this chapter we will proceed on this route. Two important steps forward are taken to construct a better and more versatile model named *RateLab*:

- (a) The equations that determine the electron density and temperature are incorporated in the model.
- (b) Time dependence of the power feeding the plasma is taken into account.

This will be described in the section 5.5.

*Global Plasma Models (GPM):*

The GPMs are popular in the field of *plasma engineering*, and made to fulfil the dream of the plasma operator to have quasi-analytical expressions that predict the mean values of internal plasma properties, such as  $n_e$  and  $T_e$ , as functions of the external plasma control parameters (the knobs) like pressure, filling-composition and plasma size. Several GPMs can be found in literature [97–99].

For the GPMs developed in the PLASIMO team, we refer to [54, 100] where a GPM is described for Ar plasmas based on the balances for the electron density and energy and on the energy equation of heavy particles. However, in order to make the model lean and flexible the chemistry had to be simplified. Only the ground states of the Ar atom and ion were taken into account. The effective conversion between these two PDRs is computed using the results of a CRM of argon. So, it looks as if a GPM can not operate as a stand-alone model. Before it can be applied, it requires some preprocessing based on a CRM.

It is the aim of the study reported in this chapter to come to a combination of the model types presented above and to construct a versatile model that can generate the combined results of a CRM, REM and a GPM. So, just as in the case of the GPMs, the input are the plasma control parameters, the result will be the mean value of the principal plasma parameters (GPM), and the ASDF components (CRM); while it will be capable to handle strongly non-linear chemistry (REM). The method will be the same as that used in REMs, so that time-dependence will come as an extra bonus.

This chapter is organised as follows. In section 5.2 we start with an introductory description of the competition between chemistry and the joined action of transport and configuration. Section 5.3 presents a general structure of the system of coupled density equations. Two approaches are described one in the species-density domain the other in the domain of reactions rates. This is followed by section 5.5 that describes

an extension of the model by including the balance equation for the electron density and energy. Section 5.6 provides an introduction to global models and their role in plasma classification. It anticipates on the classification of surface wave discharges (SWDs) as a function of pressure given in chapter 7. Finally, section 5.9 gives a description of the system of equations and the user interface of RateLab, our model under construction. As an example of the capability of the model, in section 5.9 RateLab will be applied in a time-dependent model, showing the responses of different argon atom levels to a pulsed power input.

## 5.2 Chemistry versus Transport and Configuration

The interplay between configuration, transport and chemistry is manifest in the particle balance. For species  $s$  this reads (see chapter 4)

$$\frac{\partial n_s}{\partial t} + \nabla \cdot (n_s \mathbf{v}_s) = \mathcal{S}_s \quad (5.2)$$

where we find at the left hand side transport and configuration aspects while the right hand side deals with the chemical source that can be written as

$$\mathcal{S}_s = \mathcal{P}_s - \mathcal{D}_s n_s \quad (5.3)$$

Thus the source term consists of a production  $\mathcal{P}_s$  and destruction  $\mathcal{D}_s n_s$  term; both given in  $\text{m}^{-3}\text{s}^{-1}$ . The factor  $\mathcal{D}_s$  (in  $\text{s}^{-1}$ ), known as the destruction frequency, plays an important role in the classification of species, as we will see.

To study the combined effect of transport and configuration we introduce the transport frequency defined as

$$\mathcal{T}_s = n_s^{-1} \nabla \cdot (n_s \mathbf{v}_s). \quad (5.4)$$

In our plasmas the transport is mainly diffusive so that the transport frequency can be written as  $\mathcal{T}_s = D/\Lambda^2$  [12] where  $\Lambda$ , the characteristic diffusion length, is a *configuration* aspect determined by the plasma size mainly. The intrinsic *transport* strength enters the balance via the diffusion coefficient,  $D$ .

For (excited) neutral species we have  $D_s = \frac{1}{3} \lambda v_{\text{th}}$  which, after inserting for the mean free path  $\lambda = 1/(\sigma N \sqrt{2})$  and thermal velocity  $v_{\text{th}} = \sqrt{8k_B T_h / (\pi M)}$  gives

$$D_s = \frac{1}{3} \lambda v_{\text{th}} = \frac{2}{3N\sigma} \sqrt{\frac{k_B T_h}{\pi M}} \quad (5.5)$$

where  $N$  is the density of the buffer gas,  $\sigma$  the collision cross section for elastic interaction, and  $M$  the mass of the (excited) state.

For *charged* particles we have to consider the combination of diffusion and drift. For the plasmas under study, this leads to ambipolar diffusion, which implies that the diffusion of ions is enhanced by the factor  $D_a = D_s(1 + T_e/T_h)$ .

There is not much variation in the transport frequency  $\mathcal{T}_s$ . For excited states it will vary from about 100 Hz for the high pressure (conditions found in chapter 8) to 1000 Hz for low pressure conditions (chapter 9). For the ions the ambipolar effect can give an augmentation ranging from 6, in the high pressure case, to 30, for the low pressure surfatron.

After this short analysis of the joined action of configuration and transport, we will now deal with the chemistry by studying the destruction frequency  $\mathcal{D}_s$ . In contrast to the transport frequency the destruction frequency has much more variation [75]. If  $s$  represents an excited atom or molecule,  $\mathcal{D}_s$  can easily be in the order of  $10^7$  Hz, whereas for the ion or atom ground states, the destruction rates will, for the plasmas under study, be in the order of the transport frequencies and thus somewhere between  $10^2 - 10^3$  Hz.

It is obvious that for the first category, i.e. excited atoms or molecules, transport is much less important than the local chemistry. To study this more in detail we solve

$$\frac{\partial n_s}{\partial t} + \mathcal{T}_s n_s = \mathcal{P}_s - \mathcal{D}_s n_s, \quad (5.6)$$

which is obtained by substituting  $\mathcal{T}_s$  into the combination of equations (5.2) and (5.3). Assuming that  $\mathcal{P}_s$ ,  $\mathcal{D}_s$  and  $\mathcal{T}_s$  are constant in time, we get the following result

$$n_s(t) = n_s(0) \exp [-(\mathcal{D}_s + \mathcal{T}_s)t] + [\mathcal{P}_s / (\mathcal{D}_s + \mathcal{T}_s)] \{1 - \exp [-(\mathcal{D}_s + \mathcal{T}_s)t]\} \quad (5.7)$$

where  $n_s(0)$  is some initial value. This equation shows that  $n_s(t)$  converges during  $(\mathcal{D}_s + \mathcal{T}_s)^{-1}$  to  $\mathcal{P}_s / (\mathcal{D}_s + \mathcal{T}_s)$ .

In case  $\mathcal{D}_s \gg \mathcal{T}_s$  we find that  $n_s(t)$  evolves in the timescale  $\mathcal{D}_s$  to

$$n_s = \mathcal{P}_s / \mathcal{D}_s. \quad (5.8)$$

Species for which this is applicable are named *Local Chemistry* (LC) species. Due to the large value of  $\mathcal{D}_s$  it is not likely that they get high densities. Their density is mainly determined by processes originating from species with lower  $\mathcal{D}_s$ - values, the so-called principal density reservoirs (PDRs) or transport sensitive (TS) species. As a result  $\mathcal{P}_s / \mathcal{D}_s$  will vary in a timescale that is much larger than  $\mathcal{D}_s^{-1}$ . This technique of distinguishing between LS and TS species is comparable to the QSSS procedure described by Bates *et al.* [89].

A method to get insight into the hierarchy of the various chemical species is to bring the plasma chemistry out of equilibrium and to analyse the time-responses. Prompt

responding species are LCs. An example of this method was given in [11] and will be presented in the case study given in section 5.9.

Note that the solution of equation (5.6) given in equation (5.7) is not exact; it only intends to give insight. To find the temporal behaviour of the plasma chemistry as a whole we need a numerical route that is complicated by two factors:

First, the destruction of one species will in general lead to the production of another, meaning that the particles balances have to be solved as a set of *coupled equations*.

Second, the destruction frequency of a species  $s$  can be proportional to the density of  $s$  itself thereby introducing *non-linearity*.

### 5.3 Coupled Species Equations; two Methods

To find the temporal behaviour of the plasma chemical composition we combine the balance equation (5.2) of all the chemical species to the vector equation

$$\frac{\partial \mathbf{n}}{\partial t} + \bar{\bar{\mathbf{T}}} \cdot \mathbf{n}(t) = \mathbf{S}(\mathbf{n}(t)). \quad (5.9)$$

Here  $\mathbf{n}(t) = [n_1(t), n_2(t), \dots, n_{N_s}(t)]^{tr}$  is a vector representing the density of all (relevant) species,  $\bar{\bar{\mathbf{T}}}$  a diagonal matrix giving the transport frequencies, while  $\mathbf{S}(\mathbf{n}(t))$  is the vector giving the sources of the species. It should be realised that a source of a certain species in principle depends on the densities of all others. Now, there are two possible ways to proceed; the first is to remain in the *species-density* domain, the second is to move toward the *reaction-rate* domain.

In the species-density domain we can write the source vector as a matrix vector multiplication

$$\mathbf{S} = \bar{\bar{\mathbf{F}}} \cdot \mathbf{n}, \quad (5.10)$$

where  $\bar{\bar{\mathbf{F}}}$  is a matrix containing the conversion frequencies of the transitions between the species. The diagonal of  $\bar{\bar{\mathbf{F}}}$  is filled with (minus) the destruction frequencies.

This *species-density-domain method* is most commonly used in the field of CRMs and especially suitable for the linear situations; i.e. situations for which the destruction frequency of a species  $s$  is not dependent on its own density  $n(s)$ . In the non-linear case, the *reaction-rate-domain method* is more appropriate.

To explain this method we start with a the following simple reaction



### 5.3. Coupled Species Equations; two Methods

---

of which the rate  $R$  (in  $\text{m}^{-3}\text{s}^{-1}$ ) is determined by

$$R(T, n_A, n_B) = n_A n_B^2 k(T). \quad (5.12)$$

The first two factors at the right hand side are the densities of the interacting species to the power of their *stoichiometry* coefficient, while  $k(T)$  is the rate coefficient.

In general, a reaction  $r$  can be written as



where  $v_{r,s}^d$  and  $v_{r,s}^p$  refer to the stoichiometry coefficients of the *destruction* and *production* for the particles  $A_s^d$  and  $A_s^p$  in reaction  $r$  while the corresponding reaction rate is given by

$$R_r(T, \mathbf{n}(t)) = k_r \prod_{s=1}^{N_s} n_s^{v_{s,r}^d}. \quad (5.14)$$

Here  $k_r$  is the reaction rate coefficient for the reaction labelled by  $r$  and  $N_s$  the total number of (relevant) species. Note the difference between the *rate*  $R_r$ , always expressed in  $\text{m}^{-3}\text{s}^{-1}$ , and the *rate coefficient*  $k_r$  that has a unit depending on the number of interacting species; i.e. expressed in units  $\text{m}^{3(N_d-1)}\text{s}^{-1}$ , with  $N_d = \sum_s N_s v_{s,r}^d$ .

If a species is not involved in a particular (side of a) reaction it can still be retained by taking the corresponding stoichiometry coefficient equal to zero. This implies that we can let *all species* participate in *all reactions* and that the multiplication in the above equation runs over all species.

Each time a reaction takes place, the reactants are consumed and the products produced. The net change  $S_{r,s}$  is determined by subtracting the stoichiometry coefficients on the right-hand side from those on the left-hand side of reaction 5.13. This must be done for each species. So, going back to the simple example as given above in equation 5.11 we get the change in density of species B by multiplying the reaction rate  $R$  with the net change in stoichiometry: produced minus consumed, or  $W_{B,r} = v_{B,r}^p - v_{B,r}^d = 1 - 2 = -1$ . So the net rate at which the density of particles B is changed by this reaction  $r$  is given by  $S_{B,r} = -R_r$

In general we get for the change in the density of species  $s$  due to reaction  $r$

$$S_{s,r} = W_{s,r} R_r \quad (5.15)$$

where the  $W_{s,r} = v_{s,r}^p - v_{s,r}^d$  is the net stoichiometry coefficient of the species  $s$  in reaction  $r$ .

The effect of all reactions on the density of  $s$  is given by

$$S_s = \sum_r S_{s,r} = \sum_r W_{s,r} R_r. \quad (5.16)$$



This is the source of the species  $s$ , i.e. the right-hand side of equation 5.9.

The change in the density of all species can now be cast in a matrix-vector multiplication reading

$$\mathbf{S}(\mathbf{n}) = \overline{\overline{\mathbf{W}}}\mathbf{R}. \quad (5.17)$$

The vector  $\mathbf{R}$  is a vector in reaction-rate space whereas  $\overline{\overline{\mathbf{W}}}$  is the net-stoichiometry matrix. It gives the 'weights' for all the species of how much the densities are changed by the reactions. Each row of this matrix refers to a species and each column refers to a certain reaction rate. So in fact  $\overline{\overline{\mathbf{W}}}$  describes the projection of the rate space on the density space.

Backward processes are not included using detailed balancing [101]. If they have to be taken into account this can be done by adding the backward process just as another reaction.

## 5.4 Transport and Wall Reactions

In equation (5.9) the transport is handled by means of a separate (diagonal) transport matrix  $\overline{\overline{\mathbf{T}}}$ . In principle, it is possible to incorporate the transport frequencies in the same matrix. For the species-density-domain method, this leads to the new frequency matrix  $\overline{\overline{\mathbf{F}}}^* = \overline{\overline{\mathbf{F}}} - \overline{\overline{\mathbf{T}}}$  that has the same rank as that of the old one. Thus,  $\text{rank}(\overline{\overline{\mathbf{F}}}^*) = \text{rank}(\overline{\overline{\mathbf{F}}})$ . In the same way we can define the modified source

$$\mathbf{S}^*[\mathbf{n}(t)] = \mathbf{S}[\mathbf{n}(t)] - \overline{\overline{\mathbf{T}}} \cdot \mathbf{n}(t). \quad (5.18)$$

The dimension of  $\mathbf{S}^*$  is the same as that  $\mathbf{S}$ .

For the reaction-rate-domain method the incorporation of transport is done by adding fictive reactions  $r'$ . This means that the reaction vector  $\mathbf{R}$  has to be extended with rates of the form  $R_{r',s} = \mathcal{T}_s n_s$  where  $\mathcal{T}_s$  is the transport frequency. The matrix  $\overline{\overline{\mathbf{W}}}$  has to be changed accordingly. This implies that the new reaction vector has a larger dimension than the old one. Also the rank of  $\overline{\overline{\mathbf{W}}}$  will increase.

The following expressions for the transport frequencies are taken:

For the atoms disappearing at the wall we have

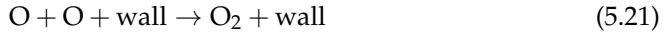
$$\mathcal{T}_s = \frac{D}{\Lambda^2}, \quad (5.19)$$

where  $\Lambda$  is the size of the plasma and  $D$  given by equation 5.5.

For the electrons and ions that diffuse to the wall we use this equation as well, but employ the ambipolar diffusion coefficient

$$D_a = \frac{2}{3N\sigma} \sqrt{\frac{k_B T_h}{\pi M}} \left( 1 + \frac{T_e}{T_h} \right). \quad (5.20)$$

In the above equation we assumed that the wall acts as a perfect sink. Active species that arrive, are removed from the plasma. However, the wall can also act as a site where species are formed. As an example, the following equation



shows that the wall acts as a sink for atomic oxygen produced in the centre and as a source of oxygen molecules that diffuses back to the centre of the discharge. A proper treatment of these processes in which also sticking coefficients play a role is postponed to further study.

## 5.5 The Electron Balances

The current model named *RateLab* is an extension of *Pyrate* presented by [11] that was aimed to study plasma activated chemistry for given values of the electron density and temperature and elemental oxygen concentrations. With respect to *Pyrate*, *RateLab* has been extended and includes the temporal behaviour of the electron density and temperature as well. The corresponding equations are discussed below.

### The Electron Particle Balance (ePB)

In the electron Particle Balance ePB (i.e. equation 5.6 with  $s = e$ )

$$\frac{\partial n_e}{\partial t} = \mathcal{P}_e - n_e(\mathcal{D}_e + \mathcal{T}_e), \quad (5.22)$$

$\mathcal{P}_e$  stands for the ionisation rate, which can be written as

$$\mathcal{P}_e = n_e \sum_s k_{ion}^s n_s, \quad (5.23)$$

where the summation runs over all types of heavy particles.

The second term,  $n_e \mathcal{D}_e$ , at the right-hand side refers to the effective rate of recombination. It is tempting to use for this the reverse process (in the sense of detailed balancing) of electron impact ionisation, i.e. two-electron recombination. However,

the corresponding rate (scaling with  $T_e^{-4.5}$ ) is very low for the plasmas under study. Instead, molecular assisted recombination (MAR) will be important, especially in case of reasonably high pressures (see chapter 8). MAR is a chain of processes in which molecular ions are formed and destroyed. The formation process in Ar plasmas, which is given by



is in most cases followed by dissociative recombination (DR)



Since the rate of DR is in general higher than that of the molecular ion formation process the latter (5.24) will give the limiting rate of the MAR chain.

The transport frequency is obtained from the transport frequency of ions by using the ambipolar condition [10, p. 49].

### The Electron Energy Balance

Including the electron energy balance opens new possibilities. In that case the model not only gives insight into *species densities* but also *energy densities*. We include the electron energy balance in simplified<sup>a</sup> form, reading

$$\frac{\partial}{\partial t} \left( \frac{3}{2} n_e k_B T_e \right) = S_{Te}, \quad (5.26)$$

where the source term

$$S_{Te} = Q_{ohm} - Q_{eh}^{elas} - Q_{eh}^{inel} - Q^{wall}, \quad (5.27)$$

contains the contribution  $Q_{ohm}$  due to Ohmic heating, whereas  $Q_{eh}^{elas}$  and  $Q_{eh}^{inel}$  refer to the exchange of energy to heavy particles by means of elastic and inelastic collisions, while  $Q^{wall}$  corresponds to the loss of kinetic energy at the walls<sup>b</sup>. The elastic term reads

$$Q_{eh}^{elas} = \sum_s \frac{3}{2} n_e \nu_{es} \left( \frac{2m_e}{m_s} \right) k_B (T_e - T_h), \quad (5.28)$$

where  $\nu_{es}$  is the average momentum transfer frequency for electrons with species  $s$ ,  $m_e$  the electron mass,  $m_s$  the mass of species  $s$  and  $T_h$  the gas temperature. The inelastic term reads

$$Q_{eh}^{inel} = \sum_i R_i \Delta \varepsilon_i, \quad (5.29)$$

---

<sup>a</sup>Simplification means among others that the energy transport due to convection and conduction is not included

<sup>b</sup>We use the term 'walls', although we are actually referring to the kinetic energy lost by the electrons as they leave the plasma and pass through the sheath.

with  $R_i$  the reaction rate, and  $\Delta\varepsilon_i$  the energy gain or loss per electron per reaction. The energy that is lost at the wall  $Q^{wall}$  is handled as explained in [102].

An important simplified case is obtained when the energy balance of electrons is in steady state, and electron energy transport is neglected,  $Q^{wall} \approx 0$ . In that case we get

$$Q_{ohm} = Q_{eh}^{elas} + Q_{eh}^{inel}. \quad (5.30)$$

This expresses that under those conditions the power that is gained from the electromagnetic waves is spent on elastic and inelastic collisions. Equation (5.30) is known as the *Local Power Balance* equation (cf. [12]).

A useful quantity is  $\theta$ , which is defined as the power needed to maintain an electron-ion pair in the plasma,

$$\theta = \theta_A = Q_{ohm}/n_e \quad (5.31)$$

or as the power lost per electron ion pair created

$$\theta = \theta_L = (Q_{eh}^{elas} + Q_{eh}^{inel})/n_e. \quad (5.32)$$

The power-density related to the energy source of the plasma can depend on time  $Q_{ohm} = Q_{ohm}(t)$ , which allows the study of pulsed plasmas.

## 5.6 Global Plasma Models and Plasma Classification

As stated before, the new model RateLab can act as a global plasma model (GPM), meaning that it can predict the mean values of internal plasma properties, such as  $n_e$  and  $T_e$  as functions of the external plasma control parameters (the knobs) like pressure, filling-composition and plasma-size. We start with the electron particle balance that can be seen as the basis of the GPM as it determines the electron temperature. To show this we start with a simplified version of equation (5.22) by neglecting the recombination and time dependence. Using  $\mathcal{T}_s = D_a/(R^2)$  the ePB leads to the following equation for the effective ionisation rate

$$k_{ion}^*(T_e) = D_a^*(Rn_1)^{-2}, \quad (5.33)$$

where  $D_a^* = D_a n_1$  is the ambipolar diffusion coefficient times the gas density (here taken equal to the ground density of argon) and  $R$  the plasma radius. The  $k_{ion}^* = \sum k_{ion}^s n_s / n_1$ , cf. equation (5.23), includes all the ionisation pathways. It can be shown that for the plasmas studied in this thesis,  $k_{ion}^*$  is close to the rate of excitation, that is, the transitions from the ground state to the first block of excited levels. For argon plasmas the corresponding formula

$$k_{ion}^* = 6.79 \cdot 10^{-17} T_e(K)^{0.5} \exp(-E_{12}/kT_e); \quad (5.34)$$

often used in global modelling [103] is close to the expression  $k_1$  used in table 7.4 in chapter 7. Note that both equation (5.34) and  $k_1$  are based on a Maxwellian EEDF.

Due to the strong dependency of  $k_{ion}^*$  on  $T_e$ , we get a prescription for  $T_e$ . The quantity  $D_a^* = n_1 D_a$  is useful since the diffusion coefficient is inversely proportional to  $n_1$ , the density of the ground state and equation (5.5) shows that  $D^*$  is only weakly dependent on other plasma parameters.

Similarity law equation (5.33) suggests that the electron temperature is determined by the product  $n_1 R$ , meaning that plasmas with the same  $n_1 R$ -value have the same  $T_e$ -value [24, 25]. This similarity law is powerful and well-known but has its limitations, especially for high pressure conditions. The higher the pressure, the more MAR will take over the quenching of electron ion pairs (see (5.24) and (5.25)). This will be discussed in chapter 7.

## 5.7 The new Model RateLab

We will now return to the main task of this chapter and discuss the main structure of the model RateLab. First, we will present the system of equations, second, we will give the structure of the input file. This will be dedicated to a case study, namely the time dependent description of a pulsed Ar plasma.

Equations (5.9) and (5.26) are coupled as

$$\frac{d\mathbf{Y}}{dt} = \mathbf{S}_{\mathbf{Y}}^*(\mathbf{Y}, t), \quad \mathbf{Y}(0) = \mathbf{Y}_0, \quad (5.35)$$

with density vector  $\mathbf{Y} = (n_1, \dots, n_{M-1}, n_e, \frac{3}{2}k_B n_e T_e)^{tr}$  and the modified source vector  $\mathbf{S}_{\mathbf{Y}}^*(\mathbf{Y}, t) = \mathbf{S}_{\mathbf{Y}} - \bar{\bar{\mathbf{T}}} \cdot \mathbf{n}$ . Here  $M$  is the total number of species densities, including electron and ground state density. Note that beside the species densities,  $\mathbf{Y}$  also carries the electron energy density.

In matrix form equation (5.35) reads

$$\frac{d}{dt} \begin{pmatrix} n_1 \\ \vdots \\ n_{M-1} \\ n_e \\ \frac{3}{2}k_B T_e n_e \end{pmatrix} = \begin{pmatrix} S_1 \\ \vdots \\ S_{M-1} \\ S_e \\ S_{T_e} \end{pmatrix} - \begin{pmatrix} \mathcal{T}_1 & \cdots & 0 & 0 & 0 \\ \vdots & \ddots & 0 & \vdots & 0 \\ & & \mathcal{T}_{M-1} & 0 & 0 \\ q_1 T_1 & & q_{M-1} T_{M-1} & 0 & 0 \\ 0 & \cdots & 0 & 0 & 0 \end{pmatrix} \cdot \begin{pmatrix} n_1 \\ \vdots \\ n_{M-1} \\ n_e \\ \frac{3}{2}k_B T_e n_e \end{pmatrix}, \quad (5.36)$$

where for the sake of clarity  $\mathbf{S}_Y^*$  is split into the source and transport part; meaning that not  $S^*$  but  $S$  is used as first term at the right-hand side of equation (5.36). The solution procedure will be performed in the reaction-rate domain, using equation (5.17).

The system of differential equations equation 5.35 is an initial value problem that is implemented and solved using Matlab and the default solvers for ordinary differential equations (ODEs) [104].

## 5.8 The User Interface

The data used to compute the source terms  $(S_1, \dots, S_{M-1}, S_e, S_{e_e})$ , that is: rate coefficients, reactions formulas, transitions energies, etc. are obtained from an input file. As an example a part of the input file for the pulsed Ar plasma case study is given in figure 5.1. A parser script converts the information given in the input file into a set of Matlab scripts, that will be used by the model.

The input files are divided into the following sections:

```
## DOCUMENTATION ##
```

As the name indicates, this section is meant to store information about the input file such as references, notes, previous initialisation values, etc. Using the special character %, comments can be included in the text of the input file sections.

```
## SPECIES ##
```

This section, specifies the names of the species involved. These will be used in the reaction formulas in section ## Reactions ##. The sequence in which the species names are given will define the order of elements in vector  $Y$ .

## REACTIONS ##

Each line in this section corresponds to a reaction. A line is subdivided into 4 parts that are separated from each other by the symbol “:”, cf. figure 5.1.

The first part represents the reaction equation. The species names defined in ## SPECIES ## are used here. The symbol “->” indicates the direction of the reaction; the reactants are defined at the left-hand side and the products at the right-hand side.

The second part of the reaction line is the rate coefficient, that can be defined as a function of the electron temperature (represented by variables  $T_{e\_eV}$  or  $T_{e\_K}$ ), the gas temperature ( $T_{h\_eV}$  or  $T_{h\_K}$ ).

The third part of the reaction line gives the corresponding energy loss by electrons in elastic or inelastic collisions.

In the last part of the reaction line we indicate whether the reaction is a volume reaction marked with the character V or a wall reaction, as it is the case of diffusion, with character W.

## INITIAL VALUES ##

The initial values are given here for the species densities (in  $m^{-3}$ ) and the electron temperature (in eV).

## TIME ##

The start and stop values for the integration time are given in this section.

## GEOMETRY ##

The variables that determine the dimensions of the plasma are given here. We require the definition of a variable called `volume`; it is used to compute the power density for a given power input.

##CONSTANT DATA ##

This section is read only once at the model initialisations; it defines global constants such as the gas temperature.

##POWER INPUT##

The power input is defined here in Watt. A function of time can be provided to simulate pulsed plasmas.

##DECLARATIONS##

This section is the most flexible in the model. It is used as a Matlab script that it is invoked by the script that generates the sources in the model. It is used to define the diffusion model and variables that are employed in the definition of the rate coefficients functions in ## Reactions ##.

As an example, typical `## SPECIES ##` and `## REACTIONS ##` sections have been shown in figure 5.1.



```

## SPECIES ##
Ar,Ar4s,Ar4p,Ar+,e;
## REACTIONS ##
% Volume Reactions
Ar + e -> Ar + e      : 1.84e-8*Te_eV^(3/2)/Y(5)      : 3/2*Te_eV*(2*me/mAr) : V ;
Ar + e -> Ar4s + e    : 5e-15*Te_eV^(0.74)*exp(-11.56/Te_eV)      : 11.56                : V ;
Ar4s + e -> Ar + e    : 4.3e-16*Te_eV^(0.74)                       : -11.56              : V ;
Ar + e -> Ar4p + e    : 1.4e-14*Te_eV^(0.71)*exp(-13.2/Te_eV)     : 13.2                : V ;
Ar4p + e -> Ar + e    : 3.9e-16*Te_eV^(0.71)                       : -13.2              : V ;
Ar4s + e -> Ar4p + e  : 8.9e-13*Te_eV^(0.51)*exp(-1.59/Te_eV)     : 1.59                : V ;
Ar4p + e -> Ar4s + e  : 3.0e-13*Te_eV^(0.51)                       : -1.59              : V ;
Ar + e -> Ar+ + e + e : 2.9e-14*(Te_eV)^(0.68)*exp(-15.759/Te_eV) : 15.759              : V ;
Ar4s + e -> Ar+ + e + e : 6.8e-15*(Te_eV)^(0.67)*exp(-4.2/Te_eV)    : 4.2                 : V ;
Ar4p + e -> Ar+ + e + e : 1.8e-13*(Te_eV)^(0.61)*exp(-2.61/Te_eV)    : 2.61                : V ;
% Wall Reactions (Diffusion Losses) ;
Ar+ + e -> Ar >>> : Deff/Reff^2 >> : 2*Vs+Te_eV/2 : W : Aeff ;
Ar4s -> Ar >>> : Dion/Reff^2 >> : 0 >>> : W : 0 ;
Ar4p -> Ar >>> : Dion/Reff^2 >> : 0 >>> : W : 0 ;

```

Figure 5.1: A part of the input file of the model RateLab applied to the case study of a pulsed Ar plasma. Only the sections # SPECIES ## and # REACTIONS ## are given. It can be seen that apart from the volume reactions also wall reactions are included. The latter represent among others the diffusive losses. For more details we refer to the text.

## 5.9 A pulsed argon plasma as case-study

In this case study RateLab is used to investigate a pulsed argon plasma. Nowadays pulsing plasmas gets a lot of attention as it is believed that due to the transient behaviour more radicals and less heat will be generated.

The argon model includes the ground state, Ar, the groups of excited states, Ar(4s) and Ar(4p), the atomic ion, Ar<sup>+</sup>, and electrons. For the conversion rates between these species, we used the data given in [98]; the radiative transitions are not included.

The plasma region is a cylinder with radius  $R_p = 3$  mm and length  $L = 450$  mm. The pressure is set to 1000 Pa and the gas temperature to 500 K.

The power pulse is nearly rectangular, with a steep linear switch-on function and an amplitude of 160 W. The duty ratio of the pulse is 0.25, resulting in an average power of 40 W. The power rises linearly (in  $10^{-4}$  s), whereas a step function is used to switch off the power at every pulse end. This behaviour is shown in the bottom of figure 5.2.

Only the diffusion in radial direction is included as transport process, for which a Bessel profile for the electron density [12] is assumed. This implies that the transport collision frequency for ions and electrons is that of an infinite cylinder [12]

$$\mathcal{T}_s = D_a / (\Lambda)^2, \quad (5.37)$$

with  $\Lambda = R / X_{01}$ , where  $X_{01} = 2.4048 \dots$  is the first zero of the zeroth order Bessel function of the first kind,  $J_0(x)$ . A similar relation holds for the transport of excited species, but with a different diffusion coefficient. The diffusion coefficients for ions and neutral excited states are computed as in [11, 58] using equations (5.20) and (5.5), respectively.

Figure 5.2 shows the results of the time-dependent behaviour of the species densities and the electron temperature. The power profile, an input to the model, is given in the frame at the bottom.

The following observations can be made:

In the top frame, showing the temporal behaviour of the densities, we see that the higher the density, the slower the corresponding species responds to power pulsing. This tendency, which can be formulated shortly as ‘large density reservoirs respond slowly’ was already announced in the analysis given around equation 5.7.

So, we see that the density of the Ar ground state is (almost) not affected and remains close to the initial value of  $10^{23} \text{ m}^{-3}$ ; a value that, via the ideal gas law, is determined by the pressure (1000 Pa) and gas temperature (500 K). On the other hand we observe the rapidly responding species (Ar(4s) and Ar(4p)); they have the lowest (averaged)

densities. The response time of the electron and ion densities is inbetween; these increase just after power switch-on by following the electron temperature. After switch-off a decay is found that is determined by ambipolar diffusion.

The electron temperature rises sharply at power on-set. This strong response of  $T_e$  to the temporal power profile can be understood from equation (5.26), which shows that a strong variation of the source  $Q_{Ohm}$  within a short time demands for a high time-derivative of  $T_e$ . The plateau values of  $T_e = 1$  eV can be found by using equation (5.33) and (5.34) in which we insert for the diffusion coefficient given in equation 5.20.

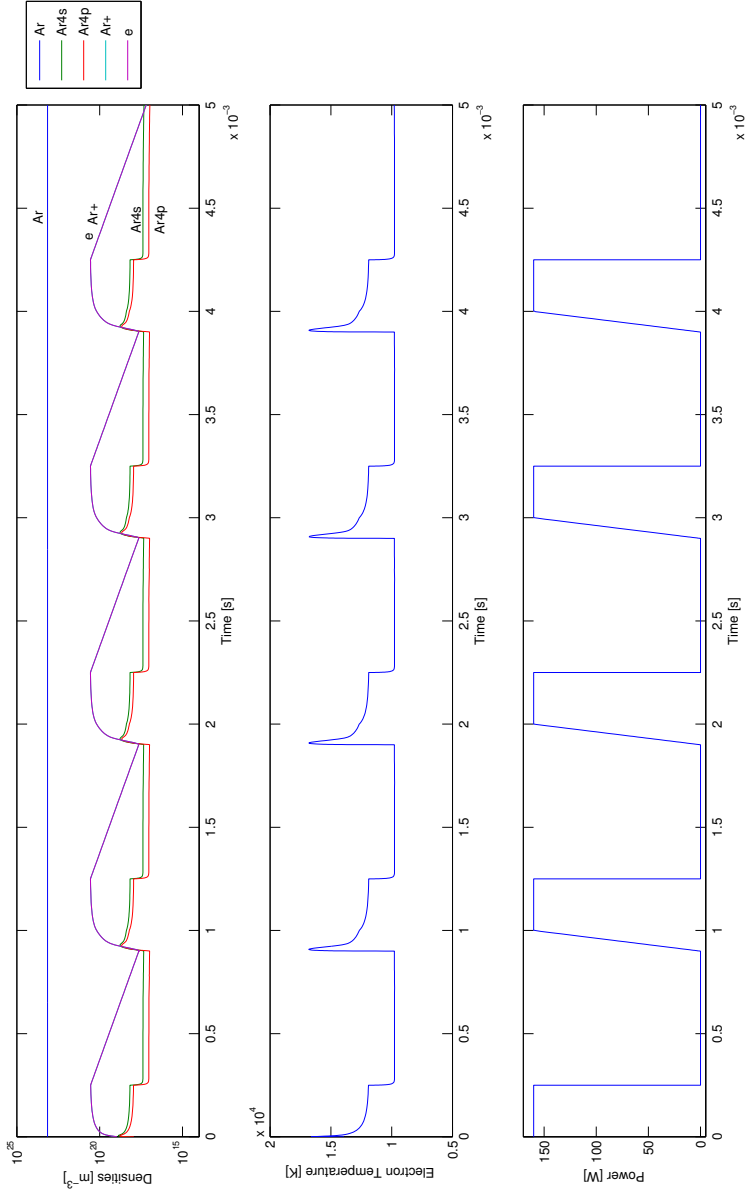


Figure 5.2: Results for the case-study of a pulsed Argon plasma, used to demonstrate RateLab. Note that due to quasi-neutrality the species density of the argon ion equals that of electrons.

## 5.10 Summary

For an efficient study of the chemistry of complex chemical plasmas, one can use zero-dimensional models in which the transport and configuration aspects are described in simplified forms. Three different main types are distinguished, each developed in its own disciplines and serving different objectives. In this chapter we have combined these model-types. The resulting RateLab code is a versatile tool that takes the plasma control parameters as input and calculates spectroscopic features and internal plasma properties, such the electron density and temperature. The method is based on a time-dependent solution of a matrix-vector equation and can handle non-linear reaction processes as well.

The lay-out of the input file facilitates the addition or removal of reaction rates and the study of the subsequent changes in the (temporal) chemistry aspects of the plasma.

In a case-study, RateLab has been applied to a pulsed argon plasma. The model convergences within 10 seconds whereas the Grand models constructed for MIPs in steady state (cf chapters 8,9,10 ) based on a similar chemistry, take convergence times between 4 and 20 hours.

**Part II**

**Applications**



---

# 6

## The effect of the remote field electromagnetic boundary conditions on microwave induced plasma torches

---



**Abstract.** A flexible versatile electromagnetic (EM) model constructed with the PLASIMO platform, is employed to explore EM features of microwave induced plasma (MIP) torches. The bases, formed by a full-vector formulation of the Maxwell equations, provides the possibility to formulate the boundary conditions in a natural way. Together with the use of a direct matrix solver this gives a convergence speed-up of more than a factor of 100 when compared to a scalar formulation on the azimuthal magnetic field that uses an iterative solver [15]. As a result this EM model is ready to act in future studies as part of the self-consistent description of plasma-EM coupling. With the EM model three types of configuration were studied; the Closed C-, Semi-open S- and Open O-configurations, all three based on the same simplified model- plasmas. It is found that the C-configuration, acting as a cavity for which the (de)tuning is extremely sensitive for the plasma conditions, is less suitable for applications in which changes in plasma compositions can be expected. The S-configuration can be seen as a model for the practice often used in laboratories to place MIP torches in a grid that aims to protect the environment against microwave EM radiation. Calculations show that this is good practice provided the radius of this cylindrical grid is in the order of 90 mm. For the most often used configuration, the open version, we found that the power balance as expressed by the coefficients of absorption, transmission and reflection, depends on the electron density of the plasma. The reason is that plasma acts as an antenna, that converts the EM waves from the co-axial structure to that of the expansion region and that this antenna function depends on the electron density. The influence of various other antenna elements is investigated as well.

## 6.1 Introduction

Microwave Induced Plasmas [12] (MIPs) are interesting subjects for academic studies and offer many possibilities for industrial applications. The latter can be found in the fields of materials processing [1–3], gas volume cleaning [4] and for the construction of sources of ions [5], radicals [6] and photons [105].

Depending on the type of microwave coupling, MIPs can be divided into plasmas inside resonant cavities [14, 106], surface-wave sustained plasmas [86] and free expanding plasma torches [16]. This paper is devoted to the last category for which we mention, as example, the microwave plasma torch (MPT) [107] and the axial injection torch (TIA) [16]. In both cases the plasma is created in the zone where the transition takes place from the electromagnetic (EM) structure of a coaxial waveguide to that of an expansion zone. The expansion can take place in open air or in a vessel. The plasma gas, in most cases argon, is generally provided via the hollow inner conductor of the coaxial waveguide.

The working power of the TIA can reach 2 kW whereas a microwave plasma torch (MPT) is limited to around 400 W at 2.45 GHz [86]. This limitation is due to the use of coaxial cables instead of rectangular waveguides [107] as the connection to transfer the EM energy from the power supply to the torch.

In the past several experiments have been carried out on both MPT and TIA plasmas. Applying absolute intensity measurements [108], [76] of atomic lines and the continuum it was possible to determine the electron density  $n_e$  and temperature  $T_e$ ; these values have been compared with the results of the Stark intersection method and Thomson scattering [109–113]. Typical reported values for the TIA are  $n_e = 3 \cdot 10^{21} \text{ m}^{-3}$  and  $T_e = 22000 \text{ K}$ . For the MPT the typical values are  $n_e = 3 \cdot 10^{20} \text{ m}^{-3}$  and  $T_e = 18000 \text{ K}$  (see [114]).

These properties of the electron gas were found to depend on experimental settings like the power level, the flow and the chemical composition of the gas flow (e.g. Ar versus He [103, 115]).

Especially the chemical composition was found to have an important impact and in line with this observation, it was understood that the internal plasma properties can also be changed by the entrainment of air. Oxygen and nitrogen molecules sucked in by the argon flow will enhance electron loss-mechanisms and will thus affect the properties of the electrons gas and the shape of the plasma flame. To study the effect of the environment, metallic plasma vessels were constructed in [108, 114, 116, 117], with the purpose of changing the gas-environment of the plasma (e.g. by replacing air by argon). It was found that chemical features of the environment indeed have an impact on the plasma. As explained in [109], when the plasma is created in a vessel filled with Ar, we get higher  $n_e$ - and lower  $T_e$ -values than when it is operated in air .

Typical changes are an increase of  $n_e$  from  $6 \cdot 10^{20} \text{ m}^{-3}$  in air to  $1.2 \cdot 10^{21} \text{ m}^{-3}$  in argon and a change in  $T_e$  from 19000 K in air to 16000 K in argon. This was associated with an increase of the plasma radius from around 1.28 mm (air) to 1.79 mm (argon).

However the question rises in how far placing the plasma into a metallic gas-purification vessel will change the electromagnetic aspects of the plasma. A metal vessel placed around the plasma can cause back-reflection of the electromagnetic waves so that the electric field at the plasma location may change as well. More generally the question can be formulated as *in how far the electromagnetic features of the environment will change the properties of microwave induced plasma*. This question also addresses the impact of metallic grids that are sometimes placed around MIPs to avoid EM interferences with devices in the surroundings. It is not impossible that these grids will change the EM structure at the plasma location as well.

This study on the impact of the environment on the operation of MIP torches is based on numerical calculations. The modular toolkit PLASIMO was employed to calculate the fields for three different type of configurations; *open*, *semi-open* and *closed* systems; they are shortly denoted by, O, S or C configurations. The role of the plasma is played by a cylindrical bar or cone of given permittivity and conductivity. Realising that the plasma, formed at a tip of a nozzle has a radial size of less than 1 mm, while the vessels used in practice have radii of about 6 cm, the aim of this paper can be formulated as the question in *to what extend the remote<sup>a</sup> field EM boundary conditions will effect the operation and the inner part of a MIP*.

In the past several numerical studies were published on one of the configurations O, S or C. In [118] a numerical EM study of the MPT is given. It deals with an *open* configuration. In [119] the coaxial microwave torch (CMT), i.e. a *semi-open* configuration (metal vessel working as a circular waveguide) was studied. After giving the EM module, it is also coupled with a plasma fluid model (where flow, temperature and species equations in local thermal equilibrium are included). In [15] a *closed* configuration is used. It consists of a circular waveguide with a metal wall at the top (shortcut).

In all three studies cited above the EM field is found by solving a time-harmonic wave equation for the *azimuthal magnetic component* (i.e. an equation similar to the Helmholtz equation). In our approach we apply a full vector formulation instead, meaning that apart from the azimuthal magnetic component we also solve the radial and axial electric field components in a coupled manner. With this formulation and the use of the staggered Yee grid [65], the boundary conditions can be fulfilled in a more natural way, which, as we will see, speeds up the convergence process. Together with the application of a direct matrix-vector solver this leads to an enhancement of

---

<sup>a</sup>The distance of the EM boundaries to the plasma is far compared to the plasma radius but not large in comparison with the wavelength; We prefer use *remote* field rather than *far-field* to avoid confusion with the terms used in antenna theory as *far-field* is used for large distances compared to the wavelength.

the convergence speed of more than a factor hundred as compared to the work of [15]. Another difference with the previous studies is that our study is not confined to just one configuration but that instead all three types of configurations, O, S and C are modelled and compared with each others. In this way a better understanding of the EM interplay of the plasma and the environment can be obtained. It was found that the O configuration is the most robust. This configuration is free from resonances so that a feed-back of the plasma on resonances can be avoided. Nevertheless we will see that the plasma still plays a role in the relative importance of the absorption, transmission and absorption of EM energy. The plasma has an antenna function in converting the wave from a TEM mode of the coaxial waveguide into that of radiation into open air. In order to get insight in this conversion the role of various antenna elements is investigated by changing the plasma density and the geometry of the transition region (*gap*).

This paper is organised as follows. Section 6.2 contains the definition of the configurations, the plasma and geometry of the setup. The physical and numerical model are explained in section 6.3. The results given in section 6.4 comprehend the effect of the field boundary condition section 6.4.1, the effect of the electron density and how it changes the antenna function of the plasma in section 6.4.2 and the effect of the shape of the transition region in section 6.4.3. We end with the conclusions in section 6.5.

## 6.2 Configuration, Plasma and Geometry

The calculations were performed on a model structure that simplifies the basic EM structure of the TIA and MPT or more generally *MIP torches*. As stated above, both the TIA and MPT plasmas can be seen as extensions of the inner conductor of a coaxial waveguide, meaning that in both cases the plasma forms part of the EM transition from the coaxial waveguide to the expansion region. In the model we can take for this expansion zone a metallic free environment or a circular wave-guide. For the latter we can take various structures that can be divided into closed and semi-open circular waveguides. This leads to the following configurations:

**C (Closed)** The plasma expands into a closed circular waveguide, i.e. a circular wave guide with a shortcut at the end (see [15, 114]).

**S (Semi-Open)** The plasma expands into an open circular waveguide (see [119]).

**O (Open)** The plasma expands into open air (see [118]).

In selecting an appropriate model-plasma we are guided by the experimental values given in [120] and the observation given in [15, 114, 118, 119]. These are depicted in

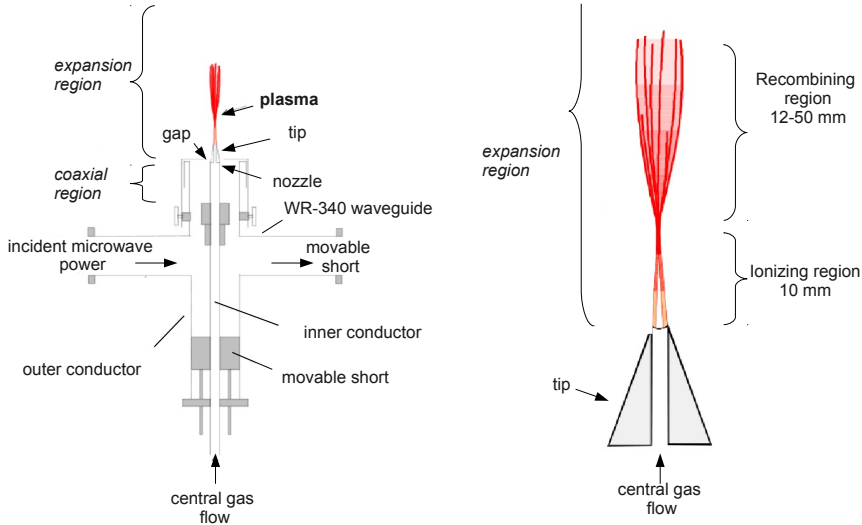


Figure 6.1: Left: a schematic view of a TIA. From the EM point of view the TIA basically consists of a coaxial structure placed perpendicular to a rectangular waveguide (WR-340). The plasma gas flows inside the inner conductor of the coaxial waveguide from the bottom via the nozzle to the expansion region. The EM energy generates the plasma just above the nozzle, thus in the region where the EM-transition takes place from the coaxial waveguide to the expansion region. Right: a schematic view of the two main plasma regions: the ionising and recombining zone.

figure 6.1 where we see that, in practice, the plasma has two zones ([114]): an ionising and a recombining zone. In constructing the model we confine ourselves to the active (ionising) part where most of the electrons are found and we will assume that this model-plasma has the simple structure of a cylindrical bar or cone, with a constant relative permittivity  $\epsilon_r$  and conductivity  $\sigma$  (see section 6.3.1). The values of  $\epsilon_r$  and  $\sigma$  are obtained from a simple model for the electron momentum balance [15, 33] that requires input values for the electron density  $n_e$ , the elastic collision frequency  $\nu_{eh}$  and the electromagnetic field frequency  $\omega$  (see [11]). In the current study, we follow [74] in taking  $\nu_{eh} = 100\omega$ , with  $\omega = 2\pi f$  while  $f = 2.45$  GHz. The electron density is set to  $n_e = 10^{21} \text{ m}^{-3}$ , except in section 6.4.2, where  $n_e$  is varied between  $10^{20} \text{ m}^{-3}$  and  $10^{22} \text{ m}^{-3}$  in a parameter study on the effect of  $n_e$  on the power response of the system.

Parameters of the set-up			
Parameter	Value	Parameter	Value
$R_1$	1 mm	$Z_1$	100 mm
$R_2$	5.5 mm	$Z_2$	106 mm
$R_3$	14.5 mm	$Z_3$	118 mm
$R_4$	variable	$Z_4$	variable

Table 6.1: Parameter distances as used in the model-setup (see figure 6.2(b))

### 6.2.1 Geometry

Figure 6.2(a) shows the geometry of the setup which exhibits a 2D axial-symmetric structure. Figure 6.2(b) depicts the structure of the corresponding computational grid. The coaxial waveguide has an inner radius  $R_2 = 5.5$  mm, an outer radius  $R_3 = 14.5$  mm and ends at  $Z_1 = 100$  mm. The nozzle starts at  $Z_1$ , transforms into the tip at  $Z_2 = 106$  mm and ends at  $Z_3 = 118$  mm. The zone into which the plasma expands (in open air or into a circular waveguide) has a radius of  $R_4$  and ends at  $Z_4$ , both of which are parameter in this study. These parameters values are given in table 6.1. As stated above, the plasma is located at the transition of the coaxial waveguide to the expansion region. As shown in figure 6.2c, the plasma region is defined by the following  $(r,z)$ - values  $(R_1, Z_3)$ ,  $(0, Z_3)$ ,  $(R_1, Z_p)$  and  $(0, Z_p)$ . All the three configurations O, S, and C are described by the same geometry. The difference lies, as we will see, in the boundary conditions for the side and top of the circular waveguide.

## 6.3 Model

This section describes the electromagnetic model. The electromagnetic equations are given in section 6.3.1, the grid is given in section 6.3.2 while their respective boundary conditions are introduced in section 6.3.3. We will comment on the numerical implementation in section 6.3.4. A summary of the model is given in table 6.2 and a comparison with other models in table 6.3.

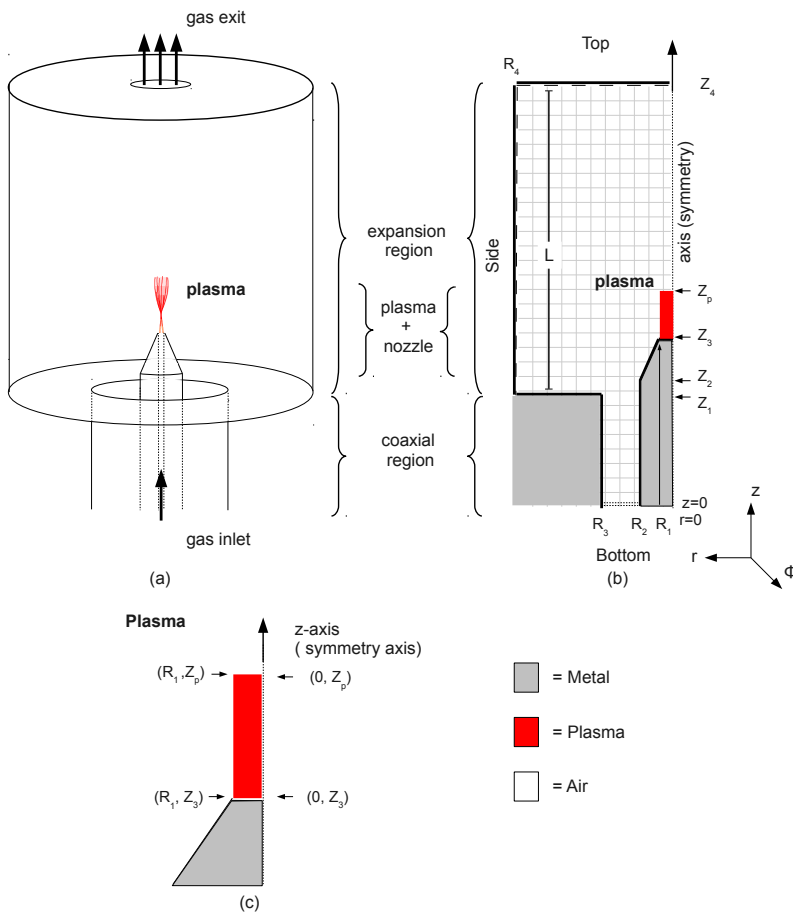


Figure 6.2: (a) the schematic geometry of the electromagnetic structure for the TIA showing 2D axial-symmetry; (b) the computational grid (see table 6.1 for values of geometry parameters); (c) detailed view of the model plasma, in this case a bar.

Main characteristics of current electromagnetic model	
Electromagnetic Problem	Deterministic (not the <i>modes</i> but the <i>fields</i> are determined) Harmonic fields ( $\exp(i\omega t)$ ) 2D (symmetry axis along $z$ , $\partial/\partial\phi = 0$ ) Full vector Maxwell Equations Transversal Magnetic ( $E_r, E_z, H_\phi$ )
Projection	Finite Differences
Grid	staggered (Yee grid)
Ohm's law	$\mathbf{J} = \hat{\sigma}\mathbf{E}$
Solver	Direct Solver (superLU)

Table 6.2: Summary of the main characteristics of the electromagnetic model.

### 6.3.1 Maxwell Equations

For a dissipative and non-magnetic linear medium and assuming harmonic time dependency  $\exp(i\omega t)$ , the Maxwell equations are

$$\nabla \times \mathbf{E} = -i\omega\mu_0\mathbf{H}, \quad (6.1)$$

$$\nabla \times \mathbf{H} = \mathbf{J} + i\omega\epsilon'_r\epsilon_0\mathbf{E}, \quad (6.2)$$

where  $\mathbf{H}$ ,  $\mathbf{E}$  and  $\mathbf{J}$  are respectively the complex magnetic and electric fields and the current density, while  $\epsilon'_r$  is the relative permittivity of the neutral and non-dispersive medium,  $\epsilon_0$  the vacuum permittivity and  $\mu_0$  the vacuum permeability. The angular frequency is  $\omega = 2\pi f$  with  $f$  the EM wave frequency.

The axial symmetry is so that the electromagnetic quantities are azimuth-independent ( $\partial/\partial\phi = 0$ ) and the problem can be described in two dimensions. This axial-symmetry is also referred to as the  $m = 0$  mode.

The dimensions of the coaxial waveguide,  $R_2$  and  $R_3$ , are selected so that only a transverse electromagnetic (TEM) mode can propagate. Due to the axial symmetry,  $m = 0$ , and because the expansion zone is being excited by a TEM mode where  $H_z = 0$ , only  $TM_0$  modes are supported in the expansion zone [62, 121, 122]. This means that only the  $E_r$ ,  $E_z$  and  $H_\phi$  field components of a  $TM_0$  mode are needed in the model.

We assume that the current density is determined by the electrons solely, and that it linearly depends on the electric field as expressed by Ohm's law,  $\mathbf{J} = \hat{\sigma}\mathbf{E}$ , where  $\hat{\sigma}$  is the complex conductivity. The last, together with the harmonic assumptions, leads to



Main differences with other electromagnetic models				
	current	Bilgic [118]	Gritsinin [119]	Alves [15]
Fields (TM)	$H_\phi, E_r, E_z$			
Equation (Comps. )	Full Vector ( $H_\phi, E_r, E_z$ )	Azimuthal Magnetic Component ( $H_\phi$ )		
Grid	Staggered (Yee)	Centred		
BC for Torch	$E_r, E_z$	$H_\phi$		
	TIA, MPT and CMT	MPT	CMT	TIA
Different 'Gaps' Configurations	3 C, S, O	1 O	1 S	1 C
Open Boundary at Exp. Reg.	Plane Wave Radial Wave	Plane Wave	Plane Wave	No
Solver	Direct	Direct	Iterative	Iterative
Grid Points, N	$\sim 10^5$	$\sim 10^4$	Not given	$\sim 10^4$
Comp. Time $t_c$	$\sim 6$ s	Not given	Not given	$\sim 600$ s

Table 6.3: Comparison of our electromagnetic model with those of [118], [119], and [15]. Here, TIA stands for *Torch à Injection Axiale* (Axial Injection Torch), MPT for Microwave Plasma Torch and CMT for Coaxial Microwave Torch.

the definition of the complex permittivity [11, 39]

$$\hat{\epsilon}_r = \epsilon'_r - i\hat{\sigma}(\epsilon_0\omega)^{-1}. \quad (6.3)$$

In the case of plasma  $\epsilon'_r = 1$  and

$$\hat{\sigma} = \frac{\epsilon_0\omega_p^2}{\nu_{eh} + i\omega} \quad (6.4)$$

with the plasma frequency  $\omega_p = \sqrt{e^2 n_e / m_e \epsilon_0}$  and  $\nu_{eh}$  the collision frequency.

The complex conductivity [11, 39] in the plasma is obtained from the current density  $\mathbf{J} = -en_e \mathbf{v}_e$  and the cold collisional electron approximation of the electron momentum balance equation for harmonic fields which reads

$$i\omega \mathbf{v}_e + \nu_{eh} \mathbf{v}_e = -\frac{e}{m_e} \mathbf{E}, \text{ thus } \mathbf{v}_e = \frac{-e\mathbf{E}}{m_e (\nu_{eh} + i\omega)}. \quad (6.5)$$

In this manner we show that  $\mathbf{J} = \hat{\sigma}\mathbf{E}$  and obtain  $\hat{\sigma}$ .

With the above assumptions, the Maxwell equations included in the model get the form

$$\frac{\partial E_z}{\partial r} - \frac{\partial E_r}{\partial z} = k_0 \tilde{H}_\phi, \quad (6.6)$$

$$\frac{\partial \tilde{H}_\phi}{\partial z} = k_0 \hat{e}_r E_r, \quad (6.7)$$

$$\frac{1}{r} \frac{\partial r \tilde{H}_\phi}{\partial r} = -k_0 \hat{e}_r E_z \quad (6.8)$$

where  $k_0 = \omega \sqrt{\mu_0 \epsilon_0}$  is the vacuum wavenumber,  $\tilde{H}_\phi = iZ_0 H_\phi$  the normalised azimuthal magnetic field component, and  $Z_0 = \sqrt{\mu_0 / \epsilon_0}$  the impedance of free space.

The time-averaged power density absorbed in the domain,  $Q$  ( $\text{W}/\text{m}^{-3}$ ), is computed as

$$Q = \frac{1}{2} \text{Re}(\mathbf{J}^* \cdot \mathbf{E}) = \frac{1}{2} \text{Re}(\hat{\sigma}) |\mathbf{E}|^2. \quad (6.9)$$

So that the total power absorbed in volume  $V$  equals

$$P_{abs} = \int_V Q dV = \frac{1}{2} \int_V \text{Re}(\hat{\sigma}) |\mathbf{E}|^2 dV. \quad (6.10)$$

The complex Poynting vector is obtained in this case as

$$\mathbf{S} = \frac{1}{2} \mathbf{E} \times \mathbf{H}^* = \frac{1}{2} \begin{vmatrix} \hat{e}_z & \hat{e}_r & \hat{e}_\phi \\ E_z & E_r & 0 \\ 0 & 0 & H_\phi^* \end{vmatrix} = \frac{1}{2} E_r H_\phi^* \hat{e}_z - \frac{1}{2} E_z H_\phi^* \hat{e}_r, \quad (6.11)$$

and the time-average Poynting vector is

$$\bar{\mathbf{S}} = \text{Re}(\mathbf{S}). \quad (6.12)$$

The conservation of electromagnetic energy is given by the Poynting theorem

$$\nabla \cdot \bar{\mathbf{S}} + Q = 0, \quad (6.13)$$

which in integral form reads

$$\oint_{\mathcal{B}} [\bar{\mathbf{S}} \cdot \mathbf{n}] db + P_{abs} = 0. \quad (6.14)$$

This merely states that the net<sup>b</sup> power of the EM radiation entering the volume  $\mathcal{V}$  enclosed by surface  $\mathcal{B}$  (with outward normal vector  $\mathbf{n}$ ) equals the power absorbed in  $\mathcal{V}$ .

<sup>b</sup>The *net* power entering a region refers to the power associated to the ingoing minus that of the outgoing waves.

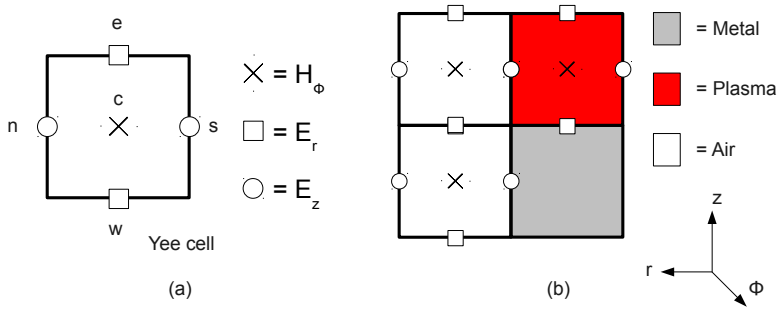


Figure 6.3: (a): general structure of a (Yee) cell used in the numerical method; (b): example of interfaces between different types of material cells.

### 6.3.2 Grid

Equations (6.6), (6.7) and (6.8), and the corresponding boundary conditions (see section 6.3.3), are projected onto a staggered grid using finite differences following the method of Yee [65]. Figure 6.3(a) shows a cell for the Yee grid, where  $H_\phi$  is defined at the nodal points and  $E_r$  and  $E_z$  at the edges of the grid cell. The location of the discrete fields components makes it possible to satisfy the continuity of the field at the edges.

The computational grid is composed of *interior* and *boundary* cells. The electromagnetic fields are only solved in the interior cells. Each nodal point of an interior cell has, depending on the type of material, certain values of the permittivity  $\epsilon_r$  and conductivity  $\sigma$ . In this study the materials used are *air* with  $\epsilon'_r = 1$  and  $\hat{\sigma} = 0$ , and *plasma* for which  $\epsilon'_r = 1$  and  $\hat{\sigma}$  is given by equation (6.4). The values at possible interfaces between two interior cells are determined by interpolation. In the boundary cells, the electromagnetic field components are not solved. These cells are only used to set the *boundary conditions* for the adjacent *interior* cell. Boundary conditions are applied to the electric field components,  $E_r$ ,  $E_z$  as they are the only field component defined at the interface of boundary cells and interior cell. They are described in section 6.3.3. The computational grid is stretched, meaning that the density of grid points is a function of radial position (see [123], [52]). The density of points close to the axis is six times higher than at radial edge of expansion zone.

### 6.3.3 Boundary Conditions

In general three different types of boundary conditions (BC) can be defined for a scalar field  $F$  at a surface  $\mathcal{B}$

1. Dirichlet:  $F(\mathbf{x}) = p(\mathbf{x})$ ,
2. Neumann:  $\mathbf{n} \cdot \nabla F(\mathbf{x}) = q(\mathbf{x})$ ,
3. Mixed:  $\mathbf{n} \cdot [\nabla F(\mathbf{x}) + h(\mathbf{x})F(\mathbf{x})] = w(\mathbf{x})$ .

Here  $\mathbf{x}$  is the position vector of a point on  $\mathcal{B}$ ,  $\mathbf{n}$  the normal on  $\mathcal{B}$  while  $p(\mathbf{x})$ ,  $q(\mathbf{x})$ ,  $h(\mathbf{x})$ , and  $w(\mathbf{x})$  are explicitly known functions of  $\mathbf{x}$ . If  $p(\mathbf{x})$ ,  $q(\mathbf{x})$  or  $w(\mathbf{x}) = 0$  for all  $\mathbf{x} \in \mathcal{B}$ , the BC is named *homogeneous*, otherwise the boundary is called *inhomogeneous*.

	Homogeneous	Inhomogeneous
Dirichlet	Perfect Electric Conductor (PEC)	
Neumann	Axis	
Mixed	Propagation Boundary Condition (PBC)	Excitation

As stated above we only need to consider the BCs of the field components  $E_r$  and  $E_z$ . So they can play the role of  $F$  given above. Below we will sketch the various types of boundaries of the configuration under study and the corresponding conditions imposed to  $E_r$  and/or  $E_z$ .

- *Symmetry-BC* ( $r = 0$ ). The axial symmetry requires at the axis a homogeneous Neumann BC i.e. type 2 with  $F = E_z$ , applied at positions  $\mathbf{x} \in \{Z_p \leq z \leq Z_4, r = 0\}$  and  $q(\mathbf{x}) = 0$ ; i.e.

$$\left. \frac{\partial E_z}{\partial r} \right|_{\mathbf{x}} = 0. \quad (6.15)$$

- *Perfect Electrical Conductors (PEC)-BC*. For metallic boundaries we assume that the E field component parallel to the surface is zero which demands for a homogeneous Dirichlet boundary conditions i.e. type 1 with  $q(\mathbf{x}) = 0$ . For example at the inner conductor of the coaxial waveguide the condition reads

$$E_z|_{\mathbf{x}} = 0 \quad (6.16)$$

at boundary positions  $\mathbf{x} \in \{0 \leq z \leq Z_1, r = R_2\}$ .

- *Propagation boundary condition (PBC) for axial propagation*<sup>c</sup>. A homogeneous mixed boundary, i.e. type 3, is used at the top-boundary positions  $\mathbf{x} \in \{z =$

<sup>c</sup>This BC is often referred to as the absorbing BC (see [68]), however since we use absorption in another meaning and since this BC deals with the propagation of the wave outside the domain we prefer to call this the Propagation BC

$Z_4, 0 \leq r \leq R_4\}$ , of the S and O configuration with  $F = E_r$ ,  $q(\mathbf{x}) = i\beta$ , and  $w(\mathbf{x}) = 0$ . Thus

$$\frac{\partial E_r}{\partial z} + i\beta E_r = 0. \quad (6.17)$$

Here  $\beta$  is the wavenumber of the wave. With this axial PBC, we assume that the EM energy leaves the domain in axial direction with a wave in the  $TM_{01}$  circular waveguide mode (see [124]) with wavenumber  $\beta = \sqrt{k^2 - (p_{01}/R)^2}$ , in which  $R$  is the radius of the circular waveguide,  $k = \omega\sqrt{\mu_0\epsilon_0\epsilon_r}$  the wavenumber of the medium, while  $p_{01} = 2.405$  is the first zero of the Bessel function  $J_0$  of first kind [125]. Note that this boundary condition assumes a plane wave propagating in the positive  $z$ -direction  $E_r \propto \exp(-i\beta z)$ . Therefore for incident plane wave with the same wavenumber that the BC assumes and a normal incidence on the boundary, the reflection is null, meanwhile if the incident wave is different the reflection will be higher depending on a number of parameters such as angle of incidence, wavenumber, etc.

This boundary condition is described in detail in [68, 69, 126].

- *PBC at side-boundary for the radial propagation.* A homogeneous mixed boundary (type 3) is used at the side-boundary  $\mathbf{x} \in \{Z_1 \leq z \leq Z_4, r = R_4\}$ , for case O,

with  $F = E_z$ ,  $q(\mathbf{x}) = k \frac{H_1^{\{2\}}(kr)}{H_0^{\{2\}}(kr)}$ , and  $w(\mathbf{x}) = 0$ . Thus

$$\frac{\partial E_z}{\partial r} + k \frac{H_1^{\{2\}}(kr)}{H_0^{\{2\}}(kr)} E_z = 0 \quad (6.18)$$

with  $H$  a Hankel function [125]. This BC, described in detail in [126], assumes an outward propagating radial wave with  $E_z \propto H_1^{\{2\}}(kr)$ .

- *Excitation-BC.* This inhomogeneous mixed BC, used at the bottom boundary  $\mathbf{x} \in \{z = 0, R_2 \leq r \leq R_3\}$ , has two components, one for the incident and one for the reflected wave. We assume that incident power driven into the plasma has a TEM mode so that the corresponding E-field component reads

$$E_r|^{+}(r, z) = \frac{C_{\text{TEM}}}{r} \exp(-i\beta z) \quad (6.19)$$

with  $C_{\text{TEM}} = \sqrt{Z_0|P_i|/\pi/\ln(R_3/R_2)}$ , and  $|P_i|$ , the (imposed) incident power. Due to the discontinuity present in the domain the incident wave will generate a wave that is reflected back to the entrance. For the corresponding component  $E_r^-$  we apply a PBC such that

$$\frac{\partial E_r^-}{\partial z} - ikE_r^- = 0. \quad (6.20)$$

In this case the wavenumber for the TEM mode coincides with the medium wavenumber,  $k$ . Note that this BC imposes at the entrance a plane wave propagating in the negative  $z$ -direction i.e.  $E_r^- \propto \exp(+ikz)$ . This is the opposite to the top boundary where  $\exp(-i\beta z)$  is used instead. As the BC should be applied to the total  $E_r$  field, we substitute the relation  $E_r^- = E_r - E_r^+$  into equation (6.20), which, using equation (6.19), gives

$$\frac{\partial E_r}{\partial z} - ikE_r = -2ik \frac{C_{TEM}}{r} \exp(-ikz). \quad (6.21)$$

As we can see the excitation- BC is of type 3 with  $F = E_r$ ,  $q(\mathbf{x}) = ik$ , and  $w(\mathbf{x}) = 2ikC_{TEM} \exp(-ikz)/r$ .

To summarise, we give an overview of the BC of the three types of configurations C, S, and O (figures 6.4(a), 6.4(b) and 6.4(c), respectively)

The configurations have in common the excitation-BC at the entrance of the coaxial waveguide, the PEC-BC at the inner and outer metallic walls of the coaxial waveguide and the symmetry-BC at the central axis of the expansion region. The differences are (see figure 6.4):

**C. Closed** the PEC-BC are applied at the side- and top- boundaries,

**S. Semi-open** the PEC-BC is applied at the radial side while an PBC acts at the top,

**O. Open** PBCs are applied to both the side (radial PBC) and top boundaries (axial PBC).

### 6.3.4 Numerics

The discretisation of equations (6.6), (6.7) and (6.8) into the Yee grid [65] (see section 3.3.2) generates a system of linear equations

$$\mathbf{A} \cdot \mathbf{v} = \mathbf{b} \quad (6.22)$$

where  $\mathbf{A}$  is a matrix that represents the operator for the Maxwell equation and the boundary conditions,  $\mathbf{v}$  a vector formed by the discrete electromagnetic field components located at the grid positions, and  $\mathbf{b}$  the source vector related to the excitation BC. The creation and management of the corresponding system of linear equations is performed using the LinSys library (see [52]). A direct solver (SuperLU, see [66]) is used to compute the solution of equation (6.22), i.e. the electromagnetic fields at the grid positions. From the distribution of the electromagnetic fields, the power

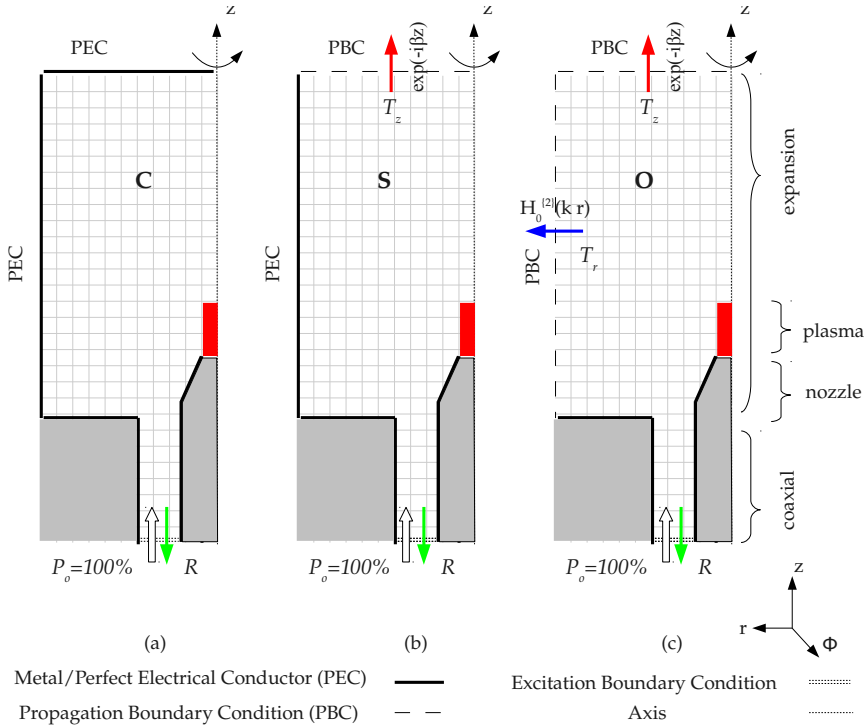


Figure 6.4: Different types of expansion regions: (a) Closed: a circular waveguide with short-cut at top i.e. a PEC-BC at the side and at the top, (b) Semi-Open: a circular waveguide open at the top side i.e. a PEC-BC at the side and axial PBC at the top and (c) Open: Open air i.e. radial PBC at the side and axial PBC at the top.

density  $Q$  is computed using a discrete version of equation (6.9) and the total power is computed integrating it over the volume.

The Poynting vector is computed using equation (6.11) for each grid cell. The Poynting vector is integrated over the surface area at the boundaries of bottom (excitation) entrance, top, and lateral sides. This gives the net power through these boundaries which is used in section 6.4 to define the reflected and transmission power coefficients.

For a grid with  $N \sim 10^5$ , the computation time is  $t_c \sim 10s$ , with a numerical precision of  $10^{-12}$ , more specifically for  $N = 75932$  the problem is solved within  $t_c = 4.94$  s in a desktop computer using a processor of type AMD PHENOM II X4 955 at 3.2 GHz and 530 MB out of 8 GB of memory of type DDR3 at 1333 MHz. The operating system is Ubuntu 10.04. This makes the EM model adequate for a future application in a self-consistent description of the fluid and electromagnetic aspects of MIPs. Apart

from torches it can also be applied to other types of MIPs like the surfatron (chapter 9) and surfaguide (chapter 8).

## 6.4 Results and Discussion

In order to study the power response of the various torch configurations, we define at the excitation boundary the incident  $P_i$  and reflected power  $P_r$ . Together they form the net power,  $P_{ns} = P_i + P_r$ , supplied to the MIP. At the boundaries (of the domain) we have  $P_t$ , that is the power transmitted to the surroundings. This can be divided into  $P_t = P_{t,z} + P_{t,r}$  thus the transmission at the top (axially emitted) and lateral side (radially emitted) (see figure 6.4). A *positive* sign refers to power *leaving* the domain (e.g.  $P_{t,z}$  and  $P_{t,r}$ ), whereas a *negative* sign refers to power *entering* the domain (e.g.  $P_i$ ). Also  $P_{abs}$  is positive; the energy used for heating the electrons can be regarded as leaving the EM domain. With this sign-convention equation (6.14) transforms into

$$\sum P = -|P_i| + |P_r| + |P_t| + |P_{abs}| = 0 \quad (6.23)$$

Dividing all terms by  $|P_i|$ , equation (6.23) can be written as

$$1 = R + T + A \quad (6.24)$$

where  $R = |P_r|/|P_i|$ ,  $T = |P_t|/|P_i|$  and  $A = |P_{abs}|/|P_i|$  are the reflection, transmission and absorption (power) coefficients of the configuration. The transmission coefficient can be further specified as  $T = T_z + T_r$ . The results given below are all based on simulations taking  $|P_i| = 100$  W. The results of  $R$ ,  $T$ , and  $A$  are obtained after normalising the corresponding powers by  $|P_i|$ , thus dividing by 100 W. The relative importance of  $R$ ,  $T$  and  $A$  will be denoted as the power response of the configuration.

### 6.4.1 Effect of the Remote Field Boundary Conditions

The power responses as functions of the vessel radius  $R_4$  of the three different configurations C, S, and O are given in figures 6.5, 6.6 and 6.7. They have in common that the model-plasma has the same electron density  $n_e = 10^{21} \text{ m}^{-3}$  and shape: a cylindrical bar with a radius of 1 mm and an axial extension of 20 mm. The height of the expansion zone,  $L = Z_4 - Z_1$ , in all three cases equals 150 mm which corresponds to  $Z_4 = 250$  mm. It should be noted, however, that only in the C-case the axial extend is limited by a physical (i.e. metallic) boundary. For the O- and S-cases the axial extend represents the position of the axial propagation BC. Mutatis mutandis the same applies to the radial extend as given by the  $R_4$ -value. In the C- and S- case this



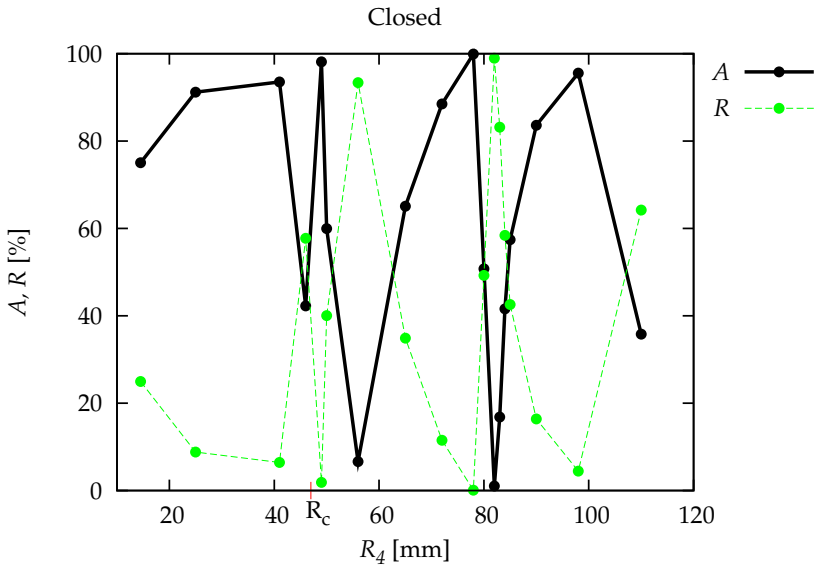


Figure 6.5: Power response of the Closed configuration with a bar-shaped plasma with of radius 1 mm, axial extension 20 mm and an  $n_e$ -value of  $10^{21} \text{ m}^{-3}$ . The height of the expansion zone equals 150 mm which corresponds with  $Z_4 = 250\text{mm}$ ; the absorption and reflection coefficients are given as functions of the radius  $R_4$ . As the configuration is closed the transmission is zero. Clear absorption peaks (resonances) can be seen at  $R_4 = 49 \text{ mm}$ ,  $78 \text{ mm}$  and  $98 \text{ mm}$ . Note the critical radius  $R_c = 47 \text{ mm}$ .

is a physical boundary, in the O- configuration the  $R_4$ -value represents the position of the radial propagation BC.

We can see in figure 6.5, that for the Closed configuration, the values for the transmission are absent. This is evident as the presence of both the radial and axial metallic limitation obstructs propagation. So only the values of the A- and R- coefficients remain. They strongly depend on the value of  $R_4$ . Strong absorption peaks ('resonances') are seen for  $R_4 = 49 \text{ mm}$ ,  $78 \text{ mm}$  and  $98 \text{ mm}$ . The positions of these peaks are comparable to those found with the analytical solution of a circular waveguides [15, 124]. However the presence of a plasma can change the positions and shapes of these peaks drastically. We can see this in figure 6.8, where curves  $A_1$  and  $A_2$  correspond to  $n_e = 10^{21}$  and  $5 \cdot 10^{21} \text{ m}^{-3}$ , respectively, both with  $\nu/\omega = 100$ . Note how the increment in  $n_e$  modifies the position and strength of the absorption peaks.

Below a critical radius ( $R_c = 47 \text{ mm}$  for  $f = 2.45 \text{ GHz}$ ) the character of the propa-

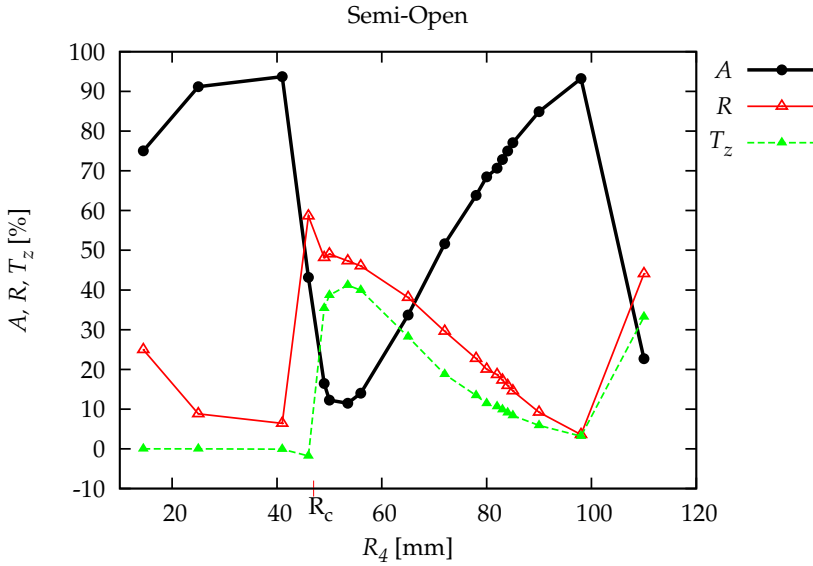


Figure 6.6: Power response of the Semi-open configuration with the same height and model plasma as that of figure 6.5; the absorption, reflection and transmission coefficients are given as functions of the radius  $R_4$ . As the configuration is closed in radial direction  $T_r$  is zero. Note that the absorption peaks at  $R_4 = 49$  mm and  $78$  mm found in the C case are no longer present; only a more broad absorption peak at  $R_4 = 98$  mm is left over. For  $R_4$  below the critical radius  $R_c = 47$  mm, the behaviour is the same as in the closed case because there is no propagating solution through the circular waveguide and the results are independent of the presence of a top metal wall.

gation changes and both C- and S- configurations share the same power response. The reason is that for  $R < R_c$ , the dispersion relation [74] provides an imaginary wavenumber and therefore only non-propagative solutions exist in the circular waveguide.

Another trend is found in the S-configuration as we can see in figure 6.6. There is no radial transmission across the metal wall, so that  $T_r = 0$ . Again the absorption and reflection depend on the radial position but this dependency is not so strong as in the C-case. The absorption peaks at  $R_4 = 49$  mm and  $78$  mm found in the C case are no longer present; only a the broad absorption peak at  $R_4 = 98$  mm is left over. Therefore, the operation of the torch around  $R_4 = 98$  mm looks reasonable.

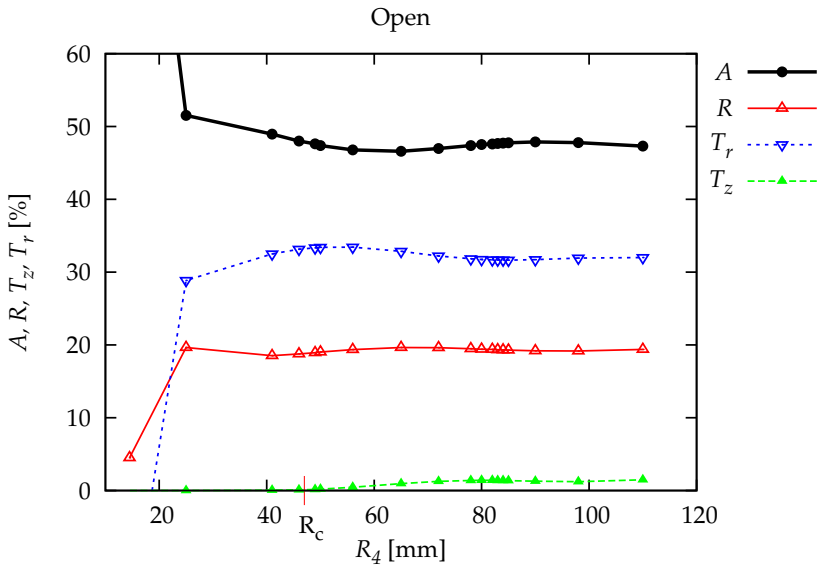


Figure 6.7: Power response of the Open configuration with the same height and model plasma that used for figures 6.5 and 6.6; the absorption, reflection coefficients and transmission are given as functions of the radius  $R_4$ . Note that there are no absorption peaks for  $R_4 \geq 40$  mm where the relative change is around 3%. For  $R_4 < 40$  mm the propagation boundary condition is apparently not adequate. For  $R_4 = 14.5$  mm the radial transmission even becomes negative i.e. power enters from the side.

As we said before for  $R < R_c$ , both the S- and C-configurations behave the same due to the presence of non-propagating solutions.

For the O-configuration we see in figure 6.7, that the power emitted in axial direction can be neglected and that all the power response coefficients are more or less independent of the radius  $R_4$  for  $R_4 > 40$  mm. The latter can be seen as a validation of the propagation boundary condition as placed at  $R_4$ . However, for  $R_4 < 40$  mm, the PBC is so close to the plasma that the electromagnetic wave is different from that assumed at the boundary and the reflections increases. Therefore the PBC formulated in equation (6.18) is not adequate for these low distances. Moreover, for  $R_4 = 14.5$  mm the radial transmission becomes negative i.e. power *enters* from the side instead of *leaving*. Of course, this cannot happen in reality and so we have to conclude that it can not be used for so small values of  $R_4$ .

The relative change is defined as  $\Delta f / f = \frac{\max(f) - \min(f)}{\max(f)}$ , with  $f = A, T, R$ . For  $R_4 >$

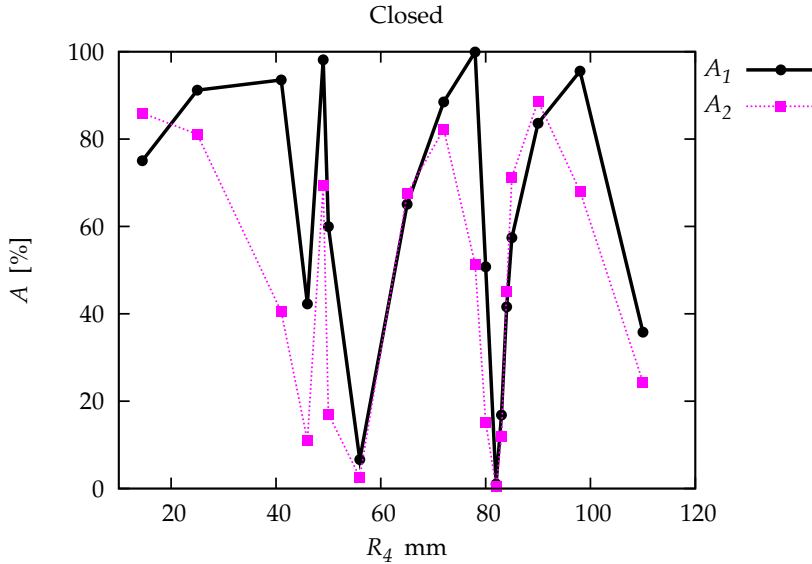


Figure 6.8: Absorbed power response as function of  $R_4$  in the closed configuration with the same height as that of figure 6.5. The model plasma is the same with exception that  $n_e$  equals  $10^{21} \text{ m}^{-3}$  in  $A_1$  and  $5 \cdot 10^{21} \text{ m}^{-3}$  in  $A_2$ . Note how the increment in  $n_e$  modifies the position and strength of the absorption peaks.

40 mm, we find slight changes with a relative change  $\Delta A/A = 3\%$ , which is even lower for the range  $R_4 > 80$  mm (where  $\Delta A/A = 1\%$  is found) in T, A and R that can be attributed to the presence of numerical dispersion i.e. the wavenumber of the wave changes at it propagates through the numerical grid (see for instance section 3.4.4 in [63]). This can be improved with an optimum grid refinement (for a detail explanation on numerical dispersion for different spacial and time discretisation schemes see [127]).

The low value of  $T_z$  for the O-configuration is better understood when looking to the radiation pattern of a monopole antenna close to a metal ground. As we can see in figure 6.9, the monopole antenna emits much more power in the radial than in the axial direction.

The figures 6.10, 6.11 and 6.12 show the influence of the axial extension of the expansion zone. In figure 6.10, giving A and R as a function of  $L = Z_4 - Z_1$  for the C-case, we see, just as in figure 6.5, sharp changes in A and thus R. The maximum in A takes place at  $L = 150$  mm, which is the value used for  $Z_4 = 250$  mm in figures 6.5, 6.6 and

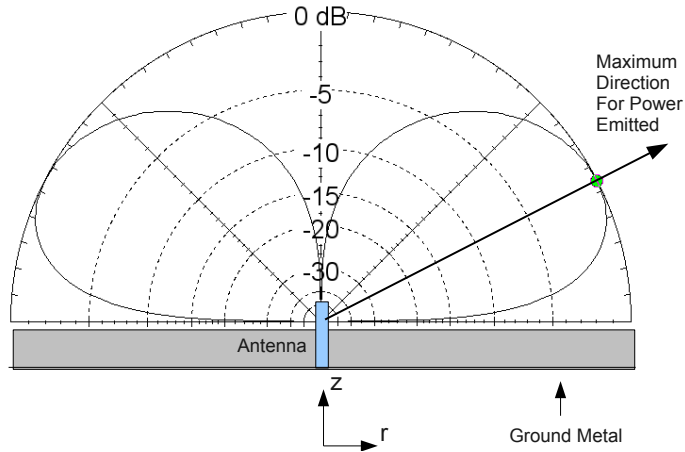


Figure 6.9: Radiation (transmission) pattern of a monopole antenna showing that an antenna close to a metallic ground transmits much more power in the radial than in the axial direction. Obtained using EZNEC (<http://www.eznec.com/>).

## 6.7.

For the O- and S-configuration, 6.7 and 6.6, we find only a slight dependence on  $Z_4$ , which again can be seen as a validation for propagation boundary condition performed at  $Z_4$ .

In the O- configuration, for  $L > 124$  mm the relative change for the absorption is  $\Delta A/A < 1\%$ . Between 124 mm and 84 mm,  $\Delta A/A \leq 3\%$ . However, for  $L = 64$  mm, the relative change becomes  $\Delta A/A > 9\%$ . This mean that the PBC is not adequate when placed at  $L < 84$  mm i.e. a distance to the plasma of 54 mm for 20 mm of plasma length.

In the S-Configuration, for L between 64 mm and 210 mm the relative change is less than 10%. This high relative change can be attributed to the presence of numerical dispersion i.e. the wavenumber of the wave changes at it propagates through the numerical grid (see for instance section 3.4.4 in [63]). This can be improved with an optimum grid refinement or by correcting (fitting) the wavenumber  $\beta$  used in equation (6.17) to minimise the reflection.

The above makes clear that especially the closed configuration shows absorption peaks as functions of the sizes of the enclosure. In previous studies it was found that the dependency of the resonances on the dimensions of the enclosure, strongly depend on plasma conditions (see [15]). If for instance the cavity is tuned such that the power absorption is at maximum for a plasma driven in argon, it will be brought

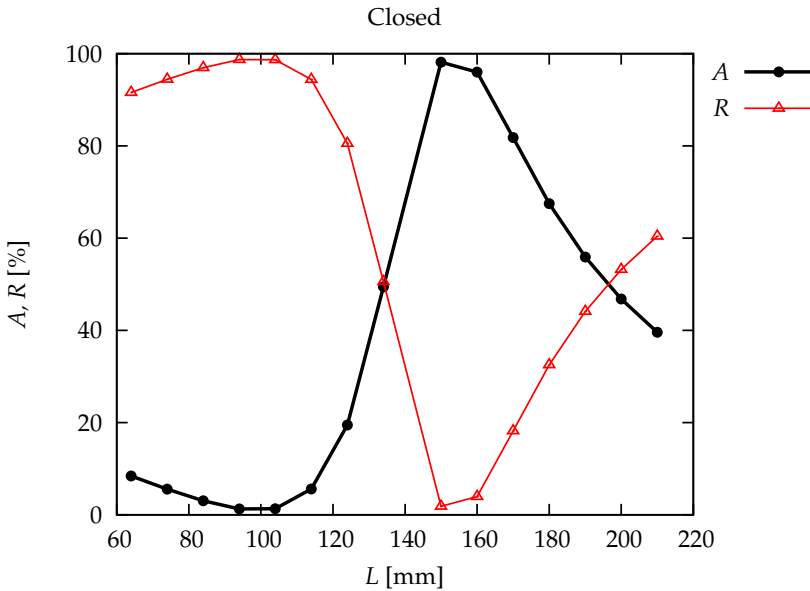


Figure 6.10: Power response of the Closed configuration with a bar-shaped plasma with of radius 1 mm, axial extension 20 mm and an  $n_e$ -value of  $10^{21} \text{ m}^{-3}$ . The radius of the expansion zone equals  $R_4 = 55 \text{ mm}$ ; the absorption and reflection coefficients are given as functions of the height of the expansion zone  $L = Z_4 - Z_1$ . As the configuration is closed the transmission is zero. Clear absorption peaks (resonances) can be seen at  $L = 150 \text{ mm}$ .

out of resonance if a small amount of  $\text{H}_2$  or other molecular species is introduced. After such a change in plasma chemistry the cavity must be returned. This implies that the C-configuration is not so suitable for plasma applications. It is illustrative to refer to the Evenson cavity [106] and the Beenakker cavity [14] with the improvement performed on it by [128].

From now on we confine ourselves to the open case which indeed nowadays is the most often used configuration.

## 6.4.2 Effect of the Electron Density Value

As stated before the plasma is located at the transition region where the electromagnetic structure of the coaxial waveguide converts into that of the expansion region. In order to investigate in how far the plasma plays a role in this conversion we studied

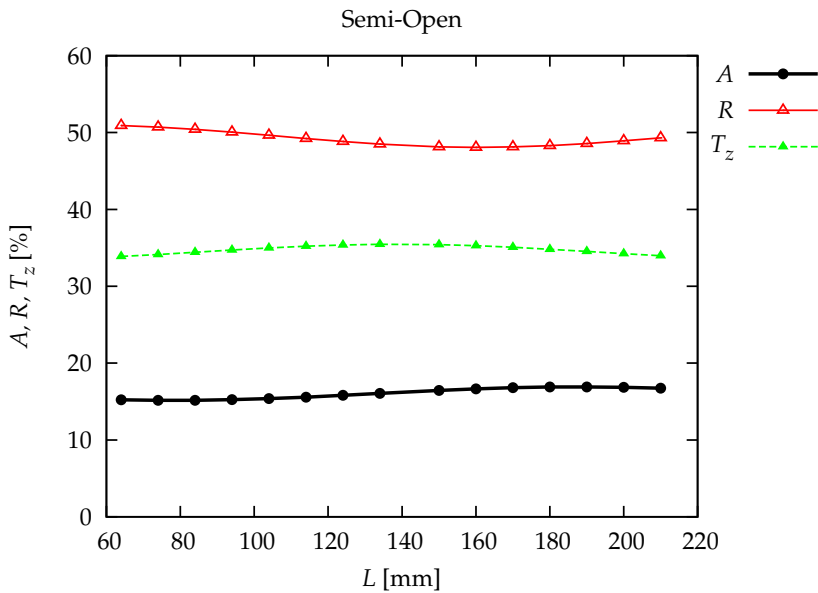


Figure 6.11: Power response of the Semi-open configuration with the same expansion zone radius and model plasma as that of figure 6.10; the absorption, reflection and transmission coefficients are given as functions of the height of the expansion zone  $L = Z_4 - Z_1$ . As the configuration is closed in radial direction  $T_r$  is zero. Note that the absorption peaks are not longer present and the relative change is around 10%.

the power response of the open configuration as a function of the electron density. In all cases the plasma shape is fixed to that of a cylindrical bar with a radius and length of 1 mm and 20 mm respectively. The results, given in figure 6.13, show that, just as in figures 6.7 and 6.12, the transmission in axial direction can be neglected. Thus the dominant power channels are the radial transmission  $T_r$ , the absorption  $A$  and reflection  $R$ . It is seen that, starting at  $n_e = 10^{21} \text{ m}^{-3}$  the A-value increases from 20 to almost 50% for increasing  $n_e$  and that this increase takes place at the expense of the R-value. Above  $n_e = 10^{21} \text{ m}^{-3}$  the radial transmission increases sharply thereby decreasing the A -value. Apparently the plasma serves as an antenna and the higher  $n_e$  the better the antenna is.

However, the better the antenna function the less energy is left over for absorption. This sets an optimum value of the plasma density. At lower  $n_e$ -values more energy is absorbed thereby increasing the plasma density. However, due to this  $n_e$ -increase the plasma improves its antenna function, so that more energy is emitted and thus less is used for the absorption in the plasma. This tends to decrease  $n_e$  which in turn leads

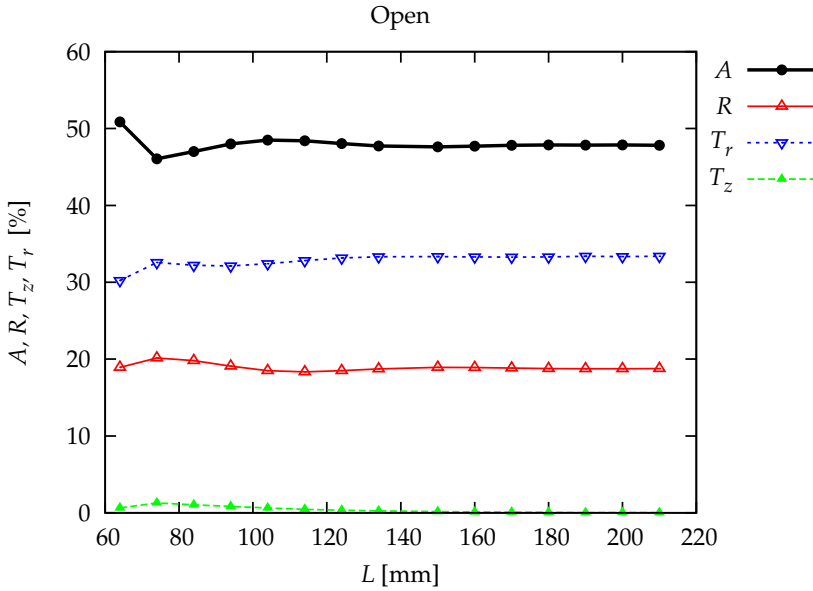


Figure 6.12: Power response of the Open configuration with the same expansion zone radius and model plasma as that of figures 6.10 and 6.11; the absorption, reflection and transmission coefficients are given as functions of the height of the expansion zone  $L = Z_4 - Z_1$ . The Open-Configuration behaves as a monopole antenna near a ground metal (see figure 6.9) and this explains that  $T_r$  is much larger than  $T_z$ . Note that the absorption peaks are not longer present and that for  $L > 124$  mm the relative change for the absorption is  $\Delta A/A < 1\%$ . Between 124 mm and 84 mm,  $\Delta A/A \leq 3\%$ . However, for  $L = 64$  mm, the relative change becomes  $\Delta A/A > 9\%$ .

to an increase in absorption. This negative feed-back might be (one of) the reason(s) for the fact that a MIP torch show an *unstable* behaviour.

### 6.4.3 Effect of the Shape of the Transition Region (the 'gap')

In order to understand the antenna function we played with other elements of the *transition region*, hereafter shortly denoted as the *gap*. The possible structures are given in figure 6.14 where the model-plasma remains unaltered; it is bar-shaped with a electron density of  $10^{21} \text{ m}^{-3}$  while the radius and length are 1 mm and 20 mm, respectively. Figure 6.14(a) shows the influence of the extension of the inner conductor given by the insertion depth  $d = Z_2 - Z_1$ , figure 6.14(b) shows a perpendicular partial



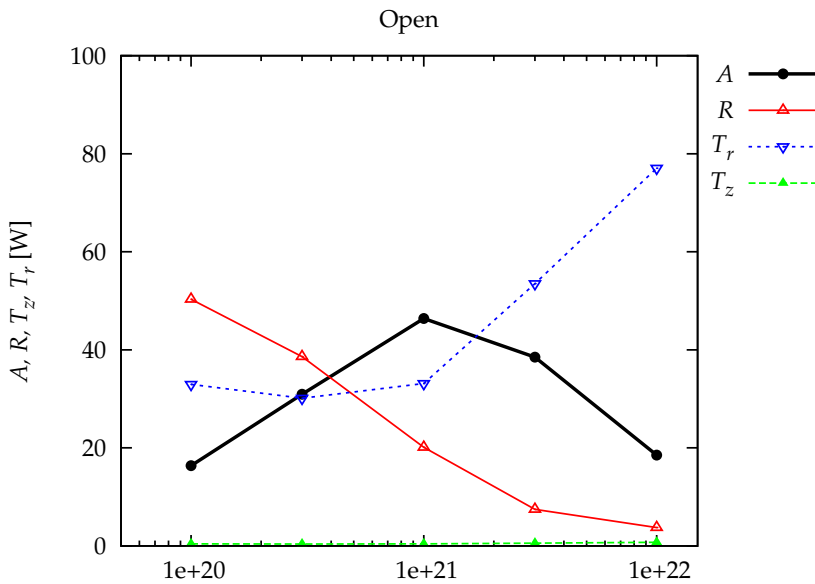


Figure 6.13: Power response of the Open configuration with the same expansion zone radius as that of figures 6.10 and same height of that of figures 6.5; the absorption, reflection and transmission coefficients are given as functions of the electron density  $n_e$ . At lower  $n_e$ -values more energy is absorbed thereby increasing the plasma density. However, due to this  $n_e$ -increase the plasma improves its antenna function, so that more energy is emitted and thus less is used for the absorption in the plasma. This tends to decrease  $n_e$  which in turn leads to an increase in absorption.

coverage of the gap, while figure 6.14(c) deals with an oblique partial coverage parallel to the tip of the inner conductor. The perpendicular coverage of figure 6.14(b) is inspired by [16] (see figure 6.1(a)). The oblique coverage is inspired by [129]. The results are schematically given in figure 6.15.

It is found that lowering the inner conductor from  $d = 6$  mm to  $-6$  mm leads to an enhancement of the reflection from about 20% to 31% but also that the absorption increases from about 46% to 55%. In figure 6.16, the extension of the nozzle is further reduced and even withdrawn into the outer cylinder of the coaxial waveguide. As we can see for  $d < -25$  mm the complete plasma is hidden in the outer conductor wall and the power response is that of the C- and S-configurations, figures 6.5 and 6.6, for  $R_4 = R_3 = 14.5$  mm. This operation seems lucrative since large absorption-values are obtained. However such a plasma in a cylinder is not very practical as it might cause ablation of the cylinder wall. Moreover, since the main plasma part will not

operate in an open region, it will not be applicable for spectrochemical analysis or for the treatment of surfaces and volumes.

The coverage of the gap has a substantial effect on the reflection which changes from 20% (no coverage) to about 32% (oblique coverage) and 52% (horizontal coverage). So the negative effect of coverage is that more power is sent back to the magnetron power generator; the positive side is that from the net power admitted to the torch a larger fraction is absorbed by the plasma.

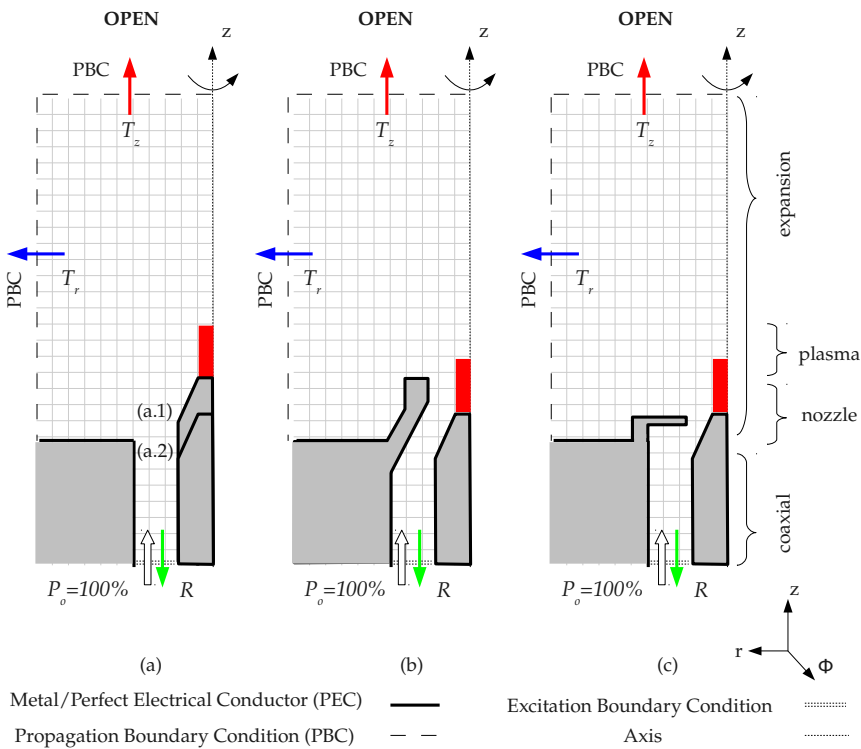


Figure 6.14: Different types of transition or 'gap-' regions: (a.1) Open gap with nozzle insertion of  $d = Z_2 - Z_1 = 6$  mm, (a.2) Open gap with nozzle insertion of  $d = -6$  mm, (b) Oblique Obstruction (similar to [129]) and (c) Obstruction perpendicular to the nozzle; similar to the gap in the TIA design [16]. The extension of the nozzle in (b) and (c) is that of (a.2). All of them are in O-configuration.

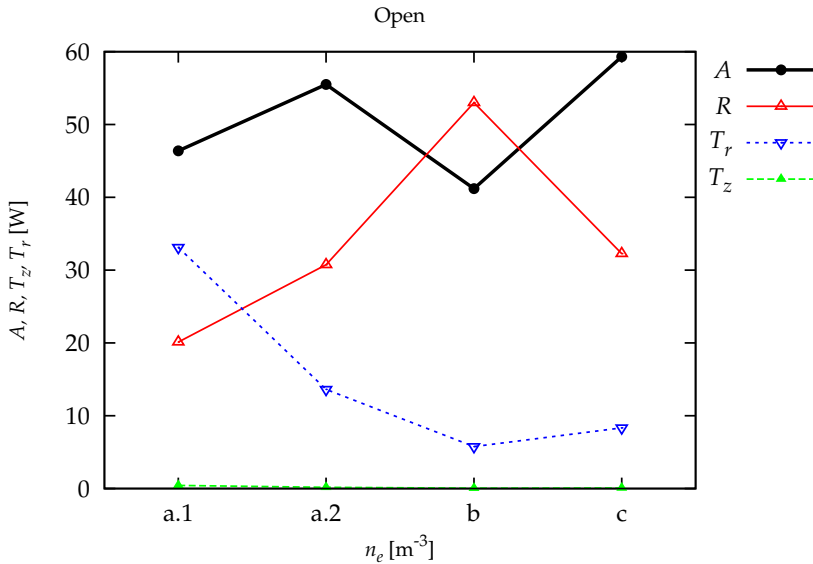


Figure 6.15: Power response versus the shape of the gap for the open configuration with the same expansion zone radius height of that of figures 6.13. (a.1) Open gap with nozzle insertion of  $d = Z_2 - Z_1 = 6$  mm, (a.2) Open gap with nozzle insertion of  $d = -6$  mm, (b) Oblique Obstruction (similar to [129]) and (c) Obstruction perpendicular to the nozzle; similar to the gap in the TIA design [16]. The extension of the nozzle in (b) and (c) is that of (a.2). All of them are in O-configuration.

## 6.5 Conclusions

A flexible and versatile EM model is constructed using the PLASIMO platform [52, 130]. It is employed to explore the EM features of axi-symmetric microwave induced plasma (MIP) torches. The basis of the model is formed by the Maxwell equations used in a full vectorial form, meaning that for the TM mode the three vector components  $E_r$ ,  $E_z$  and  $H_\phi$  are solved in coupled manner. This is an important difference with most of the others methods found in literature for which the EM problem is described as a Helmholtz-like wave equation for the  $H_\phi$  component solely.

The full-vector approach has the advantage that the boundary conditions can be implemented in a natural way. This, together with the employment of a direct matrix solver, leads to a speed-up in convergence by a factor 100 when compared to [15]. For a grid of  $N \sim 10^5$  cells the solution is reached in  $t_c \sim 10$  s whereas the iterative

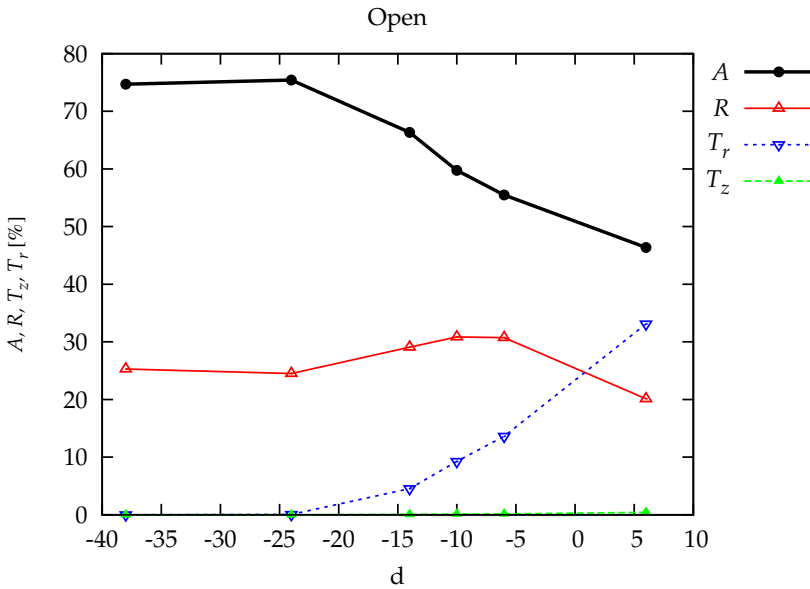


Figure 6.16: Power response versus the insertion depth  $d = Z_2 - Z_1$  of the nozzle for the Open gap with the same expansion zone radius and height of that of figures 6.15. Lowering the inner conductor from  $d = 6$  mm to  $-6$  mm leads to an enhancement of the reflection from about 20% to 31% but also that the absorption increases from about 46% to 55%. For  $d < -25$  mm the complete plasma is hidden in the outer conductor wall and the power response is that of the C- and S-configurations, figures 6.5 and 6.6, for  $R_4 = R_3 = 14.5$  mm. Note that  $T_z = 0$ , because the region below the outer conductor for  $z$  between  $Z_p$  and  $Z_3$  acts as a circular waveguide which radius  $R_3$  is below the critical radius  $R_c = 47$  mm and therefore waves cannot propagate.

process depicted in [15], demands  $t_c \sim 10^3$  s for  $N \sim 10^4$ .

Three types of configurations were investigated; they are classified as Closed C-, Semi-open S- and Open -configurations. Changing from one configuration-type to another is realised by simply changing the boundary condition of the expansion zone.

It is found that the C-configuration, for which the expansion takes place in a closed cylindrical cavity, strongly depends on the radial  $R$  and axial extension  $L$ . For various  $R$ - and  $L$ -values sharp resonances (strong absorption peaks) were found. Especially the radial sizes for which resonance are obtained are extremely sensitive to plasma features. This makes the C configuration less suitable for applications in the field for which (sudden) changes in the plasma conditions can be expected such as found in

the field of spectrochemistry and the treatment of surfaces and volumes.

The features of the S-configurations, for which the wave expansion takes place in an open circular wave guide, are much less dependent of the sizes and therefore not so sensitive to plasma chemistry. These S-configuration can be seen as a model for the practice often used in laboratories to place MIP torches in an open cylindrical grid with the purpose to protect the environment against microwave EM radiation. Calculations show that this is good practice provided the radius of this grid is around 90 mm.

Most attention is paid to torches of the open configuration as these are most often used in practice. It is found that the power balance as expressed by the values of the absorption, transmission and reflection depends on the electron density of the plasma. The reason is that plasma is an essential element in the conversion of the EM waves of the co-axial structure to the EM-structure of the expansion region. This antenna function is better for increasing  $n_e$ - values. However, this implies that for increasing  $n_e$  the absorption decreases so that the plasma does not get enough energy to keep  $n_e$  high. This negative feed-back might be the reason for the instabilities often seen in the operation of open configured MIP torches.

Apart from the electron density we also investigated other aspects of the antenna- say gap- region. So for instance it is found that the plasma absorption strongly depends on the presence of a metallic obstruction placed at the end of the coaxial waveguide and the degree at which the inner conductor of this coaxial waveguide extends into the expansion zone. The influence of two different gap obstructions were investigated namely a horizontal and an oblique one. It is found that these both enhance the reflection and absorption.

Due the flexibility of this EM model it can be used in future for further explorations of the impact of the various construction elements on the performance of torches and other types of MIPs. Moreover, it is ready to be used in combination with a set of transport equations to get a self-consistent description of the plasma-EM interaction.

---

# 7

## Surface Wave Discharges: Introduction, Characteristics, and Simulations

---

## 7.1 Introduction

A particular sub-class of MIPs is the group of surface wave discharges (SWDs). The specific feature of this class is that an electromagnetic wave propagates along the plasma column creating the plasma that, at the same time, serves as a propagation medium bringing the energetic wave to regions located further away from the *field applicator*. This device that transfers the energy from the microwave power supply to the SWD is also known as the *launcher*. We will focus on cylindrical discharges in which waves are launched in the axial  $z$ - direction.

The EM waves studied in the coming chapters are part of a much bigger family of waves known as surface waves; waves that propagate along the interface between differing media, for instance two fluids with different densities or seismic wave in the earth crust between two different type of materials. In our case of *electromagnetic* surface waves, the propagation is guided by a gradient of the refractive index. In radio transmission, a ground wave or gliding wave is a surface wave that propagates close to the surface of the Earth [131]. Lower frequencies, especially AM broadcast waves in the medium and long-wavelength bands, travel efficiently as surface waves. This is because they are more efficiently diffracted by the shape of the Earth due to their low frequencies. The Earth has one refractive index and the atmosphere, mainly due to the ionosphere, has another. Thus, together they constitute an interface that supports the surface wave transmission. These ground waves have been used since the beginning of the previous century for broadcast and communication purposes.

During the World War II the effort on developing the radar (an acronym for RAdio De-tection And Ranging) resulted in a huge quantity of information and new techniques in the microwave field, see e.g. the Waveguide Handbook of Nathan Marcuvitz [132]. In 1958, Trivelpiece studied the slow wave propagation [17] for plasma-filled waveguides. He described that when the plasma partially fills the waveguide, a surface wave mode can propagate. It was not shown until 1977 by Moisan [22] that EM surface waves can be used for *sustaining* long plasmas columns. Two types of sources were proposed: the surfatron [86] and the surfaguide [133]. Both configurations are studied in the coming chapters.

This chapter starts in section 7.2 with a short overview of the modelling of surface wave discharges (SWDs). In section 7.3, we introduce the SWDs that are modelled in chapters 8, 9 and 10. We will also comment on the simulation similarities of these discharges with respect to their configuration, in sections 7.3.1 and 7.3.2 and chemistry, in section 7.3.3.

## 7.2 Surface Wave Discharge Modelling

In the past many models [23, 24, 42, 86] were constructed to model the wave propagation region, whereas less attention was paid to the plasma region inside the wave launcher. One of the reasons is that the plasma zones in the launcher are not easy to observe.

The models developed in the past [23, 24, 86] in general have two components. A zero-dimensional electromagnetic model that describes the axial propagation of the EM wave, known as the *dispersion relation*, and a zero-dimensional model to describe the plasma aspects, i.e. the *local power balance* [12]. The wave and plasma module are solved in conjunction with each others; the wave module needs the value of the electron density and the momentum transfer collision frequency, whereas the plasma needs the absorbed power density. A central role is played by the parameter  $\theta$ , the power needed to maintain an electron-ion pair in the discharge (see equations (4.36 and (5.31), in chapters 4 and 5, respectively).

The plasma modules were mainly based on the positive column model, meaning that the plasma column description was based on the balance between ionisation production and transport losses. Basically the balance has the same structure as equation (5.33) given in chapter 5 which sets the condition for the electron temperature. Its validity implies that  $\theta$  is independent of the electron density [42].

More advanced are the plasma models based on a combination of a collisional radiative model and a Boltzmann Solver [41, 42, 83]. Here  $\theta$  will generally depend on the electron density.

An overview of characteristic of argon SWDs for different electron creation and losses regimes is given in table 7.1 as a function of  $pR_p$ , the product of pressure and radial size of the plasma.

At low pressure ( $< 1$  Pa) the ionisation is *direct* in nature while the transport is close to the *free-fall* regime [134]. This implies that  $\theta$  is independent from the electron density.

As the pressure increases ( $\sim 10$  Pa), non-linear electron processes such as *step-wise* ionisation, in which excited states are involved, become more important, and  $\theta$  becomes dependent on the electron density [42, 135]. This demands for a coupled and thus iterative solution. Note that, for this intermediate pressure range, the recombination is still small, so that the plasma remains wall-stabilised. This means that due to the absence of *volume* recombination the plasma extends to the wall where it is quenched due to wall-recombination.

As the pressure is further increased the volume recombination becomes more important. The leading recombination mechanism is not the inverse of electron impact ionisation, known as two-electron recombination [100], but a reaction scheme based



on the formation and destruction of molecular ions (cf. 5.24 and 5.25). This is denoted by molecular assisted recombination (MAR) [31, 46, 120]. Therefore, the discharge changes from diffusion toward recombination controlled. A characteristic of the recombination regime is the contraction of the discharge [31, 35]; the discharge is no longer *attached* to the wall.

The two-component structure of the models described above assumes that plasma and electromagnetic parameters are slowly-changing functions of the axial position. This assumption is normally referred to as the WKB approximation cf. [136]. The condition is no longer fulfilled if the plasma is strongly recombining. Another shortcoming of the classical SWD models is that they only provide information on the plasma down-wave, that is the plasma outside the launcher. Thus, there is no attention paid to the discharge enclosed by the launcher and the residual power, that is the power carried by the wave beyond the plasma-wave interaction.

We are interested in a more complete description of SWDs that combines the plasma inside the launcher, the wave guided plasma outside the launcher and the residual EM power. To that end we had to design a two dimensional model (chapters 4, 9) which we did using the PLASIMO tool-kit.

The study of the residual power transmitted to the environment is especially important to get insight of the deposition reactor used in Draka Communications. The reason is that the residual power can create superimposed standing wave patterns in the plasma due to the reflection of waves with metals in the environment.

$pR_p$ [Pa · mm] ([Torr · cm])	$NR_p$ [ $m^{-2}$ ]	Main Electron Production Mechanism	Main Electron Losses Mechanism	Shape and Behaviour
$\lesssim 5 \cdot 10^{-1}$ ( $\lesssim 3.7 \cdot 10^{-4}$ )	$\lesssim 1.2 \cdot 10^{14}$	DI	FD	Large sheath thickness $\lesssim R_p$ [137], Length <i>increasing</i> with p [25].
10 – 1300 ( $\lesssim 7.5 \cdot 10^{-3} - 1$ )	$2.4 \cdot 10^{15}$ $-3.2 \cdot 10^{17}$	SI	AD	Radial uniform, Small sheath thickness $\ll R_p$ , Single or double Filaments at the end.
1300 – 2.600 (1 – 2)	$3.2 \cdot 10^{17}$ $-6.3 \cdot 10^{17}$	Transition region from AD regime to AD-MAR regime [138].		
2600 – $10^4$ (2 – 7.5)	$6.3 \cdot 10^{17}$ $-2.4 \cdot 10^{18}$	SI	AD-MAR	Radial Uniformity disturbed by MAR, Single or double Filaments at the end, Length <i>decreasing</i> with p <i>increasing</i> .
$10^4 - 5 \cdot 10^4$ (7.5 – 38)	$2.4 \cdot 10^{18}$ $-1.2 \cdot 10^{19}$	SI	MAR	Contraction, Filament(s) on background Diffusive discharge [139].
$\gtrsim 5 \cdot 10^4$ ( $\gtrsim 38$ )	$\gtrsim 1.2 \cdot 10^{19}$	SI	MAR	Filament structures, Other spatial structures [140].

Table 7.1: Characteristics of argon SWDs as a function of  $pR_p$ , the product of pressure and radial size of the plasma (see [25, 41, 42, 135, 138–140]). The parameter  $NR_p$  is the gas density times the radius obtained from  $pR_p$  using the ideal gas law with a gas temperature of 298 K. Note that these  $pR_p$ -ranges, here given for argon, depend on different discharge operating conditions: the EM frequency, gas temperature, nature of filling gas, power range, etcetera. *Abbreviations:* DI = Direct Ionisation, FD = Free-fall Diffusion, SI = Step-wise Ionisation, AD = Ambipolar Diffusion, MAR = Molecular Assisted Recombination. Note that diffusion is seen as a loss mechanism for electron-ions pairs because it is followed by recombination at the wall.

## 7.3 Simulations

In the coming chapters we report on the study of three different types of SWDs. They mainly differ from each other in launcher-type. However, the launchers have in common that they act as cavities designed to create high  $E$  fields with rotational symmetry<sup>a</sup> at the launcher gap region. The main differences from one SWD to the other, comes from the shape of the launcher.

- Surfaguide at atmospheric pressure (chapter 8)

Designed in 1978 by Moisan, [86], the surfatron is based on a rectangular waveguide feeding the launcher. The surface wave generated at the gap of the launcher creates its own propagating medium i.e. the plasma column.

We discuss the contraction phenomena and how it is ruled by MAR processes. The relation between absorbed power and plasma length will be given and compared with experimental results [141]. It is found that the plasma contraction strongly depends on the wall temperature.

- Surfatron at intermediate pressures (chapter 9)

Designed in 1975 by Moisan, [142], this construction is based on a coaxial antenna feeding the launcher. Three plasma regions are distinguished: the column between the *gas side*<sup>b</sup> and the launcher, the column *inside* the launcher, and the column between the launcher and the *pump side*. Special attention is given to the latter two.

The plasma column inside the launcher is important as its behaviour is similar to that of the deposition reactor modelled in chapter 10.

- Deposition reactor at intermediate pressure (chapter 10)

Designed by Philips Research Laboratories in 1976 [3, 20], the (plasma-chemical-vapour-) deposition reactor consists of a launcher fed by a rectangular waveguide. The plasma of interest is the discharge formed inside the launcher. Two chokes in the metal wall of the launcher function to confine the plasma region, their task is to minimise the power leaving this region, thus to reduce the residual power. We will use the term *deposition reactor* instead of launcher, because this set-up is designed to confine the waves *inside* rather than *launching* them as in the case of the surfatron and surfaguide launchers.

Table 7.2 gives a summary of the features of the three SWDs under study.

---

<sup>a</sup>azimuthally constant in this work i.e.  $m = 0$  for a dependency of the form  $\exp(im\phi)$ , where the integer number  $m$  defines an  $m$ -fold rotational symmetry

<sup>b</sup>Here *gas side* and *pump side* indicate boundary names as given in figure 7.1.

Configuration	Surfatron	Surfaguide	Reactor
$P_{abs}$ [W]	32,59	100 – 200	50
$p_{out}$ [Pa]	660, 2000, 8800	$10^5$	$10^3$
$f$	2.45 GHz		
$\Phi_{max}[10^{-6}m^3/s]$	$\sim 0.7$	19.6	26.5
$v_{b,z}$ [m/s]	$\sim 0.05$	2	0.3
$\mu$ [kg m <sup>-1</sup> s <sup>-1</sup> ]	$< 10^{-4}$	$10^{-4}$	$10^{-4}$
Re	$4 \cdot 10^{-3} - 4 \cdot 10^{-2}$	10 – 100	$10^{-3}$
$n_e$ [m <sup>-3</sup> ]	$5 \cdot 10^{19}$	$10^{21}$	$5 \cdot 10^{19}$
$T_e$ [K]	12500-10500	10000	13000
$N_{Debye}$	60-50	10	70
$\nu_{eh}$ [Hz]	$3 \cdot 10^9 - 1.5 \cdot 10^{10}$	$1.5 \cdot 10^{11}$	$2.5 \cdot 10^9$
$\omega/\nu_e$	$\sim 10^5$	$2 \cdot 10^3, 5 \cdot 10^3$	$10^5$

Table 7.2: Summary of the features of the three SWDs under study: the Surfatron, Surfaguide and Deposition Reactor. Here  $P_{abs}$  is the total power absorbed by the plasma,  $p_{out}$  the pressure at the pump side of the dielectric tube,  $f$  the EM microwave frequency,  $\Phi_{max}$  the maximum value of the (volumetric) flow rate,  $v_{b,z}$  the central value of the bulk velocity in axial direction,  $\mu$  the dynamic viscosity, Re the Reynolds number,  $n_e$  the electron density,  $T_e$  the electron temperature,  $N_{Debye}$  the number of particles in a Debye sphere,  $\nu_{eh}$  the collision frequency for momentum transfer from electrons to heavy particles,  $\omega (= 2\pi f)$  the angular frequency of the EM wave and  $\nu_e = 2(m_e/m_h)\nu_{eh}$  the frequency of energy transfer from electrons to heavy particles via elastic collisions.

### 7.3.1 Configuration: Geometry

The description of the geometrical aspects of the three SWDs under study will be guided by figure 7.1. This figure gives the geometry of the most simple configuration, that of the surfaguide (chapter 8). It can be seen as the basic computational domain used in chapters 8, 9 and 10.

The three SWDs have in common that the plasma is created in a cylinder with inner radius  $R_p$ . The electromagnetic domain is composed of four zones: plasma, dielectric tube, air and launcher. The latter consists basically of a metal cylinder with a gap. The precise structure depends on the type of SWD and will be given in each chapter.

The launcher is often overlooked in SWD modelling. However, in the plasma of chapter 10 the active region for deposition is located inside the launcher. This is one of the reasons why we are interested in modelling this region as well.

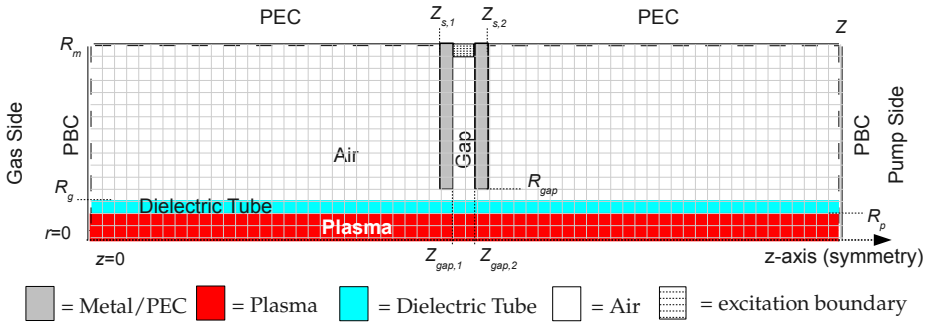


Figure 7.1: The basic computational domain for SWDs modelling is that of a surfaguide (chapter 8). In chapters 9 and 10, we show the modifications needed to represent the surfatron and the deposition reactor, respectively. The common feature is a two-fold composition of a cylindrical *plasma region* with radius  $R_p$  and an electromagnetic region that contains the plasma region and the dielectric tube and air parts. with radii  $R_g$  and  $R_m$ . The launcher consists of a metal cylinder with a gap and an electromagnetic excitation boundary. The boundary types are treated in chapter 3 for the EM field. Note that the EM boundary conditions in the radial direction can easily be changed from Perfect Electrical Conductor (PEC) boundary condition to Propagative Boundary Condition (PBC). In this way we can easily include or exclude a metal cylinder with radius  $R_m$ . For the meaning and values of geometrical parameters like  $Z_{s,1}$  and  $Z_{gap,1}$ , we refer to section 8.2.1 and table 8.1.

### 7.3.2 Configuration: Boundary conditions and Control Parameters

Appropriate boundary conditions are needed for solving the transport equations: the species balance (4.3), the bulk continuity (4.27), the Navier-Stokes (4.28), the heavy particle energy balance (4.31) and the electron energy balance (4.34). These are given in table 7.3 and of course only applicable for the plasma region. The pump side pressure is fixed to  $p_{out}$ , whereas at the gas side the pressures is set to  $p_{in}$ . This requires the boundary conditions for the bulk velocity components shown in table 7.3. Note that it is possible to use an alternative approach by setting the flow rate at the gas side. This implies the use of a different set of boundary conditions (see chapter 8). The gas temperature is set constant at the gas side and at the wall of the discharge tube. In other cases we have used the continuity of heat flux at the plasma-wall interface and set the temperature at the outer dielectric tube wall.

The boundary condition for the electron temperature at the tube wall, gas side and pump side is of type homogeneous Neumann. The effect of this boundary condition (applied at the tube wall) on the solutions was addressed in [30], where it is compared with a more advanced boundary condition [30, 33] that takes into account the electron energy loss across the sheath, using the *Bohm criterion* [143].

The densities at the wall, are determined by describing the associated flux  $\Gamma_{s,\perp}$  using the Bohm velocity for charged species and the thermal velocity for neutral species [10, 33]. A recombination coefficient is included as well. This is given in the form of a special Neumann boundary condition [10, 33]

$$\Gamma_{s,\perp} = -D_s \frac{\partial n_s}{\partial \mathbf{n}} = \Gamma_{s,\perp}^{out} - \Gamma_{s,\perp}^{in} \quad (7.1)$$

with the destruction flux equals to

$$\Gamma_{s,\perp}^{in} = \gamma_i v_s^{av} n_s \quad (7.2)$$

where  $v^{av}$  is the Bohm velocity for (positive) ions or the thermal velocity for neutrals. The total creation of species  $s$  at the wall through wall reaction is described by the production flux and equals

$$\Gamma_{s,\perp}^{out} = \sum_{r=Wall} v_{r,s}^p \Gamma_r^{in}, \quad (7.3)$$

with  $v_{r,s}^p$  the stoichiometric coefficient for wall reaction  $r$  that produces species  $s$ .

For the gas and pump sides and the axis, a homogeneous Neumann boundary condition is used.

In chapters 9 and 10, the density of the ion  $\text{Ar}^+$  (see section 7.3.3) is set to a constant value at the wall, gas and pump sides. The Dirichlet BC reads  $n_{\text{Ar}^+} = 7.5 \cdot 10^{17} \text{ m}^{-3}$ .

Par.	Gas Side	Pump Side	Tube wall	Axis
$p$	$p_{in}$	$p_{out}$	$\frac{\partial p}{\partial r} = 0$	$\frac{\partial p}{\partial r} = 0$
$v_{b,z}$	$\frac{\partial v_{b,z}}{\partial z} = 0$	$\frac{\partial v_{b,z}}{\partial z} = 0$	$v_{b,z} = 0$	$\frac{\partial v_{b,z}}{\partial r} = 0$
$v_{b,r}$	$v_{b,r} = 0$	$\frac{\partial v_{b,r}}{\partial z} = 0$	$v_{b,r} = 0$	$v_{b,r} = 0$
$T_h$	$T_{h,w}$	$\frac{\partial T_h}{\partial z} = 0$	$T_{h,w}$	$\frac{\partial T_h}{\partial r} = 0$
$T_e$	$\frac{\partial T_e}{\partial z} = 0$	$\frac{\partial T_e}{\partial z} = 0$	$\frac{\partial T_e}{\partial r} = 0$	$\frac{\partial T_e}{\partial r} = 0$
$n_{Ar^+}$	constant	constant	constant	$\frac{\partial n_{Ar^+}}{\partial r} = 0$
$n_+$	$\frac{\partial n_+}{\partial z} = 0$	$\frac{\partial n_+}{\partial z} = 0$	$-D_+ \frac{\partial n_{ion}}{\partial z} = \Gamma_{s,\perp}^{out} - \Gamma_{s,\perp}^{in}$	$\frac{\partial n_+}{\partial r} = 0$
$n_*$	$\frac{\partial n_*}{\partial z} = 0$	$\frac{\partial n_*}{\partial z} = 0$	$-D_* \frac{\partial n_*}{\partial z} = \Gamma_{s,\perp}^{out} - \Gamma_{s,\perp}^{in}$	$\frac{\partial n_*}{\partial r} = 0$

Table 7.3: Boundary conditions for the standard cases. Here  $p$  is the pressure,  $v_{b,z}$  and  $v_{b,r}$ , respectively, the axial and radial components of the plasma bulk flow velocity,  $T_h$  the gas temperature,  $T_e$  the electron temperature,  $D$  the diffusion coefficient and  $T_{h,w}$  the constant value of the gas temperature at the wall. Note that we use the symbols '+' and '\*' to refer to ions and excited states species, respectively.

This is done to avoid under-dense plasma<sup>c</sup> conditions and resonance phenomena that appears as consequence of the cold approximation for electron momentum balance (see appendix A).

### 7.3.3 Chemistry

The species included in the model are the lumped states of the 4s and 4p groups Ar(4s), Ar(4p) and atomic and molecular ions Ar<sup>+</sup>, Ar<sub>2</sub><sup>+</sup>. All these species are treated as Transport Sensitive species (see chapters 4 and 5) meaning that their densities are described with a balance equation of type 4.3 i.e. including transport. This does not apply for the electrons {e} and argon atoms in the ground state Ar. The electron density follows from charge neutrality whereas the Ar density follows from the equation of state. The rate coefficients for the reactions converting these species into each other were obtained from [35], with the exception of those in which Ar(4p) is involved; in this case the rate coefficients were obtained from [98].

An overview of the reactions is given in table 7.4 and figure 7.2. Note that we do not include radiative decay of excited states.

<sup>c</sup>an under-dense plasma region is defined as  $n_e < n_{e,c}$  with  $n_{e,c}$  the critical density that makes the real part of the complex plasma permittivity (chapter 3) equals to zero, i.e.  $\text{Re}\{\hat{\epsilon}_p\} = 0$ . Consequently, an over-dense plasma region is defined for  $n_e > n_{e,c}$ .

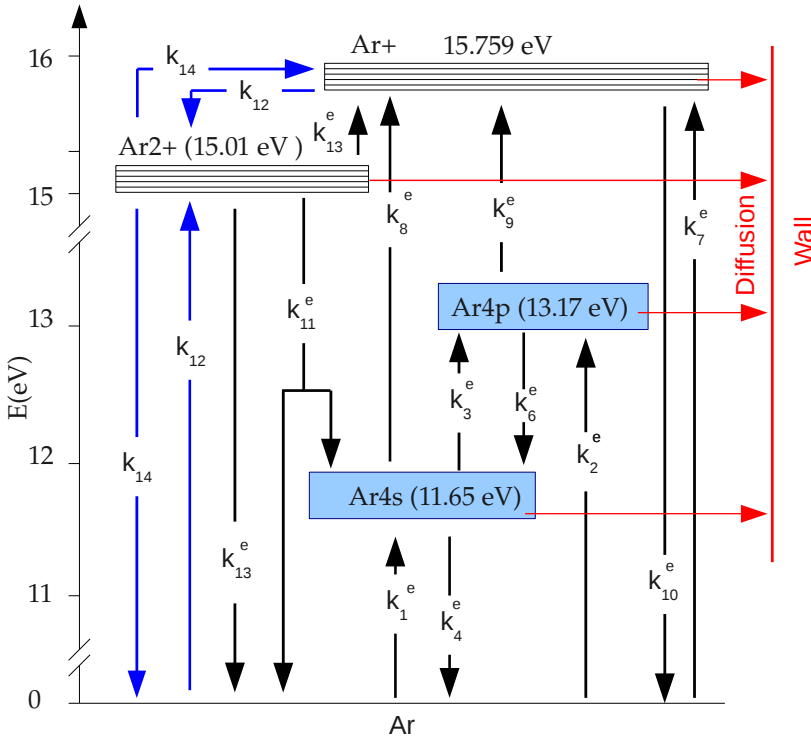


Figure 7.2: Energy level diagram for species included in the model. The relevant conversion reactions are labelled with a rate coefficient that can be found in table 7.4. For low pressure the main competition is that between direct ionization ( $k_7^e$ ) and diffusion. For increasing pressure the processes at the left of this schematic drawing become more and more important

At intermediate pressure (chapters 9 and 10) step-wise ionisation will be the most important production channel for electrons [144].

For higher pressures as in the case chapter 8, molecular recombination channels may play an important role [46, 144]. Molecular Ions (MIs) can provide a fast volume recombination channel via Dissociative Recombination (DR) (see the MAR reactions (5.24 and (5.25)).

The elastic collision frequencies are obtained using the method given in [45]. Other transport coefficients are obtained according to the rules given in chapter 4.



Interaction	Rate Coefficient/frequency	Ref.
Elastic Collision Frequency		
$e + M \rightarrow e + M$ $M = \text{Ar}, \text{Ar}^+, \text{Ar}_2^+,$ $\text{Ar}(4s), \text{Ar}(4p)$	See Transport Coef. Section	[45], [52], [10]
Diffusion		
$M \rightarrow \text{wall}$ $M = \text{Ar}, \text{Ar}^+, \text{Ar}_2^+,$ $\text{Ar}(4s), \text{Ar}(4p)$	See Transport Coef. Section.	[45], [52], [10]
Excitation		
(R1) $\text{Ar} + e \rightarrow \text{Ar}(4s) + e$	$k_1 = 4.50 \cdot 10^{-17} T_e^{0.5}$ $\exp[(E_{Ar} - E_{Ar(4s)}) / (k_b T_e)]$	[35]
(R2) $\text{Ar} + e \rightarrow \text{Ar}(4p) + e$	$k_2 = 1.82 \cdot 10^{-17} T_e^{0.71}$ $\exp[(E_{Ar} - E_{Ar(4p)}) / (k_b T_e)]$	[98]
(R3) $\text{Ar}(4s) + e \rightarrow \text{Ar}(4p) + e$	$k_3 = 7.5238 \cdot 10^{-15} T_e^{0.51}$ $\exp[(E_{Ar(4s)} - E_{Ar(4p)}) / (k_b T_e)]$	[98]
Deexcitation		
(R4) $\text{Ar}(4s) + e \rightarrow \text{Ar} + e$	$k_4 = 4.32 \cdot 10^{-18} T_e^{0.5}$	[35]
(R5) $\text{Ar}(4p) + e \rightarrow \text{Ar} + e$	$k_5 = 5.0722 \cdot 10^{-19} T_e^{0.71}$	[98]
(R6) $\text{Ar}(4p) + e \rightarrow \text{Ar}(4s) + e$	$k_6 = 2.54 \cdot 10^{-15} T_e^{0.51}$	[98]
Ionization		
(R7) $\text{Ar} + e \rightarrow \text{Ar}^+ + 2e$	$k_7 = 1.179 \cdot 10^{-16} T_e^{0.5}$ $\exp[(E_{Ar} - E_{Ar^+}) / (k_b T_e)]$	[35]
(R8) $\text{Ar}(4s) + e \rightarrow \text{Ar}^+ + 2e$	$k_8 = 1.2859 \cdot 10^{-17} T_e^{0.67}$ $\exp[(E_{Ar(4s)} - E_{Ar^+}) / (k_b T_e)]$	[35]
(R9) $\text{Ar}(4p) + e \rightarrow \text{Ar}^+ + 2e$	$k_9 = 5.9685 \cdot 10^{-16} T_e^{0.61}$ $\exp[(E_{Ar(4p)} - E_{Ar^+}) / (k_b T_e)]$	[98]
2-Electron Recombination		
(R10) $\text{Ar}^+ + 2e \rightarrow \text{Ar} + e$	$k_{10} = 2.64 \cdot 10^{-47} T_e^{2.25}$	[35]
Molecular Reactions		
(R11) $\text{Ar}_2^+ + e \leftrightarrow \text{Ar}(4s) + \text{Ar}$	$k_{11} = 1.04 \cdot 10^{-12} (T_e / 300K)^{-0.67}$ $\times \frac{1 - \exp(-418K / T_h)}{1 - 0.31 \exp(-418K / T_h)}$	[35]
(R12) $\text{Ar}^+ + 2\text{Ar} \rightarrow \text{Ar}_2^+ + \text{Ar}$	$k_{12} = 2.25 \cdot 10^{-43} (T_h / 300.0K)^{0.4}$	[35]
(R13) $\text{Ar}_2^+ + e \leftrightarrow \text{Ar}^+ + \text{Ar} + e$	$k_{13} = 1.11 \cdot 10^{-12}$ $\exp\left\{-\frac{2.94 - 3[T_h(eV) - 0.026 eV]}{T_e(eV)}\right\}$	[35] [144]
(R14) $\text{Ar}_2^+ + \text{Ar} \rightarrow \text{Ar}^+ + 2\text{Ar}$	$k_{14} = 5.22 \cdot 10^{-16} (T_h(eV) / eV)^{-1}$ $\exp[-1.304eV / T_h(eV)]$	[35]

Table 7.4: Reactions included in the model. All rate coefficients  $k$  are expressed in  $[\text{m}^3\text{s}^{-1}]$ , except  $k_{10}$  and  $k_{12}$   $[\text{m}^6\text{s}^{-1}]$ . The temperatures  $T_e$  and  $T_h$  are in K except when eV is indicated. The energy for the considered levels are  $E_{Ar} = 0$  eV,  $E_{Ar(4s)} = 11.56$  eV,  $E_{Ar(4p)} = 13.17$  eV,  $E_{Ar_2^+} = 15.01$  eV and  $E_{Ar^+} = 15.76$  eV. The energy level diagram is given in figure 7.2. The backward rate coefficients for the reverse reactions (R11) and (R13) are obtained using detailed balancing [145].

### 7.3.4 The Iterative Scheme

The Grand model has three components, configuration, transport and chemistry. An important configuration aspect is the EM wave propagation for which we used the description given in chapter 3. For the transport equations we follow chapter 4. The structure of the chemistry models is dealt with in chapter 5, and here we use the reactions described in section 7.3.3.

Although transient problems can also be studied with PLASIMO [54], the Grand model in this thesis is time-independent. An iterative scheme deals with the coupling between the mathematical equations as it is shown in the flow chart of the model given in figure 7.3. A first step in the initialisation consists of generating the computational domain and the corresponding grid for the geometry given in the input (see chapter 2). Following that we obtain the initial values for the main plasma parameters (temperatures, densities, flow) and the boundary conditions. The main loop starts with the data for elastic and inelastic particle interactions, given in the chemistry part, being used to update the transport coefficient and the source terms. The conductivity is required by the EM model to obtain the Ohmic dissipation, the most important contribution to the source term of the electron energy equation. Next, the pressure, velocity and total mass density of the plasma bulk are obtained from the Navier-Stokes and the continuity equations using the SIMPLE algorithm [10]. The diffusion model is used to obtain the diffusive velocities. Once the bulk velocity and the diffusive velocity are known, we solve the species balance equations. Following that, the energy balance equations are solved, first for the heavy particles and then for the electrons. The loops continue until the convergence criterion is met, meaning that the residue for the plasma parameters and its relative change are below the requested values.

## 7.4 Summary

In this chapter we have provided an overview of Surface Wave Discharges dealt in this thesis and their main characteristics. We have introduced briefly how the PLASIMO tool-kit has been used to study three different SWDs that are presented in the following, chapters 8, 9 and 10. The common components of the models are given with respect to configuration (geometry, boundary conditions, control parameters and electromagnetic model), transport and the chemistry for an argon plasma. The iterative scheme used to obtain the coupled solution between the different equations is presented as well

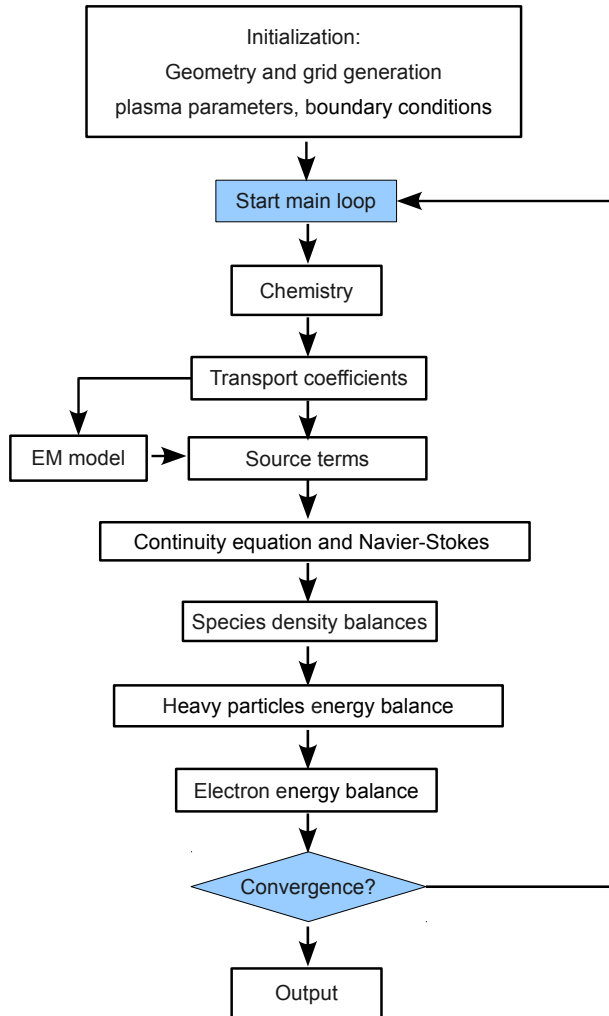


Figure 7.3: Flow chart of the model constructed with PLASIMO

---

8

Surfaguide Argon Plasma Model at High Pressure

---

## 8.1 Introduction

Surface-wave sustained discharges (SWDs) are well-known microwave plasma sources [86] than can efficiently produce long plasma columns. In this chapter we present a model for a surface wave sustained argon plasma at atmospheric pressure. The surfaguide launcher [86] consists on a tapered rectangular waveguide in which an aperture is made, see figure 8.1. At this gap a high field is created and shaped such that it is able to launch a surface wave in a plasma column. Thus, the surface wave generated at the gap of the launcher creates its own propagating medium i.e. the plasma column. It is a mechanism in which electromagnetic and discharge aspects are tightly interrelated.

In order to study the interplay between electromagnetic, transport and chemical aspects we constructed a Grand model using the plasma modelling platform PLASIMO (PLASma SIMulation MOdel) [52, 130]. This plasma model factory has successfully been used in the past for the simulation of several plasma sources such as cascade arcs [146], microwave plasmas for fibre production [10, 11], and for low and high pressure light sources [8, 52, 54, 58, 130] (see also section 2.2 in chapter 2).

In the next section 8.2, the physical model is introduced, together with the boundary conditions and the numerical method. In section 8.3, we show results for an argon plasma at a pressure of  $p = 10^5$  Pa, and we will study how the axial and radial extension of the discharge are influenced by molecular assisted recombination (MAR). It is found that the wall temperature has an important impact on the population of molecular ions and, as a consequent, on the wave propagation.

## 8.2 Model

The equations that describe plasma transport, introduced in chapter 4, have been extended by adding the description of the electromagnetic aspects as explained in chapter 3. Note that we solve the 3 component equations of a transversal magnetic mode. This stands in contrast to [35] where only the azimuthal magnetic field component equation is used.

The flow chart of the model was given in figure 7.3 in chapter 7.

### 8.2.1 Geometry

The geometry of the surfaguide plasma is depicted in figure 8.1; the corresponding parameters values and boundary conditions are given in section 8.2.2. The discharge

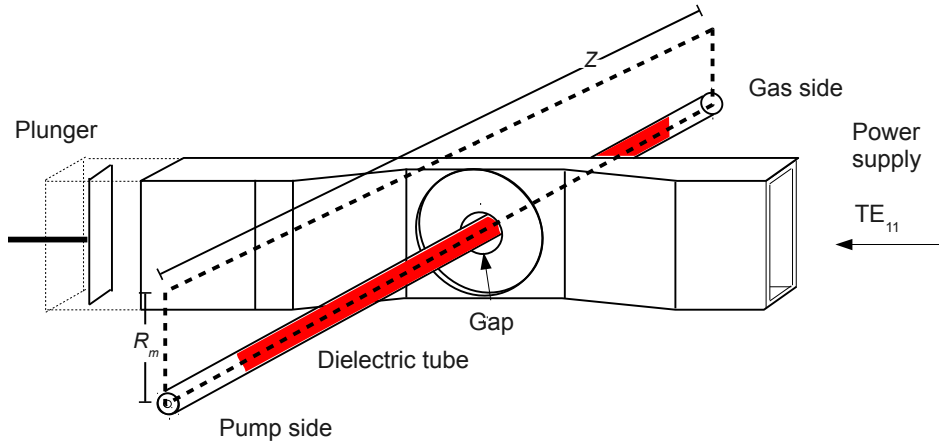


Figure 8.1: The surfaguide and discharge tube as described in [86]. Note that for the sake of clarity we have not drawn the metal screen with radius  $R_m$  that in some experimental situations surrounds the plasma tube. The dashed lines indicate the edge of the computational domain given in figure 8.2.

is sustained in a dielectric tube that has as internal and external radii  $R_p = 2$  mm and  $R_g = 2.6$  mm. The tube is inserted into a tapered section of a waveguide where due the tapering the local electric field in the waveguide is enhanced. By means of a plunger one can get the maximum strength of the E field at the gap region. In [141] the plasma tube is surrounded by a metal screen of radius  $R_m = 25$  mm. This is not shown in figure 8.1 for sake of clarity, but it is included in the model, so we can compare our calculations with the experimental results given in [141]. The model is two-dimensional and rotational symmetric around the axis of the dielectric tube (see figure 8.2). The launcher starts at  $Z_{s,1}$  and ends at  $Z_{s,2}$ , with inner walls defining the gap distance from  $Z_{gap,1}$  to  $Z_{gap,2}$  (see figure 8.2). The dimensions are given in table 8.1.

## 8.2.2 Boundary Conditions

Figure 8.2 schematically describes the computational domain with the different boundaries.

Appropriate boundary conditions are needed for solving the balance equations for the species densities, equation (4.3), the mass, (4.27), momentum, (4.28), the kinetic energy of heavy particles, (4.31) and electrons, (4.34). These were given in table 7.3 and are of course only applicable for the plasma region.

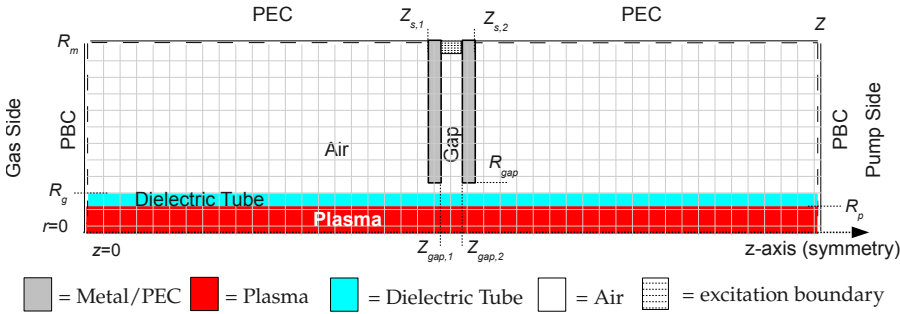


Figure 8.2: Computational domain of the surfaguide modelled in cylindrical coordinates. The axis of symmetry is the axis of the tube. PEC, Perfect Electrical Conductor, PBC = Propagation Boundary Condition. See table 8.1 for the values of the dimensions.

Par	Value	Par	Value
$R_m$	25 mm	$R_p$	2 mm
$R_g$	3 mm	$R_{gap}$	4 mm
$Z_{s,1}$	144, 194, 398 mm	$Z_{s,2}$	$Z_{s,1} + 18$ mm
$Z_{gap,1}$	$Z_{s,1} + 6$ mm	$Z_{gap,2}$	$Z_{s,1} + 12$ mm
$Z$	300, 400, 800 mm		

Table 8.1: Dimensions of the geometry in the surfaguide plasma simulations. Note that the different values of  $Z$  refer to the 3 different axial length that are used in the computations. The position of the launcher changes such that it remains close to the centre of the computational domain.

In this particular case, the boundary condition for velocity and pressure are set using a flow rate. Therefore the pump side pressure is fixed to  $p_{out}$ , while we impose at the gas side a constant derivative of the pressure meaning that  $\partial^2 p / \partial z^2 = 0$ . The velocity at the gas inlet is prescribed by a second order power law [10].

$$v_b(z = 0, r) = v_0 \left[ 1 - \left( \frac{r}{R_p} \right)^2 \right] \quad (8.1)$$

The central value  $v_0$  is obtained from the flow rate  $\Phi$  by  $v_0 = 2\Phi / (\pi R_p^2)$ . Note that the constant derivative of the pressure is used in order to avoid an overdetermined set of boundary conditions [146].

For the other boundaries, the boundary conditions are those shown in tables 8.2 and 8.3.

Par.	Gas Side	Pump Side	Tube wall	Axis
$p$	$\frac{\partial^2 p}{\partial z^2} = 0$	$10^5 \text{ Pa}$	$\frac{\partial p}{\partial r} = 0$	$\frac{\partial p}{\partial r} = 0$
$v_{b,z}$	$v_{b,z} = v_0 \left[ 1 - \left( \frac{r}{R_p} \right)^2 \right]$	$\frac{\partial v_{b,z}}{\partial z} = 0$	$v_{b,z} = 0$	$\frac{\partial v_{b,z}}{\partial r} = 0$
$v_{b,r}$	$v_{b,r} = 0$	$\frac{\partial v_{b,r}}{\partial z} = 0$	$v_{b,r} = 0$	$v_{b,r} = 0$
$T_h$	$T_{h,w}$	$\frac{\partial T_h}{\partial z} = 0$	$T_{h,w}$	$\frac{\partial T_h}{\partial r} = 0$
$T_e$	$\frac{\partial T_e}{\partial z} = 0$	$\frac{\partial T_e}{\partial z} = 0$	$\frac{\partial T_e}{\partial r} = 0$	$\frac{\partial T_e}{\partial r} = 0$

Table 8.2: Boundary conditions for the surfaguide plasma model. Here  $p$  is the pressure,  $v_{b,z}$  and  $v_{b,r}$  are, respectively, the axial and radial components of the plasma bulk flow velocity,  $T_h$  is the gas temperature and  $T_e$  is the electron temperature

Par	Value	Par	Value
$p_{out}$	$10^5 \text{ Pa}$	$P_{in}$	variable
$f$	915 MHz, 2.45 GHz	$T_{h,w}$	variable
$v_0$	1 m/s		

Table 8.3: Control parameters for the surfaguide plasma simulations.

The gas temperature is set constant at the gas side and at the wall of the discharge tube. Unless noted differently we take for  $T_w = 800 \text{ K}$ . In section 8.3.2 we will change  $T_w$  and study the effect of these changes on the external and internal plasma properties.

The boundary condition for the electron temperature at the tube wall, gas side and pump side is of type homogeneous Neumann, meaning that  $(\nabla T_e) \cdot \mathbf{n} = 0$  (see chapter 2).

For the gas side, pump side and at the central axis a homogeneous Neumann boundary is used for the densities.

## 8.3 Results and Discussion

In section 8.3.1, we calculate the dependency of the plasma column shape and length on the plasma absorbed power. The results are compared with experimental results [141]. In section 8.3.2, we show how the wall temperature affects the contraction in both radial and axial directions.



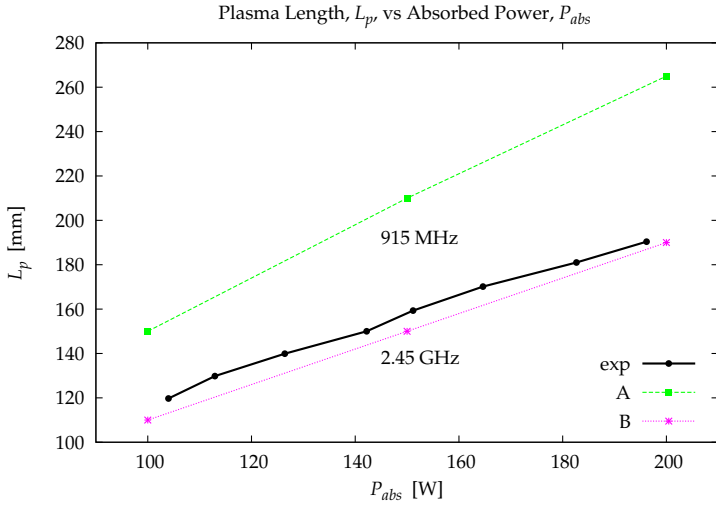


Figure 8.3: Plasma length  $L_p$ , as a function of the absorbed power  $P_{abs}$ . In all cases the inner and outer tube radius equal  $R_p = 2$  mm and  $R_g = 3$  mm, respectively, whereas the radius of the metal screen  $R_m = 25$  mm. The experimental data (exp), as given in [141] are found for  $f = 2.45$  GHz. The length of the column is obtained assuming that the electron density at the axial end equals:  $n_e^{fit} = 2.5 \cdot 10^{19} \text{ m}^{-3}$ . In case A:  $f = 915$  MHz; for B:  $f = 2.45$  GHz. In all cases  $p = 10^5$  Pa.

### 8.3.1 Effect of the Absorbed Power on the Plasma Column Length

Figure 8.3 gives the length of the plasma column,  $L_p$  as a function of the power absorbed in the plasma,  $P_{abs}$ . As the plasma column extends at both sides of the launcher, we can define the plasma length as the distance between the two points on the axis at different sides of the gap that have the same electron density, indicated by  $n_e^{fit}$ . This value was chosen to be  $n_e^{fit} = 2.5 \cdot 10^{19} \text{ m}^{-3}$ , such that the length in the numerical model equals the length measured by [141] at 100 W for 2.45 GHz. This means that we are comparing the *shape* of the  $n_e$ -curve rather than the absolute value of the *length*. We can see that the theoretical trend given by curve B in figure 8.3 fits rather well to the experimental results.

We repeated the calculations for a frequency of 915 MHz, which generates curve A in figure 8.3. This curve is positioned higher, meaning that for the same power the length is larger; moreover the slope of A is steeper than that of B. The reason is that for a lower frequency the gas temperature is higher. This apparently means, as we will see, that the losses of electrons due to MAR processes are lower.

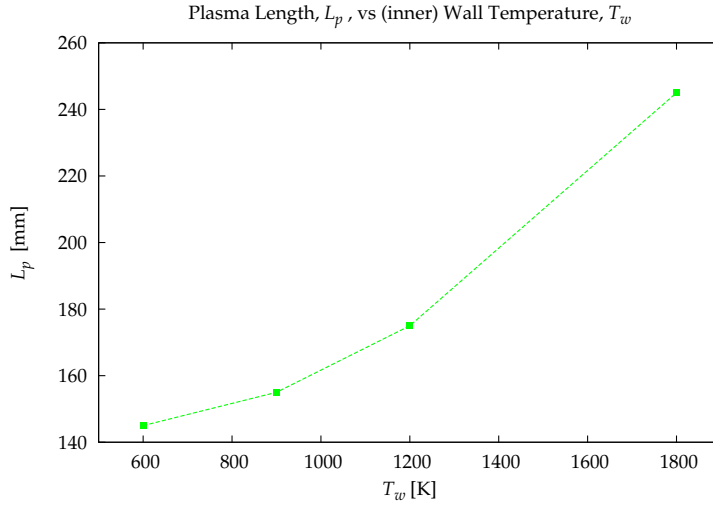


Figure 8.4: Plasma length  $L_p$  as a function of the (inner) wall temperature  $T_w(r = R_p)$  for  $P_{abs} = 100$  W and  $f = 915$  MHz. In all cases  $p = 10^5$  Pa.

### 8.3.2 Influence of the Wall Temperature on Contraction

Figure 8.4 shows that the plasma length increases with increasing wall temperature. An explanation is given by figure 8.5 which demonstrates that for lower  $T_g$ -values the plasma is more contracted. The reason is that in high pressure plasmas the electrons are lost mainly due to molecular assisted recombination, which is more important for higher gas density i.e. lower gas temperature at a constant pressure.

In figure 8.6, we show the radial distributions for densities of the electrons, the atomic and molecular ions, and the excited states for the case  $T_w = 600$  K.

The radial distribution for Ar(4s) and Ar(4p) resembles that of  $\text{Ar}_2^+$ , with maximum values at 0.55 mm for and 0.50 mm, respectively. Apparently, the excited states in the plasma mantle are created by reaction (R11) (see table 7.4) which is faster for higher gas temperatures [147]. Consequently, this means that for lower gas temperatures the destruction of molecular ions by atomic impact (R14) is slower and its population is higher. This can be seen in figure 8.6 where in the plasma mantle (from radial position  $r = 0.5$  mm toward the wall  $r = R_p$ ) the molecular ions density becomes more important and comparable to those of the atomic ions. In this region molecular assisted recombination (MAR) i.e. reaction (R13) in table 7.4 provides fast electron recombination, which explains the low electron density.

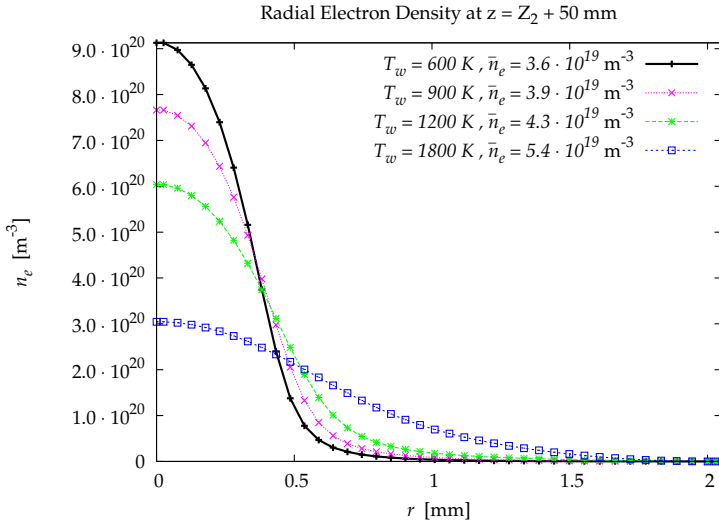


Figure 8.5: Radial distribution of the electron density at an axial distance of 50 mm from the gap position  $Z_{s,2}$  for different values of the wall temperature  $T_w = 600, 900, 1200, 1800$  K. In all cases  $p = 10^5$  Pa. It is clear that lower  $T_w$ -values and thus higher argon densities leads to more contraction.

## 8.4 Conclusions

We have presented a model for a surfaguide argon plasma at high pressure. The results have been compared to experimental results that give the dependency of the plasma length on the absorbed power.

The agreement between modelling and experiment is fairly good. It is found that the plasma is less contracted as the wall temperature is increased. The reason is that a higher gas temperature leads to lower population of molecular ions whereas the electron density increases.

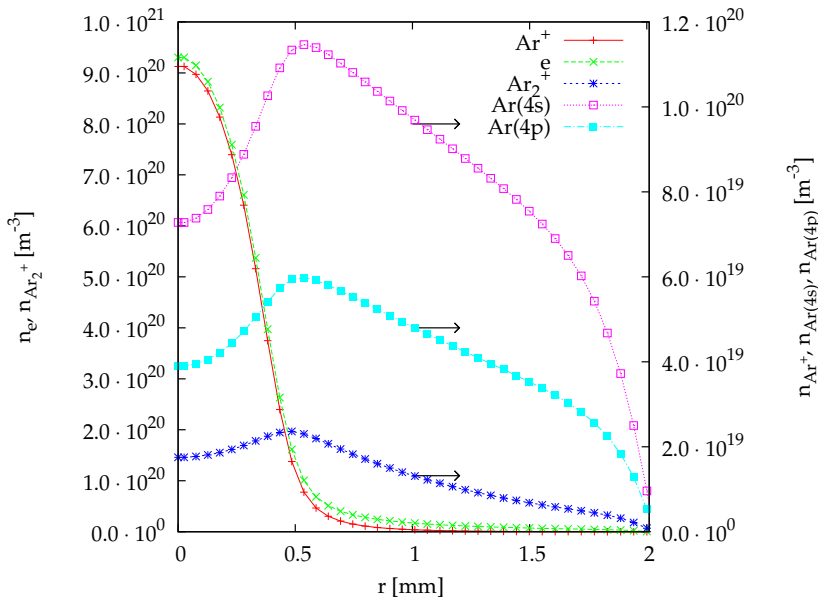


Figure 8.6: Radial distribution of the electron and  $Ar^+$  densities on the left and  $Ar(4s)$ ,  $Ar(4s)$  and  $Ar_2^+$  densities on the right at  $z = 200$  mm. For  $p = 10^5$  Pa and  $P_{abs} = 150$  W. Note the two different scales at the vertical axes.



---

9

Surfatron Argon Plasma at Intermediate Pressures

---

## 9.1 Introduction

The surfatron launcher, figure 9.1, is an electromagnetic structure designed to produce surface wave discharges (SWDs). The main features and mechanism of SWDs and their launchers were presented in chapters 7 and 8. The launchers have in common that they create high  $E$  values that are rotational symmetric<sup>a</sup>. The surfaguide (see chapter 8) was designed to launch high EM powers (in the order of kW) which is possible due to the rectangular waveguide feeding system. In the case of the surfatron the launcher is coupled to the microwave power supply via a coaxial cable which due to dielectric losses limits the power to about 400 W at 2.45 GHz (see [86]). It also means that the surfatron is more flexible. This becomes useful when performing active spectroscopy such as Thomson scattering (TS) [13, 76].

The surfatron plasma can work over a wide range of pressures and radial extensions with characteristics that were discussed in chapters 7, particularly in table 7.2.

In the case of using SWDs for deposition processes like for the production of optical fibres (Draka Comteq Eindhoven in the Netherlands) or the creation of thin solar cells (Energy research Centre of the Netherlands ECN) best results can be expected for the intermediate pressure range. Then high fluxes of ions and radicals can be created while the plasma is more or less homogeneous. Working at argon pressures higher than 5000 Pa most likely creates constriction and filamentation which leads to inhomogeneity in the produced surface layer.

The main objective of this chapter is to investigate the effect of increasing pressure on the structure and shape of the plasma. This will be done by means of numerical modelling using a pure argon discharge as case study. It will be shown that increasing the pressure leads to the formation of molecular ions and that these facilitate volume recombination processes. As a consequence the plasma will not expand to the wall and will be constricted in both the radial and axial direction. The results of modelling for which plasmas of increasing pressures of  $p = 660, 2000$  and  $8800$  Pa are explored, will be compared with those of Thomson scattering measurements. A fairly good agreement between modelling and experiments is found showing that even for the intermediate pressure range of  $2000-8800$  Pa volume recombination is already important and comparable to ambipolar diffusion [138].

---

<sup>a</sup>azimuthally constant in this work, meaning  $m = 0$  in the dependency of the form  $\exp(im\phi)$ ; the integer number  $m$  defines an  $m$ -fold rotational symmetry

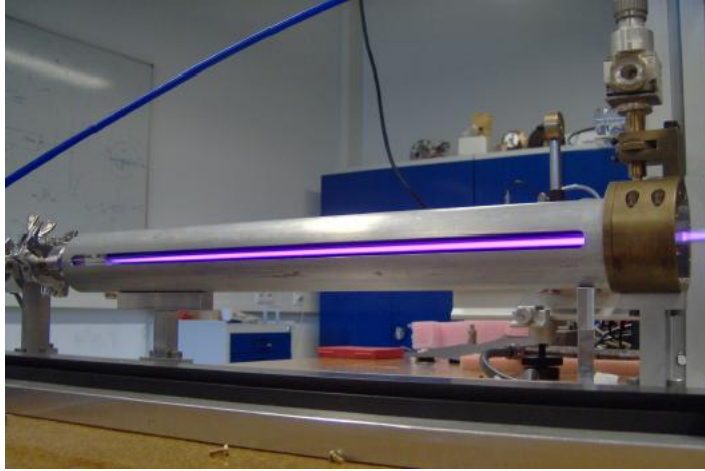


Figure 9.1: The surfatron plasma setup as used in [76]. At the right we find the launcher. There is a coaxial structure on the top of the launcher that feeds the EM energy. From the launcher toward the left, we find the plasma column surrounded by a metal screen.

## 9.2 Physical Model

The numerical model is basically the same as that used for the study of the surfaguide (see chapter 8). Meaning that the model consists of three main building blocks, electromagnetism as introduced in chapter 3, transport described in chapter 4 and argon plasma chemistry as given in section 7.3.3 of chapter 7. The model is constructed using the PLASIMO numerical framework (see chapter 2) and the basics features are explained in chapter 7. We refer to the above chapters for more details.

The following sections show the main differences between the surfatron and other SWDs. These are found in the geometry, the boundary conditions, and control parameters such as pressure and absorbed power. For the common aspects we refer to chapter 7.

### 9.2.1 Configuration: Geometry

The geometry of the surfatron launcher (see figure 9.2) consists of two coaxial metal cylinders forming a section of a coaxial line. The inner metal cylinder has an inner radius  $R_{gap} = 5.7$  mm and outer radius  $R_{c,1} = 13$  mm whereas the outer cylinder has an inner radius of  $R_{c,2} = 52$  mm and outer radius  $R_m = 66$  mm. There are metal walls



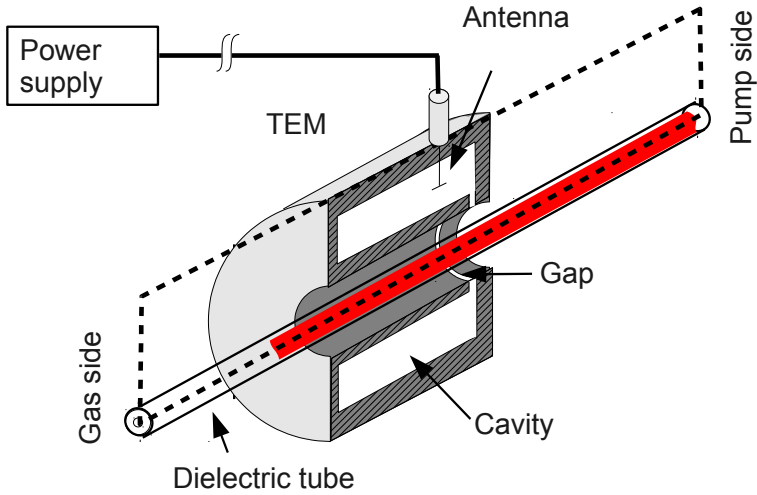


Figure 9.2: Schematic view of the surfatron launcher and the dielectric tube as described in [12]. The dashed line indicates the computational domain in figure 9.3.

ending the coaxial line. At the gas-side the metal wall starts axially at  $Z_{s,1} = 72$  mm and ends at  $Z_c = 87$  mm; it represents a short-circuit. At the pump-side the metal wall starts at  $Z_{gap,2} = 108$  mm and ends at  $Z_{s,2} = 111$  mm. A gap starts at  $Z_{gap,1} = 105$  mm and ends at  $Z_{gap,2} = 108$  mm separating the inner metal cylinder from the metal wall at the pump-side of the surfatron launcher. Note that the metal cylinders and the metals walls at the axial ends form an electromagnetic cavity inside the surfatron launcher.

This cavity is designed to provide a maximum value of the electric field  $|E|$  at the gap in a rotational symmetric way. This EM distribution is required to excite the transversal magnetic surface waves in the  $m = 0$  mode (azimuthally independent) that propagates along the plasma column [22, 142].

The plasma column is created inside a dielectric tube of inner radius  $R_p = 3.1$  mm and outer radius  $R_g = 4.4$  mm mounted between a gas supplier and pump.

The computational domain is shown in figure 9.3. The dimensions are given in table 9.1 together with the boundary conditions and control parameters in section 9.2.2.

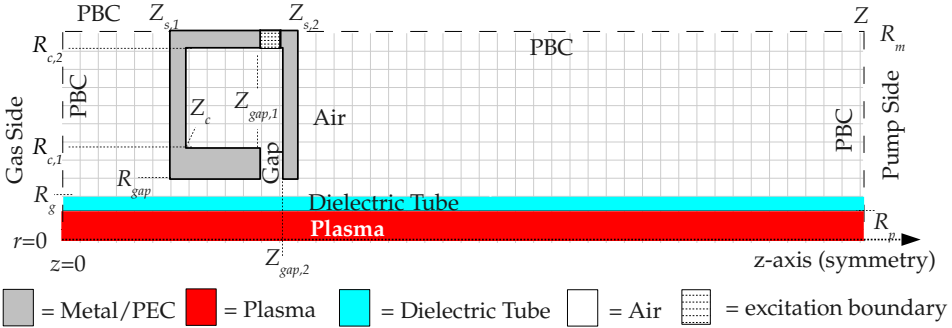


Figure 9.3: Computational domain of the surfatron. PEC = Perfect Electrical Conductor, PBC = Propagation Boundary Condition. The value of the dimensions and the boundary conditions are given in section 9.2.2.

Par	Value	Par	Value
$R_m$	66 mm	$R_p$	3.1 mm
$R_g$	4.4 mm	$R_{gap}$	5.7 mm
$R_{c,1}$	13 mm	$R_{c,2}$	52 mm
$Z_{s,1}$	72 mm	$Z_{s,2}$	111 mm
$Z_{gap,1}$	105 mm	$Z_{gap,2}$	108 mm
$Z_c$	87 mm	$Z$	800, 700 mm

Table 9.1: Dimensions of the geometry in the surfatron plasma simulations.

## 9.2.2 Configuration: Boundary Conditions

The boundary conditions (BCs) needed to solve the plasma transport equations are basically the same as those given in section 7.3.2. They are summarised in tables 9.2 and 9.3.

Compared to the standard case described in chapter 7, there are slight differences in the BCs of the heavy particle energy balance i.e. for the gas temperature  $T_h$ . Here the BC at the tube wall is given by the continuity of the heat flux at the wall-plasma interface

$$\lambda_h \frac{\partial T}{\partial r} \Big|_{r=R_p} = \lambda_w \frac{\partial T}{\partial r} \Big|_{r=R_g} \quad (9.1)$$

with  $\lambda_h$ ,  $\lambda_w$  the thermal conductivity of the plasma (heavy particles) and of the dielectric tube, respectively. Using the same assumptions as in [10], we can cast the

Par.	Gas-Side	Pump-Side	Tube wall	Axis
$p$	$p_{in}$	$p_{out}$	$\frac{\partial p}{\partial r} = 0$	$\frac{\partial p}{\partial r} = 0$
$v_{b,z}$	$\frac{\partial v_{b,z}}{\partial z} = 0$	$\frac{\partial v_{b,z}}{\partial z} = 0$	$v_{b,z} = 0$	$\frac{\partial v_{b,z}}{\partial r} = 0$
$v_{b,r}$	$v_{b,r} = 0$	$\frac{\partial v_{b,r}}{\partial z} = 0$	$v_{b,r} = 0$	$v_{b,r} = 0$
$T_h$	$T_{h,w}$	$\frac{\partial T_h}{\partial z} = 0$	$\lambda_h \frac{\partial T_h}{\partial r} \Big _{r=R_p} = \frac{\lambda_w (T_{env} - T_{h,w})}{R_p \text{Ln} \left( \frac{R_g}{R_p} \right)}$	$\frac{\partial T_h}{\partial r} = 0$
$T_e$	$\frac{\partial T_e}{\partial z} = 0$	$\frac{\partial T_e}{\partial z} = 0$	$\frac{\partial T_e}{\partial r} = 0$	$\frac{\partial T_e}{\partial r} = 0$

Table 9.2: Boundary conditions for the surfatron plasma model.

right-hand-side term in an analytical form, so that the BC transforms into

$$\lambda_h \frac{\partial T_h}{\partial r} \Big|_{r=R_p} = \frac{\lambda_w (T_{env} - T_{h,w})}{R_p \text{Ln} \left( \frac{R_g}{R_p} \right)}. \quad (9.2)$$

The thermal conductivity of the dielectric tube is taken to be  $\lambda_w = 1.4 \text{ W m}^{-1} \text{ K}^{-1}$ . For the outer temperature of the dielectric tube we take  $T_{env} = 300 \text{ K}$ . This BC, of the type mixed Neumann BC (see chapter 2), allows to set the temperature at the outer part of the tube. As a BC for the Navier-Stokes equation, we set the pressure difference between the gas-side  $p_{in}$  and the pump-side  $p_{out}$  to 2 Pa instead of selecting the flow rate at the gas side. The pressures are  $p_{out} = 660, 2000, 8800 \text{ Pa}$  for the pump-side and  $p_{in} = 662, 2002, 8802 \text{ Pa}$  for the gas-side, respectively.

For the electromagnetic fields, a homogeneous Neumann boundary condition is applied at the axis to the axial component of the electric field. At the metal walls the perfect electrical conductor (PEC) boundary condition is used, so that the component of the electric field tangential to the metallic surface is zero.

The antenna inside the cavity of the launcher is not modelled as it would require a three-dimensional model. Instead an excitation boundary condition sets the *guessed* value of  $E_z$  at  $r = R_{c,2}$ , see figure 9.3. In each iteration, the electromagnetic model scales the power density distribution to obtain the power absorbed in the domain as prescribed by the control parameter  $P_{abs} = 50 \text{ W}$ . This is the *Power Absorbed in Domain* excitation BC that was introduced in section 3.4.

A propagation boundary condition PBC is used at the rest of boundaries for the electric fields. For more information on the boundary condition for EM fields we refer to chapters 3 and 6.

The density of the ion  $\text{Ar}^+$  (see section 7.3.3) is set equal to  $8.5 \cdot 10^{17} \text{ m}^{-3}$  at the wall, gas- and pump-side, so that an under-dense plasma is avoided (see appendix A).

Par	Value	Par	Value
$p_{in}$	662, 2002, 8802 Pa	$p_{out}$	660, 2000, 8800 Pa
f	2.45 GHz	$P_{in}$	32, 59 W
$T_{h,w}$	$T_h(z, r = R_p)$	$T_{env}$	300 K

Table 9.3: Control parameters for the surfatron plasma simulations.

## 9.3 Numerical Model

The numerical model is the same as the one used for the surfaguide model in chapter 8. It is a Grand model in which the coupling between the different (sub)models for electromagnetic (chapter 3), transport (chapter 4) and -argon- chemical (section 7.3.3 in chapter 7) aspects has been implemented and solved using the PLASIMO numerical framework (chapter 2). We refer to the above chapters for more details.

## 9.4 Results and Discussion

In section 9.4.1 we will study the behaviour of the plasma region *inside* the launcher. This is done, among other reasons, to anticipate on chapter 10 which is entirely devoted to the deposition reactor that can be seen as an inner launcher region. Afterwards, we will focus in section 9.4.2 on the plasma region *outside* the launcher. Finally, the results for the axial distribution of the electron density and electron temperature are compared to experimental results in section 9.4.3.

### 9.4.1 Plasma Region Inside the Launcher

In most SWD studies the behaviour of the plasma inside the launcher is overlooked [12, 41, 42]. We could find only one reference that studied numerically how the distance between the metal screen and the plasma affects the electron density and wave propagation along the axial direction [148]. However, this inner-launcher region deserves attention not only because it is the region where the wave is created and launched, but also because it plays an important role in industrial applications. In the Draka set-up, used for fibre fabrication (see chapter 10), the deposition takes place *inside* the launcher, which is known as the deposition reactor in that context.

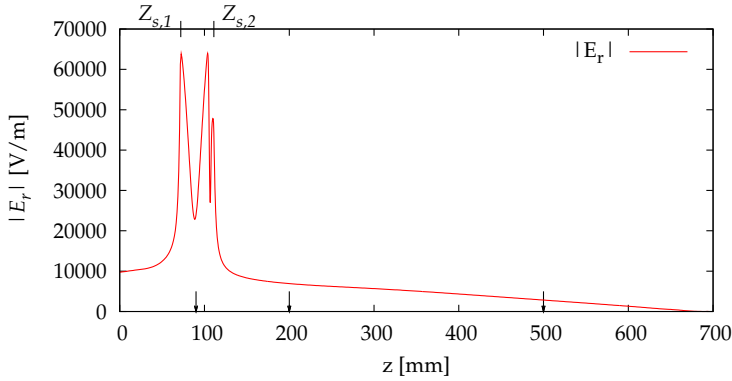


Figure 9.4: Axial distribution of the absolute value of the radial electrical field component  $|E_r|$  at a radial position of  $r = 4.5$  mm (i.e. outside the tube); the pressure is  $p_{out} = 2000$  Pa and the absorbed power  $P_{abs} = 59$  W. The arrows mark the axial positions used in figure 9.7.

### The electric field

Due to the launcher construction, which brings its inner metal cylinder close to the plasma, the local electrical field is enhanced substantially. This can be seen in figure 9.4 where we show the axial distribution of  $|E_r|$  outside the tube at  $r = 4.5$  mm. We study here  $E_r$  since in general for a SWD  $|E_r| \gg |E_z|$  outside the plasma (see also chapter 10). This figure shows that the field *inside* the launcher is much higher than *outside* the launcher. This is even valid for the position of the local minima<sup>b</sup>.

In order to understand the increase of the EM field strength we will consider the power flow of a wave propagating through a waveguide with changing cross-section (see figure 9.5).

We apply the conservation of energy as given by equation (6.14) to a section of the waveguide limited in axial direction by surfaces of area  $A_1$  and  $A_2$  and assume that there is no power absorbed in the volume in between these surfaces. Denoting the time-averaged Poynting vector at surfaces of area  $A_1$  and  $A_2$  by  $S_1$  and  $S_2$ , respectively, equation (6.14) reduces to  $S_1 A_1 = S_2 A_2$ . This implies that  $S$  and accordingly the square of the electric field strength is inversely proportional to the cross-sectional area of the waveguide. This gives an idea to understand the high value of  $|E_r|$ , found in figure 9.4, inside the launcher where the cross-sectional area is smaller.

<sup>b</sup> The local maximum values of  $|E_r|$  seem to be associated with waveguide discontinuities as they are found -from left to right- at axial positions  $z = Z_{s,1}$ ,  $z = Z_{gap,1}$  and for the last peak in between  $Z_{s,2}$  and  $Z_{gap,2}$

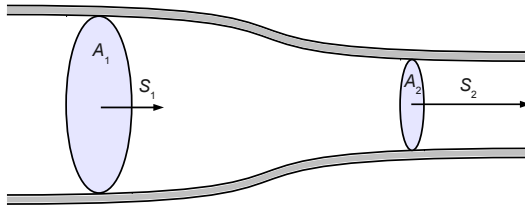


Figure 9.5: A waveguide with cross-section changing from  $A_1$  to  $A_2$ . The time-averaged Poynting vectors at the surfaces are denoted by  $S_1$  and  $S_2$ , respectively. At places where  $A$  is small, the corresponding  $S$  will be large.

This behaviour is similar to the increase of the flow velocity for a fluid flowing through a pinched pipe; at the place where the cross-sectional area is smaller the flow velocity will be higher. Both phenomena results from a conservation or continuity equation. Of course the power absorbed by the plasma plays a role in the conservation of energy and will affect the change in the EM field. But the main trend is given by the simple conservation consideration given above.

Figure 9.6 gives the axial distribution of  $|E_z|$  *inside* the plasma at  $r = 3$  mm, while figure 9.7 shows the corresponding radial distributions inside the plasma. This is done for three different axial positions,  $z = 90, 200, 500$  mm (marked with arrows in figures 9.4 and 9.6). It can be seen that close to wall in the launcher ( $z = 90$  mm) the field strengths and gradients are higher than outside the launcher ( $z = 200, 500$  mm). In the latter region the field components are both radially and axially more homogeneous than inside the launcher.

The shape of the electric field has a big influence, on the electron density and gas temperatures. On the other hand the electron temperature is not much affected as we will see below.

### The electron density and gas temperature

Figure 9.8(a) shows that the electron density in the launcher is much higher than outside the launcher. This is consistent with the numerical results found in [148] where the value and gradient of  $n_e$  are found to be higher if the distance between the metal tube and the dielectric tube is smaller. Moreover, it can be understood from the behaviour of the electric field discusses above in combination with the electron energy balance.

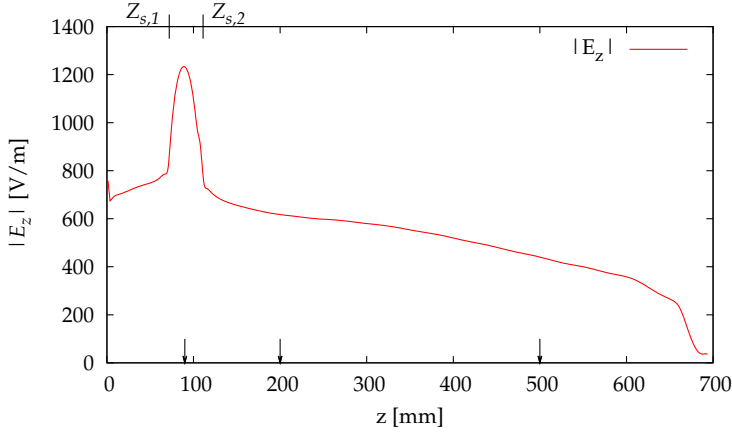


Figure 9.6: Axial distribution of the axial electrical field component at a radial position of  $r = 3$  mm (i.e. inside the plasma). For a pressure of  $p_{out} = 2000$  Pa and an absorbed power of  $P_{abs} = 59$  W. The arrows mark the axial positions used in figure 9.7.

The higher field strength inside the launcher leads, as given by equations (5.26) and/or (4.34), to a high power density and therewith high  $n_e$ -values. The high electron density leads in turn to enhanced gas heating and thus high gas temperatures (see figure 9.8(b)).

The combination of high  $n_e$ - and  $T_g$ -values destroys the population of molecular ions as can be deduced from the dependencies of the rate coefficients for reactions (R13) and (R14) given in table 7.4. The effect is indeed clearly manifest in figure 9.9(a) showing deep minima in the  $Ar_2^+$  population.

### The electron temperature; the similarity law.

In figure 9.9(b) we observe that in contrast to the electron density, the electron temperature  $T_e$  is not much affected by the local enhanced power density. The reason is that  $T_e$  is determined by the electron particle balance (ePB) rather than by the electron energy balance (which is ruled by the power density).

For a better understanding of these trends we refer to the form of the ePB as given by equation (5.33), which for convenience is reproduced here as

$$k_{ion}^*(T_e) = D_a^*(R_p n_1)^{-2}, \quad (9.3)$$

where  $k_{ion}^*$  is the effective ionisation rate coefficient and  $D_a^* = D_a n_1$  the ambipolar diffusion coefficient times the ground density of argon  $n_1$ , and  $R_p$  is the plasma radius.

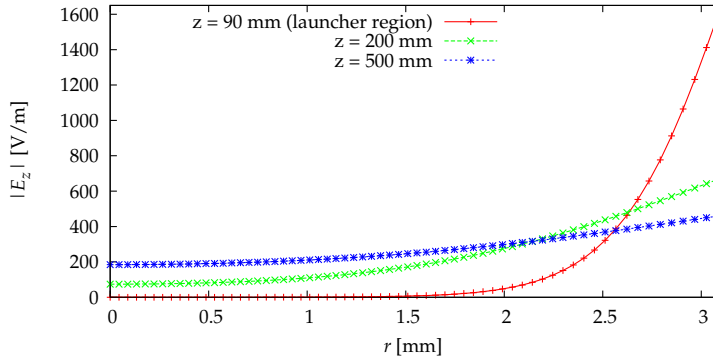


Figure 9.7: Radial distribution of the axial electrical field component for three axial positions  $z = 90, 200, 500$  mm inside the plasma, for a pressure of  $p_{out} = 2000$  Pa and an absorbed power of  $P_{abs} = 59$  W. Note that  $z = 90$  mm refers to a position inside the launcher.

The latter is being used here as an approximation of the characteristic diffusion length [12].

As stated before, this electron particle balance sets a demand for  $T_e$ ; a large local drain of charge particles, e.g. due to diffusion to the wall, demands for a high  $T_e$ -value. The (small) increase in  $T_e$  at the launcher-slit for the pressures 660 and 2000 Pa can be seen as a consequence of the local reduction of  $n_1$ ; the consequence of an increase of  $T_g$  at constant pressure.

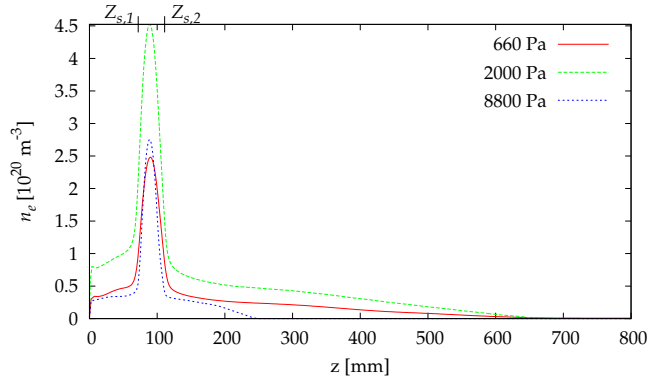
A decrease of  $n_1$  has two effects, first it facilitates diffusion and therefore enhances the lost of electron-ion pairs, second it reduces the number of ionisable particles. This quadratic effect in  $n_1$  is diminished due the exponential dependence of  $k_{ion}^*(T_e)$  on  $T_e$  (cf. equation 5.34). A small change in  $T_e$  already leads to dramatic changes in  $k_{ion}^*(T_e)$ . This explains why  $T_e$  increases only moderately in the launcher.

Expression (9.3) is related to a well-known similarity law often used in the field of SWDs [24, 25]. It states that plasmas with the same  $R_p n_1$  values<sup>c</sup> will have (almost) the same  $T_e$ . The reason is that  $D_a^*$  is not much dependent on plasma properties (see equation (5.20)).

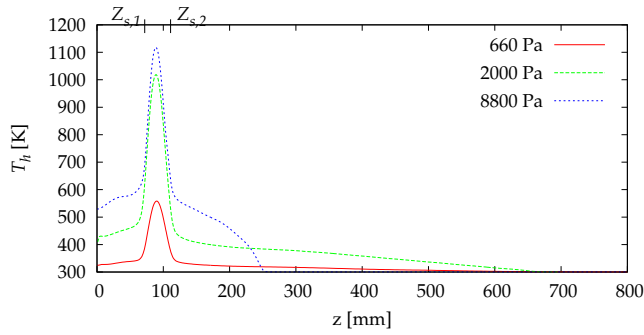
It is remarkable that the moderate increase in  $T_e$  seen for the low pressures is not present for the relative high pressure of 8800 Pa. This points to the role of molecular assisted recombination (MAR). As dealt with in chapter 8 we can expect that for

<sup>c</sup>Note that the original similarity parameter  $pR_p$  deals with the product of pressure and size, rather than  $n_1 R_p$ . However, in plasmas with low pressure for which the gas temperature stays close to room temperature,  $pR_p$  directly scales with  $n_1 R_p$ .



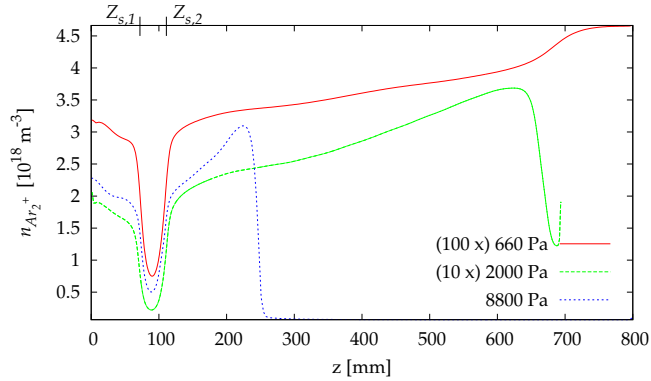


(a)

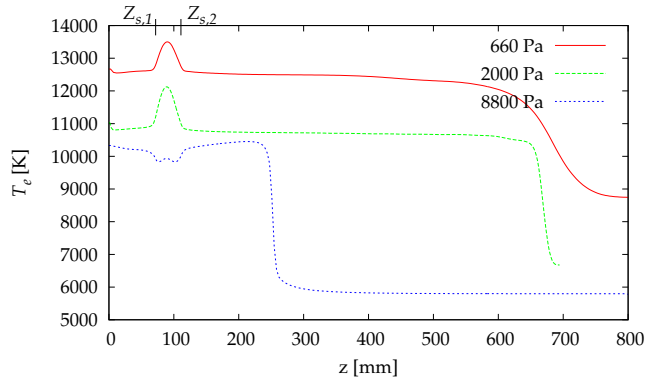


(b)

Figure 9.8: Axial distribution of the electron density (a) and the gas temperature (b) at the centre of the discharge for a pressure of  $p_{out} = 660, 2000$  and  $8800$  Pa and an absorbed power of  $P_{abs} = 32$  W for  $660$  Pa and  $59$  W for  $2000$  and  $8800$  Pa. The inner-launcher region is situated between positions  $Z_{s,1}$  and  $Z_{s,2}$ . Note that for  $8800$  Pa (due to the Molecular Assisted Recombination -MAR- processes) the decay of electrons is not linear anymore. See also figure 9.3.



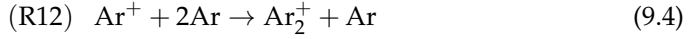
(a)



(b)

Figure 9.9: Axial distribution of the molecular ion density (a) and the electron temperature (b) at the centre of the discharge for the same operation conditions as those corresponding to figure 9.8 (pressures  $p_{out} = 660, 2000$  and  $8800$  Pa and absorbed power  $P_{abs} = 32$  W for  $660$  Pa and  $59$  W for  $2000$  and  $8800$  Pa). Note that for  $8800$  Pa (due to the Molecular Assisted Recombination -MAR- processes) the decay of electrons is not linear anymore and that the electron temperature increases along the plasma column with respect to the values in the launcher region.

increasing pressures molecular ions will be formed and subsequently destroyed, herewith reducing the degree of ionisation. Assuming that reaction (R12)



is the limiting step in the chain of MAR processes, we get for the effective recombination rate

$$k_{12}n_+n_1^2 = k_{12}n_en_1^2, \quad (9.5)$$

where we assumed in the last step that the atomic ions are still dominating ( $n_{\text{Ar}^+} \gg n_{\text{Ar}_2^+}$ ) so that  $n_{\text{Ar}^+} \sim n_e$ .

The action of MAR processes implies that the plasma is no longer purely diffusive and that the right-hand-side of the electron particle balance must be modified by adding a recombination term that depends on the square of the argon density. This will modify (9.3) into

$$k_{ion}^*(T_e) = D_a^*(R_p n_1)^{-2} + k_{12}n_1. \quad (9.6)$$

Now, if the gas temperature in the launcher increases and  $n_1$  subsequently decreases, it is obvious that recombination will decrease. So the increase of the frequency of diffusive losses is (partially) compensated by the decrease in recombination, resulting in a  $T_e$  value that remains more or less constant.

Note that the presence of MAR will destroy the applicability of the similarity law discussed above (see table 7.1 in chapter 7).

Further analysing the results obtained for the inner-launcher region, we see that increasing the pressure from 660 to 8800 Pa leads to higher values of  $n_e$  and  $T_e$ . The latter can be understood since the transfer of kinetic energy from electrons  $\{e\}$  to heavy particles  $\{h\}$ , see equation (5.28), depends on the product of  $n_1$  and  $n_e$ . Another trend observed for increasing pressure is that  $T_e$  decreases. This can be understood from equation (9.3). But the most dramatic effect in changing the pressure is manifested in the density of molecular ions. The reason is, as stated before, that the principal source of these ions depends on the square of the neutral atom density.

## 9.4.2 The Plasma Outside the Launcher

In figure 9.8(a), the axial profile of the electron density for different pressures is shown. Figure 9.9(b) gives the corresponding electron temperature. Note that a lower value of the absorbed power (32 W vs 59 W) is used for a pressure of 660 Pa. This is done to limit the axial extension of the discharge to a computational domain not larger than 800 mm. For the two lowest pressures we see that the density decreases almost linearly with the distance from the launcher whereas the electron temperature  $T_e$  remains constant along the column.

The (approximately) constant electron density gradient and constant electron temperature are consistent with the similarity laws shown in [24, 25, 149] for low pressures SWDs. One of the similarity laws is the ePB, equation (9.3), stating that  $T_e$  depends on the product of  $n_1 R_p$ . As  $R_p$  is constant whereas  $n_1$  does not change much we can expect a constant  $T_e$ -value. One should note that this behaviour is also found experimentally in the work of [150] where the electron temperature is determined from Absolute Line Intensities using the so-called ALI method. As the line intensity does not change (much) along the column we can expect that the same yields for the  $T_e$  deduced from ALI.

The dependence of  $T_e$  on the pressure is the same as what we found for the inner-launcher region. However, the linear decrease in  $n_e$  and constant value of  $T_e$  is not present for the case of the highest pressure of 8800 Pa. The  $n_e$ -decrease shown in figure 9.8(a) is no longer linear whereas  $T_e$  clearly rises along the plasma column (figure 9.9(b)). It reaches a maximum close to the plasma end and decreases sharply afterwards; i.e. at the location where the plasma ends. This rise in  $T_e$  for the 8800 Pa case can be explained by the extra loss mechanism of electron-ion pairs due to MAR processes (see section 9.4.1). This is supported by the behaviour of the  $\text{Ar}_2^+$  density. As soon as the concentration of  $\text{Ar}_2^+$  exceeds a few percent of the total ion density it will enhance the loss of electrons drastically. Indeed figure 9.9(a) shows that at 8800 Pa the  $\text{Ar}_2^+$  concentration is 2 order of magnitude higher than in the 660 Pa case and that the  $\text{Ar}_2^+$  concentration sharply increases towards the end of the plasma column. Further evidence of the role of MAR is found in the radial profiles given in figure 9.11 which show that in the high pressure case the electron temperature rises more towards the wall than in the lower pressure cases. For 660 and 2000 Pa the  $T_e$ -profile is nearly constant as we show in figure 9.11. This again can be attributed to the increase of the  $\text{Ar}_2^+$  density approaching the wall. An effect that is more prominent for higher pressures as found in figure 9.10.

### 9.4.3 Comparison with Experimental Results

Figures 9.12 and 9.13 compare the model results with those obtained experimentally in our group [151] giving the electron density and the temperature as functions of the axial position. These experimental  $n_e$ - and  $T_e$ -values are obtained by Thomson scattering (TS) [13, 76, 152] for similar plasma conditions. Here we present the result for the pressure of 2000 Pa and a total absorbed power of 59 W. In the experiments the power supply delivers 100 W; but only a part of this is absorbed by the plasma, whereas the rest is transmitted to the environment or used to heat-up the launcher. As the length of the measured plasma column is shorter than in the model we believe that the absorbed power in reality is even lower than 59 W (the model value).

This leads to a correction in figure 9.12(b) and figure 9.13(b) where the experimental

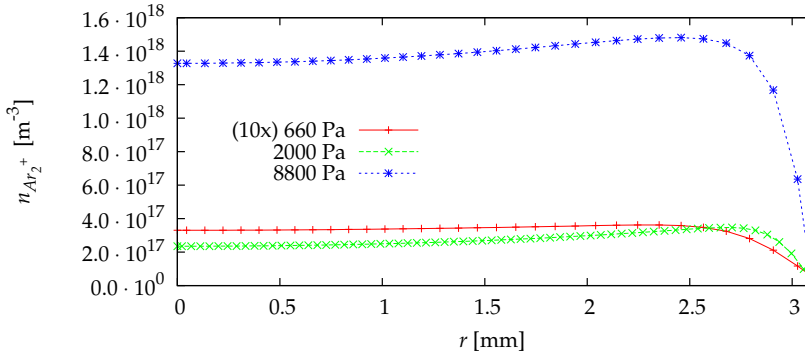


Figure 9.10: Radial distribution of molecular ions densities for pressures of 660 , 2000 and 8800 Pa at axial position  $z = 200$  mm.

curve  $n_e(TS)$  is axially shifted 175 mm such that the end of column (approximately) matches the ‘end of the column’ of the calculations. The position of the end of column in the model is estimated as  $z = 600$  mm, which is the position of the maximum value of the measured  $T_e$  (TS) in figure 9.13(b).

As we can see in figure 9.12(b), the simulation results for the axial distribution of the  $n_e$  follow the same trend of a linear decay toward the end of the column as the experimental results; moreover the absolute values of  $n_e$  for the region outside the launcher are (after shifting) comparable to those found experimentally.

Surprising is the axial distribution of the electron temperature figure 9.13(a). The measured  $T_e$ - values are strongly *increasing*, approaching the end of the plasma column whereas the model results points towards a *constant*  $T_e$  value; as discussed above, a behaviour that is more in agreement with the results obtained by ALI measurements and with the electron particle balance (equation (9.3)).

The difference between, on the one hand the results of ALI measurements, the ePB equation (9.3) and our Grand model and on the other hand the results of TS can be traced back to the fact that Thomson scattering measures the *bulk* of the electron energy distribution function (EEDF). This EEDF can change in form due to the plasma creation activity (excitation and ionisation). The creation of electron-ion pairs that is needed to support the outward diffusion or the losses of electron-ion pairs will lead to a depopulation of the tail of the EEDF. This depletion can easily be restored if the ionisation degree  $\alpha = n_e/n_1$  in the plasma is high i.e. if the electron-electron interaction is large. However, if  $\alpha$  is low the population of the tail will be depleted.

In using the models we basically solve equation (9.3) in which a *Maxwellian* form of the rate coefficient  $k_{ion}^*$  is used (cf. equation (5.34)). The temperature obtained in

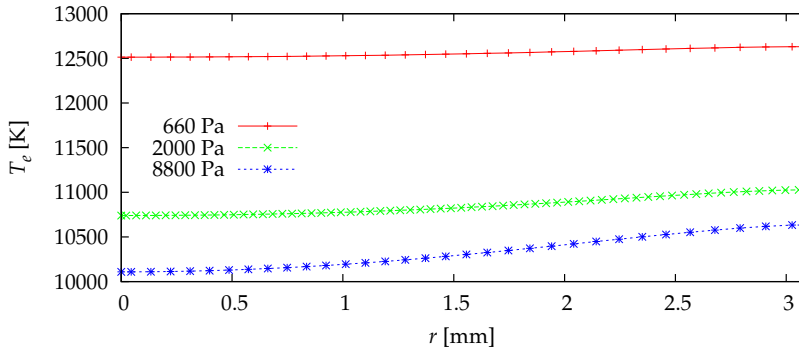


Figure 9.11: Radial distribution of electron temperature for pressures of 660 , 2000 and 8800 Pa at axial position  $z = 200$  mm.

this way is denoted by the *creation temperature*  $T_{crea}$ : defined as the temperature that a Maxwellian electron gas needs in order to create plasma with a rate that is large enough to support the removal of electron-ion pairs. If the EEDF is non-Maxwellian we need another formula for the rate; in general it no longer depends on just one single temperature but in principle on the whole EEDF. However, one can proof that for moderate deviations from Maxwell equilibrium the rate can be written as

$$k(\text{EEDF}) = k^*(T_{bulk})f(\alpha), \quad (9.7)$$

where the first factor (at the right-hand-side) is the Maxwellian rate given by the bulk temperature (or mean energy) whereas  $f(\alpha)$  gives a correction factor depending on the ionisation degree.

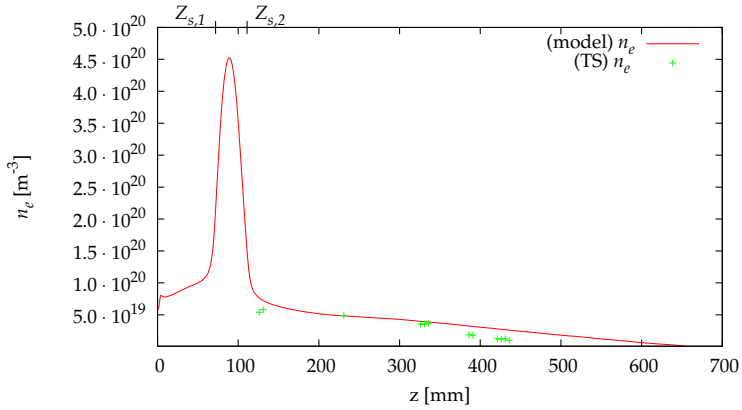
So the ePB we can written as

$$k^*(T_{bulk})f(\alpha) = D_a^*/(R_p n_1)^2 \equiv k^*(T_{crea}), \quad (9.8)$$

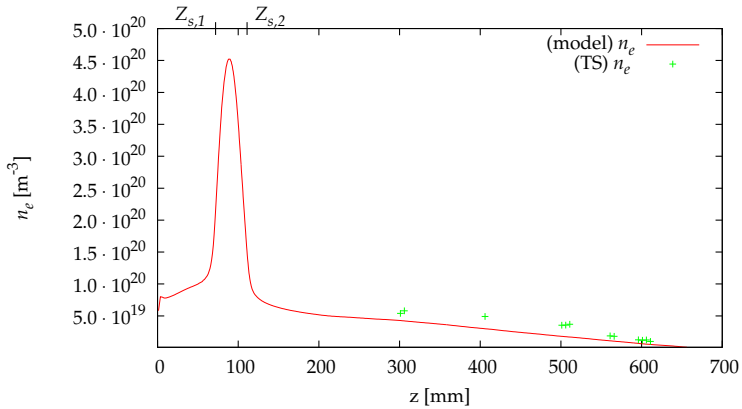
where the first part takes the deviation from Maxwell equilibrium into account, whereas the identity simple gives the definition of  $T_{crea}$ .

Now let us focus on  $f(\alpha)$ . This function is such that a decreasing  $\alpha$  leads to a lower value of  $f(\alpha)$ . That is what we get moving down-wave;  $n_e$  will decrease whereas  $n_1$  will increase (as  $T_g$  decreases). The resulting decrease in  $f(\alpha)$  will demand for a higher  $k^*(T_{bulk})$  and thus higher  $T_{bulk}$  value. This is indeed what the results of Thomson Scattering (TS) show.

Solving equation (9.8) for all kind of  $\alpha$ -values and comparing these with the value obtained for  $\alpha = 1$  we can obtain a relation  $F(\alpha) = T_{bulk}/T_{crea}$  between the  $T_{bulk}$  and

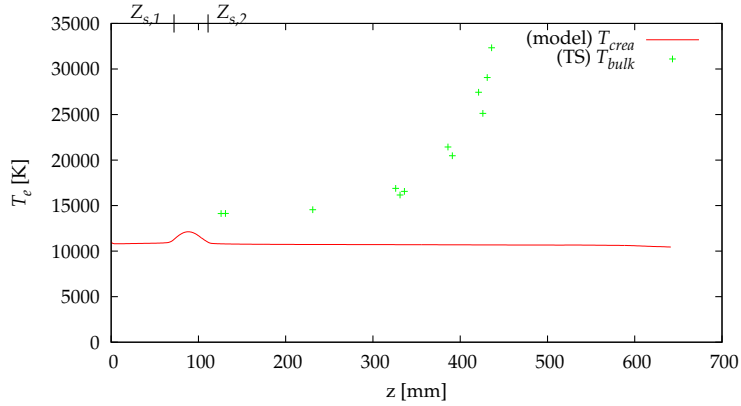


(a)

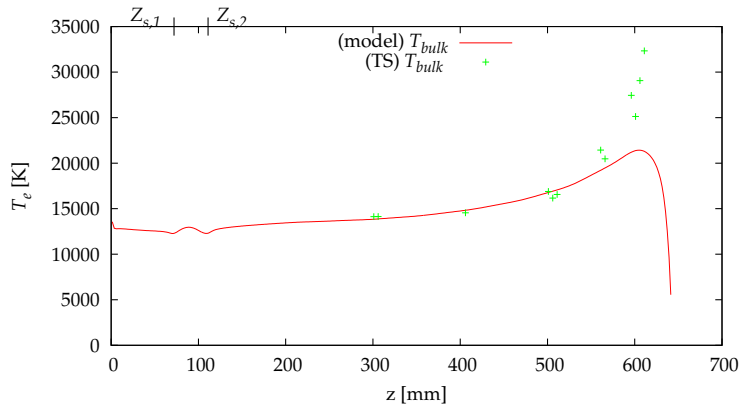


(b)

Figure 9.12: In (a) the calculated electron density (model)  $n_e$  along the plasma column compared to the measured electron density (TS). Note that the measured plasma column is shorter. The reason is that the 100 W given by the power supply differs from the power absorbed by the plasma which we believe that is in reality lower than the absorbed power in the model 59 W. In (b) we have shifted the  $n_e$ (TS) is axially ([76, 152]) 175 mm such that the end of column (approximately) coincides the computational end of the column of (model)  $n_e$ .



(a)



(b)

Figure 9.13: In (a) the calculated creation temperature (model)  $T_{crea}$  along the plasma column compared to the measured bulk temperature (TS)  $T_{bulk}$ . In (b) the measured electron temperature (TS)  $T_{bulk}$  along the plasma column compared to the bulk temperature (model)  $T_{bulk}$  which is obtained applying equation (9.9) to the numerical results and using the computational obtained ionisation degree  $\alpha = n_e/n_1$ . In (b) the experimental results are shifted so that the plasma ends (numerical and experimental) coincide (see figure 9.12).



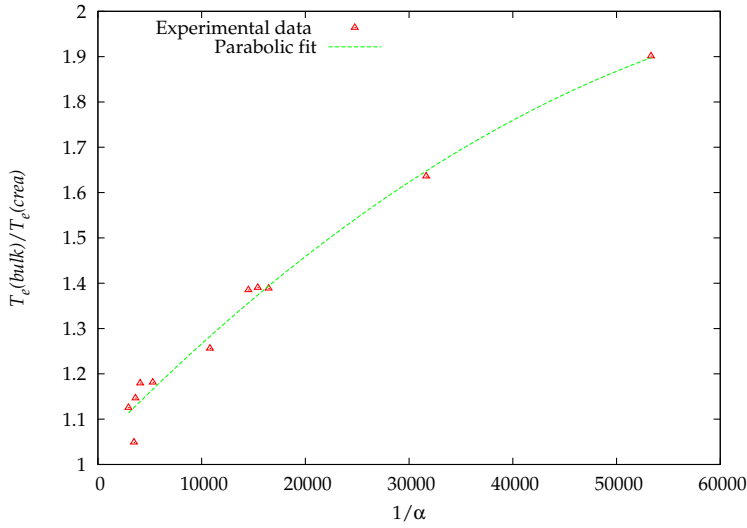


Figure 9.14: Bulk to creation temperature ratio as function of the ionisation degree as found experimentally for several plasmas (see [76])

the corresponding  $T_{crea}$  as a function of  $\alpha$ . This can be done theoretically for instance using the Bolsig+ code [32] but an experimental approach is possible as well.

The latter route was followed in [76] using the experimental results of  $T_{crea}$  and  $T_{bulk}$  obtained for Microwave Induced Plasmas operating under different settings i.e. different powers, pressures and  $\alpha$  values. By plotting the resulting  $T_{bulk}/T_{crea}$  as a function of  $\alpha$  we get the result given in figure 9.14.

It is striking that although the results are found for different plasma settings we still get just one single curve, meaning that  $T_{bulk}/T_{crea}$  only depends on  $\alpha$ . This experimentally obtained function, that can be fitted by

$$F(\alpha) = 1.046 + 2.347 \cdot 10^{-5}(1/\alpha) - 1.405 \cdot 10^{-10}(1/\alpha)^2 \quad (9.9)$$

can now be used to translate the model results into the bulk temperature. The results are subsequently compared with those of TS.

This is done in figure 9.13(b) where the results are again shifted to the end of the column. It shows similar trends and values as found experimentally.

## 9.5 Conclusions

In this chapter we have presented a Grand model for argon surfatron plasmas at intermediate pressures. Apart from the plasma *outside* the surfatron launcher, we have also studied the plasma *inside* the launcher as its behaviour is expected to be similar to the plasma inside the deposition reactor used in chapter 10. We showed that there is a strong increment inside the launcher of the electron density,  $n_e$ , and gas temperature,  $T_g$ , whereas the molecular ions are destroyed efficiently. Outside the launcher, we found an approximately linear decay of the central value of  $n_e$  in the axial direction, and an electron temperature,  $T_e$ , that is more-or-less constant for the pressures 660 and 2000 Pa. This means that at these pressures, the plasma is mainly diffusion-controlled. For 8800 Pa, there is no linear decay-profile for the axial  $n_e$  whereas  $T_e$  rises toward the end of the column. This indicates that at higher pressures, due to the formation and destruction of molecular ions, volume recombination becomes more important than diffusion followed by wall recombination.

We have also compared the model results with the measurements obtained with the active diagnostic method of Thomson scattering (TS). There is a reasonable agreement between the  $n_e$  found with the models and the experiments; both in trend as in values. However, for  $T_e$  we found large apparent discrepancies. We use the adjective "apparent" because the nature of the  $T_e$  obtained with the models is different from that obtained by TS. In the models we use rate-coefficients that are based on Maxwellian electron energy distribution functions (EEDF). Whereas TS gives the bulk temperature of an EEDF (thus the mean energy) that in practice may deviate from Maxwell. This apparent discrepancy is also found between the results of different experimental methods. The (experimental)  $T_e$ -values, derived from light emission features (ALI), agree quite well with the model results and thus deviate from the TS values. This deviation, that, experimentally, was found to be dependent on the degree of ionization,  $\alpha$ , can be used to convert the  $T_e$  found by ALI into the  $T_e$  determined by TS. If this experimental determined conversion [76] is applied to the model results we can derive from  $T_e$  and  $\alpha$  the electron temperature of the bulk of a non-Maxwellian EEDF. This procedure gives a model-based bulk temperature that follows the same trends and gives similar values as what is found experimentally with TS.



---

10

Deposition Reactor Argon Plasma at Intermediate  
Pressure

---

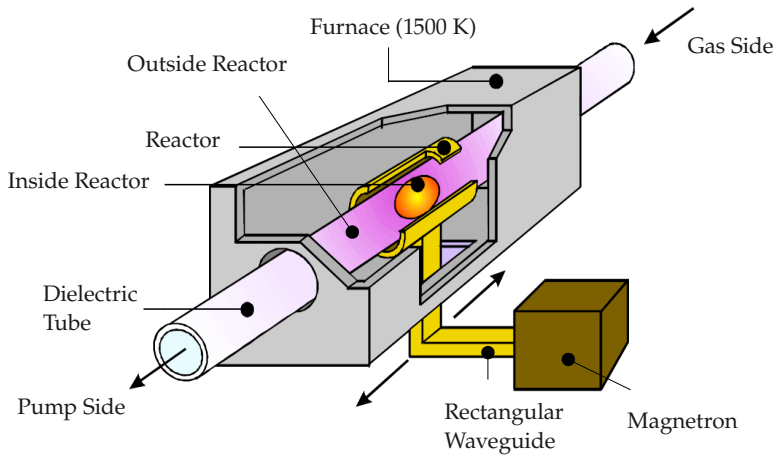


Figure 10.1: The plasma-activated chemical vapour deposition (PCVD) reactor used for the production of fibre optics.

## 10.1 Introduction

A well-known application of MIPs is Plasma-activated Chemical Vapour Deposition (PCVD) used for instance for the production of optical fibres [3, 19] or solar cells [153].

We will focus on the microwave deposition reactor described in [10, 11, 19]. This set-up, shown in figure 10.1, is employed in the first steps of fibre fabrication as performed at Draka. As shown in figure 10.2 the fabrication of fibre optics consists on three steps: Deposition, Collapsing and Drawing.

- Deposition

Plasma-activated chemical deposition (PCVD) process is the first step in the fibre production. It is the step in which a plasma is used. A microwave reactor surrounds a quartz tube that is mounted between a pump and a gas supply and delivers electromagnetic energy to the flowing gas thereby creating a plasma in non local thermal equilibrium. The gas composition is  $\text{SiCl}_4$  and  $\text{O}_2$ , plus some dopant used to control the refractive index. For example, germanium (introduced via  $\text{GeCl}_4$ ) increases the refractive index while fluorine (given in the form of  $\text{C}_2\text{F}_6$ ) decreases it. It is interesting to mention that  $\text{SiH}_4$  is not used to provide Si because the associated OH contamination introduces resonant losses to the light, increasing an unwanted attenuation at the resonant frequency. Nevertheless OH contamination will be created as result of the water found in

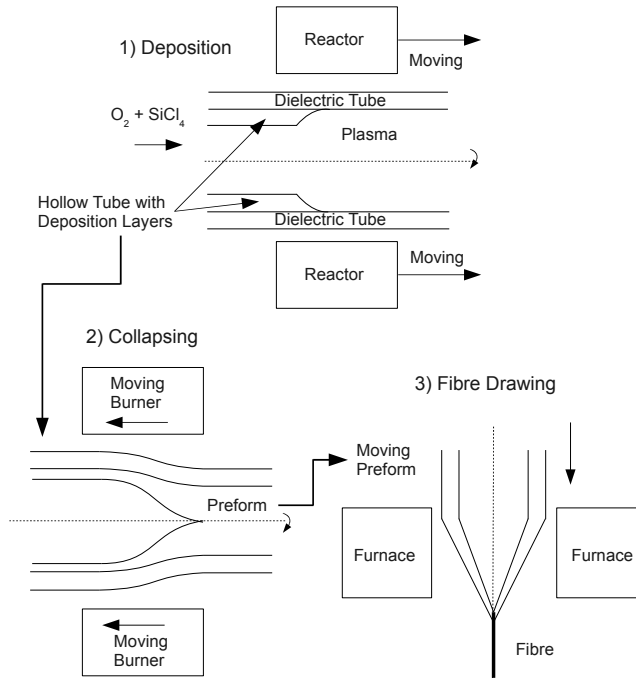


Figure 10.2: The production of fibre optics consist of three steps: 1) Deposition: A moving deposition reactor is used to create layers in the inner wall of a hollow dielectric (quartz) tube. 2) Collapsing: The hollow tube with deposited layers is heated by a burner and compressed into a core rod, i.e. the *preform* of the fibre. 3) Drawing: The preform is moved into the drawing tower. A furnace provides heat and the fibre is drawn. For more details we refer to [154].

the environment and possible contamination of the gas supply. It was found [154] that Fluorine reduced the OH contamination.

The reactor moves along the dielectric (quartz) tube back and forward creating at each stroke a deposition film. A layer is formed when a series of films with the same refractive index is deposited. We can control the refractive index of each layer depending on operation conditions such as the composition of the feeding gas, pressure, temperature, and power supplied. Thus a radial profile for the refractive index is created. This refractive index profile determines the characteristics of the fibre (for example losses, number of propagation modes, resistance against bending, etcetera).

In literature (see [155, 156]), we can find various studies on the *static* deposition

profile (fixed reactor). The reason is that it provides better and more information than the deposition profiles obtained for a *moving* plasma (see chapter 11).

However at the working conditions for the fibre production, the plasma cannot stay at one position for more than a few seconds, otherwise the plasma heating would melt the quartz tube.

- Collapsing

The hollow tube with the deposited layers is mounted with a burner around it. The heat and surface tensions collapses the hollow tube so that a core rod is obtained i.e. the *preform* of the fibre.

- Drawing

The preform is moved into a *drawing tower*. A furnace and the application of vertical stress converts the preform into the final fibre.

As said, we are only interested in the first step of the fibre fabrication process in which the electromagnetic-plasma coupling plays a key role. The electromagnetic power is delivered from a microwave power supply via a waveguide system into the cavity of the reactor. The power is coupled into the plasma via a gap, in the form of wave modes propagating in both axial directions. We will refer to the region consisting of plasma, quartz, and air surrounded by the reactor as the *reactor region*.

Part of the energy carried by EM waves will leak out of the reactor, in the form of surface waves that sustain an external smaller plasma while another fraction will be transmitted to the environment. The latter is particularly important, as reflections of waves with metal pieces in the environment will cause unwanted standing waves. The standing wave pattern can produce a similar standing pattern in the deposition profile in the preform. This is not convenient as the deposition profile is required to be as homogeneous as possible (see chapter 11).

In order to avoid the launching of waves and their transmission to the environment, the metal wall in the reactor is equipped with two quarter-wave short-circuit chokes [157]. These are (normally) positioned at a few centimetres from the ends of the reactor, in our case around 20 mm. A choke is a discontinuity in the inner metal wall of the reactor (see figure 10.4). As every discontinuity, it can be optimized to generate maximum reflection of the propagation wave in the waveguide. In the case of a quarter-wave choke, it acts as a short-circuit due to the *depth* of  $\lambda/4$ , with  $\lambda$  the wavelength of the propagating mode inside the reactor region. However the plasma is a dispersive medium, meaning that the wavelength  $\lambda$  depends on plasma parameters. Of course, depending on how much power is confined in the region inside the reactor, the plasma parameters will change. A proper description of the situation requires a

coupled solution of the electromagnetic and plasma aspect as was done in the Grand model presented and used in chapters 7, 8 and 9.

The Grand model mainly consists of three parts: Configuration, Transport, and Composition.

For the composition we will use the argon chemistry as described in section 7.3.3. The fact that this differs largely from what is used in the industrial practice is not so relevant since we are mainly interested in the confinement aspects of the EM fields inside the reactor.

For the transport part we use the tools described in chapter 4.

The configuration forms the main difference with those of the other SWD Grand models. The reactor is a metal cylinder with a length of about 200 mm, and a radius such that the distribution of the electromagnetic fields are shaped to optimal conditions. An important role is played by the features of the chokes.

Before to discuss the model and its results, we want to stress the difference between the *reactor* and the *surfatron*. The surfatron was designed to create a surface wave sustained plasma *outside* the launcher, the plasma inside the launcher is of not importance. The deposition reactor is designed for the opposite, i.e. to confine the plasma *inside* the launcher, here referred to as the reactor.

## 10.2 Model

The numerical model is basically the same as that used for the study of the surfatron in chapter 9. Meaning that the model consists of three main building blocks, *electromagnetism* as introduced in as introduced in chapter 3, *transport* described in chapter 4 and argon plasma *chemistry* as treated in chapter 7. The model is constructed using the PLASIMO numerical framework (chapter 2) of which the basic features are introduced in chapter 7. We refer to the above chapters for more details.

The main differences between the deposition reactor and the surfatron are found in the geometry, the boundary conditions, and control parameters such as pressure and absorbed power. We give these differences in the following sections. For the common aspects we refer to chapter 7.

### 10.2.1 Configuration: Geometry

In order to describe the geometry in two dimensions, we assume that the EM structure is rotational symmetric. The geometry is given in figure 10.5, with the parameters



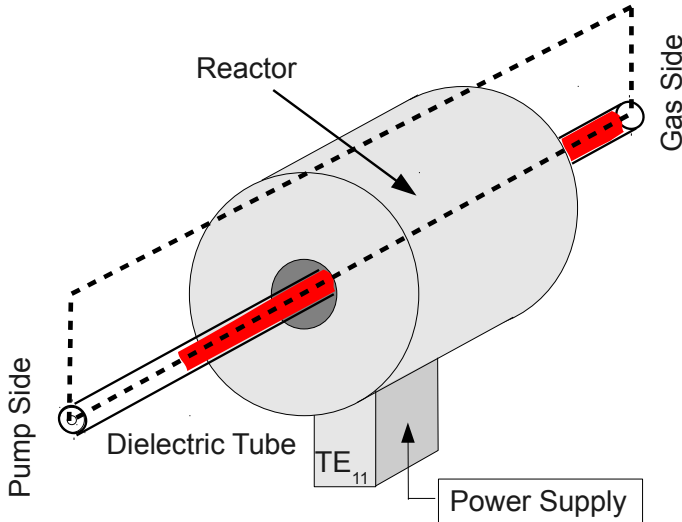


Figure 10.3: The set-up for fibre production using PCVD [155]. The deposition reactor, [11, 19] surrounds a dielectric (quartz) tube mounted between a gas supplier and a pump. A rectangular waveguide carries the power in the form of a TE<sub>11</sub> mode into the reactor. The cross-section is given in figure 10.4

values given in table 10.2. The discharge is sustained in a dielectric tube that has as internal and external radii  $R_p = 2$  mm and  $R_g = 2.6$  mm, respectively. The relative complex permittivity of the quartz is given by  $\hat{\epsilon}_r = 3.93 - i0.22$  at 1500 K [10].

The electromagnetic frequency equals  $f = 2.45$  GHz, and the power absorbed in the domain (plasma and quartz) is set to  $P_{abs} = 50$  W (see table 10.1). The reason behind the relatively low power is that we are primarily interested in the efficiency of the chokes containment of the EM waves.

## 10.2.2 Configuration: Boundary Conditions

The boundary conditions needed to solve the plasma transport equation are basically the same as those given in section 7.3.2.

Different is the BC of the heavy particle energy balance that is given by the continuity of the heat flux at the wall-plasma interface

$$\lambda \frac{\partial T}{\partial r} \Big|_{r=R_p} = \lambda_w \frac{\partial T}{\partial r} \Big|_{r=R_g} \quad (10.1)$$

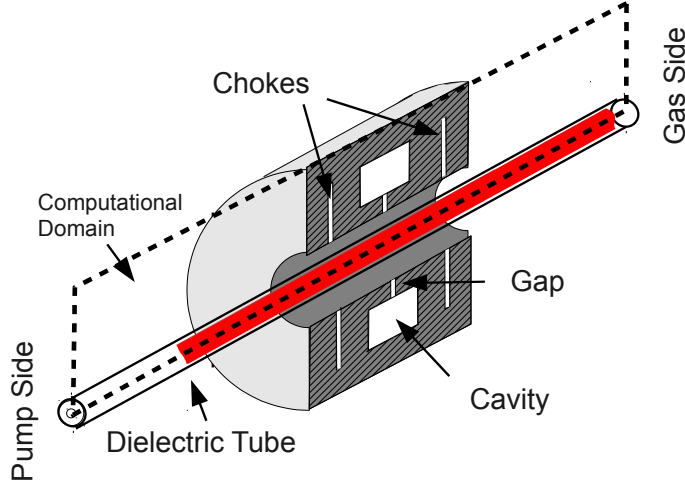


Figure 10.4: A cross-section of the reactor given in figure 10.3. We distinguish the cavity, chokes and gap. The EM fields are shaped by the cavity to get the best coupling through the gap toward the *reactor region* i.e. the part of plasma, quartz and air inside the reactor. The chokes also shape the EM fields by creating standing waves in the *reactor region* and limiting the EM power leakage to the environment. The dashed line indicates the edge of the computational domain given in figure 10.5.

Using the same assumptions as in [10], we obtain the right hand side term in analytical form, so that the BC transform into

$$\lambda_h \frac{\partial T_h}{\partial r} \Big|_{r=R_p} = \frac{\lambda_w (T_{fur} - T_{h,w})}{R_p \ln \left( \frac{R_g}{R_p} \right)} \quad (10.2)$$

This BC is of the type mixed Neumann as explained in chapter 2. This BC allows to set the temperature at the outer part of the tube. The BCs for the solution of the EM equations are given in figure 10.5.

For the electromagnetic fields a homogeneous Neumann boundary condition is applied to the electric field at the axis, whereas at the metal walls the perfect electrical conductor (PEC) boundary condition is used so that the component of the electric field tangential to the metallic surface is zero. The gap has been approximated as a parallel radial waveguide [62, 132] driven by the excitation boundary condition  $E_z|_{r=R_m} = E_0$ . This means that we do not model the EM cavity inside the reactor (the section in between by the two metal cylinders just above the gap in figure 10.4). The power density distribution is adjusted in order to obtain the power absorbed in the domain as prescribed by the control parameter  $P_{abs} = 50 \text{ W}$ . This is the *Power*

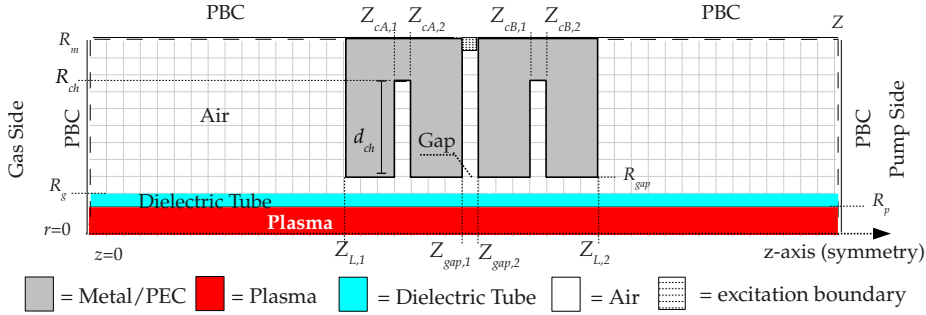


Figure 10.5: Computational domain of the deposition reactor. PEC, Perfect Electrical Conductor, PBC = Propagation Boundary Condition (see chapter 3). The dimensions parameters are given in table 10.2.

Par	Value	Par	Value
$p_{in}$	1000 Pa	$p_{out}$	1002 Pa
$T_{h,w}$	1500 K	$P_{abs}$	50 W
$f$	2.45 GHz		

Table 10.1: Control parameters for the Draka simulations.

Parameter	Value	Parameter	Value
$R_m$	50 mm	$R_p$	7.5 mm
$R_g$	9 mm	$R_{gap}$	10 mm
$R_{ch}$	variable		
$Z_{L,1}$	145 mm	$Z_{cA,1}$	178 mm
$Z_{cA,2}$	189 mm	$Z_{gap,1}$	244 mm
$Z_{gap,2}$	256 mm	$Z_{cB,1}$	311 mm
$Z_{cB,2}$	322 mm	$Z_{L,2}$	354 mm
$Z$	500 mm		

Table 10.2: Dimensions of the geometry in the deposition reactor simulations.

*Absorbed in Domain* excitation BC that was introduced in section 3.4.

A propagation boundary condition PBC is used at the rest of boundaries for the electric fields. For more information on the boundary condition for EM fields we refer to chapters 3 and 6.

The density of the ion  $\text{Ar}^+$  (see section 7.3.3) is set equal to  $8.5 \cdot 10^{17} \cdot \text{m}^{-3}$  at the wall, gas and pump sides, so that an under-dense plasma is avoided (see appendix A). In this model the deexcitation of  $\text{Ar}(4s)$  and  $\text{Ar}(4s)$  at the wall is disabled.

## 10.3 Results

Figure 10.6, giving the computed radial distribution of the electromagnetic field components, shows the expected discontinuity of the  $E_r$ -component at the dielectric interfaces, and the typical behaviour of the fields for surface waves i.e. higher values of the field components as they approach the dielectric interface both from the plasma and air sides. Note that in the air-region, with  $r > R_g$ ,  $|E_z|$  is one order smaller than  $E_r$  (e.g.  $|E_z| = 1400 \text{ V/m}$  and  $|E_r| = 12000 \text{ V/m}$  at  $r = 10 \text{ mm}$ ).

The radial profile of the electromagnetic fields inside the plasma is given in figure 10.6(b) and, in logarithm scale, in figure 10.6(c). We note that the  $E_z$  component is the most important inside the plasma (e.g.  $|E_z| = 300 \text{ V/m}$  and  $|E_r| = 5 \text{ V/m}$  at  $r = 7 \text{ mm}$ ), whereas  $E_r$  is higher in dielectric and air regions. Moreover, the  $E_r$  component changes drastically from  $|E_r| = 13000 \text{ V/m}$  at  $r = 9 \text{ mm}$  (air-region) toward  $|E_r| = 5 \text{ V/m}$  at  $r = 7 \text{ mm}$  (plasma-region).

The electromagnetic decay in the plasma is quite dramatic which is related to the high electron density (i.e. high conductivity). This is in analogy with the skin effect found in conductors. A difference with the normal skin effect in e.g. copper is that in the plasma the conductivity is radially non-uniform.

Results of the spatial distributions in the form of colour-map plots are shown in figures 10.7 and 10.8 for 1000 Pa and a depth for the chokes of  $d_{ch} = 38.5 \text{ mm}$ . Figure 10.7(a) gives the electron density distribution, which shows that the discharge is almost completely contained inside the Draka reactor with a maximum value of the electron density of  $n_e = 1.1 \cdot 10^{20} \text{ m}^{-3}$  axially situated at 4 cm from the entrance gap (i.e.  $z = 290 \text{ mm}$ ). This is substantially higher than the  $n_e = 1.2 \cdot 10^{18} \text{ m}^{-3}$  found at  $z = 374 \text{ mm}$ , that is outside the reactor at a distance of 10 mm from to the edge of the deposition reactor.

Figure 10.9 shows the radial distribution of  $n_e$  and the excited state densities at  $z = 300 \text{ mm}$ . The Bessel-like profile of  $n_e$  indicates that the discharge is diffusion controlled, meaning that  $n_e$  decreases toward a value close to zero as it approaches

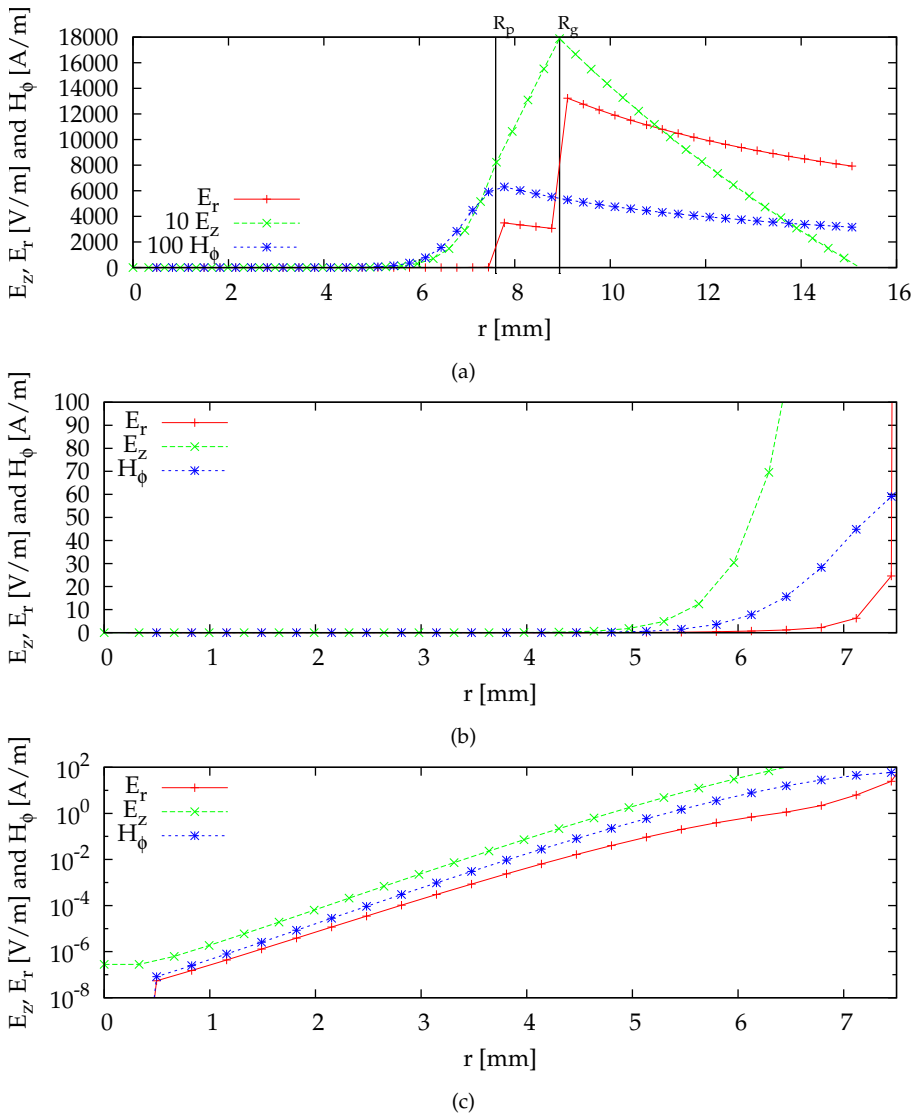


Figure 10.6: Radial distribution of EM field components at  $z = 300$  mm, that is, in the active plasma zone. The top figure gives a complete radial cross section, that is the plasma plus dielectric and air; the middle frame is devoted to the field components in the plasma in linear scale; the bottom gives the same information in logarithm scale. Note the different scales for  $E_z$  and  $H_\phi$  in (a). We find that  $|E_r| \gg |E_z|$  outside the plasma whereas for the plasma region  $|E_r| \ll |E_z|$ .

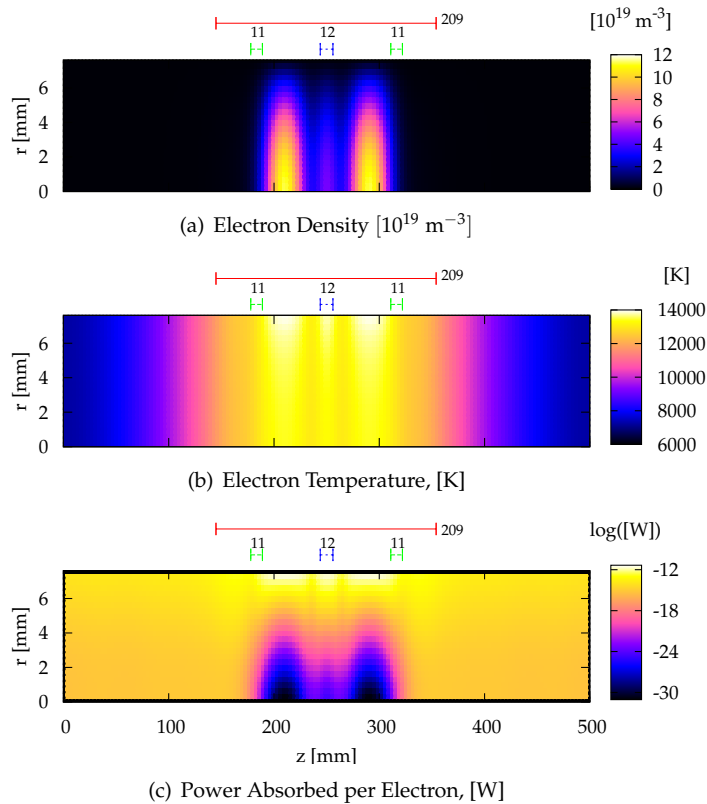


Figure 10.7: Colour-map plots of (a) the electron density  $n_e$  in [ $10^{19} \text{ m}^{-3}$ ], (b) electron temperature  $T_e$  in [K], (c) the power per electron-ion pair  $\theta$  in [W] (logarithm scale). Note that above each frame we have indicated the length of the reactor (209 mm), and the width of the chokes (11 mm each) and the gap (12 mm).

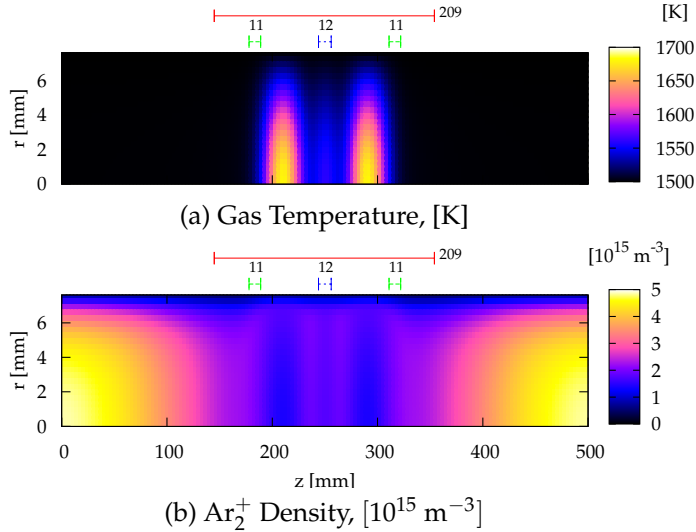


Figure 10.8: Colour-map plots of (a) the gas Temperature and (b) the density of  $\text{Ar}_2^+$ . Note that above each frame we have indicated the length of the reactor (209 mm), and the width of the chokes (11 mm each) and the gap (12 mm).

the wall. On the other hand the excited states 4s and 4p increase toward the wall. Especially the 4p distribution is important since it can be used for the validation of the model. The reason is that 4p generates most of the radiation that is easy observable. This computed radial 4p distribution is in agreement with the observation that the plasma emission has a donut-shape: a relative dark inner region surrounded by a brighter ring. This is experimentally shown in figure 12 of [158] for comparable conditions.

The value of the power absorbed per electron-ion pair  $\theta$  inside the reactor ranges from  $10^{-12}$  W at positions close to the wall tube to  $10^{-22}$  W at the centre of the discharge tube. Furthermore,  $\theta$  shows a minimum at the positions where  $n_e$  attains a maximum. These strong differences are due to the strong radial inhomogeneity of the electric field as given in figure 10.6(b).

In figure 10.8(a), we see that the gas temperature values are much higher than those obtained in figure 9.8 for the surfatron. However, this is a direct consequence of the boundary condition of the gas temperature that is taken to be 1500 K; a value, in agreement with reality where the whole deposition reactor is placed in a furnace, In the deposition reactor the gas temperatures varies in the range 1500 K to 1700 K (figure 10.8) whereas in the surfatron the range equals 330 K to 550 K for 660 Pa (see figure 9.8(b)).

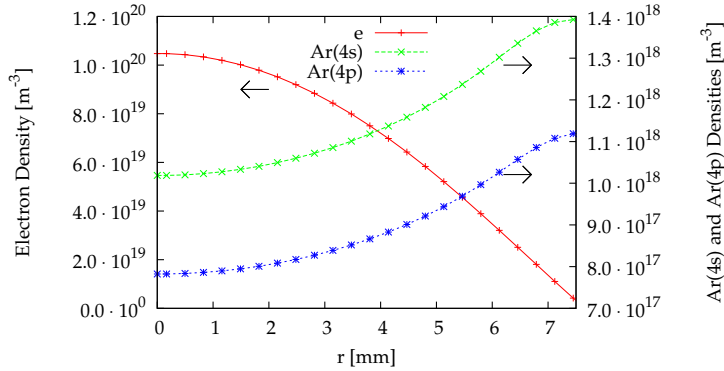


Figure 10.9: Radial distribution of the density of electrons and excited states in  $[\text{m}^{-3}]$  at  $z = 300$  mm. The radial distribution of the radiative state Ar(4p) is consistent with the donut-like profile found experimentally; that is darker in the centre.

### 10.3.1 Effect of the Choke Depth on Transmission

A quarter-wave short-circuit is applied in order to reflect incoming waves with wavelength  $\lambda$ . As said before, the aim of this construction is to confine the EM power inside the reactor region.

This works fine for non-dispersive components in waveguide circuits. However, the plasma is dispersive and therefore it will modify the wavelength of the propagating/reflecting wave. So, depending on the plasma density and other parameters the surface wave will have a longer or smaller wavelength. And depending on the chokes depth, more power will be contained inside the reactor and a higher electron density will be found, changing the wavelength.

In order to find the optimum value of the choke-depth, we need a self-consistent model for which different depths of the chokes are used as parameter. This is shown in figure 10.10 where a maximum was found for a choke-depth of  $d_{ch} = 38.5$  mm. This corresponds to a wavelength of 154 mm, which is around 30 mm longer than the vacuum wavelength at  $f = 2.45$  GHz.

In figure 10.11 we show the axial distribution of the electron density at the center of the discharge for different values of  $d_{ch}$ . The axial distribution for the power density at  $r = 7.2$  mm is given in figure 10.12. We see that the power density has a superimposed standing pattern outside the reactor close to the pump and gas sides. The reason is that the propagation boundary conditions (see chapter 6) induce the incident wave to be partially reflected at the pump- and gas-side boundaries. Only for the optimum confinement case (C), the oscillations disappear outside the reactor.



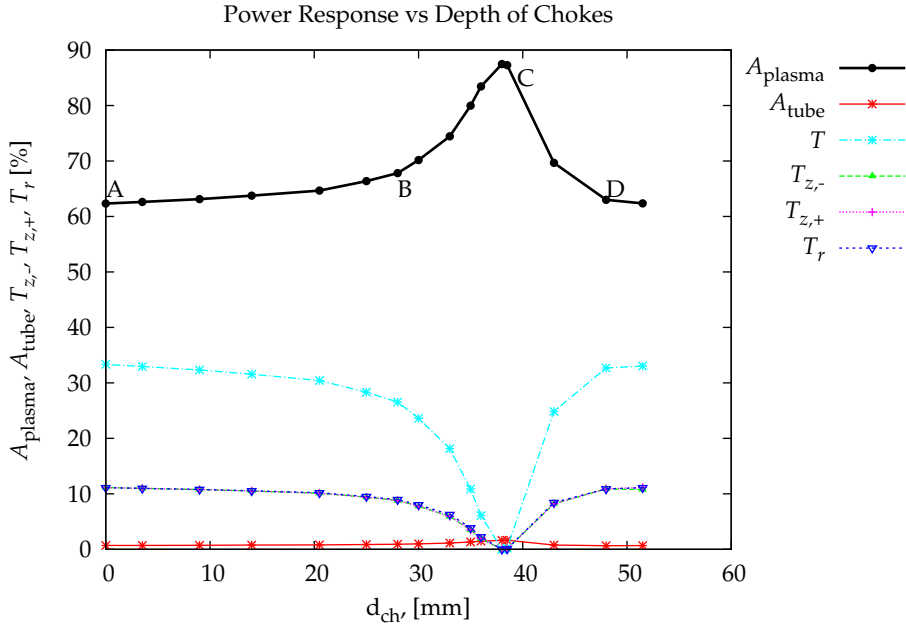


Figure 10.10: Power response as a function of the depth of the chokes,  $d_{ch} = R_{ch} - R_{gap}$ . All the coefficients are percentages of the net power absorbed in the domain  $P_{abs} = 50$  W. The coefficient  $A_{plasma}$  is the percentage of power absorbed in the plasma,  $A_{tube}$  the power absorbed in tube,  $T = T_{z,+} + T_{z,-} + T_r$  total transmitted power through the computational boundaries i.e. pump side  $T_{z,+}$ , gas side  $T_{z,-}$ , and radially  $T_r$ . The symbols A, B, C, and D refer to the chokes depths and corresponding axial profiles given in figures 10.11 and 10.12. It is clear that C is the optimum choke depth for power containment in the reactor.

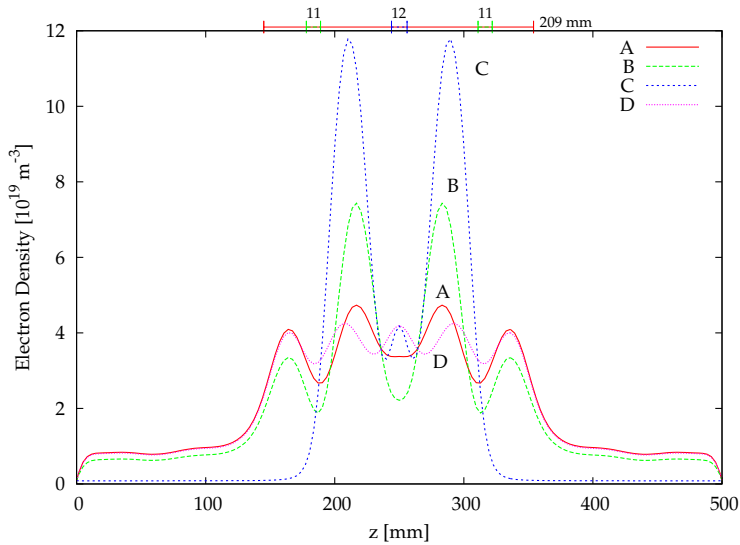


Figure 10.11: Axial distribution of the electron density at the center ( $r = 0$  mm) of the discharge for different choke depths  $d_{ch} = 0$  (A), 28 (B), 38.5 (C) and 48 mm (D). Above the frame the length of the reactor (209 mm), and the width of the chokes (11 mm each) and the gap (12 mm) are indicated.

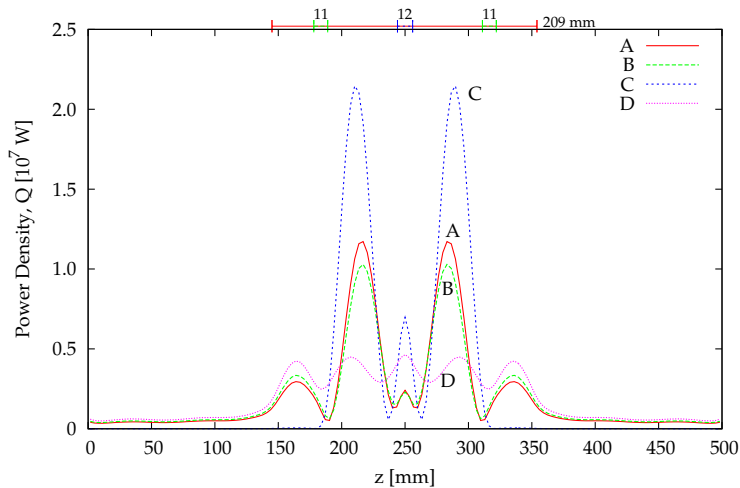


Figure 10.12: Axial distribution of the power density at  $r = 7.2$  mm for different choke depths  $d_{ch} = 0$  (A), 28 (B), 38.5 (C) and 48 mm (D). Above the frame the length of the reactor (209 mm), and the width of the chokes (11 mm each) and the gap (12 mm) are indicated.

## 10.4 Conclusions

We have shown and discussed the results of a Grand model applied to the electromagnetic plasma created within, and in the direct vicinity of, a deposition reactor. This model is applied to understand and validate the design of the chokes. It is found that a choke-depth of  $d_{ch} = 38.5$  mm is the optimum value to confine EM energy inside the reactor for the control parameters used in this study such as  $P_{abs} = 50$  W,  $p = 1000$  pa. In the future one should investigate whether the standing pattern for the electron density might influence the deposition profile.

---

# 11

Static and dynamic plasma deposition model:  
analytical and semi-empirical determination of  
local profiles and optimization of dynamic profiles

---

## 11.1 Introduction

The characterisation of plasma deposition kinetics is of wide interest in industrial applications and the optimisation of the deposition profile is usually as much important as the chemical purity (and/or controlled dopants addition) of the deposit. In chapter 10, we presented a Grand model for the deposition reactor used for optical fibre production at Draka Comteq. The Grand model provides a description of the plasma based on fundamental physical aspects such as configuration, transport and chemical composition (see chapter 2). While including a detailed chemistry of the  $\text{SiCl}_4/\text{O}_2$  into the Grand model, the latter will give an accurate description of the static deposition profile, corresponding to a resonator that is standing still. This profile is commonly referred as the *static deposition profile* [3, 156].

However for practical reasons (like local overheating of the tube which finally leads to the melting of the glass tube), in real production systems the reactor is moving along the tube in industrial (fast) deposition conditions. The deposition profile that is thus realised on the substrate is known as the *global deposition profile*.

In order to be able to calculate the global deposition profile from a static deposition profile, as obtained by the plasma model, and a given resonator velocity function  $v_R(r)$ , we have created the *forward deposition model*. This numerical tool is a first step towards the development of another tool, the so-called *inverse deposition model*, which recovers the local deposition profile from the global deposition profile and the resonator velocity.

This chapter has been organised as follows. In section 11.2 we discuss a model for local deposition profile, based on an earlier model by Weling *et al.* [156]. We will develop this model in more detail for the special case that the creation of the deposition precursor  $\text{SiO}_2$  happens in a small axial region. The resulting (exponential) profiles allow an analytical evaluation of the resulting global profiles for various reactor velocity functions, which will be presented in sections 11.3 and 11.4. In section 11.5 we discuss the numerical evaluation of the global deposition profile for arbitrary reactor velocity functions.

## 11.2 Local Deposition Profile

Weling *et al.* [156] created a deposition model to study the deposition profile for the static reactor. The starting point of Weling's model is the species balance equation (4.3) with Fick's law for the diffusion transport,

$$\nabla \cdot (\mathbf{v}n_s) - \nabla \cdot D_s \nabla n_s = S_s. \quad (11.1)$$

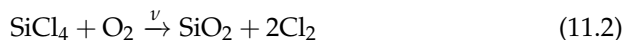
Here  $v$  is the flow velocity,  $D_s$  the diffusion coefficient,  $n_s$  the species density and  $S_s$  the net production of species  $s$  in reactions. The model considers three regions inside the tube: a plasma region, and the inlet and outlet sections in front and behind the plasma, respectively. It is based on the following model of the deposition process:

### Convection

The axial transport is by convection. All quantities in the model are functions of the axial position only, obtained by averaging over the tube cross section.

### Reactants conversion

The  $\text{SiCl}_4$  and  $\text{O}_2$  molecules are transported by convection to the plasma region. When they enter the plasma region, the following reaction starts to take place:



with  $\nu = k_0 n_{\text{O}_2}$  the *effective reaction frequency*, and  $k_0$  the effective reaction coefficient. Due to the large excess of  $\text{O}_2$  (e.g.  $n_{\text{O}_2} > 5n_{\text{SiCl}_4}$ ), the variation of the oxygen density is assumed to be negligible with respect to the change in the density of  $\text{SiCl}_4$  during the reaction.

### Diffusion

After the deposition precursor (here  $\text{SiO}_2$ ) is created, it is transported towards the wall with an effective transport frequency  $\nu_d$ . This is characterised by the *effective diffusion coefficient*  $D$ .

On the basis of this model, Weling was able to derive analytical expressions for the local deposition profile. The results are too cumbersome to allow an analytical calculation of the resulting *global* profiles, even for simple reactor velocity profiles.

In order to derive expressions for the local deposition profile that are realistic, but allow an analytical evaluation of the global profiles at the same time, we have developed a simplified version of Weling's model, which has been illustrated in figure 11.1. It is based on the assumption that  $\text{SiCl}_4$  is converted into  $\text{SiO}_2$  at a frequency  $\nu$ , so high that the reaction can be considered instantaneous, compared to the convective and diffusive time scales. In this case the flux density of  $\text{SiO}_2$  that enters the active region equals that of  $\text{SiCl}_4$  just before the active region. In the active region, the  $\text{SiO}_2$  flux is gradually reduced, since part of the molecules are transported to the wall by diffusive transport to the walls, where the molecules are deposited.

Küppers *et al.* [3] showed that the *local deposition profile* is an exponential function which, in the case of high flow velocity  $v$ , can be considered to start at a position  $z_0$  and decay toward the outlet with a decay rate  $\alpha$ . We refer to  $z_0$  as the *deposition front*, and in the following we take  $z_0 = z_R$ , with  $z_R$  the axial position of the reactor. This assumption does not induce any loss of generality in the treatment of the problem.

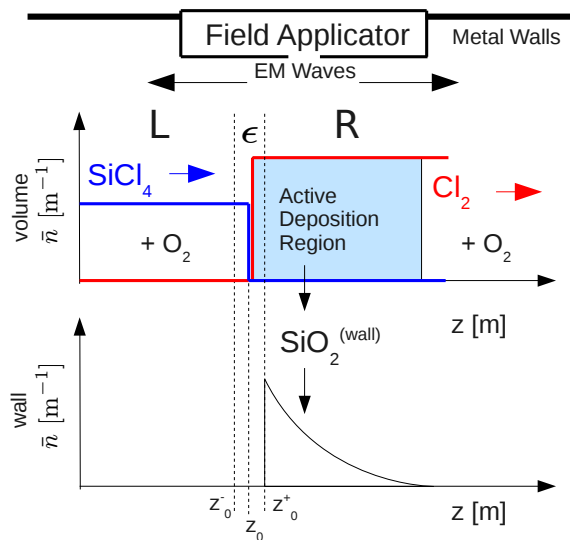


Figure 11.1: Schematic view of the deposition process assumed in the model. Above, meanwhile flowing along region L, the density of  $\text{SiCl}_4$  is constant. Then it enters into the Active Deposition Region,  $\epsilon$  and R. In the region  $\epsilon$ , the power and electron density are critical and all the  $\text{SiCl}_4$  molecules are converted instantaneously into the precursor and  $\text{Cl}_2$ . We assume region  $\epsilon$  as an infinitesimal small region starting at  $z_0^- = z_0 - \epsilon$  and ending at  $z_0^+ = z_0 + \epsilon$  with  $\epsilon \rightarrow 0$ . Therefore,  $z_0$  defines the deposition front. Below, as the precursors flows along region (II), it disappears and yields a  $\text{SiO}_2$  deposit profile along the tube walls.

In figure 11.2, we can see an example of static deposition profile at different deposition times. We can distinguish between two deposition regions: one small in the up-stream direction and another one in the down-stream direction. The later is much larger than the first, becoming even larger when the flow velocity increases (compared to figure 11.2 the flow rate is 10 times higher in [159]). This is the reason why for optical fibres, we assume in our model the extreme case in which the deposition region in the upstream direction is neglected, which implies that up-stream diffusion is neglected. Consequently, a step profile of the deposition is chosen, which sharply starts at the *deposition front*, as we show in figure 11.1 and figure 11.3.

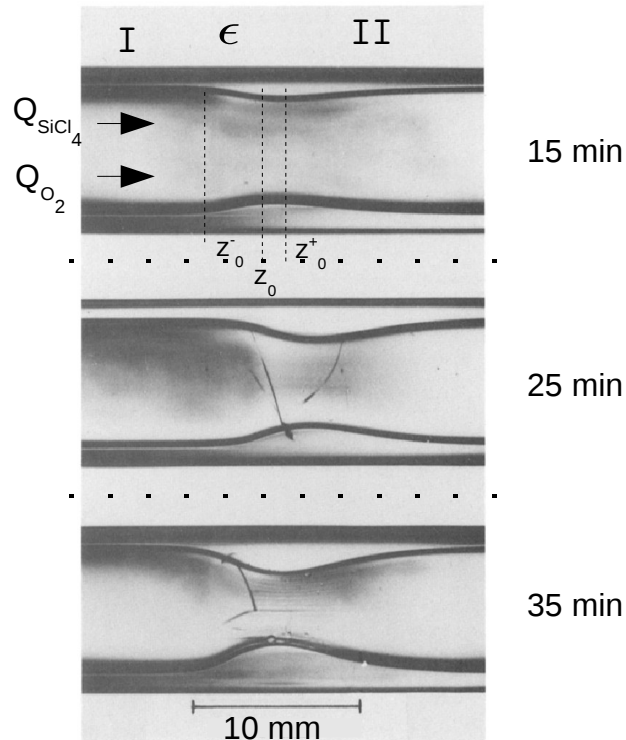


Figure 11.2: Deposition of  $\text{SiO}_2$  in the interior of a quartz glass tube with a stationary plasma (top, 15 min, middle 25 min bottom 35 min) The operating conditions are: Furnace Temperature,  $T_f = 970$  K, Flow,  $Q_{\text{O}_2} = 30$  sccm and  $Q_{\text{SiCl}_4} = 3.2$  sccm , Pressure,  $p = 10.7$  mbar, Power  $P = 75$  W. According to [155].



We will now develop a quantitative expression for the local deposition profile. First we define the precursor mass flow  $[\dot{m}(z)]$  in  $\text{kg s}^{-1}$  as

$$\dot{m}(z) = 2\pi M_{\text{pr}} \int_0^{R_p} v(r, z) n(r, z) r dr \quad (11.3)$$

which is the total number of precursor molecules that can be deposited inside the tube with radius  $R_p$  per unit of time in the case of an infinitely long tube or effective deposition efficiency of 100% for a tube of total length  $L_t$ . Here  $M_{\text{pr}}$  is the molar mass of the precursor, with units in  $\text{kg/mol}$  and the density  $n(r, z)$  is expressed in  $\text{mol}$ .

The precursor will gradually disappear in its course through the tube such that

$$\frac{d\dot{m}}{dz} = -\dot{\mu}, \quad (11.4)$$

where  $\dot{\mu}$  is the deposition rate per unit length with units  $\text{kg m}^{-1} \text{s}^{-1}$ .

We assume that the deposition rate per length  $\dot{\mu}$  is proportional to the mass flow available for deposition  $\dot{m}(z)$

$$\dot{\mu} = \alpha \dot{m}(z). \quad (11.5)$$

This assumption can be justified using the diffusion-convection equation (see equation (11.1)) [3]. Since no production of  $\text{SiO}_2$  takes place in the region where deposition takes place, this yields

$$\nabla \cdot (\mathbf{v}n) = \nabla \cdot D\nabla n, \quad (11.6)$$

where  $n$  is the concentration of the precursor  $\text{SiO}_2$ . With appropriate effective (radially averaged) parameters, equation (11.6) is simplified to

$$\frac{d}{dz} [\bar{v}(z)\bar{n}(z)] = -v_d \bar{n}(z) \quad (11.7)$$

with  $\bar{n}(z)$  and  $\bar{v}(z)$  are the axial distribution of the radially averaged flow velocity and concentration of  $\text{SiO}_2$ , defined as

$$\bar{n}(z) = \frac{2\pi}{\pi R_p^2} \int_0^{R_p} n(r, z) r dr. \quad (11.8)$$

and

$$\bar{v}(z) = \frac{2\pi}{\pi R_p^2 \bar{n}(z)} \int_0^{R_p} v(r, z) n(r, z) r dr, \quad (11.9)$$

so that  $\bar{v}(z)\bar{n}(z) = \dot{m}(z)$ . The effective transport frequency  $v_d$  (also defined in chapter 5) depends on the effective diffusion coefficient  $D$ .

After some rearrangement, we can rewrite equation (11.7) as

$$\frac{d\dot{m}}{dz} = -\frac{v_d}{\bar{v}}\dot{m}(z), \quad (11.10)$$

meaning that  $\alpha = v_d/\bar{v}$  is a reasonable approximation, and it is consistent with the results given in [3]. The characteristic deposition length  $1/\alpha$  is proportional to the flow velocity and inversely proportional to the radial effective transport frequency to wall  $v_d$ .

Substitution of equation (11.5) into equation (11.4) gives

$$\frac{d\dot{m}}{dz} = -\alpha\dot{m}(z), \quad (11.11)$$

which is indeed equation (11.10), although the nature of  $\alpha$  does not have to come from equation (11.6) i.e. it can include other unknown processes.

Let's take the precursor mass flow available at  $z = z_0$  equals to  $\dot{m}_0$ . With this boundary condition, the solution of equation (11.11) in the active deposition zone ( $z > z_0$ ) is

$$\dot{m}(z) = \dot{m}_0 \exp \left[ -\int_{z_0}^z \alpha(z') dz' \right]. \quad (11.12)$$

The decay coefficient  $\alpha$  is related to the *characteristic deposition length*  $w$  via  $w = \alpha^{-1}$ . Using this and equation (11.5), we can write the deposition rate per unit length as

$$\dot{\mu}(z) = \frac{\dot{m}_0}{w} \exp \left[ -\int_{z_0}^z \frac{dz'}{w} \right]. \quad (11.13)$$

In the following we will refer to  $\dot{\mu}/\dot{m}_0$  as the *local deposition profile*. A spatial dependency of  $w$  will arise from the non-uniformity of the plasma, via diffusion and convection, the sticking probability, the environment temperature, background power distribution, etc. However, under optimal plasma deposition conditions, this will not be the case as  $w(z) \neq w$  means a non homogeneous global deposition profile.

If we consider an axially constant  $w$  and a deposition front at  $z_0 = 0$ , and calculate the local deposition profile in the active region ( $z > z_0$ ), it gives

$$\frac{\dot{\mu}(z)}{\dot{m}_0} = \frac{1}{w} \exp \left( -\frac{z}{w} \right). \quad (11.14)$$

Figure 11.3 shows the corresponding local deposition profiles for  $w = 0.1L$  and  $w = 0.2L$ . Here  $L$  is a renormalisation quantity that we introduce in section 11.4.

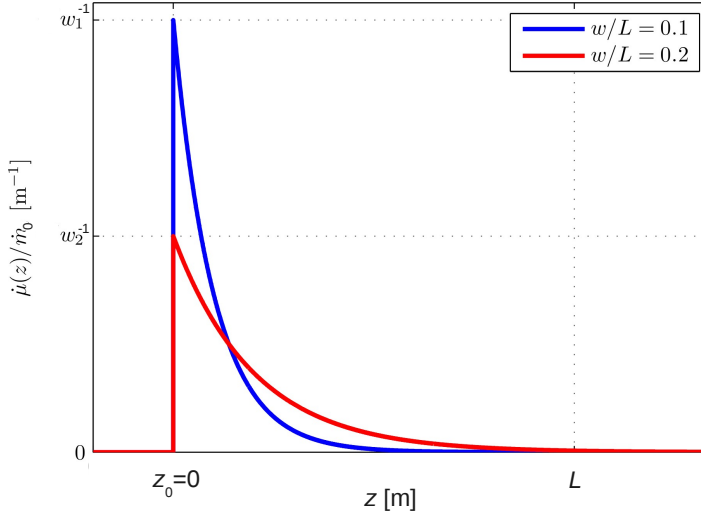


Figure 11.3: Local deposition profile for two values of  $w$ :  $w = 0.1L$  and  $0.2L$ . Here  $L$  is a normalisation length. Note that the deposition front is at  $z_0 = 0$ .

### 11.3 Deposition Profile for a Static Reactor

The mass deposited per unit length after the deposition time,  $T$  in the case of a static reactor is obtained from the integral over time of the local profile,  $\dot{\mu}$ ,

$$\mu(z, T) = \int_0^T \dot{\mu}(t) dt. \quad (11.15)$$

Its units are in kg/m. If  $\dot{\mu}$  is time-independent, we obviously get

$$\mu(z, T) = \dot{\mu}(z)T, \quad (11.16)$$

so the global deposition profile at time  $T$  is proportional to the local deposition profile.

Normally,  $\dot{\mu}$  can be assumed constant for small deposition times during which control and plasma parameters are constant. For instance, the times must be at least small enough such that plasma is not affected by the change in the inner radius due to the deposition. When equation (11.16) holds, the deposition profile for the static reactor can be directly translated into the local deposition profile, which provides important information about the plasma parameters.

## 11.4 Global Deposition Profile: Moving Deposition Reactor

As equation (11.15) and figure 11.2 show, the global deposition profile is not uniform along  $z$ . Of course, this is a non-desired situation as in the creation of optical fibres uniform deposition profiles are needed. To solve this problem, the deposition front is moved with a velocity profile that is chosen such that the length of the axially uniform global deposition profile is optimised. To move the deposition front, two solutions are possible and practically used

1. Static reactor: plasma length modulation of SWDs with power.
2. Moving Reactor: the plasma follows the reactor.

In the first case, we have the plasma discussed in chapter 9. Here we use the end of the plasma column as the deposition front, which changes while changing the power. This set-up is discussed in [11], and is practically interesting for its easy accessibility with respect to diagnostics techniques.

In the second case, the deposition reactor moves along  $z$  and with it, the plasma and the deposition front. This deposition reactor is the same as that discussed in chapter 10, and this is the solution which is eventually used at Draka Comteq.

We will focus on the second case, and show how, from the selection of an appropriate reactor velocity profile, we can optimise the constant deposition profile region. The global deposition profile is obtained as in equation (11.15), with the difference that instead of the total deposition time  $T$ , we use  $T_s$ , the duration of one stroke, and that we assume some dependency of the local profile on the deposition reactor position  $z_R$ . Therefore

$$\mu(z) = \int_0^{T_s} \dot{\mu}[z; z_R(t)] dt. \quad (11.17)$$

Note that  $T = N \times T_s$ , with  $N$  the number of strokes.

The key to determine the global profile is the velocity of the microwave plasma reactor, so we will relate the reactor position  $z_R$  to the velocity  $v_R$  so that

$$dt = \frac{dz_R}{v_R(z_R)}, \quad (11.18)$$

and we can define the following relation

$$z_R(t) = z_R(0) + \int_0^t v_R(\tau) d\tau. \quad (11.19)$$

For simplicity, we choose  $z_R(0) = 0$  and  $z_R(T) = L$ , with  $L$  the length of one stroke of the reactor, and equation (11.17) becomes

$$\mu(z) = \int_0^L \frac{\dot{\mu}(z; z_R)}{v_R(z_R)} dz_R. \quad (11.20)$$

The local deposition profile shown in equation (11.14) can be generalised for a moving deposition reactor

$$\frac{\dot{\mu}(z; z_R)}{\dot{m}_0} = \frac{1}{w(z; z_R)} \exp \left[ - \int_{z_0(z_R)}^z \frac{1}{w(z'; z_R)} dz' \right] H[z - z_0(z_R)], \quad (11.21)$$

where we have normalised to  $\dot{m}_0$ . The Heaviside function  $H$  is defined as zero for negative argument, i.e. outside the active deposition region ( $z < z_0$ ) and one for positive argument i.e. inside the active deposition region ( $z > z_0$ ).

Using the properties of the Heaviside function and equation (11.21), and taking  $z_0(z_R) = z_R + \Delta z_0(z_R)$ , equation (11.20) can be rewritten as,

$$\mu(z) = \begin{cases} 0, & z \leq z_0(0), \\ \int_0^{z - \Delta z_0(z_R)} \frac{\dot{\mu}(z; z_R)}{v_R(z_R)} dz_R, & z_0(0) \leq z \leq z_0(L), \\ \int_0^L \frac{\dot{\mu}(z; z_R)}{v_R(z_R)} dz_R, & z \geq z_0(L). \end{cases} \quad (11.22)$$

with  $v_R(z_R)$  the velocity profile for the reactor as function of its position  $z_R$ .

For a constant characteristic deposition length  $w(z; z_R) = w$ , and constant offset  $\Delta z_0(z_R) = \Delta z_0$ , equation (11.21) converts into

$$\dot{\mu}(z) = \frac{\dot{m}_0}{w} \exp \left( - \frac{z - z_R - \Delta z_0}{w} \right). \quad (11.23)$$

Note that equation (11.23) reduces to equation (11.14) when  $z_R = 0$  and  $\Delta z_0 = 0$ .

### 11.4.1 A Constant Reactor Velocity Profile

With equation (11.23), and a constant reactor velocity  $v_R(z_R) = v_R$  we calculate equation (11.22) and obtain the global deposition profile as

$$\mu(z) = \frac{\dot{m}_0}{v_R} \begin{cases} 0, & z \leq \Delta z_0, \\ \left[ 1 - \exp\left(-\frac{z - \Delta z_0}{w}\right) \right], & \Delta z_0 \leq z \leq L = \Delta z_0, \\ \exp\left(-\frac{z - L - \Delta z_0}{w}\right) \left[ 1 - \exp\left(-\frac{L}{w}\right) \right], & z \geq L + \Delta z_0. \end{cases} \quad (11.24)$$

Examples of global deposition profiles with  $\Delta z_0 = 0$  and for  $w = 0.1L$  and  $w = 0.2L$ , are shown in figure 11.4.

As we can see, the global deposition profile is not constant along  $z$  for a constant velocity profile. The non-uniform region is referred to as *taper*, and its length is defined as the distance in which the variation of the global deposition profile is higher than 10%. This is consistent with the result of [159] shown in figure 11.5. As we can see, we obtain similar effect than when changing the value of the characteristic deposition length in figure 11.4. This is an empirical validation of the simplification  $w = \bar{v}/v_d$  [3], as  $\bar{v}$  is closely related to the flow rate  $Q$  as given by

$$Q = 2\pi M_{pr} \int_0^{R_p} v(r)n(r)rdr.$$

Moreover, an appropriate velocity profile for the reactor allows to deposit more  $\text{SiO}_2$  at the taper region and reduce its length. As it is done in the industrial set-up, we define the profile for the squared deposition reactor velocity,  $v_R^2$ , which corresponds to piece-wise constant acceleration.

Note that the integral in equation (11.17) is always regular, while the integral in equation (11.20) becomes singular if turning points are taken into account, because  $v_R(0) = v_R(T) = 0$ .

### 11.4.2 An Arbitrary Reactor Velocity Profile (Multiple Ramps)

Let us now evaluate equation (11.17) under the assumptions that

1. the square of the reactor velocity is a piece-wise continuous linear function of

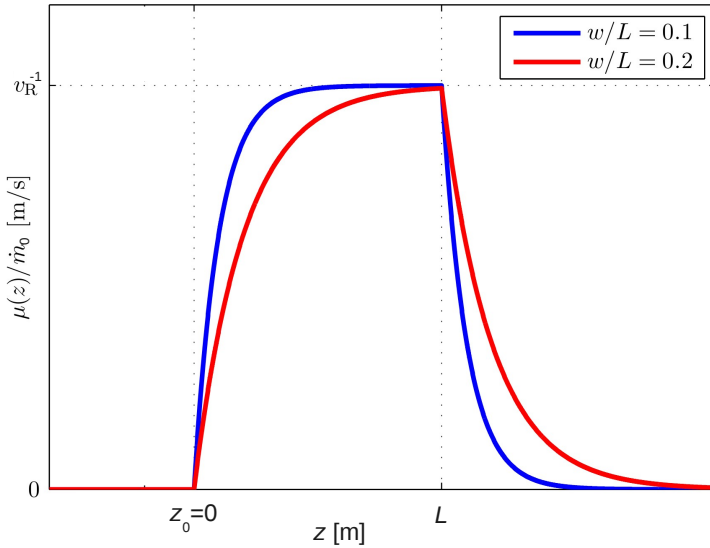


Figure 11.4: Global deposition profiles normalised to  $\dot{m}_0$  for two values of  $w$ :  $w = 0.1L$  and  $0.2L$ .

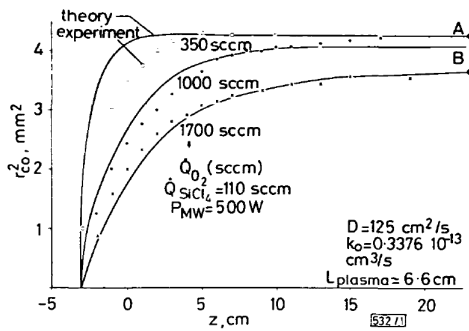


Fig. 1 Dynamic deposition profiles

Oxygen flows  $Q_{O_2}$  between 350 and 1700 sccm,  $SiCl_4$  flow  $Q_{SiCl_4} = 110$  sccm  
 $r_{co}$  is the radius of the cylinder formed by the deposited material in the collapsed preform

Figure 11.5: Global deposition profiles as given in [159] for different flow rates  $Q$ . As we can see, we obtain similar effects than when changing the value of the characteristic deposition length in figure 11.4. This is consistent with the simplest model  $w = \bar{v}/v_d$  [3], as  $\bar{v}$  is closely related to the flow rate  $Q$ .

## 11.4. Global Deposition Profile: Moving Deposition Reactor

$z_R$ . In general, we can define  $N$  regions for the squared velocity profile. This corresponds to piece-wise (de)acceleration.

2. the characteristic deposition length is constant with respect to  $z_R$  in each region  $I$ , and we can take into account a dependency on  $z$

$$w_I = w(z; z_R), \quad \text{with } (z_{R;I-1} \leq z_R \leq z_{R;I}) \quad (11.25)$$

3. the deposition front depends on  $z_R$ , i.e.  $z_0 = z_0(z_R)$

$$z_0(z_R) = z_R + \Delta z_0(z_R) \quad (11.26)$$

where the offset  $\Delta z_0$  is a well-behaved function on  $z_R$ . The offset is constant in each region  $I$

$$\Delta z_0^I = \Delta z_0(z_{R;I}) \quad \text{with } (z_{R;I-1} \leq z_R \leq z_{R;I}). \quad (11.27)$$

The global profile depends on the velocity profile chosen for the deposition reactor movement. For  $N$  regions, the squared velocity profile ( $v_R^2(z_R)$ ) is given by

$$v_R^2(z_R) = \begin{cases} v_1^2 + 2a_1 z_R, & z_{R;1} \leq z_R \leq z_{R;2}, & \text{Region 1,} \\ \vdots & \vdots & \\ v_I^2 + 2a_I(z_R - z_{R;I}), & z_{R;I} \leq z_R \leq z_{R;I+1}, & \text{Region } I, \\ \vdots & \vdots & \\ v_N^2 + 2a_N(z_R - z_{R;N}), & z_{R;N} \leq z_R \leq z_{R;N+1}, & \text{Region } N. \end{cases} \quad (11.28)$$

The pairs  $(z_{R;I}, v_I)$  are the speed point at each region  $I$  and together with the number of regions  $N$ , they define the squared velocity profile. The (constant) acceleration in region  $I$ ,  $a_I$  (i.e.  $z_{R;I} \leq z_R \leq z_{R;I+1}$ ) equals

$$a_I = \frac{1}{2} \frac{v_{I+1}^2 - v_I^2}{z_{R;I+1} - z_{R;I}}. \quad (11.29)$$

We introduce  $\mu_I(z)$  as the contribution to the global deposition profile during the time spent by the reactor in travelling through region  $I$ . This allows us to obtain the global deposition profile  $\mu(z)$  with arbitrary input profile as

$$\mu(z) = \sum_{I=1}^N \mu_I(z). \quad (11.30)$$



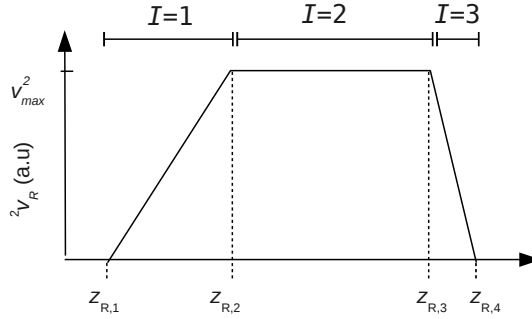


Figure 11.6: A squared reactor velocity profile as function of the reactor position  $z_R$ . It is composed by 3 regions ( $N = 3$ ) with  $I = 1$  and  $I = 3$  being ramps and  $I = 2$  a constant reactor velocity region.

Note that

$$\mu_I(z) = 0, \quad \text{for } z \leq z_{R;I} + \Delta z_0(z_{R;I}), \quad (11.31)$$

if  $\Delta z_0$  is a well-behaved function.

The deposition profile in region  $I$  is (as from equation (11.20))

$$\mu_I(z) = \int_{z_R=z_{R;I}}^{z_{R;I+1}} \frac{\dot{\mu}(z; z_R)}{v_R(z_R)} dz_R. \quad (11.32)$$

We will compute  $\mu_I(z)$  only for two different squared velocity profiles,  $v_R^2(z_R)$ , namely

$$\mu_I(z) = \begin{cases} \mu_I^C(z; v_I), & \text{if } a_I = 0 \text{ (i.e. constant } v_R^2(z_R)), \\ \mu_I^L(z), & \text{if } a_I \neq 0 \text{ (i.e. linear } v_R^2(z_R)). \end{cases} \quad (11.33)$$

As an example, consider three regions ( $N = 3$ ) with region  $I = 1$  and  $I = 3$  being ramps and region  $I = 2$  having a constant reactor velocity as shown in figure 11.6. Then, equation (11.30) reduces to,

$$\mu(z) = \mu_1^L(z) + \mu_2^C(z; v_2) + \mu_3^L(z). \quad (11.34)$$

#### 11.4. Global Deposition Profile: Moving Deposition Reactor

For computing  $\mu_I^L(z)$ , the singularity at  $v_R(z_R) = 0$  is avoided by using the change of variables

$$\frac{1}{v_R(z_R)} dz_R = \frac{1}{a_I} d \left[ v_I^2 + 2a_I(z_R - z_{R;I}) \right]^{1/2}, \quad (11.35)$$

which regularises the singular integral in equation (11.32)

$$\begin{aligned} \mu_I^L(z) &= \frac{1}{a_I} \int_{z_R=z_{R;I}}^{z_{R;I+1}} \dot{\mu}(z; z_R) d \left[ v_I^2 + a_I(z_R - z_{R;I}) \right]^{1/2} \\ &= \frac{1}{a_I} \int_{z_R=z_{R;I}}^{z_{R;I+1}} \dot{\mu}(z; z_R) dv_R(z_R). \end{aligned} \quad (11.36)$$

#### Linear Squared Velocity Profile

Another analytical solution can be obtained while assuming a local profile with axial invariant properties (i.e. offset  $\Delta z_0^I$  and characteristic deposition length  $w_I$  are constant) within  $z_{R;I} < z_R < z_{R;I+1}$ . Equation (11.14) is substituted in equation (11.36) to obtain

$$\mu_I^L(z) = \dot{m}_0 \sqrt{\frac{\pi}{2a_I w_I}} \exp \left[ -\chi_I^2(z - \Delta z_0^I) \right] \times \begin{cases} 0 & z - \Delta z_0^I \leq z_{R;I}, \\ \text{Erfi} \left[ \chi_I(z - \Delta z_0^I) \right] - \text{Erfi} \left[ \chi_I(z_{R;I}) \right], & z_{R;I} \leq z - \Delta z_0^I \leq z_{R;I+1}, \\ \text{Erfi} \left[ \chi_I(z_{R;I+1}) \right] - \text{Erfi} \left[ \chi_I(z_{R;I}) \right], & z - \Delta z_0^I \geq z_{R;I+1}, \end{cases} \quad (11.37)$$

where  $\chi_I(z_R)$  has been introduced as

$$\chi_I(z_R) = \frac{1}{\sqrt{2a_I w_I}} \left[ v_I^2 + 2a_I(z_R - z_{R;I}) \right]^{1/2}. \quad (11.38)$$

Furhermore, Erfi is the imaginary error function (see [125]) defined as

$$\text{Erfi}(x) = \frac{2}{\sqrt{\pi}} \int_{x'=0}^x \exp(x'^2) dx'. \quad (11.39)$$

### Constant (Squared) Velocity Profile

For  $\mu_I^C(z; v_I)$ , we also assume a local deposition profile with axial invariant properties as in section 11.4.2. We can write

$$\mu_I^C(z; v_I) = \frac{\dot{m}_0}{v_I} \int_{z_R=z_{R;I}}^{z_{R;I+1}} \frac{1}{w_I} \exp\left(-\frac{z - z_R - \Delta z_0^I}{w_I}\right) H(z - z_R - \Delta z_0^I) dz_R. \quad (11.40)$$

The integration result is similar to the one required to obtain equation (11.24), but with the following substitutions in equation (11.24),

$$\begin{aligned} L &\rightarrow z_{R;I+1} - z_{R;I} \\ \Delta z_0 &\rightarrow z_{R;I} + \Delta z_0^I \end{aligned} \quad (11.41)$$

which leads to the expression,

$$\mu_I^C(z; v_I) = \frac{\dot{m}_0}{v_I} \begin{cases} 0, & z - \Delta z_0^I \leq z_{R;I}, \\ \left[ 1 - \exp\left(-\frac{z - z_{R;I} - \Delta z_0^I}{w}\right) \right], & z_{R;I} \leq z - \Delta z_0^I \leq z_{R;I+1}, \\ \exp\left(-\frac{z - z_{R;I+1} - \Delta z_0^I}{w}\right) \left[ 1 - \exp\left(-\frac{z_{R;I+1} - z_{R;I}}{w}\right) \right], & z - \Delta z_0^I \geq L. \end{cases} \quad (11.42)$$

Figure 11.7 gives an example of global deposition profile obtained using a velocity profile divided in 3 regions: one ramp of length  $L_{\text{ramp}} = z_2 - z_1 = w$  to increase the deposit at the taper, a region with constant velocity and a very small ramp at the end (where we do not want more deposit here).

In figure 11.8, we show that the model can be used to minimise the taper length (maximise the length of the uniform region in the global deposition profile) for  $L_{\text{ramp}} = 0.85w$ .

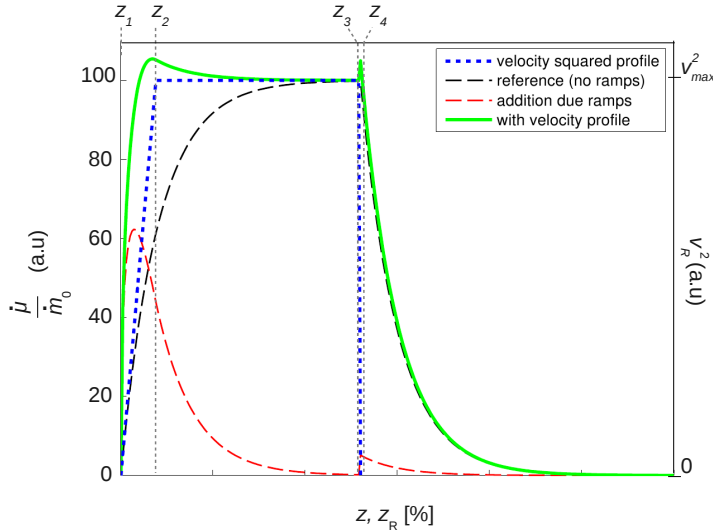


Figure 11.7: Global deposition profile (left axis) calculated for a 3 regions squared velocity profile (right axis). Broad ramp at region 1 ( $z_1 < z_R < z_2$ ), constant value at region 2 ( $z_2 < z_R < z_3$ ), and very thin ramp at region 3 ( $z_3 < z_R < z_4$ ). The characteristic deposition length  $w$  and the offset  $\Delta z_0$  are constant values. The 'reference' curve (left axis) is obtained for a constant velocity profile along the 3 regions. The 'addition due ramps' curve (left axis) results from the extra mass deposited as consequence of the slower velocity of the reactor at the ramps. The length of the first ramp ( $L_{\text{ramp}} = z_1 - z_2$ ) equals  $L_{\text{ramp}} = w$ .

## 11.5 Numerical Integration

We will now discuss a numerical recipe for calculating the global deposition profile for arbitrary local deposition profiles and reactor velocity functions. This numerical treatment is based on the analytical solutions obtained in section 11.4.2. Our aim is to compute the global profile  $\mu(z_j)$  at positions  $z_j$ , for  $1 \leq j \leq J$ . The squared velocity profile is discretised into  $N'$  regions ( $z'_{R,i} < z_R < z'_{R,i+1}$ ). Note that the index  $I$  refers to the  $N$  regions that define the profile for the squared velocity, meanwhile the index  $i$  refer to the  $N'$  regions used to discretise the squared velocity profile.

Equation (11.30) is used as the deposition profile  $\mu'_i(z)$  due to (discretise) region

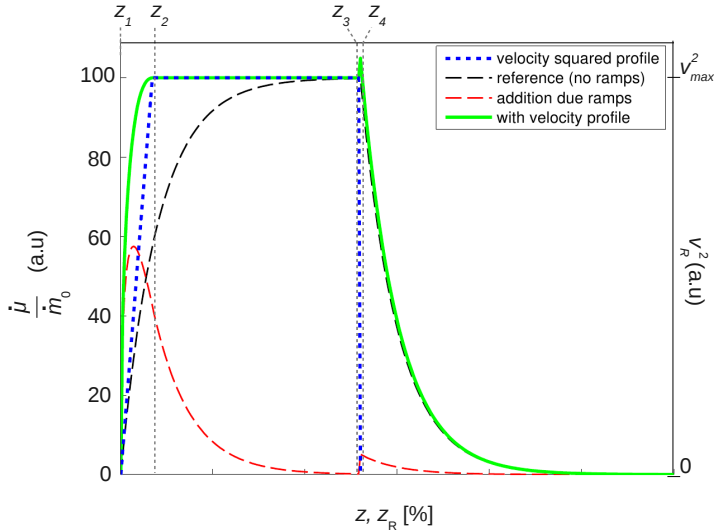


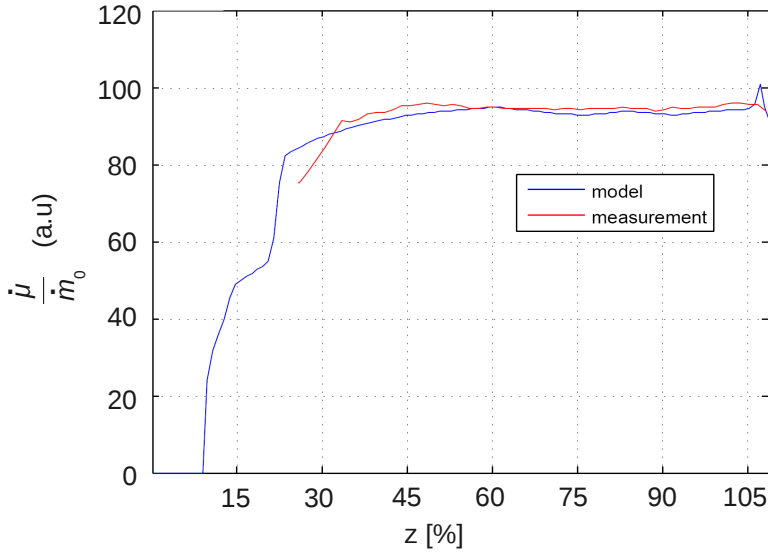
Figure 11.8: Global deposition profile for the same conditions as in figure 11.7. A value of  $L_{\text{ramp}} = 0.85w$  is needed to minimise the taper length i.e. maximise the length of the uniform region in the global deposition profile.

$$z'_{R;i} < z_R < z'_{R;i+1},$$

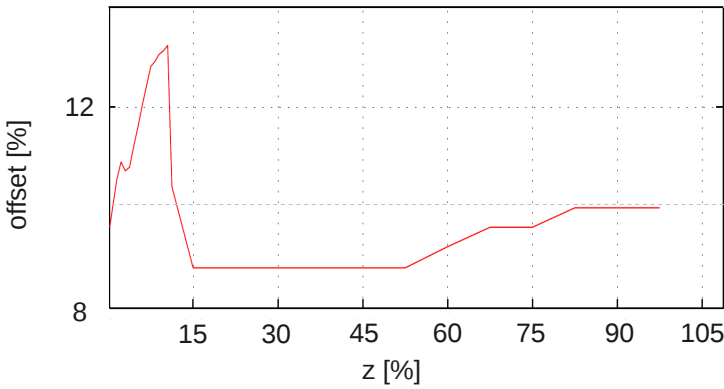
$$\mu(z_j) = \sum_{i=1}^{N'} \mu'_i(z_j). \quad (11.43)$$

Special consideration must be taken at the turning points where the velocity is zero and at the points where we change from non-constant to constant velocity. The input parameters for model equation (11.43) are the speed profile ( $z_{R;i}, v_i$ ), and the local deposition profile at positions  $z_j$ :  $\Delta z_j^i$ , and  $\alpha_{j;i} = w_{ji}^{-1}$ . We refer to this procedure as *forward deposition model*.

The forward model can be used to calculate the global model for various local profiles and a given velocity function. By matching the results with an experimentally obtained profile, the corresponding local profile can be determined. We refer to this procedure as *inverse deposition model* and, at present, it must be carried out manually. As an example, in figure 11.9 we fitted the offset of the local deposition profiles for  $\text{SiO}_2$  such that the calculated global deposition profile fits the deposition profile measured.



(a)



(b)

Figure 11.9: In (a) the curve 'model' is the global deposition profile obtained from the forward model fitted to the curve 'measurement' obtained from experimental measurements, both as function of the axial position (in % of the stroke length  $L$ ). In (b) the profile of the offset (in % of the stroke length  $L$ ); the fitting parameter used to find curve 'model' in (a).

## 11.6 Conclusions

In this chapter we have presented a model that can be used to analyse the deposition profile obtained from measuring a preform made with the PCVD technology. The model links the measurable global deposition profile to the non-measurable static local profile in industrial deposition conditions. We have shown how for a given velocity ramp profile of the plasma reactor, a global profile of the deposited layer can be calculated. The flow velocity and the static deposition profile are linked through a simple parameter  $\alpha$  which is a characteristic spatial decay time of the deposition profile who is directly proportional to the mass flux through the system and inversely proportional to the characteristic transport frequency  $v_d$  of the deposition precursor to the wall. The model allows to use the latter as input but also output of the model.

Acknowledgements: This model was developed under the supervision of Mathé van Stralen at Draka Comteq offices in Eindhoven.

---

12

General Conclusions

---



## 12.1 Introduction

When we started this project the aim was two-fold:

- to create an experimentally validated Grand model for microwave induced plasmas
- to investigate how the electromagnetic field components affect the plasma and vice versa.

In order to achieve the first objective, Grand models had to be constructed for simulating surfatron and surfaguide plasmas whereas the numerical results had to be compared with corresponding experimental results.

For the second objective, we had to simulate the Draka deposition reactor, and to show how the tuning of electromagnetic components, like the slit, the chokes and the dielectric components together with step-changes in the metallic configuration, influence the electromagnetic field and thus the plasma.

In the course of project we realised that several intermediate steps had to be taken and that various new ingredients had to be added to the PLASIMO platform while some existing model-components had to be improved. This implied that several sub-objectives had to be defined; sub-objectives that initiated the design of, and studies with new models and modules.

This chapter starts in section 12.2 with giving the conclusions that are related to the design and (re)construction of new model components. In section 12.3 we will address the conclusions of the scientific studies that have been made possible with these new model-features. Finally we will end in section 12.4 by giving recommendations for future work.

## 12.2 Design of new models and modules

As stated in the introduction, this thesis presents one specific, two global and three Grand models.

The specific model is a stand alone tool for the study of the EM responses of a system to microwaves (chapter 6). One of the global models is designed to provide a platform to explore the influence of chemical species and reactions on plasma features (chapter 5). The other is a global deposition model that intends to predict the deposition profile of a moving deposition reactor (chapter 11).

The three Grand models are all dedicated to Surface Wave Discharges (SWD); a special class of MIPs (chapters 7, 8, 9 and 10).

In presenting the most important conclusions we follow the structure of the thesis.

Chapter 2 clarifies that the main plasma ingredients can be divided into three interconnected parts: Configuration, Transport and Chemistry. This is also reflected in the structure of PLASIMO. For the configuration PLASIMO has two main components: 1) Geometry and Grid-structure and 2) the Electro-Magnetic (EM) fields.

An improvement made to PLASIMO is the new grid generation module that, using the multi-region method, is now capable to implement *step-changes* and *obstructions* in the geometry. This, together with the facility to follow smooth boundary curves using ortho-curvilinear (OCL) coordinates and local grid refinement, largely facilitates the applicability of the models to MIPs with different configurations.

Chapter 3 is entirely devoted to the other configuration component, namely electro-magnetism, and deals with the numerical solution of the system of three coupled EM equations for  $E_z$ ,  $E_r$  and  $H_\phi$ .

The boundary conditions (BCs) were classified and new BCs were introduced. The most important are the propagation BC and the excitation BC. The first one, also known as absorbing BC [68, 126], allows the simulation of waves that (partially) leave the computational domain. The second one, the excitation BC, guides the entrance of waves into the domain and thus provides the (power) sources of the electromagnetic model. It is (sub)divided into two types: *Power Absorbed in Domain* which imposes the value of the field at the boundary, and expects that the scaling of the power density matches the required power absorbed in the domain; *Power entering into the domain* sets the forward power entering in the domain e.g. via a coaxial waveguide, and allows the domain to respond with a reflected power.

The study on the convergence-behaviour as a function of grid refinement shows that the truncation error is essentially second-order in the grid-cell size. This error also depends on the axial position due to numerical dispersion. A method to correct the model results by anticipating on numerical dispersion is given. With chapter 3 we created a solid basis for chapter 6, the specific EM model.

Chapter 4 deals with transport, that is the transport as carried by particles (mass, momentum and energy). An overview of the transport equations in PLASIMO is given and it is shown how common features of these equations can be deduced from their common origin: the Boltzmann equation. It is also shown how these similarities lead to the canonical transport equation, the  $\phi$ -equation: one of the key-stones of the modularity of the object oriented architecture of PLASIMO. Since transport is driven by sources and facilitated by transport-coefficients these have to be programmed as well. An overview is given of the role of elastic and inelastic processes. Chapter 4 is

organised such that links with other PLASIMO transport constituents are given that are not directly used for MIP modelling.

Chapter 5, dedicated to chemistry, starts with a classification of the various plasma species. Guided by the comparison between transport and chemistry, it is found to be useful to divide species into Transport Sensitive and Local Chemistry species. By excluding the second category and by correcting for their elimination, we can reduce the relevant species drastically. This can speed up the convergence of Grand models substantially.

We analysed the existing methods that deal with the role of species and reactions. These methods, found in literature, are all zero dimensional in space but were derived in different sub-disciplines and intended to serve different goals.

We came to the construction of a new Global Plasma Model named RateLab; it can be seen as a synthesis of the existing methods and models-types. RateLab turns out to be a valuable platform (indeed a 'laboratory') for the exploration of the role of rates and species and to give insight into global trends and chemical properties of plasmas. It is applied in a case study of a power-pulsed Ar plasma. This transient model converges within 10 seconds whereas Grand models constructed for MIPs in Steady State (cf. chapters 8, 9 and 10) based on a similar chemistry, take convergence times between 4 and 20 hours. Thus, RateLab is found to be of great use for the interpretation of the results of Grand models and for the planning of a road map for in-depth research. However, it can by no means replace Grand modelling. Especially in the study of the two-dimensional aspects of plasma-wave interactions Grand Modelling is indispensable.

In chapter 6, the features introduced in chapter 3 are used to construct a model, dedicated to the study of the EM responses of a system, composed of metallic, dielectric and plasma structure elements. It is used as a stand-alone model for the study of the electromagnetic aspect in MIP torches but it is prepared to function as an important component of the Grand modelling of SWD in the chapters 8, 9 and 10.

The introduction of the excitation boundary condition makes it possible to get insight in the EM power balance and to find for a system the ratio between the entering, reflected, absorbed and transmitted power.

It is shown that the use of a direct solver and the Yee discretisation scheme increases the convergence speed with a factor of 100 compared to the work of Álvarez [74] that before our study was recognised as state of the art in the field of MIP-torch modelling.

Chapter 7 lays the basis for the Grand models that are used in chapters 8, 9 and 10, all dedicated to SWDs. Comparing our SWD modelling with the activities of other groups in the past, we can distinguish between the method of coupled zero-dimensional models and 2 dimensional models. With respect to the first category, that

represents most of the literature, we can conclude that especially for higher pressure the scaling laws that they claim are not applicable and that an in-depth understanding of the wave propagation inside the launcher plasma can not be achieved with coupled 0-D models.

Two other groups did 2D modelling, Hagelaar *et al.* [32] and Kabouzi *et al.* [35]. The work of the first is devoted to the study of the effect of a step transition in the tube diameter of a low pressure (400 Pa) argon surfatron plasma. The second group studied the contraction on an argon surfaguide plasma at atmospheric pressure. Comparing our results with those of the previous 2D studies generates the following conclusions:

- By implementing more chemical species and reactions we get more insight in the role of the formation and destruction of molecular ions (MIs). This chain of reactions leading to so-called Molecular Assisted Recombination MAR is responsible for the contraction observed at higher pressures.
- The gradual importance of MAR as a function of pressure can be studied systematically.
- The decay of the electron density as a function of the distance to the launcher, a very specific feature of SWD, is obtained with our model. Furthermore, the transition from linear to non-linear axial decay as the pressure increases is also shown.
- The systematic comparison with experimental results like Thomson scattering (TS) and Absolute line intensity (ALI) gives more insight in the deviation of the EEDF from the equilibrium Maxwellian form.

Chapter 11 presents a model that can be used to analyse the preform deposition profile. The model links the measurable global deposition profile to the non-measurable static local profile under industrial deposition conditions.

## 12.3 Scientific Insight Obtained

### Chapter 6: the stand-alone EM model

The stand-alone electromagnetic model was used to study the effect of the remote electromagnetic boundary conditions on EM field shaping for microwave induced plasma torch. This has generated the following scientific results.

It is shown that the open configuration provides the best power response, since it depends neither on the metal wall chamber, nor on the plasma shape. In this

configuration we observe how the plasma behaves as an antenna and that the antenna function is better for increasing  $n_e$ -values. This implies that for increasing  $n_e$  the absorption decreases so that the plasma does not get enough energy to keep  $n_e$  high. This interplay might be the reason for the instabilities found in the shape and position of MIP torches.

### **Chapter 8: the atmospheric surfaguide**

For atmospheric pressure conditions the role of MAR is very important. The plasma is no longer diffusive: it is not controlled by wall recombination but rather by volume recombination. A plasma ruled by volume recombination does not need to “search for wall stabilisation” in order to get rid of its degree of ionisation, it becomes constricted and filamentary. The Grand model is validated by comparing the calculated plasma length as function of the plasma absorbed power with the experimental curve obtained by Muñoz in [141]. Since the formation of molecular ions (MIs) strongly depends on the gas temperature we can tune the length and width of the plasma by changing the wall temperature  $T_w$ . For higher  $T_w$  we get a wider and longer plasma. The dependence of the gas temperature on the plasma power explains why at high power the discharge is longer. A high  $T_g$  destroys MIs and therewith counteracts MAR. This suppression of volume recombination makes the discharge longer. Good agreements with experimental results were found.

### **Chapter 9: the surfatron at intermediate pressures**

The Grand model is validated by comparing the numerical results with the experimental ones. It showed that the role of molecular ions (MIs) increases with increasing pressure. Not only because the increasing density make them comparable with the density of atomic ions but more importantly because they facilitate Molecular Assisted Recombination (MAR). In particular, we have found that MIs and MAR become non-negligible for the relatively low pressure of 2000 Pa for a plasma radius of 3 mm.

The fraction of the wave-power absorbed by the plasma inside the surfatron-launcher can not be neglected. Due to the proximity of the metal inside the launcher, the electric fields are higher than those found outside the launcher. This enhances the local power absorption and the creation of high electron density values, which leads to a high gas temperature and blocks the recombination route formed by MAR.

### Chapter 10: The Draka reactor

The plasma has an important impact on the wave propagation: the electron density changes the wavelength. This is especially important when designing the quarter-wave short-circuits, i.e. the chokes that have to confine the plasma in the deposition reactor. Depending on the depth of the chokes  $d_{ch}$ , the confinement can be improved, so that subsequently the power absorption inside the reactor can be enhanced. This changes the electron density and therefore the wavelength of the wave. The Grand model allowed to find an optimum choke-depth for maximum confinement of  $d_{ch} = 38.5$  mm, meaning that the wavelength in the plasma right below the chokes equals  $\lambda = 154$  mm.

### Chapter 11: the deposition model

We showed how the characteristic deposition length is proportional to the flow velocity and inversely proportional to the diffusion frequency. We also demonstrated that for a given velocity ramp-profile of the plasma reactor, a global profile of the deposited layer can be calculated, and how the length of the first ramp can be tuned to minimise the taper length of the deposition profile.

## 12.4 Recommendations for Future Work

The versatility of the EM model will allow the modelling of other SWDs as well, such as the linear microwave sources (coaxial SWDs) used for solar cell production in ECN.

The electromagnetic model can be extended to six EM field components. This can even be done in two dimensions, as shown in [160] where the azimuthal dependency of the fields expressed in  $\exp(im\phi)$  is introduced explicitly into the Maxwell equations. The  $m > 0$  modes are interesting as they will change the spatial distribution of the plasma, for example the radial distribution of radical species that are essential in the deposition process.

Another recommended improvement of the Grand MIP models is to include time-dependency. The reason is that this might improve the stability of the calculation for complex chemistry; moreover it will be needed to perform Grand modelling of pulsed plasmas. This will be useful for future investigations in the deposition reactor of Draka and also in the modelling of plasmas for solar cell production (e.g. ECN).

The time-dependency of the model will require to change the iterative scheme and update the current electromagnetic model after a certain number of time-steps. Another solution is to create a time-domain version of the EM model [33], which is

the original formulation of Yee [65]. This must be combined with a time-dependent electron momentum equation.

In order to investigate and improve the chemical reaction scheme for argon, we recommend the following actions. First, we should analyse the different contributions of all the reactions to the production and destruction of each species. This can be done by means of a chemistry analysis such as that presented in [161]. Second, we should increase the self-consistency of the plasma-electromagnetic interaction by means of coupling the set of rate coefficients with the electric field, using a Boltzmann solver such as Bolsig+ (cf. [32]).

The boundary condition for the electron temperature can be improved. Right now, the so-called adiabatic condition prevents interaction of the electron gas with the sheath. This current version of the BC has an unwanted effect on the radial distribution of the electron temperature, as shown in [30]. It would be interesting to include the *warm approximation* for the electron momentum equation [38, 39]. For harmonic fields we can follow the approach given in [39].

Other possible improvements are the introduction of a description of plasma resonances and non-collisional heating [36, 37].

Finally, we recommend that the global plasma model RateLab presented in chapter 5 is re-implemented and incorporated into the PLASIMO platform. Not only will this enrich Plasimo's feature set, it will also facilitate the management of the RateLab code.

---

# A

## Study on Model Resonances Using Equivalent Circuit Theory

---

Equivalent circuit theory is a well-known technique that it is used to model MIPs [17, 22]. It consists in expressing the microwave components (and the plasma) as equivalent impedances that together form an equivalent circuit. This is deduced from the current density

$$\mathbf{J}_{tot} = \hat{\sigma}\mathbf{E} + i\omega\epsilon_0\mathbf{E} \quad (\text{A.1})$$

obtained from equation (3.9) taking  $\epsilon'_r = 1$ .

If we apply this to a plasma slab of depth,  $d$ , and cross section  $A$ , and we substitute  $|\mathbf{J}_{tot}| = I/A$  and  $|\mathbf{E}| = V/d$ , we obtain

$$I = V\{e^2n_e/(m_e)(i\omega + \nu)^{-1} + i\omega\epsilon_0\}A/d = V/Z = VY, \quad (\text{A.2})$$

with the admittance equals to

$$Y = Z^{-1} = \left\{e^2n_e/(m_e)(j\omega + \nu)^{-1} + i\omega\epsilon_0\right\} (A/d). \quad (\text{A.3})$$

It shows that there are two current branches one being purely capacitive, the other consisting of the series arrangement of an inductance and a resistance.

The quality factor [162, 163] for a complex impedance  $Z = R + jX$  is defined as

$$Q = \frac{|X|}{|R|}. \quad (\text{A.4})$$

It measures of the ratio of the stored to the lost energy of the *oscillator*.



We will compute  $Q$  and the resonance frequency of the circuit.

*The resonance for collisionless case  $\nu = 0$*

The resonance in a circuit is obtained when  $Y = 0$ . For a collisionless plasma the collision frequency is null and equation (A.3) transforms into

$$e^2 n_e / (m_e \epsilon_0) (i\omega)^{-1} \epsilon_0 (A/d) = -i\omega \epsilon_0 A/d, \quad (\text{A.5})$$

giving

$$\omega^2 = e^2 n_e / (m_e \epsilon_0) = \omega_p^2, \quad (\text{A.6})$$

which defines the plasma frequency  $\omega_p$  i.e. the frequency at which the electrons oscillate in a cold plasma.

In a warm plasma the electron thermal speed must be incorporated and this relation transforms into the Bohm-Gross dispersion relation [38, 39]. The plasma oscillations turns into plasma waves that travels along the discharge. This is an extra damp mechanism for electron and it is not discussed here.

In general an under-dense plasma region is defined for  $n_e < n_{e,c}$  with  $n_{e,c}$  the critical density that makes the real part of the complex plasma permittivity (chapter 3) equals to zero, i.e.  $\text{Re}\{\hat{\epsilon}_p\} = 0$ . Consequently, an over-dense plasma region is defined for  $n_e > n_{e,c}$ .

If there are no collisions, the resistance  $R$  will be zero, and consequently  $Q$  will be infinity.

*The resonance for collisional case  $\nu \neq 0$*

In the collisional case, the resonance is also found at  $\omega^2 = \omega_p^2$ . However as the resistance is non null, the  $Q$  is finite and we have an attenuated resonance.

We define the capacitance  $C = \epsilon_0 A/d$  and the variable  $D = \omega_p^2 / (\omega^2 + \nu^2)$  and substitute them into equation (A.3)

$$Z^{-1} = CvD + i\omega C(1 - D). \quad (\text{A.7})$$

The impedance can be obtained as

$$Z = CvD/E - i\omega C(1 - D)/E \quad (\text{A.8})$$

where  $E = (CvD)^2 + [\omega C(1 - D)]^2$ . Then we can show that the quality factor becomes

$$Q = \frac{|X|}{|R|} = \frac{|\omega C(1 - D)|}{|v(CD)|} = \left| \frac{\omega}{v} \left( 1 - \frac{\omega^2 + \nu^2}{\omega_p^2} \right) \right| \quad (\text{A.9})$$

As an example we give the value of  $Q$  together with the needed input parameters in the table below for two argon plasmas configurations: a) a surfatron and b) a surfaguide.

---

Case	Set-up	$p$ [Pa]	$\omega$ [GHz]	$\nu$ GHz	$n_e$ [ $\text{m}^{-3}$ ]	$\omega_p$ GHz	$Q$
a)	Surfaguide	$10^5$	$2\pi \cdot 2.45$	200	$10^{18}$	$6 \cdot 10^4$	0.08
b)	Surfatron	$2 \cdot 10^3$	$2\pi \cdot 2.45$	1	$10^{18}$	$6 \cdot 10^4$	15

For a value of  $Q < 0.5$ , the circuit is over-damped meaning that when displaced from equilibrium it will return to it without oscillations. The time that the circuit needs to recover the equilibrium is larger for smaller values of  $Q$ .

For a value of  $Q > 0.5$ , the circuit is under-damped and therefore when displaced from equilibrium it will return to it oscillating around the plasma frequency. The time that the circuit needs to recover the equilibrium is larger for bigger values of  $Q$ .

As explained by [37, 164], when in an iterative scheme the plasma is under-dense at some position, and the plasma density increases for some reason (e.g. from one iteration to the next) the plasma permittivity will decrease. After this, the electric field will increase giving a lower value for the plasma permittivity, i.e. there is a positive feedback and the simulation becomes unstable.

For  $Q = 0.08$ , the plasma permittivity reacts so slow from iteration to iteration that it is still possible to find a global convergence for a steady state solution. Another reason can be that molecular reactions are more important close to the wall and they do not depend so strongly on the electron temperature i.e. the electric fields.

For  $Q = 15$  the positive feedback is very fast and the electron density and the electron temperature increase until the plasma is again over-dense, however next to this over-dense region, there will be other under-dense regions and peaks are unstable appearing and disappearing around the under-dense region. This is the reason why we avoid the under-dense plasma region in our surfatron and deposition reactor simulations, by means of setting the density of  $Ar^+$  at the wall higher than the critical density.



---

## Bibliography

---

- [1] M. I. Boulos, P. Fauchais, and E. Pfender. *Thermal plasmas: fundamentals and applications*. Plenum Press, 1994.
- [2] L. Paquin, D. Masson, M. R. Wertheimer, and M. Moisan. Amorphous silicon for photovoltaics produced by new microwave plasma-deposition techniques. *Canadian Journal of Physics*, 63, 831, 1985.
- [3] D. Küppers and H. Lydtin. Preparation of optical waveguides with the aid of plasma-activated chemical vapour deposition at low pressures. *Topics in Current Chemistry*, 89, 107, 1980.
- [4] V. T. Airoidi, C. F. M. Borges, M. Moisan, and D. Guay. High optical transparency and good adhesion of diamond films deposited on fused silica windows with a surface-wave sustained plasma. *Applied Optics*, 36, 4400, 1997.
- [5] L. Pomathiod, J. L. Michau, and M. Hamelin. Design and characteristics of sippi, an ion source for a long-distance sims analysis of the phobos surface. *Review of Scientific Instruments*, 59, 2409, 1988.
- [6] A. Montaser and D.W. Golightly. *Inductively coupled plasmas in analytical atomic spectrometry*. VCH Publishers, 1992.
- [7] H. W. P. van der Heijden. *Modelling of Radiative Transfer in Light Sources*. PhD thesis, Eindhoven University of Technology, The Netherlands, 2003.
- [8] C. W. Johnston. *Transport and Equilibrium in Molecular Plasmas: the sulfur lamp*. PhD thesis, Eindhoven University of Technology, The Netherlands, 2003.
- [9] G. J. M. Hagelaar. *Modeling of Microdischarges for Display Technology*. PhD thesis, Eindhoven University of Technology, The Netherlands, 2000.
- [10] G. M. Janssen. *Design of a General Plasma Simulation Model, Fundamental Aspects and Applications*. PhD thesis, Eindhoven University of Technology, The Netherlands, 2000.

- [11] M. J. van den Donker. *Modelling microwave plasmas for deposition purposes : exploring the freedom in space and chemistry*. PhD thesis, Eindhoven University of Technology, The Netherlands, 2008.
- [12] M. Moisan and J. Pelletier. *Microwave excited plasmas*, volume 4 of *Plasma Technology*. Elsevier Science Publishers B.V., 1992.
- [13] J. M. Palomares Linares. *Spectroscopic diagnosis of microwave induced plasmas*. PhD thesis, Universidad de Córdoba, Spain, 2010.
- [14] C. I. M. Beenakker. A cavity for microwave-induced plasmas operated in helium and argon at atmospheric pressure. *Spectrochimica Acta Part B: Atomic Spectroscopy*, 31(8-9), 483–486, 1976.
- [15] L. L. Alves, R. Álvarez, L. Marques, S. J. Rubio, A. Rodero, and M. C. Quintero. Modeling of an axial injection torch. *The European Physical Journal Applied Physics*, 46(2), 21001, may 2009.
- [16] M. Moisan, G. Sauve, Z. Zakrzewski, and J. Hubert. An atmospheric pressure waveguide-fed microwave plasma torch: the tia design. *Plasma Sources Science and Technology*, 3(4), 584, 1994.
- [17] A. W. Trivelpiece. *Slow wave propagation in plasma waveguides*. PhD thesis, Eindhoven University of Technology, The Netherlands, 1958.
- [18] Q. Zhang, G. Zhang, S. Wang, and L. Wang. A large-volume microwave plasma source based on parallel rectangular waveguides at low pressures. *Plasma Sources Science and Technology*, 20(1), 015025, 2011.
- [19] H. Rau and B. Trafford. Rotationally symmetrical electric fields and electron density distributions in a microwave plasma used in optical fibre production. *Journal of Physics D: Applied Physics*, 22(11), 1613, 1989.
- [20] P. Geittner, D. Küppers, and H. Lydtin. Low-loss optical fibers prepared by plasma-activated chemical vapor deposition (cvd). *Applied Physics Letters*, 28(11), 645–646, 1976.
- [21] E. L. Norton. Design of finite networks for uniform frequency characteristic. Technical report, Bell Laboratories, 1926.
- [22] M. Moisan, Z. Zakrzewski, and R. Pantel. The theory and characteristics of an efficient surface wave launcher (surfatron) producing long plasma columns. *Journal of Physics D: Applied Physics*, 12(2), 219, 1979.

- 
- [23] V. M. M. Glaude, M. Moisan, R. Pantel, P. Leprince, and J. Marec. Axial electron density and wave power distributions along a plasma column sustained by the propagation of a surface microwave. *Journal of Applied Physics*, 51(11), 5693–5698, 1980.
- [24] C. M. Ferreira. Modelling of a low-pressure plasma column sustained by a surface wave. *Journal of Physics D: Applied Physics*, 16(9), 1673, 1983.
- [25] A. Sola, A. Gamero, J. Cotrino, and V. Colomer. Empirical similarity laws for argon plasmas produced by a surface wave at 2.45 ghz. *Journal of Physics D: Applied Physics*, 21(7), 1112, 1988.
- [26] I. Zhelyazkov, E. Benova, and V. Atanassov. Axial structure of a plasma column produced by a large-amplitude electromagnetic surface wave. *Journal of Applied Physics*, 59(5), 1466–1472, 1986.
- [27] U. Kortshagen. On the influence of energy transfer efficiency on the electron energy distribution function in hf sustained rare gas plasmas: experimental and numerical study. *Journal of Physics D: Applied Physics*, 26(8), 1230, 1993.
- [28] T. Petrova, E. Benova, G. Petrov, and I. Zhelyazkov. Self-consistent axial modeling of surface-wave-produced discharges at low and intermediate pressures. *Phys. Rev. E*, 60(1), 875–886, Jul 1999.
- [29] C. M. Ferreira. Theory of a plasma column sustained by a surface wave. *Journal of Physics D: Applied Physics*, 14(10), 1811, 1981.
- [30] I. B. Denysenko, N. A. Azarenkov, and M. Y. Yu. Radial structure of surface-wave sustained plasmas. *Physica Scripta*, 65(1), 76, 2002.
- [31] E. Castaños-Martinez, Y. Kabouzi, K. Makasheva, and M. Moisan. Modeling of microwave-sustained plasmas at atmospheric pressure with application to discharge contraction. *Phys. Rev. E*, 70(6), 066405, Dec 2004.
- [32] G. J. M. Hagelaar and L. C. Pitchford. Solving the boltzmann equation to obtain electron transport coefficients and rate coefficients for fluid models. *Plasma Sources Science and Technology*, 14(4), 722, 2005.
- [33] G. J. M. Hagelaar, K. Hassouni, and A. Gicquel. Interaction between the electromagnetic fields and the plasma in a microwave plasma reactor. *Journal of Applied Physics*, 96(4), 1819–1828, 2004.
- [34] K. Hassouni, T. A. Grotjohn, and A. Gicquel. Self-consistent microwave field and plasma discharge simulations for a moderate pressure hydrogen discharge reactor. *Journal of Applied Physics*, 86(1), 134–151, 1999.

- [35] Y. Kabouzi, D. B. Graves, E. Castaños-Martinez, and M. Moisan. Modelling of atmospheric-pressure plasma columns sustained by surface waves. *Physical Review E*, 75, 016402–1, 2007.
- [36] Y. M. Aliev., A. V. Maximov, U. Kortshagen, H. Schlüter, and A. Shivarova. Modeling of microwave discharges in the presence of plasma resonances. *Phys. Rev. E*, 51(6), 6091–6103, Jun 1995.
- [37] "I. P. Ganachev". Numerical Simulation Research in Plasma Technologies 3. Kinetic Computer Modeling of Microwave Surface-Wave Plasma Production. *Journal of Plasma and Fusion Research*, 80, 119–125, 2004.
- [38] J. A. Bittencourt. *Fundamentals of Plasma Physics, Third Edition*. Springer-Verlag, New York, 2004.
- [39] K. J. Bowers. *High frequency electron resonances and surface waves in unmagnetized bounded plasmas*. PhD thesis, University of California, Berkeley, 2001.
- [40] M. Moisan, A. Shivarova, and A. W. Trivelpiece. Experimental investigations of the propagation of surface waves along a plasma column. *Plasma Physics*, 24(11), 1331, 1982.
- [41] I. Zhelyazkov and V. Atanassov. Axial structure of low-pressure high-frequency discharges sustained by travelling electromagnetic surface waves. *Physics Reports.*, 255, 79–201, 1995.
- [42] H. Schlüter and A. Shivarova. Travelling-wave-sustained discharges. *Physics Reports*, 443, 121–255, may 2007.
- [43] J. van Dijk, G. M. W. Kroesen, and A. Bogaerts. Plasma modelling and numerical simulation. *Journal of Physics D: Applied Physics*, 42(19), 190301, 2009.
- [44] M. Jimenez-Diaz, J. van Dijk, and J. J. A. M. van der Mullen. Effect of remote field electromagnetic boundary conditions on microwave-induced plasma torches. *Journal of Physics D: Applied Physics*, 44(16), 165203, 2011.
- [45] D. A. Benoy. *Modelling of Thermal Argon Plasmas*. PhD thesis, Eindhoven University of Technology, The Netherlands, 1993.
- [46] J. van Dijk. *Modelling of Plasma Light Sources — an object-oriented approach*. PhD thesis, Eindhoven University of Technology, The Netherlands, 2001.
- [47] A. Hartgers. *Modelling of a Fluorescent Lamp Plasma*. PhD thesis, Eindhoven University of Technology, The Netherlands, 2003.

- 
- [48] B. H. P. Broks, W. J. M. Brok, J. Remy, J. J. A. M. van der Mullen, A. Benidar, L. Biennier, and F. Salama. Numerical investigation of the discharge characteristics of the pulsed discharge nozzle. *Physical Review E*, 71(3), 036409, Mar 2005.
- [49] M. L. Beks. *Modelling additive transport in metal halide lamps*. PhD thesis, Eindhoven University of Technology, The Netherlands, 2008.
- [50] G. J. M. Hagelaar. *Modeling of microdischarges for display technology*. PhD thesis, Eindhoven University of Technology, The Netherlands, 2000.
- [51] S. V. Patankar, editor. *Numerical Heat Transfer and Fluid Flow*. New York: McGraw-Hill, 1980.
- [52] J. van Dijk, K. Peerenboom, M. Jimenez, D. Mihailova, and J. J. A. M. van der Mullen. The plasma modelling toolkit plasimo. *Journal of Physics D: Applied Physics*, 42(19), 194012, 2009.
- [53] J. D. Jackson. *Classical Electrodynamics*. Wiley & Sons, New York, 1975.
- [54] B. H. P. Broks. *Multi-fluid Modeling of Transient Plasmas*. PhD thesis, Eindhoven University of Technology, The Netherlands, 2006.
- [55] Harm van der Heijden and Joost van der Mullen. General treatment of the interplay between fluid and radiative transport phenomena in symmetric plasmas: the sulphur lamp as a case study. *Journal of Physics D: Applied Physics*, 35(17), 2112–2125, 2002.
- [56] M. H. L. van der Velden, W. J. M. Brok, J. J. A. M. van der Mullen, W. J. Goedheer, and V. Banine. Particle-In-Cell Monte Carlo simulations of an extreme ultraviolet radiation driven plasma. *Physical Review E*, 73(3), 036406, 2006.
- [57] W. J. M. Brok, E. Wagenaars, J. van Dijk, and J. J. A. M. van der Mullen. Numerical description of pulsed breakdown between parabolic electrodes. *Plasma Science, IEEE Transactions on*, 35(5), 1325–1334, 2007.
- [58] W. J. M. Brok. *Modelling of Transient Phenomena in Gas Discharges*. PhD thesis, Eindhoven University of Technology, The Netherlands, 2005. ISBN 90-386-2291-0.
- [59] S. B. Pope. The calculation of turbulent recirculating flows in general coordinates. *Journal of Comp. Phys.*, 26, 197, 1978.
- [60] Z. U. A. Warsi. *Fluid Dynamics — Theoretical and Computational Approaches*. CRC Press, 2nd edition, 1998.



- [61] V. Yordanov, A. Blagoev, I. Ivanova-Stanik, E. M. van Veldhuizen, S. Nijdam, J. van Dijk, and J. J. A. M. van der Mullen. Surface ionization wave in a plasma focus-like model device. *Journal of Physics D: Applied Physics*, 41(21), 215208, 2008.
- [62] R. F. Harrington. *Time-harmonic electromagnetic fields*. IEEE Press Series on Electromagnetic Wave Theory. IEEE Press, 2001.
- [63] R. C. Rumpf. *Design and optimization of nano-optical elements by coupling fabrication to optical behaviour*. PhD thesis, University of Central Florida Orlando Florida, 2006.
- [64] Yong-Jiu Zhao, Ke-Li Wu, and K. K. M. Cheng. A compact 2-d full-wave finite-difference frequency-domain method for general guided wave structures. *Microwave Theory and Techniques, IEEE Transactions on*, 50(7), 1844–1848, July 2002.
- [65] K. S. Yee. Numerical solution of initial boundary value problems involving maxwell's equations in isotropic media. *IEEE Transactions on Antennas and Propagation*, 14, 302–307, 1966.
- [66] J. W. Demmel, S. C. Eisenstat, J. R. Gilbert, Z. S. Li, and J. W. H. Liu. A supernodal approach to sparse partial pivoting. *SIAM Journal on Matrix Analysis and Applications*, 20(3), 720–755, 1999.
- [67] Joseph W. H. Liu. Modification of the minimum-degree algorithm by multiple elimination. *ACM Trans. Math. Softw.*, 11, 141–153, June 1985.
- [68] B. Engquist and A. Majda. Absorbing boundary conditions for numerical simulation of waves. *Mathematical of Computation*, 31, 629–651, 1977.
- [69] G. Mur. Absorbing boundary conditions for the finite-difference approximation of the time-domain electromagnetic field equations. *IEEE Transactions on Electromagnetic Compatibility, EMC-23*, 377–382, 1981.
- [70] D. B. Meade, C. Piellusch-Castle, and A. F. Peterson. Derivation and comparison of radiation boundary conditions for the two-dimensional helmholtz equation with non-circular artificial boundaries. *SIAM Proceedings in Applied Mathematics*, 77, 506–514, 1995.
- [71] A. Marchi and C. Henrique. Unidimensional numerical solution error estimation for convergent apparent order. *Numerical Heat Transfer, Part B: Fundamentals: An International Journal of Computation and Methodology*, 42(2), 167 – 188, 2002.
- [72] A. Taflove and S. C. Hagness, editors. *Computational Electrodynamics: the Finite-Difference Time-Domain Method*. (London: Artech House), 1995.

- 
- [73] G. B. Arfken and H. J. Weber, editors. *Mathematical Methods for Physicists*. (Amsterdam : Elsevier), 2005.
- [74] R. Álvarez and L. L. Alves. Two-dimensional electromagnetic model of a microwave plasma reactor operated by an axial injection torch. *Journal of Applied Physics*, 101(10), 103303, 2007.
- [75] D. Mihailova. *Sputtering Hollow Cathode Discharges designed for Laser Applications. Experiments and Theory*. PhD thesis, Eindhoven University of Technology, The Netherlands, 2010.
- [76] E. Iordanova. *Poly-diagnostic validation of spectroscopic methods: in-depth monitoring of microwave induced plasmas*. PhD thesis, Eindhoven University of Technology, The Netherlands, 2010.
- [77] M. Mitchner and J. Charles H. Kruger. *Partially Ionized Gases*. John Wiley & Sons, 1973.
- [78] D. Mihailova, M. Grozeva, G. J. M. Hagelaar, J. van Dijk, W. J. M. Brok, and J. J. A. M. van der Mullen. A flexible platform for simulations of sputtering hollow cathode discharges for laser applications. *Journal of Physics D: Applied Physics*, 41(24), 245202, 2008.
- [79] D. Mihailova, J. van Dijk, M. Grozeva, G. J. M. Hagelaar, and J. J. A. M. van der Mullen. A hollow cathode discharge for laser applications: influence of the cathode length. *Journal of Physics D: Applied Physics*, 43(14), 145203, 2010.
- [80] L. G. H. Huxley and R.W. Crompton. *The diffusion and drift of electrons in gases*. Wiley series in plasma physics. Wiley, 1974.
- [81] D. Petrović, T. Martens, J. van Dijk, W. J. M. Brok, and A. Bogaerts. Modeling of a dielectric barrier discharge used as a flowing chemical reactor. *Journal of Physics: Conference Series*, 133(1), 012023, 2008.
- [82] J. van Dijk K. S. C. Peerenboom, M. J. van de Donker. Describing diffusion in a magnetized plasma with a self consistent friction approach. *Phys. Rev. E*, 71(3), 036409, Mar 2005.
- [83] C. M. Ferreira and M. Moisan. *Microwave Discharges: Fundamentals and Applications*. Plenum Press, 1993.
- [84] J. O. Hirschfelder, C. F. Curtiss, and R. B. Bird. *Molecular Theory of Gases and Liquids*. John Wiley & Sons, 1964.
- [85] R. K. Zeytounian. *Theory and applications of nonviscous fluid flows*. Physics and astronomy online library. Springer, 2002.

- [86] M. Moisan and Z. Zakrzewski. Plasma sources based on the propagation of electromagnetic surface waves. *Journal of Physics D: Applied Physics*, 24(7), 1025, 1991.
- [87] L. S. Frost. Influence of thermal electron motion on surface wave discharge characteristics. *J. Appl. Phys.*, 32, 2029, 1961.
- [88] L. G. Christophorou and J. K. Olthoff. *Fundamental electron interactions with plasma processing gases*. Physics of atoms and molecules. Kluwer Academic/-Plenum Publishers, 2004.
- [89] D. R. Bates and A. E. Kingston. Collisional-radiative recombination at low temperatures and densities. *Proceedings of the Physical Society*, 83(1), 43, 1964.
- [90] T. Fujimoto. Validity criteria for local thermodynamic equilibrium and coronal equilibrium. *Journal of the Physical Society of Japan*, 34(1), 216–224, 1973.
- [91] B. van der Sijde, J. J. A. M. van der Mullen, and D. C. Schram. Collisional radiative models in plasmas. *Beiträge aus der Plasmaphysik*, 24(5), 447–473, 1984.
- [92] J. J. A. M. van der Mullen. Excitation equilibria in plasmas; a classification. *Physics Reports*, 2&3(191), 109–220, 1990.
- [93] A. Hartgers, J. van Dijk, J. Jonkers, and J. J. A. M. van der Mullen. Crmodel: A general collisional radiative modeling code. *Computer Physics Communications*, 135, 199–218, April 2001.
- [94] J. van Dijk, B. Hartgers, J. Jonkers, and J. J. A. M. van der Mullen. Collisional radiative models with multiple transport-sensitive levels - application to high electron density mercury discharges. *Journal of Physics D: Applied Physics*, 34(10), 1499, 2001.
- [95] A. Flitti and S. Pancheshnyi. Gas heating in fast pulsed discharges in n2-o2 mixtures. *The European Physical Journal Applied Physics*, 45, 21001, 2009.
- [96] J. J. Munro and J. Tennyson. Global plasma simulations using dynamically generated chemical models. *Journal of Vacuum Science and Technology A: Vacuum, Surfaces, and Films*, 26(4), 865–869, 2008.
- [97] T. H. Chung, H. J. Yoon, and D. C. Seo. Global model and scaling laws for inductively coupled oxygen discharge plasmas. *Journal Applied Physics*, 86(7), 3536–3542, 1999.
- [98] S. Ashida, C. Lee, and M. A. Lieberman. Spatially averaged (global) model of time modulated high density argon plasmas. *American Vacuum Society*, 13(5), 2498, 1995.

- 
- [99] S. Kim. *An improved global model for electronegative discharge and ignition conditions for peripheral plasma connected to a capacitive discharge*. PhD thesis, University of California, Berkeley, 2006.
- [100] B. H. P. Broks and J. J. A. M. van der Mullen. Creating a global plasma model using disturbed bilateral relations. *Journal of Physics: Conference Series*, 44(1), 53, 2006.
- [101] J. J. A. M. van der Mullen. *Excitation Equilibria in Plasmas — a classification*. PhD thesis, Eindhoven University of Technology, The Netherlands, 1986.
- [102] R. Zorat, J. Goss, D. Boilson, and D. Vender. Global model of a radiofrequency h 2 plasma in denise. *Plasma Sources Science and Technology*, 9(2), 161, 2000.
- [103] J. J. A. M. van der Mullen and J. Jonkers. Fundamental comparison between non-equilibrium aspects of icp and mip discharges. *Spectrochimica Acta Part B: Atomic Spectroscopy*, 54(7), 1017, 1999.
- [104] L. F. Shampine. *Numerical solution of ordinary differential equations*. Number v. 4 in Chapman & Hall mathematics. Chapman & Hall, 1994.
- [105] D. O. Wharmby. Electrodeless lamps for lighting: a review. *Science, Measurement and Technology, IEE Proceedings A*, 140, 465, 1993.
- [106] F. C. Fehsenfeld, K. M. Evenson, and H. P. Broida. Microwave discharge cavities operating at 2450 mhz. *Review of Scientific Instruments*, 36(3), 294–298, 1965.
- [107] Q. Jin, C. Zhu, M. W. Borer, and G. M. Hieftje. A microwave plasma torch assembly for atomic emission spectrometry. *Spectrochimica Acta Part B: Atomic Spectroscopy*, 46, 417, 1991.
- [108] J. Jonkers, H. P. C. Vos, J. J. A. M. van der Mullen, and E. A. H. Timmermans. On the atomic state densities of plasmas produced by the 'torche à injection axiale'. *Spectrochimica Acta Part B: Atomic Spectroscopy*, 51(5), 457, 1996.
- [109] J. Jonkers, L. J. M. Selen, J. J. A. M. van der Mullen, E. A. H. Timmermans, and D. C. Schram. Steep plasma gradients studied with spatially resolved thomson scattering measurements. *Plasma Sources Science and Technology*, 6(4), 533, 1997.
- [110] C. Prokisch, A. M. Bilgiç, E. Voges, J. A. C. Broekaert, J. Jonkers, M. van Sande, and J. J. A. M. van der Mullen. Photographic plasma images and electron number density as well as electron temperature mappings of a plasma sustained with a modified argon microwave plasma torch (mpt) measured by spatially resolved thomson scattering. *Spectrochimica Acta Part B: Atomic Spectroscopy*, 54(9), 1253, 1999.

- [111] M. J. van de Sande and J. J. A. M. van der Mullen. Thomson scattering on a low-pressure, inductively-coupled gas discharge lamp. *Journal of Physics D: Applied Physics*, 35(12), 1381–1391, 2002.
- [112] J. J. A. M. van der Mullen, M.J. van de Sande, N. de Vries, B. Broks, E. Iordanova, A. Gamero, J. Torres, and A. Sola. Single-shot thomson scattering on argon plasmas created by the microwave plasma torch; evidence for a new plasma class. *Spectrochimica Acta Part B: Atomic Spectroscopy*, 62(10), 1135–1146, 2007.
- [113] R. Álvarez, A. Rodero, and M. C. Quintero. An abel inversion method for radially resolved measurements in the axial injection torch. *Spectrochimica Acta Part B: Atomic Spectroscopy*, 57(11), 1665, 2002.
- [114] E. A. H. Timmermans. *Atomic and molecular excitation processes in microwave induced plasmas a spectroscopic study*. PhD thesis, Eindhoven University of Technology, The Netherlands, 1999.
- [115] R. Álvarez, M. C. Quintero, and A. Rodero. Radial description of excitation processes of molecular and atomic species in a high-pressure helium microwave plasma torch. *Journal of Physics D: Applied Physics*, 38(20), 3768, 2005.
- [116] J. Jonkers, J. M. de Regt, J. J. A. M. van der Mullen, H. P. C. Vos, F. P. J. de Groot, and E. A. H. Timmermans. On the electron temperatures and densities in plasmas produced by the ‘torche à injection axiale’. *Spectrochimica Acta Part B: Atomic Spectroscopy*, 51(11), 1385–1392, 1996.
- [117] E. A. H. Timmermans, J. Jonkers, I. A. J. Thomas, A. Rodero, M. C. Quintero, A. Sola, A. Gamero, and J. J. A. M. van der Mullen. The behavior of molecules in microwave-induced plasmas studied by optical emission spectroscopy. 1. plasmas at atmospheric pressure. *Spectrochimica Acta Part B: Atomic Spectroscopy*, 53(11), 1553–1566, 1998.
- [118] A. M. Bilgiç, K. Garloff, and E. Voges. Finite difference calculations of electromagnetic fields in arbitrary curvilinear coordinates for coaxial microwave plasma sources. *Plasma Sources Science and Technology*, 8(2), 325–331, 1999.
- [119] S. Gritsinin, I. Kossyi, E. Kulumbaev, and V. Lelevkin. Calculation of a coaxial microwave torch. *Plasma Physics Reports*, 32, 872–879, 2006.
- [120] J. Jonkers. *Excitation and transport in small scale Plasmas*. PhD thesis, Eindhoven University of Technology, The Netherlands, 1998.
- [121] J. G. Maloney, G. S. Smith, and W. R. J. Scott. Accurate computation of the radiation from simple antennas using the finite-difference time-domain method. *IEEE Transactions on Antennas and Propagation*, 38(7), 1059–1068, July 1990.

- 
- [122] Y. C. Noh and H. J. Eom. Radiation from a flanged coaxial line into a dielectric slab. *IEEE Transactions on Microwave Theory and Techniques*, 47(11), 2158–2161, November 1999.
- [123] C. D. Mobley and R. J. Stewart. On the numerical generation of boundary-fitted orthogonal curvilinear coordinate systems. *Journal of Computational Physics*, 34(1), 124, 1980.
- [124] D. M. Pozar. *Microwave engineering*. John Wiley & Sons, Inc, 2nd edition, 1998.
- [125] M. Abramowitz and I. A. Stegun, editors. *Mathematical handbook of functions*. (New York: Dover), 1965.
- [126] F. X. Canning. On application of some radiation boundary conditions. *IEEE Transactions On Antennas And Propagation*, 38, No. 5, 740–745, 1990.
- [127] Y. Liu. Fourier analysis of numerical algorithms for the maxwell equations. *Journal of Computational Physics*, 124(2), 396–416, 1996.
- [128] J. P. J. van Dalen, P. A. de Lezenne Coulander, and L. de Galan. Improvements of the cylindrical tm<sub>010</sub> cavity for an atmospheric pressure microwave-induced plasma. *Spectrochimica Acta Part B: Atomic Spectroscopy*, 33(8), 545–549, 1978.
- [129] A. Kirichenko, A. Motornenko, and O. Suvorova. Structure of a discharge induced by a coaxial microwave plasmatron with a gas-supply channel in the inner electrode. *Plasma Physics Reports*, 29, 528–533, 2003.
- [130] <http://plasimo.phys.tue.nl/>.
- [131] H. M. Barlow and J. Brown. *Radio surface waves*. International monographs on radio. Clarendon Press, 1962.
- [132] N. Marcuvitz. *Waveguide handbook*. IEE electromagnetic waves series. Peter Peregrinus Ltd on behalf of the Institution of Electrical Engineers, 1986.
- [133] M. Moisan, Z. Zakrzewski, R. Pantel, and P. Leprince. A waveguide-based launcher to sustain long plasma columns through the propagation of an electromagnetic surface wave. *Plasma Science, IEEE Transactions on*, 12(3), 203–214, September 1984.
- [134] A. Durandet, Y. Arnal, J. Margot-Chaker, and M. Moisan. Investigation of a plasma source sustained by an electromagnetic surface wave at 2.45 ghz under free-fall regime. *Journal of Physics D: Applied Physics*, 22(9), 1288, 1989.
- [135] J. Berndt, K. Makasheva, H. Schlüter, and A. Shivarova. Diffusion-controlled regime of surface-wave-produced plasmas in helium gas. *Plasma Sources Science and Technology*, 11(2), 208, 2002.

- [136] G. G. Lister and T. R. Robinson. Strongly damped surface waves in plasmas. i. the wkb approximation. *Journal of Physics D: Applied Physics*, 24(11), 1993, 1991.
- [137] T. Paunská, A. Shivarova, and K. Tarnev. Low-pressure discharges in surface-wave fields. *Vacuum*, 76(2-3), 377–380, 2004. 13th International School on Vacuum, Electron and Ion Technologies (VEIT 2003).
- [138] J. Cotrino, A. Gamero, A. Sola, and V. Colomer. Effective recombination coefficients in argon surface-wave-produced plasma. *Journal of Physics D: Applied Physics*, 21(9), 1377, 1988.
- [139] N. Djermanova, D. Grozev, K. Kirov, K. Makasheva, A. Shivarova, and Ts. Tsvetkov. Self-organization of surface wave sustained discharges in the pressure range from 10 to 200 torr. *Journal of Applied Physics*, 86(2), 738–745, 1999.
- [140] V. Atanassov and E. Mateev. Spatial structures arising along a surface wave produced plasma column: an experimental study. *Journal of Physics: Conference Series*, 63(1), 012025, 2007.
- [141] J. Muñoz and M. D. Calzada. Experimental research on surface wave ar–he discharges at atmospheric pressure. *Journal of Physics D: Applied Physics*, 41(13), 135203, 2008.
- [142] M. Moisan, C. Beaudry, and P. Leprince. A small microwave plasma source for long column production without magnetic field. *IEEE Transactions on Plasma Science*, 3(2), 55–59, June 1975.
- [143] K. U. Riemann. The bohm criterion and sheath formation. *Journal of Physics D: Applied Physics*, 24(4), 493, 1991.
- [144] J. Jonkers, M. van de Sande, A. Sola, A. Gamero, A. Rodero, and J. J. A. M. van der Mullen. The role of molecular rare gas ions in plasmas operated at atmospheric pressure. *Plasma Sources Science and Technology*, 12(3), 464, 2003.
- [145] J. J. A. M. Mullen and B. Broks. Disturbed bilateral relations: a guide for plasma characterization and global models. *Journal of Physics: Conference Series*, 44(1), 40, 2006.
- [146] G. M. Janssen, J. van Dijk, D. A. Benoy, M. A. Tas, K. T. A. L. Burm, W. J. Goedheer, J. A. M. van der Mullen, and D. C. Schram. Plasimo, a general model: I. applied to an argon cascaded arc plasma. *Plasma Sources Science and Technology*, 8(1), 1, 1999.
- [147] Y. Kabouzi, M. D. Calzada, M. Moisan, K. C. Tran, and C. Trassy. Radial contraction of microwave-sustained plasma columns at atmospheric pressure. *Journal of Applied Physics*, 91, 1008–1019, feb 2002.

- 
- [148] E. Benova and I. Zhelyazkov. Theoretical study of the influence of a metal enclosure on the parameters of a plasma column sustained by a travelling electromagnetic surface wave. *Physica Scripta*, 43(1), 68, 1991.
- [149] J Cotrino and F J Gordillo-Vazquez. Discharge characteristics of high-frequency non-equilibrium argon plasmas from a three-level atomic model. *Journal of Physics D: Applied Physics*, 28(9), 1888, 1995.
- [150] N. de Vries. *Spectroscopic study of microwave induced plasmas : exploration of active and passive methods*. PhD thesis, Eindhoven University of Technology, The Netherlands, 2008.
- [151] E. Carbone. Eindhoven University of Technology. Private Communication.
- [152] J. M. Palomares, E. Iordanova, E. M. van Veldhuizen, L. Baede, A. Gamero, A. Sola, and J. J. A. M. van der Mullen. Thomson scattering on argon surfatron plasmas at intermediate pressures: Axial profiles of the electron temperature and electron density. *Spectrochimica Acta Part B: Atomic Spectroscopy*, 65(3), 225 – 233, 2010.
- [153] H. Schlemm, A. Mai, S. Roth, D. Roth, K. M. Baumgurtner, and H. Muegge. Industrial large scale silicon nitride deposition on photovoltaic cells with linear microwave plasma sources. *Surface and Coatings Technology*, 174-175, 208–211, 2003. Proceedings of the Eight International Conference on Plasma Surface Engineering.
- [154] D. Küppers. Deposition of fluorine-doped silica layers from a  $\text{sicl}_2/\text{sif}_4/\text{o}_2$  gas mixture by the plasma-cvd method. *J. Electrochem. Soc.: Solid State Science and Technology*, 1979.
- [155] D. Küppers, J. Koenings, and H. Wilson. Codeposition of glassy silica and germania inside a tube by plasma-activated cvd. *J. Electrochem. Soc.: Solid State Science and Technology*, 1976.
- [156] F. Weiling. A model for the plasma-activated chemical vapor deposition process. *J. Appl. Phys.*, 57 (9), 1985.
- [157] A. H. E. Breuls, M. J. N. Van Stralen, and A. H. Van Bergen. Method of manufacturing an optical fiber, a preform rod and a jacket tube as well as the optical fiber manufactured therewith. *Plasma Optical Fibre B.V., Eindhoven (NL)*, (US 6,849,307 B2), 2005.
- [158] M. Moisan, R. Pantel, A. Ricard, V. M. M. Glaude, P. Leprince, and W. P. Allis. Distribution radiale de la densité électronique et de la densité des atomes excités dans une colonne de plasma produite par une onde de surface. *Revue de Physique Appliquée (Paris)*, 15(8), 1383–1397, 1980.



- [159] P. Geittner, H. J. Hagemann, J. Warnier, F. Weling, and H. Wilson. Reduction of geometric taper losses in the pcvd process. *Electronic Letters*, 21(19), 870, 1985.
- [160] V. L. Y. Loke, T. A. Nieminen, S. J. Parkin, N. R. Heckenberg, and H. Rubinsztein-Dunlop. Fdfd/t-matrix hybrid method. *Journal of Quantitative Spectroscopy and Radiative Transfer*, 106(1-3), 274 – 284, 2007. IX Conference on Electromagnetic and Light Scattering by Non-Spherical Particles.
- [161] D. Mihailova, J. van Dijk, M. Grozeva, G. Degrez, and J. J. A. M. van der Mullen. Towards a reduced chemistry module of a he–ar–cu hollow cathode discharge. *Journal of Physics D: Applied Physics*, 44(19), 194001, 2011.
- [162] K.C.A Smith and R.E. Alley. *Electrical circuits: an introduction*. Electronics texts for engineers and scientists. Cambridge University Press, 1992.
- [163] J. Bird. *Electrical circuit theory and technology*. Electrical circuit theory and technology series. Newnes, 2007.
- [164] I. P. Ganachev. Shibaura Mechatronics Corporation, Yokohama 247-8560, Japan.

---

## Acknowledgements

---

The thesis that you hold in your hands is the result of more than four year work. This would not have been possible without the help and support of a number of persons that I want to thank.

I would like to express my gratitude to my supervisor Joost van der Mullen. Thanks for having always time to discuss, and being such a good boss and better person. This thesis would not have been possible without you, your guidance, and all the comments during these last four years and especially during the writing period. Thanks. I cannot forget your wife, Simona to whom I owe a big 'thank you' for sharing Joost with me, even during Christmas and Easter.

I wish to thank Jan van Dijk for all the help and guidance with Plasimo and all my work, and also his comments about the manuscript. I am also grateful to him for showing me the Eindhoven Style, and infecting me with his love for this city, which I consider also mine.

Thanks to the employees of Draka Comteq, especially to Mathé van Stralen and Igor Milicevic. In particular, I would like to thank Mathé for his guidance and supervision especially at the beginning of this journey. Thanks for teaching me Matlab, Latex and everything I know about the exciting world of fibre production.

Thanks to Gerjan Hagelaar for all your invaluable comments on this work.

Thanks to Emile for all the interesting discussion that we have related and un-related to this thesis.

Thanks to Efe Kemaneci for all the discussion and comments, particularly on the error analysis of the electromagnetic model. I owe you a few drinks, my friend.

Thanks to all the people in EPG group, especially to its group leader Gerrit Kroesen, and to Rina for being the best secretary ever, and all the members of the Plasimo team, in particular Wouter, Kim.

Thanks to my office mates, Mark Beks, Sara Rahimi and Ana Sobota for the nice ambience that they created in the office and their sense of humour. It was especially nice to have Ana writing her thesis at the same time as me. Thanks for the support.

Thanks to Jose for being such a good friend and sharing so many good moments since we met around 10 years ago.

Thanks to Katia and Dani for sharing such a good time together and being very good friends. They form an incredible couple and I am sure they will create the best family in the world. They also saved me from starving countless times. Thanks a lot.

Thanks to Diana for being the best friend I will ever have. Thanks for helping me in so many moments, being there and supporting me while I was writing and during the last 4 years, of course.

Thanks to my best Spanish friends Vanessa and Isaac, they are the sweetest couple in the world and during some period they even 'adopted' me. We have shared a lot, and I am sure we will be friends for many more years. I am also sure that they are going to be very happy together and create the best family ever.

Thanks to my former professors Antonio Sola and Antonio Gamero for the fruitful discussions.

Thanks to Eindhoven and its people, for being a place I can call home ('ik heb eigenlijk nooit last van heimwee gehad').

I want to end with some Spanish words dedicated to my family: my parents Manolo and Conchi, my brother Carlos and sister Patricia:

A mis padres: Gracias por todo, desde que nacimos nos habéis apoyado a mí y a mis hermanos y sacado fuerzas de donde no había para que encontráramos nuestro camino. Nunca os habéis rendido, nunca os habéis conformado, siempre habéis luchado por lo que más amáis en la vida: vuestra familia. Nunca podre pagaros la mejor herencia que una persona puede recibir de su padres: Una Educación, Unos Valores y la capacidad de amar y querer a otras personas. Y se que siempre seguiréis allí. A mi hermanos lo mismo, os quiero y aquí estoy para lo que necesitéis, como sé que vosotros estáis para lo que necesite. Os quiero a todos. Besos.

The above words deserve to be read by everybody, so they are translated here:

To my parents: Thanks for everything, since we were born you have supported us, me and my brother and sister, and use all your strength, even when there was nothing left, to give me the chance to find my way. You never surrendered, you never conformed, you always fought for what you love the most in your life: your family. And you will be there for us always, I am sure. To my brother and sisters the same applies, I am here for everything you need, in the same way I know you will be there for me. I love you. Kisses.

---

## Curriculum Vitae

---

**12 September 1982**

Born in Córdoba, Spain

**1996-2000**

Secondary Education at Blas Infante high school, Córdoba, Spain

**2000-2005**

B.Sc. + M.Sc. in Physics, University of Córdoba, Spain

**2006-2011**

Ph.D. Project at the Group Elementary Processes in Gas Discharges, Department of Applied Physics, Eindhoven University of Technology, Eindhoven, The Netherlands. Subject: Modelling of Microwave Induced Plasmas: The interplay between electromagnetism, plasma chemistry and transport.

